# Modeling of turbulence and acoustics in complex compressible flows using Theory, Large Eddy Simulation and Machine Learning

Alexis Giauque

Université Claude Bernard Lyon 1

ÉCOLE CENTRALE LYON

N° identificateur : 2024 HDR XXX

Année 2024

# HABILITATION A DIRIGER DES RECHERCHES

**Spécialité :**
**Mécanique des Fluides**

Soutenue publiquement
le 04/07/2024 par

**Alexis GIAUQUE**

---

# Modeling of turbulence and acoustics in complex compressible flows using Theory, Large Eddy Simulation and Machine Learning

---

Devant le jury composé de :

| | | | |
|---|---|---|---|
| Guardone, Alberto | Professeur | Politecnico di Milano | Rapporteur |
| Gicquel, Laurent | Docteur HdR | CERFACS | Rapporteur |
| Balarac, Guillaume | Professeur | Ense3 UGA | Rapporteur |
| Moreau, Stéphane | Professeur | Univ. Sherbrooke | Examinateur |
| Trontin, Pierre | Professeur | UCBL (Lyon I) | Examinateur |
| Pecnik, René | Professeur | Univ. Delft | Examinateur |
| Di Mare, Francesca | Professeure | Ruhr-Univ. Bochum | Examinatrice |
| Bailly, Christophe | Professeur | ECL | Examinateur |

**Laboratoire de Mécanique des Fluides et d'Acoustique (LMFA) - UMR 5509**

# Thanks

So many people should be mentioned in this section!
Let me start by acknowledging the work of the reviewers of this manuscript : Alberto Guardone, Guillaume Balarac and Laurent Gicquel. All the members of the jury should also be thanked for their work in the evaluation of this work : Stéphane Moreau, Pierre Trontin, René Pecnik and Francesca Di Mare. A special mention to you Christophe Bailly who accepted to be part of the jury even though you already reviewed my PhD!

The CFD team at CERFACS has my deepest thoughts. A very large thank you to all of you and especially to the young and the "not so young anymore" people with whom I shared so many things : Gabriel Staffelbach thank you for all the incredible work you did with AVBP over the years and good luck (do you need it?) at ONERA. Thanks Florent Duchaine, Olivier Vermorel, Nicolas Odier, Guillaume Daviller, Antoine Dauptain, Jérôme Dombard, and of course Eléonore Riber, Bénedicte Cuenot, Michelle Campassens, Chantal Nasri and so many others! Keep on the good work under the vigilant eye of Thierry Poinsot. Just kidding ;-) - or am I? Ok. Thierry, if you read it I should say that a lot of what I did I owe it to the environment you created in the 1990's at CERFACS and brought to this crazy expertise level. So thank you for all that. Of course at this moment I also think to you Simon Mendez, Franck Nicoud, Laurent Selle, Ghislain Lartigue, Laurent Benoit, Marta Garcia and all those who were part of the team that I met and whose company I enjoyed.

The ACOU team team at ONERA also has a good place in my mind when it comes to this section. I know the team is not called like that anymore but hey you guys will always be ACOU to me. A very large thank you to you Maxime Huet. Maxime, I think the entropy noise part of my work would definitely not have been the same without you! Many thanks to Jun Zheng who had to be my first supervised PhD student (there always has to be one ;-). My thoughts to Fabrice Falissard, Sylvette Canard, Yves Delrieux, Alain Chélius, Thomas Le Garrec, Ingrid Legriffon, Gabriel Reboul, Stéphanie Péron and everyone I met while working in this so nice office building in Châtillon (ok maybe a bit old...but with a good view over Paris!).
My time at ONERA also leads me to thank members of the EM2C lab at CentraleSupelec, Sebastien Ducruix, Franck Richecoeur and of course Sébastien Candel for their incredible support and trust.

It has now been ten years that I work at LMFA and I met so many interesting and nice people that I won't be able to cite them all but let me thank a few of them in particular. Thank you Jérôme Boudet, with whom I push LES to its limits every time I get the chance. I really enjoy working with you! Also a very large thank you to you Christophe Corre who trusted me when I came in 2015 with only very few results regarding dense gas flows! Many thanks to Aurélien Vadrot and Jean Al Am with whom we did great work during their PhDs. I was so lucky to find you both! Martin Buisson, thank you for bearing me even when we swear like carters in the office because

the code does not even compile! I hope we can finally find a way to work together in the near future. All my thought also go to Yannick Rozenberg and his family. I miss you so much my friend. To say the truth, I could mention almost everyone at LMFA because this is really a great place to be when one wants to be at the forefront of research and yet find time to have a laugh every chance one gets. Thank you Vincent Clair, Lucien Vienne, Emmanuel Levesque, Pierre Laucher, Pierre Duquesne, Stephane Aubert, Xavier Ottavy, Christoph Brandstetter, Benoit Paoletti, Sébastien Goguey, Alexandra Schneider, Anne-Lise Fiquet, Didier Dragna, Fatima El Boukhrissi and basically everyone I know!

**As I finish the writing of this document, my thoughts of course go to my wife Anne and my children Alice and Adam. I love you so much. Thank you for all your support over the years!!!**

# Contents

# List of Figures

# List of Tables

# Chapter 1

# Activity Report

## Contents



## 1.1 Personal Information


| | | |
|---|---|---|
| ◇ | Name | Alexis Giauque |
| | Date and place of birth | May 13, 1979 in Paris (75) |
| | Nationality | French |
| | Marital status | Maried |
| | Current position | Associate Professor ECL |
| ◇ | Professional adress | Laboratoire LMFA UMR 5509, Ecole Centrale de Lyon<br>36 Av. Guy de Collongue, 69134 Écully<br>Bat. I11,<br>69134 Ecully |
| | Phone | 04 72 18 61 44 |
| ◇ | email | alexis.giauque@ec-lyon.fr |
| | Web page | http://agiauque.github.io |


## 1.2 Employment and education

◇ **Since September 2013** Associate Professor ECL, Ecole Centrale de Lyon / Laboratoire LMFA, UMR 5509.

◇ **June 2009 - September 2013** Research Engineer at Office National d'Etudes et de Recherches Aérospatiales (ONERA), Département de Simulation Numérique des écoulements et Aéroacoustique (DSNA).

◇ **April 2007 - June 2009** Post Doctoral Fellow, Center for Turbulence Research, Stanford University, California, Etats-Unis

| | |
|---|---|
| Subject | Numerical modeling of combustion noise |
| PI | Heinz Pitsch |

◇ **March 2003 - March 2007** PhD Student, Mechanical Engineering

| | |
|---|---|
| Place | CERFACS – INP Toulouse |
| PhD thesis title | Fonctions de transfert de flamme et énergies des perturbations dans les écoulements réactifs |
| Director | Thierry Poinsot |
| Defense date | le 03 mars 2007 |
| Grade | Très honorable avec félicitations |

Jury

| | | |
|---|---|---|
| *reviewer* | Christophe Bailly | Professeur – Ecole Centrale de Lyon |
| *reviewer* | Joeffrey Searby | Directeur de Recherche CNRS/IRPHE |
| *examiner* | François Vuillot | Ingénieur/Chercheur ONERA/DSNA |
| *examiner* | Sébastien Ducruix | Professeur – Ecole Centrale de Paris |
| *examiner* | Frank Nicoud | Professeur – Université de Montpellier II |
| *director* | Thierry Poinsot | Directeur de Recherche CNRS/IMFT |

## 1.3 Teaching Activities

### 1.3.1 Details of teaching activities

My teaching approach aims to create as much as possible a connection between teaching and research. To achieve this, I rely as much as possible on concrete examples of application and on an illustrated presentation of the major challenges that students will have to face during their careers. I mainly teach at the Ecole Centrale de Lyon at the L3 level for the general fluid mechanics course and at the Master 2 level for more specialized courses dealing with turbines for energy production, aerothermodynamics of turbomachinery, unsteady flows in turbomachinery, combustion for propulsion, as well as transonic aerodynamics. For these courses, emphasis is placed on the practical application of knowledge and experimentation. For example, I am responsible for organizing the practical training component of the general fluid mechanics course, which involves approximately 200 students each semester. This includes hands-on activities using machines for which students themselves must decide on the experiments to be carried out in order to achieve their objectives. Organizing and supervising this training activity is very interesting because it gives students maximum freedom and allows them to develop their analytical skills beyond mere mathematical resolution.

The aerothermodynamics of turbomachinery course (M2), for which I am responsible, has the particularity of introducing a design study phase. Over 8 hours, students will design, starting from a blank sheet, a complete stage of axial compressor and visualize it in 3D using Matlab libraries. They acquire not only skills in turbomachinery design but also capabilities in implementing digital visualization of their results. In the medium term, there are plans to further this logic by allowing students to 3D print their compressor blades at the ECL FabLab.

As part of the propulsion track of the International AeroSpace Master at ECL (M2), I have developed a long-term educational activity (3 months) for students aimed at helping them develop their skills in document synthesis and presentation to their peers. This activity involves groups taking on the role of the professor and presenting a 20-minute lecture focusing on a current research theme in the field of aeronautical propulsion. They present to their peers as well as to a wider audience consisting of doctoral students or researchers. I lead this activity in partnership with a CNRS researcher, further facilitating the transfer of knowledge between research and teaching.

Finally, since 2015, I have been invited every year to Ecole CentraleSupelec to teach the aerothermodynamics of turbomachinery course in a slightly shorter format as part of the 3A energy and aeronautics options (M2).

### 1.3.2 Brief presentation of teaching assigments

All the courses for which I am responsible and in which I participate are part of the initial training at Ecole Centrale de Lyon (or CentraleSupelec). The table below provides a summary of the average workload (approximately 260 hours per year). They may vary slightly from year to year but are representative of the services provided in recent years.

| **Course (Level LMD) responsibility** | **CM** | **TD/BE** | **TP** | **Students** |
|---|---|---|---|---|
| **Ecole Centrale de Lyon** | | | | |
| Mécanique des fluides et énergie (L3) responsable | | 55 | 45 | 25 |
| Introduction au Travail en mode Projet (L3) | | 18 | | 18 |
| Projet d'études (L3) | | 12 | | 6 |
| Accompagnement au projet professionnel (L3/M1) | | 8 | | 6 |
| Projet recherche (M1) | | 16 | | 6 |
| Projet de pré-dimensionnement d'un avion d'affaire (M2) | | 8 | | 25 |
| Aérodynamique transsonique (M2) | | 4 | | 15 |
| Ecoulements instationnaires en turbomachine (M2) responsable | 8 | | | 15 |
| AéroThermodynamique des Turbomachines (M2) responsable | 14 | 8 | 12 | 40 |
| Les turbines pour la production d'énergie (M2) responsable | 4 | 4 | 8 | 55 |
| Combustion pour la propulsion (M2) responsable | 8 | 8 | | 15 |
| Gestion de projet (L3) | | 10 | | 15 |
| TOTAL 250hETD | 34h | 151h | 65h | |
| **CentraleSupelec** | | | | |
| AéroThermodynamique des turbomachines (M2) responsable | 9 | 9 | | 15 |

### 1.3.3 Pedagogical Responsibilities

Since 2017, I have been responsible for the practical training component within the Fluid Mechanics course. This training emphasizes practice and experimentation. In addition to organizational and pedagogical tasks, this responsibility involves supervising (with the assistance of the technical team) the operational status of all test benches present in the two platforms of the MFAE department (more than twenty installations).
Since 2021, I have been responsible for coordinating the Fluid Mechanics and Energy track within the Mechanical Engineering Master's program jointly offered by Ecole Centrale de Lyon and the University of Lyon I. This responsibility includes tasks such as student recruitment (from among the hundred applications received), assisting students in selecting the most appropriate tracks, providing internship opportunities, and monitoring these internships.
Since my arrival at Ecole Centrale de Lyon, I have also participated in three graduation juries. Associated tasks include validating grades and paths, making decisions regarding the

awarding of honors, or, conversely, potential sanctions or exclusions.

## 1.4 Research Activities

### 1.4.1 Publications

I am the author or co-author of 17 articles in international journals with peer review.

| Authors | Title | Journal/Conference | Year |
|---|---|---|---|
| Giauque, A; Selle, L; Gicquel, L; Poinsot, T; Buechner, H; Kaufmann, P; Krebs, W | System identification of a large-scale swirled partially premixed combustor using LES and measurements | **Journal of Turbulence** | 2005 |
| Giauque, A; Poinsot, T; Brear, M; Nicoud, F | Budget of disturbance energy in gaseous reacting flows | Proc. of the Summer Program | 2006 |
| Sengissen, A; Giauque, A; Staffelbach, G; Porta, M; Krebs, W; Kaufmann, P; Poinsot, T | Large eddy simulation of piloting effects on turbulent swirling flames | Proceedings of the Combustion Institute | 2007 |
| Giauque, A; Nicoud, F; Brear, M | Numerical assessment of stability criteria from disturbance energies in gaseous combustion | 13th AIAA/CEAS Aeroacoustics Conference (28th AIAA Aeroacoustics Conference) | 2007 |
| Talei, M; Brear, M; Nicoud, F; Bodony, D; Giauque, A | Transport of disturbance energy in hot and cold turbulent jets | 13th AIAA/CEAS Aeroacoustics Conference (28th AIAA Aeroacoustics Conference) | 2007 |
| Giauque, A; Birbaud, AL; Pitsch, H | Entropy generated noise: a comparison between compressible simulations and Golstein's acoustic analogy | APS Division of Fluid Dynamics Meeting Abstracts | 2007 |
| Giauque, A; Pitsch, H | Detailed modeling of combustion noise using a computational aeroacoustics model | Stanford CTR Annual Research Briefs | 2007 |
| Giauque, A | Flame transfer function and disturbance energies in gaseous reacting flows | PhD thesis | 2007 |
| Giauque, A; Poinsot, T; Nicoud, F | Validation of a flame transfer function reconstruction method for complex turbulent configurations | 14th AIAA/CEAS Aeroacoustics Conference (29th AIAA Aeroacoustics Conference) | 2008 |
| Giauque, A; Pitsch, H | Detailed modeling of combustion noise using a hydrodynamic/acoustic splitting model | Center for Turbulence Research, Annual Research Briefs | 2008 |
| Delrieux, Y; Chelius, A; Giauque, A; Canard, S.; Falissard, F; Beaumier, P.; Ortun, B.; Decours, J.; Servera, G | An overview of Onera aeroacoustic activities in the framework of propellers and open rotors | 4th CEAS-ASC Workshop, Warsaw | 2010 |
| Brear, MJ; Nicoud, F; Talei, M; Giauque, A; Hawkes, E R | Disturbance energy transport and sound production in gaseous combustion | **Journal of Fluid Mechanics** | 2012 |
| Giauque, A; Ortun, B; Rodriguez, B; Caruelle, B | Numerical error analysis with application to transonic propeller aeroacoustics | **Computers & Fluids** | 2012 |
| Giauque, A; Huet, M; Clero, F | Analytical analysis of indirect combustion noise in subcritical nozzles | **Journal of Engineering for Gas Turbines and Power** | 2012 |
| Huet, M; Giauque, A | A nonlinear model for indirect combustion noise through a compact nozzle | **Journal of Fluid Mechanics** | 2013 |
| Giauque, A; Huet, M; Cléro, F; Ducruix, S; Richecoeur, F | Thermoacoustic shape optimization of a subsonic nozzle | **Journal of Engineering for Gas Turbines and Power** | 2013 |
| Zheng, J; Huet, M; Giauque, A; Cléro, F; Ducruix, S | A 2D-axisymmetric analytical model for the estimation of indirect combustion noise in nozzle flows | 21st AIAA/CEAS Aeroacoustics Conference | 2015 |
| Giauque, A; Boudet, J; Ma, H; Wei, W | Large Eddy Simulation of an axial compressor rotor passage: Preliminary comparison with experimental measurements | CFM 2015-22ème Congrès Français de Mécanique | 2015 |
| Giauque, A; Corre, C; Menghetti, M | Direct numerical simulations of homogeneous isotropic turbulence in a dense gas | Journal of Physics: Conference Series | 2017 |

| | | | |
|---|---|---|---|
| Giauque, A; Corre, C; Vadrot, A | Direct Numerical Simulation of Turbulent Dense Gas Flows | International Seminar on Non-Ideal Compressible-Fluid Dynamics for Propulsion & Power | 2018 |
| Vadrot, A; Giauque, A; Corre, C | Investigation of turbulent dense gas flows with direct numerical simulation | Congrès français de mécanique. AFM | 2019 |
| Emmanuelli, A; Zheng, J; Huet, M; Giauque, A; Le Garrec, T; Ducruix, S | Description and application of a 2D-axisymmetric model for entropy noise in nozzle flows | **Journal of Sound and Vibration** | 2020 |
| Boudet, J; Giauque, A | Adaptation and evaluation of a weak recycling strategy for inflow boundary layers in large-eddy simulation | **Computers & Fluids** | 2020 |
| Giauque, A; Corre, C; Vadrot, A | Direct numerical simulations of forced homogeneous isotropic turbulence in a dense gas | **Journal of Turbulence** | 2020 |
| Vadrot, A; Giauque, A; Corre, C | Analysis of turbulence characteristics in a temporal dense gas compressible mixing layer using direct numerical simulation | **Journal of Fluid Mechanics** | 2020 |
| Giauque, A; Vadrot, A; Errante, P; Corre, C | Towards subgrid-scale turbulence modeling in dense gas flows | Proceedings of NICFD 2020 | 2021 |
| Al-Am, J; Clair, V; Giauque, A; Boudet, J; Gea-Aguilera, F | A parametric study on the LES numerical setup to investigate fan/OGV broadband noise | **International Journal of Turbomachinery, Propulsion and Power** | 2021 |
| Vadrot, A; Giauque, A; Corre, C | Direct numerical simulations of temporal compressible mixing layers in a BetheZel'dovichThompson dense gas: influence of the convective Mach number | **Journal of Fluid Mechanics** | 2021 |
| Giauque, A; Vadrot, A; Errante, P; Corre, C | A priori analysis of subgrid-scale terms in compressible transcritical real gas flows | **Physics of Fluids** | 2021 |
| Al-Am, J; Clair, V; Giauque, A; Boudet, J; Gea-Aguilera, F | Effet du débit sur le bruit propre d'un étage soufflante/redresseur en régime d'approche | Congrès des Jeunes Chercheurs en Mécanique-Méca-J | 2021 |
| Al Am, J; Clair, V; Giauque, A; Boudet, J; Gea-Aguilera, F | Direct noise predictions of fan broadband noise using LES and analytical models | 28th AIAA/CEAS Aeroacoustics 2022 Conference | 2022 |
| Al Am, J; Clair, V; Giauque, A; Boudet, J; Gea-Aguilera, F | On the effects of a separation bubble on fan noise | **Journal of Sound and Vibration** | 2022 |
| Al-Am, J; Clair, V; Giauque, A; Boudet, J; Gea-Aguilera, F | Fan/OGV broadband noise predictions using LES | EuroHPC Summit Week 2022 | 2022 |
| Al Am, J; Clair, V; Giauque, A; Boudet, J; Gea-Aguilera, F | Effet du débit sur le bruit propre dune étage soufflante/redresseur en présence dune bulle de recirculation | 16ème Congrès Français d'Acoustique, CFA2022 | 2022 |
| Al-Am, J; Clair, V; Giauque, A; Boudet, J; Gea-Aguilera, F | Aeroacoustic analysis of the tip-leakage flow of an ultrahigh bypass ratio fan stage | **Physics of Fluids** | 2023 |
| Giauque, A; Vadrot, A; Corre, C | Development, Validation and Application of an ANN-Based Large Eddy Simulation Subgrid-Scale Turbulence Model for Dense Gas Flows | Proceedings of NICFD 2022 | 2023 |
| Schuster, D; Ince, Y; Giauque, A; Corre, C | Assessment of Density and Compressibility Corrections for RANS Simulations of Real Gas Flows Using SU2 | Proceedings of NICFD 2022 | 2023 |
| Al Am, J; Clair, V; Giauque, A; Boudet, J; Gea-Aguilera, F | Direct noise predictions of a 360 full fan stage using LES | AIAA AVIATION 2023 Forum | 2023 |
| Giauque, A; Schuster, D; Corre, C | High-fidelity numerical investigation of a real gas annular cascade with experimental validation | **Physics of Fluids** | 2023 |
| Giauque, A; Giguet, C; Vadrot, A; Corre, C | A priori test of Large-Eddy Simulation models for the Sub-Grid Scale turbulent stress tensor in perfect and transcritical compressible real gas Homogeneous Isotropic Turbulence | **Computers & Fluids** | 2024 |

### 1.4.2 Doctoral and scientific supervision

Since 2018, I have had the opportunity to supervise or co-supervise 7 Master internships (M1 or M2), 6 doctoral thesis (including 4 ongoing), and two post-doctoral positions.

**Master internships**

- 2018 (Aurélien Vadrot - niveau M2) Simulation of turbulence in organic dense gas flows
- 2019 (Jean Al Am - niveau M2) Large Eddy Simulation for Fan Broadband Noise Applications
- 2021 (Corentin Giguet - niveau M1) Machine-learning-assisted turbulence modeling in dense gas flows
- 2021 (Fares Saad Habibi - niveau M2) Dynamics of Corner Separation in a linear compressor cascade - Investigation with Large Eddy Simulation (LES)
- 2022 (Yusuf Ince - niveau M2) Simulation of dense gas flows using the SU2 solver
- 2023 (Antonio Lattanzio - niveau M1) Machine-learning-assisted turbulence modeling in dense gas flows
- 2023 (Hassan Ali - niveau M2) Machine-learning-assisted turbulence modeling in dense gas flows

**PhD thesis**

- 2018-2021 (Aurélien Vadrot) Modélisation de la turbulence dans les écoulements compressibles de gaz denses ; Ecole Centrale de Lyon (involvement 60%)
- 2019-2022 (Jean Al Am) Modélisation du bruit large-bande de soufflantes aéronautiques ; Ecole Centrale de Lyon (involvement 33%)
- 2022-2025 (Allan Beurville) Modélisation du bruit large-bande de soufflantes aéronautiques ; Ecole Centrale de Lyon (involvement 33%)
- 2023-2026 (Isa Helal) Modélisation de la turbulence dans les écoulements compressibles de gaz denses à l'aide de l'apprentissage automatique ; Ecole Centrale de Lyon (involvement 80%)
- 2023-2026 (Pierre-Louis Pape) Modélisation du bruit large-bande de soufflantes aéronautiquesănon-carénées ; Ecole Centrale de Lyon (involvement 33%)
- 2024-2027 (Anubhave Gokhale) Interaction Fluide-Structure : Etude des instabilités non-synchones dans les turbomachines ; Ecole Centrale de Lyon (involvement 40%)

**Post-doctoral positions**

- 2019-2021 (Paolo Errante) Modélisation de la turbulence dans les écoulements compressibles de gaz denses ; Ecole Centrale de Lyon
- 2021-2022 (Dominik Schuster) Modélisation de la turbulence dans les écoulements compressibles de gaz denses ; Ecole Centrale de Lyon

### 1.4.3 Dissemination

I evaluate approximately one project per year for the open calls of the ANR.
In 2021, I was solicited as an expert to evaluate a project for an ERC Advanced Grant.
Since 2021, I have been a nominated member of the international scientific council of the "International Conference on Flow Dynamics" organized annually by Tohoku University in Japan.
I participate in reviewing about 4 articles per year for various international peer-reviewed

journals such as "Journal of Fluid Mechanics" or "Physics of Fluids".
I participated in an external thesis jury as an examiner on 06/02/2018 (Mélissa Férand) on the topic of Far-field combustion noise modeling of turbofan engine at Toulouse INPT.
I participated in an external thesis jury as an examiner on 05/10/2023 (Adrien Grenouilloux) on the topic of high-fidelity simulation of the aerothermal performances of a turbofan thrust reverser at CORIA, Rouen.
In 2019, I organized the launch seminar of the ANR JCJC EDGES project (10 participants), which brought together researchers from LEGI (Grenoble), INRIA (Paris), and Cerfacs (Toulouse) for a day.
In 2021, I had the opportunity to present my research work on turbomachinery on the RCF radio program "Dis Pourquoi?".
Since 2015, I have been an active member of the HAIDA research network (challenges in aerothermal and aerodynamic research). This research network, initiated by Safran in 2012, aims to accelerate research and development in the fields of aerothermics and aerodynamics by strengthening networking with research laboratories, partners of the Group.
My research activities, particularly in fan noise modeling, have led me to take an active role in the ANR-SAFRAN ARENA industrial research chair, launched in 2019 and led by C. Bailly at LMFA.

### 1.4.4 Scientific responsibilities

Between 2018 and 2022, I led the working group formed by a doctoral student, a postdoctoral researcher, and another permanent researcher through the ANR EDGES project. This leadership involved weekly meetings as well as tracking of the schedule and expenses.
Since 2022, I have been leading a new working group (currently informal) focused on the use of artificial intelligence for numerical simulation of fluid flows. This group includes approximately 8 participants from the University of Lyon 1 and Ecole Centrale de Lyon. We meet every 3 months to review each other's progress and share best practices in the field of AI.
In 2022/2023, I obtained two European PRACE grants, the first one (LESFAN-30MCPUh) on broadband noise in turbomachinery and the second one (EDGES-40MCPUh) on turbulence modeling in dense gases.

Below is the list of the main national and international projects that I coordinate or have participated in the past five years:

- FLORA (European Project 2018-2022), FLOw control in RAdial compressor  Budget 450k — Role: expertise and participation in a research action
- ARENA (ANR-SAFRAN Industrial Chair 2019-2023), AeRoacoustics of nEw eNgine Architectures in aeronautics  Budget 2M — Role: leading a research action
- EDGES (ANR JCJC 2018-2022), Modeling turbulent flows of dense gas using Large-Eddy Simulation  Budget 400k — Role: project direction, management, and administrative and financial coordination
- M3AT (CNRS-INSIS 2021), Machine learning-assisted modeling of turbulence in dense gas flows – Budget 10k — Role: project direction, management, and administrative and financial coordination
- CONDOR (ANR-SAFRAN Industrial Chair 2023-2027), aeroelastiCs Of faNs anD cOmpressors  Budget 2M — Role: participation in research action
- AUFRANDE (European CoFund 2023-2027), Australia-France Network of Doctoral Excellence  Budget 16M — Role: supervision of a doctoral project

## 1.5 Administrative and collective activities

In 2021, I was elected to the Administrative Board of the Ecole Centrale de Lyon for a 4-year term to participate in defining and monitoring the major directions of research and teaching at the institution.
This responsibility involves various tasks. The Administrative Board, in its restricted formation, meets approximately every 3 weeks to address all matters related to the careers of the faculty members of the ECL (such as advancement, career development plans, restructuring, etc.).
Additionally, I serve as a rapporteur for the disciplinary commission of the institution. In this role, I am required to hear from all parties involved in matters falling under this commission and then write summary notes to enable the commission to make the best decisions.

# Chapter 2

## General Introduction–*Non-linear interactions in a viscous heat-conducting compressible gas*

While I was working at CERFACS during my PhD in 2005, a paper from 1958 had a strong impact on me and (I did not know that at the time) would shape the research path I would later follow. That paper is entitled: "Non-linear interactions in a viscous heat-conducting compressible gas", Journal of Fluid Mechanics, by Chu B.-T., Kovasznay L.S.G. in 1958. Its abstract starts as follows:

**The linearized equations of motion show that in a viscous heat-conducting compressible medium three modes of fluctuations exist, each one of which is a familiar type of disturbance.** *The vorticity mode occurs in an incompressible turbulent flow, the entropy mode is familiar as temperature fluctuations in low speed turbulent heat transfer problems, and the sound mode is the subject of conventional acoustics. A consistent higher order perturbation theory is presented with the only restrictions being that the Prandtl number is 3/4 and the viscosity and heat conductivity are monotonic functions of the temperature alone. The theory is based on expansion of the disturbance fields in powers of an amplitude parameter . The non-linearity of the full Navier-Stokes equations can be interpreted as interaction between the three basic modes;* **in order to help physical insight the interactions are classed as mass-like, force-like, and heat-like effects.**. Since this article, those physical interactions have been renamed as "entropy", "acoustic" and "vorticity" modes. but the framework of their interactions which the authors describe in their study remains completely relevant to this day.

A few years back, as I was asked what was my research topics, this article came back to my mind as it perfectly explains the motivations that are behind all the research initiatives I have lead since then. Fluctuations in fluids are everywhere, from large pressure changes that characterize hurricanes to the heat felt when opening the door of the oven. In a sense understanding the formation, propagation, interaction and dissipation of these fluctuations in fluids is as old as physical science itself. My goal is to bring my own contribution to this overarching endeavor. Before diving into the specifics of each research topic I have been exploring these last 15 to 20 years, I would like to have a few words about high fidelity simulation tools and the evolution of computational power as they will also reflect in my research and in the future directions it might take.

Since the dawn of the computer era, researchers have designed computational algorithms and solvers to predict and comprehend the behavior of fluids and more especially of turbulence and waves in systems that would become more complex every year. In the 1980's the computational power available in laboratories made possible the Direct Numerical Simulation of turbulent channel flows at moderate Reynolds numbers and turbulence modeling

gained a new tool that would reveal itself very useful. It was soon realized however that if high fidelity simulation had to be pursued, DNS in itself would never enable researchers and engineers to reach industrial Reynolds numbers. Fueled by Moore's law, the 1990's and 2000's saw the rise of Large Eddy Simulation, with most of the turbulence models (necessary to account for the unresolved part of the turbulent spectrum) developed at that time. The very positive byproduct of the explosion of computational power that occurred during this period was the ever increasing capabilities made available for the understanding of complex flows, including combustion, multiphase, aeroacoustics, etc...

This document, which is intended to summarize the research I made during the last 20 years, focuses on the three main research topics I have been pursuing. First, I found important to better describe the equations used to analyze the flow and the specifics of the AVBP solver used in numerous research actions over the years. We then dwelve into numerical combustion and more especially into numerical combustion noise with a focus on indirect combustion noise. Even though I don't have currently any active research initiative on that topic, I would like to take the opportunity of this document to present the main results we obtained over the years with the hope that they will be better understood and possibly more widely spread among the community. The next two chapters, focus on my present research and deal with (i) aeronautical fan noise simulation and modeling and (ii) turbulence in dense gas flows modeling. Presenting the details of my research for those two topics will also give me the opportunity of clarifying the role and implication of Machine Learning. At the end of each chapter, further research initiatives are presented, some with very real present implications and some with more speculative potentials. Even though I know there is an acknowledgement section in this document I cannot help but thank all the persons I am in debt to who contributed sometimes very significantly to all the results we gathered over the years.

## Layout of the manuscript – research topics

**Chapter 3 : Combustion noise modeling:**
This chapter describes in more details my contributions regarding combustion noise. The question of the modeling of the Flame Transfer Functions (FTF) for the analysis of thermo-acoustic stability maps is first adressed. Results concerning the analytical modeling of indirect combustion noise as well as the optimal design implications are then presented. Finally, the work devoted to the derivation and analysis of disturbance energies in reacting flows is summarized.

**Chapter 4 : Broadband rotor noise modeling:**
Fan noise sources are presented as well as the LMFA testing facility hosting the ECL5 Fan/OGV stage configuration. After a quick summary of the numerical setup for LES, the numerous results obtained through numerical analysis are described. Namely, the impact on the acoustics of a recirculation bubble is presented. The tip gap region is analyzed through its peculiar aerodynamic and aeroacoustic behavior. Finally, the 360° results are confronted to the experiments.

**Chapter 5 : Turbulence in dense gas flows modeling:**
In this chapter, after a brief introduction to the specifics of dense gas flows, DNS of academic flows involving dense gases are presented. The peculiar features of turbulence in Homogeneous Isotropic Turbulence (HIT) and compressible mixing layer are analyzed. The behavior of SubGrid-Scale (SGS) terms is explored through a-priori filtering and through the analysis of the performance of existing SGS model. New SGS models are developed using machine learning techniques (especially Artificial Neural Networks). Their merits are analyzed a-priori and a-posteriori using experimental results from Cambridge University.

# Chapter 3

# Conservation equations and Numerical models for perfect and dense gas flow LES and DNS

## Contents

Most of the research work I have done required the use of precise and efficient LES and DNS CFD solvers. Since my PhD thesis, I have add the opportunity to use numerous CFD solvers such as SU2, OpenFoam, elsA, CEDRE, Fluent, CFX,... Yet, in numerous occasions I have had the opportunity to observe the undoubtful relevance of the solver AVBP, developed at CERFACS. Although some of the work presented in this document could have been achieved with a different solver (and some actually has been), certainly not all of it could have been done. Although they appear in good place in the Thanks section, let me take this opportunity to acknowledge the tremendous work done by the developing team of AVBP at CERFACS.

This section is by no means a complete description of the numerical tool AVBP, nor of its methods. It is merely a compilation of the specific aspects of it that have proven extremely useful to adress the various research topics I looked into over the years. Some of them had to be implemented by us within the solver in particular to account for the dense gas aspects of the flows we were interested in.

## 3.1 The AVBP solver

This research initiative was accomplished by solving the governing equations of Large Eddy Simulations (LES) and Direct Numerical Simulation (DNS) using the AVBP solver [29], an explicit, unstructured, fully compressible LES solver developed by CERFACS [29].
AVBP is based on the finite volume (FV) method. There are two common techniques for implementing FV methods: the so called cell-vertex and the cell-centered formulation. In the latter, not used in AVBP, discrete solution values are stored at the center of the control volumes (or grid cells), and neighboring values are averaged across cell boundaries in order to calculate fluxes. In the alternative cell-vertex technique, used as underlying numerical discretization method of AVBP, the discrete values of the conserved variables are stored at the cell vertices (or grid nodes). The mean values of the fluxes are then obtained by averaging along the cell edges as illustrated in Figure 3.1.
AVBP is written in Fortran 90. It has been widely ported to all state-of-the-art architec-

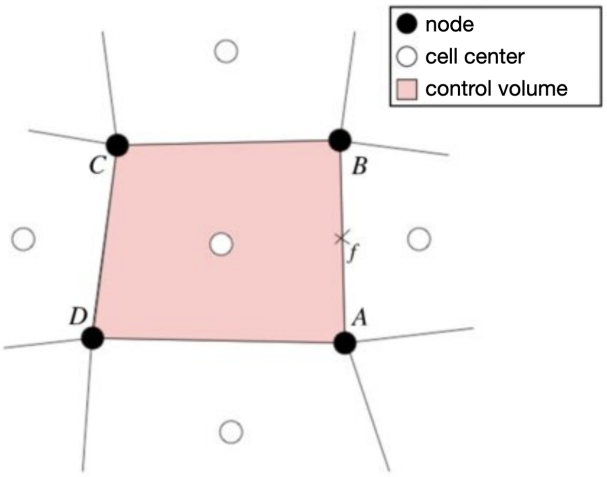


Figure 3.1: Mesh used with the cell-vertex method. The control volumes (highlighted) are defined by the cells, and the variables are stored at the nodes. Figure inspired from Nicolas Lamarque PhD Thesis [1]

tures available today (X86, Power, Bluegene, XeonPhi, etc.). The solver relies on the MPI

library for parallel communication. Based on a domain decomposition method, parallel partitioning uses the ParMETIS or PTSCOTCH libraries. Input/output for the large data sets uses Parallel HDF5. Off-line partitioning can also use the METIS library or the RIB and RCB algorithms. To avoid memory bottlenecks and CPU resources waste, the partitioning mapping is only generated in the first execution of the code (or off-line) and then used as a cached element for the rest of the computation. An md5 signature check between the mesh and the mapping avoids any computational mishap.
To illustrate the parallelism capabilities of the software, strong scaling results for a 300M and 1Billion element cases are reported in the in Figure 3.2. In both case full nodes were used ( 128 mpi per node ) and flat MPI. Performance is excellent up to 65k and 131k cores respectively.

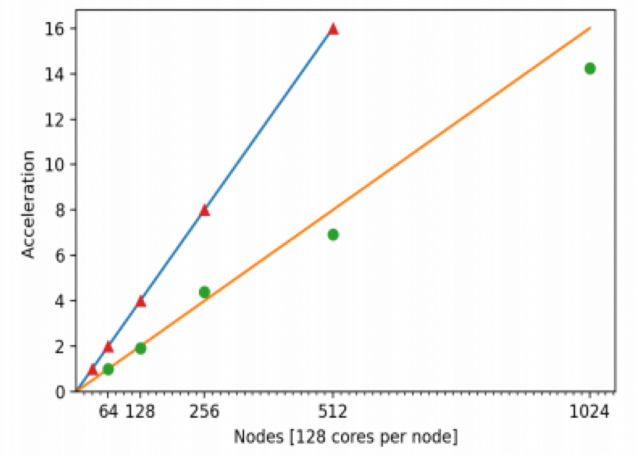


Figure 3.2: strong scaling for AVBP on IRENE Rome - 300M and 1B element cases. Results reported in iterations per second (higher is better)

## 3.2 Conservation equations and Numerical models for perfect and dense gas flow LES and DNS

### 3.2.1 Filtered equations and Subgrid-scale terms

The Navier-Stokes equations for the conservative quantities density $\rho$, momentum $\rho\boldsymbol{u}$ and density weighted total energy $\rho E$ read, using the implicit Einstein summation:

$$\begin{aligned}
\frac{\partial \rho}{\partial t} + \frac{\partial (\rho u_j)}{\partial x_j} &= 0 \\
\frac{\partial \rho u_i}{\partial t} + \frac{\partial (\rho u_i u_j)}{\partial x_j} &= -\frac{\partial p}{\partial x_i} + \frac{\partial \tau_{ij}}{\partial x_j} \\
\frac{\partial \rho E}{\partial t} + \frac{\partial (\rho E u_j)}{\partial x_j} &= -\frac{\partial (p u_j)}{\partial x_j} + \frac{\partial (\tau_{ij} u_i)}{\partial x_j} - \frac{\partial q_j}{\partial x_j}
\end{aligned} \tag{3.1}$$

with $p$ the pressure, $\tau_{ij} = \mu\left(\frac{\partial u_i}{\partial x_j} + \frac{\partial u_j}{\partial x_i} - \frac{2}{3}\delta_{ij}\frac{\partial u_k}{\partial x_k}\right)$ the viscous stress tensor ($\mu$ being the dynamic viscosity), $E = e + \frac{1}{2}u_i u_i$ is the total specific energy and $q_j = -\kappa\frac{\partial T}{\partial x_j}$ the heat flux following Fourier's law, $\kappa$ being the thermal conductivity. The viscosity $\mu$ and conductivity $\kappa$ are computed using the Chung's constitutive equations [30] in the case of a real gas (see section 3.3.3), and $\mu$ following Sutherland's law [31] when a perfect gas is considered.

Those dynamic equations are completed by an EoS describing the behavior of the fluid. When necessary for real gases, the calorific and thermal Martin & Hou (MH) EoS (Equations (3.2)) are used, with $b = v_c(1-(-31.888Z_c+20.533)/15)$, $k = 5.475$ and $A_i$, $B_i$, $C_i$ numerical constants [27, 28] (see section 3.3.4). $Z_c$ is the compressibility factor, $T_c$ and $v_c$ are the critical temperature and critical specific volume, respectively and the notation $(\cdot)_{ref}$ refers to the reference state.

$$\begin{aligned} \text{MH}_T\text{: } p &= \frac{RT}{v-b} + \sum_{i=2}^{5} \frac{A_i + B_i T + C_i e^{-kT/T_c}}{(v-b)^i} \\ \text{MH}_C\text{: } E_{int} &= E_{int,ref} + \int_{T_{ref}}^{T} c_v(T')\mathrm{d}T' + \sum_{i=2}^{5} \frac{A_i + C_i(1+kT/T_c)e^{-kT/T_c}}{(i-1)(v-b)^{(i-1)}} \end{aligned} \tag{3.2}$$

Large eddy simulation consists in the filtering of equations (3.1). In AVBP, the filtering is implicit and relies on the grid used for the resolution of these equations. When needed for the a-priori analysis of DNS results, the explicit filtering of a given quantity $f$ results from the convolution of $f$ with a kernel $G(x-\xi)$, as shown in Equation (3.3) with a Gaussian kernel. $\zeta$ is a parameter acting on the filter's selectivity, while $\Delta$ is the filter width. In the following, filtering is done using a Gaussian kernel with $\zeta = 6$ (see Garnier et al. [32]).

$$\begin{aligned} \overline{f}(x) &= \int_\Omega G(x-\xi) f(\xi)\mathrm{d}\xi \\ G(x-\xi) &= \left(\frac{\zeta}{\pi\Delta^2}\right)^{1/2} \exp\left(-\zeta\left(\frac{x-\xi}{\Delta}\right)^2\right) \end{aligned} \tag{3.3}$$

Be the filtering implicit or explicit, the quantity $f$ can then be decomposed into $f = \overline{f} + f'$, where $\overline{f}$ is the filtered (or resolved) term and $f'$ the residual (or SGS) term. Filtering equations (3.1) and assuming commutativity between the filtering operator and temporal derivative or spatial gradient operators (ergodicity assumption) yields the following set of equations:

$$\frac{\partial \overline{\rho}}{\partial t} + \frac{\partial \overline{\rho}\widetilde{u_j}}{\partial x_j} = 0, \tag{3.4}$$

$$\frac{\partial \overline{\rho}\widetilde{u_i}}{\partial t} + \frac{\partial \overline{\rho}\widetilde{u_i}\widetilde{u_j}}{\partial x_j} = -\frac{\partial \overline{p}}{\partial x_i} + \frac{\partial \overline{\tau_{ij}}}{\partial x_j}, \tag{3.5}$$

$$\frac{\partial \overline{\rho}\widetilde{E}}{\partial t} + \frac{\partial \overline{\rho}\widetilde{E u_j}}{\partial x_j} = -\frac{\partial \overline{p u_j}}{\partial x_j} + \frac{\partial \overline{\tau_{ij} u_i}}{\partial x_j} - \frac{\partial \overline{q_j}}{\partial x_j}, \tag{3.6}$$

where $\widetilde{f}$ represents the Favre filtered quantity $\frac{\overline{\rho f}}{\overline{\rho}}$. Some terms (such as $\widetilde{Eu_j}$) are unknown in equations (3.4)-(3.6) because they involve subgrid-scale correlations, the filtered pressure ($\overline{p}$) or temperature ($\overline{T}$).

The filtered pressure $\overline{p}$ and temperature $\overline{T}$ are indeed unknown quantities because there is no commutativity between the filtering operator and the thermal or caloric Martin-Hou EoS (equations 3.2). In the following, the computable temperature and pressure are respectively denoted $\breve{T}$ and $\breve{P}$ (equations (3.9)-(3.10)): they represent the temperature and the pressure computed from the filtered conservative variables.

$$\overline{T} = \overline{\text{MH}_C(\rho, \rho u_i, \rho E)}, \tag{3.7}$$

$$\overline{P} = \overline{\text{MH}_T(T, \rho)}, \tag{3.8}$$

$$\breve{T} = \text{MH}_C(\overline{\rho}, \overline{\rho}\widetilde{u_i}, \overline{\rho}\widetilde{E}) \neq \overline{T}, \tag{3.9}$$

$$\breve{P} = \text{MH}_T(\overline{\rho}, \breve{T}) \neq \overline{P}, \tag{3.10}$$

where $\mathrm{MH}_T$ and $\mathrm{MH}_C$ refer respectively to the thermal and caloric Martin-Hou EoS.

The transport coefficients are also influenced by the filtering process. $\breve{\kappa}$ and $\breve{\mu}$ denote respectively the conductivity and the viscosity computed from the filtered density $\overline{\rho}$ and the available temperature $\breve{T}$. These observations eventually lead to the following set of equations [33] where all subgrid-scale terms are in bold type and labeled and resolved terms are in light:

$$\frac{\partial \overline{\rho}}{\partial t} + \frac{\partial \overline{\rho}\widetilde{u_j}}{\partial x_j} = 0, \tag{3.11}$$

$$\begin{aligned}\frac{\partial \overline{\rho}\widetilde{u_i}}{\partial t} + \frac{\partial \overline{\rho}\widetilde{u_i}\widetilde{u_j}}{\partial x_j} &= -\frac{\partial \breve{p}}{\partial x_i} + \frac{\partial \breve{\tau_{ij}}}{\partial x_j} \\ &\underbrace{-\frac{\boldsymbol{\partial}\left[\overline{\boldsymbol{p}} - \breve{\boldsymbol{p}}\right]}{\boldsymbol{\partial x_i}}}_{\text{Pressure}} \underbrace{+\frac{\boldsymbol{\partial}\left[\overline{\boldsymbol{\tau_{ij}}} - \breve{\boldsymbol{\tau_{ij}}}\right]}{\boldsymbol{\partial x_j}}}_{\text{Viscous}} \underbrace{-\frac{\boldsymbol{\partial \overline{\rho}}\left[\widetilde{\boldsymbol{u_i u_j}} - \widetilde{\boldsymbol{u_i}}\widetilde{\boldsymbol{u_j}}\right]}{\boldsymbol{\partial x_j}}}_{\text{Turbulent stress}},\end{aligned} \tag{3.12}$$

$$\begin{aligned}\frac{\partial \overline{\rho}\widetilde{E}}{\partial t} + \frac{\partial \overline{\rho}\breve{E}\widetilde{u_j}}{\partial x_j} &= -\frac{\partial \breve{p}\widetilde{u_j}}{\partial x_j} + \frac{\partial \breve{\tau_{ij}}\widetilde{u_i}}{\partial x_j} - \frac{\partial \breve{q_j}}{\partial x_j} \\ &\underbrace{-\frac{\boldsymbol{\partial}\left[\overline{\boldsymbol{p u_j}} - \breve{\boldsymbol{p}}\widetilde{\boldsymbol{u_j}}\right]}{\boldsymbol{\partial x_j}}}_{\text{Pressure work}} \underbrace{+\frac{\boldsymbol{\partial}\left[\overline{\boldsymbol{\tau_{ij} u_i}} - \breve{\boldsymbol{\tau_{ij}}}\widetilde{\boldsymbol{u_i}}\right]}{\boldsymbol{\partial x_j}}}_{\text{Viscous work}} \\ &\underbrace{-\frac{\boldsymbol{\partial}\left[\overline{\boldsymbol{q_j}} - \breve{\boldsymbol{q}}_{\boldsymbol{j}}\right]}{\boldsymbol{\partial x_j}}}_{\text{Heat Flux}} \underbrace{-\frac{\boldsymbol{\partial \overline{\rho}}\left[\widetilde{\boldsymbol{E u_j}} - \breve{\boldsymbol{E}}\widetilde{\boldsymbol{u_j}}\right]}{\boldsymbol{\partial x_j}}}_{\text{Energy flux}}\end{aligned} \tag{3.13}$$

Note that $\breve{\tau_{ij}} = \breve{\mu}\left(\frac{\partial \widetilde{u_i}}{\partial x_j} + \frac{\partial \widetilde{u_j}}{\partial x_i} - \frac{2}{3}\frac{\partial \widetilde{u_k}}{\partial x_k}\delta_{ij}\right)$ and $\breve{q_i} = -\breve{\kappa}\frac{\partial \breve{T}}{\partial x_i}$. The set of equations (3.11)-(3.13) is the equivalent for real gases of the "system II" used in Vreman *et al.*[34] for perfect gases. All terms within brackets are unknown.

## 3.3 Wall modeling and Shock capturing

### 3.3.1 Wall modeling

When needed and because the cost of large-eddy simulations (LES) of wall-bounded flows that resolve all the important eddies depends strongly on the Reynolds number, methods to bypass the wall layer are required to perform high-Reynolds-number LES at a reasonable cost. When needed, a turbulent law of the wall is imposed. The model is such that the shear stress $\tau_w$ is assumed to be constant between the wall and the first point and is linked to the shear velocity such that:

$$\tau_w = \rho_w * u^{\star 2}$$

where

$$u^\star = \begin{cases} \sqrt{u\mu_w/(y_w\rho_w)} & \text{Inner region: } y^+ \leq 11.445 \\ (0.41u)/\log(9.2y^+) & \text{Outer region: } y^+ > 11.445 \end{cases}$$

For real/dense gas, it is known since the work of Sciacovelli [35] that turbulent boundary layers are deeply influenced by the nature of the fluid. Since the work of Pecnik [36] an universal scaling has been proposed that enables to better represent the evolution of turbulent boundary layers in dense gas flows. Yet at the time when we started this research topics, this scaling was not known and no model with a better description than the one presented above was available.

### 3.3.2 Shock capturing

A shock capturing methodology is used to preserve the positivity of the solution in regions where very strong gradients exist. To this end, an additional dissipation term proportional to the local velocity divergence is dynamically computed using the approach of Cook and Cabot [37] and added as a source term to the momentum equation. This numerical strategy can be interpreted as a localized modification of the viscous stress tensor $\tau_{ij}$ in which a local hyperviscosity $\beta(\vec{x})$ is added:

$$\tau_{ij\,\text{modified}} = \left(\beta(\vec{x}) - \frac{2}{3}\mu\right)\frac{\partial u_k}{\partial x_k}\delta_{ij} + \mu\left(\frac{\partial u_i}{\partial x_j} + \frac{\partial u_j}{\partial x_i}\right)$$

### 3.3.3 Chung et al. [30] Transport coefficients model – Dense gas only

In order to take into account dense-gas effects, the dense-gas viscosity $\mu$ is written as the sum of two terms:

$$\mu = \mu_k + \mu_p \tag{3.14}$$

where $\mu_k$ a modified dilute-gas viscosity and $\mu_p$ a correction term. Chung et al. [30] prescribe that

$$\mu_k = \mu_0\left[\frac{1}{G} + A_6 Y\right] \tag{3.15}$$

$$\mu_p = 36.44\times10^{-6}\frac{(MT_c)^{1/2}}{v_c^{2/3}}A_7 Y^2 G exp\left[A_8 + A_9(T^\star)^{-1} + A_{10}(T^\star)^{-2}\right] \tag{3.16}$$

$$\text{and } \mu_0 = 40.785\frac{F_c(MT)^{1/2}}{v_c^{2/3}\Omega_v} \tag{3.17}$$

where $M$ is the molecular weight, $T$ the temperature, $T_c$ the critical temperature, $v_c$ the critical volume and all inner parameters such as $A_{6\ldots10}$, $F_c$, $G$, $T^\star$, $Y$, and $\Omega_v$ can be directly computed using the relations detailed in [30].
Using the same approach as for viscosity, the dense-gas thermal conductivity $\kappa$ is computed as:

$$\kappa = \kappa_k + \kappa_p \tag{3.18}$$

with

$$\kappa_k = \kappa_0\left[\frac{1}{H} + B_6 Y\right] \tag{3.19}$$

$$\kappa_p = 3.039\times10^{-4}\sqrt{\frac{T}{M}}\frac{1}{v_c^{2/3}}B_7 Y^2 H \tag{3.20}$$

The dilute-gas component $\kappa_0$ is written as

$$\kappa_0 = 7.452\frac{\mu_0\Psi_\kappa}{M} \tag{3.21}$$

The reader is referred to [30] for the computation of the parameters $H$, $B_{6,7}$ and $\Psi_\kappa$.

### 3.3.4 Martin & Hou [27] Equation of State – Dense gas only

The calorific and thermal Martin & Hou (MH) EoS are used in this study:

$$\begin{aligned} p &= \frac{RT}{v-b} + \sum_{i=2}^{5}\frac{A_i + B_i T + C_i e^{-kT/T_c}}{(v-b)^i} \\ E_{int} &= E_{int,ref} + \int_{T_{ref}}^{T} c_v(T')\mathrm{d}T' + \sum_{i=2}^{5}\frac{A_i + C_i(1+kT/T_c)e^{-kT/T_c}}{(i-1)(v-b)^{(i-1)}} \end{aligned} \tag{3.22}$$

with $b = v_c(1-(-31.888Z_c+20.533)/15)$, $k = 5.475$. $Z_c$ is the compressibility factor, $T_c$ and $v_c$ are the critical temperature and critical specific volume, respectively and the notation $(\cdot)_{ref}$ refers to the reference state.
The numerical constants $A_i$, $B_i$, $C_i$ are computed following equations 3.23 to 3.31.

$$C_2 = \frac{\left(f_2 + bRT_p + (RT_p)^2 \frac{1-Z_c}{P_c}\right)(T_b - T_c) + (f_2 + bRT_b)(T_c - T_p)}{(T_b - T_c)\left(e^{-k} - e^{[-kT_p/T_c]}\right) - (T_c - T_p)\left(e^{[-kT_b/T_c]} - e^{-k}\right)} \tag{3.23}$$

$$B_2 = \frac{-f_2 - bRT_b - C_2\left(e^{[-kT_b/T_c]} - e^{-k}\right)}{T_b - T_c} \tag{3.24}$$

$$C_3 = C_2 \frac{(v_c - b)^3 - (v_c/2 - b)^3}{(v_c/2 - b)^2 - (v_c - b)^2} \tag{3.25}$$

$$C_5 = -C_2(v_c - b)^3 - C_3(v_c - b)^2 \tag{3.26}$$

$$A_2 = f_2 - B_2T_c - C_2e^{-k} \tag{3.27}$$

$$A_4 = f_4 \tag{3.28}$$

$$B_5 = \frac{f_5 - C_5e^{-k}}{T_c} \tag{3.29}$$

$$B_3 = m(v_c - b)^3 - R(v_c - b)^2 - B_2(v_c - b) - \frac{B_5}{(v_c - b)^2} \tag{3.30}$$

$$A_3 = f_3 - B_3T_c - C_3e^{-k} \tag{3.31}$$

where

$$f_2 = 9P_c(v_c - b)^2 - 3.8RT_c(v_c - b)$$
$$f_3 = 5.4RT_c(v_c - b)^2 - 17P_c(v_c - b)^3$$
$$f_4 = 12P_c(v_c - b)^4 - 3.4RT_c(v_c - b)^3$$
$$f_5 = 0.8RT_c(v_c - b)^4 - 3P_c(v_c - b)^5$$

The variables $T_p$ and $m$ can be computed following the procedure proposed by Martin & Hou [27].

## 3.4 LES models for the SGS Reynolds stress tensor

The vast majority of the subgrid scale models is based on the eddy-viscosity approximation developed by Boussinesq [38]. This approximation, also referred as the Linear Boussinesq Hypothesis (LBH), assumes that the energy transfer from the unresolved to the resolved scales is analogous to the molecular diffusion of the viscous stresses. The LBH yield the following linear relation between the anisotropic SGS stress tensor and the strain rate tensor $\widetilde{S}_{ij} = \frac{1}{2}\left(\frac{\partial \widetilde{u}_i}{\partial x_j} + \frac{\partial \widetilde{u}_j}{\partial x_i}\right)$:

$$t_{ij} - \frac{2}{3}\overline{\rho}k_{SGS}\delta_{ij} = -2\overline{\rho}\nu_T\left(\widetilde{S}_{ij} - \frac{1}{3}\widetilde{S}_{kk}\delta_{ij}\right), \tag{3.32}$$

with $k_{SGS} = \frac{1}{2}(\widetilde{u_iu_i} - \widetilde{u}_i\widetilde{u}_i)$ the residual kinetic energy.

This strong assumption considerably reduces the modeling effort as it focuses on the Eddy-viscosity term $\nu_T$. Following a simple dimensional analysis, the most natural model for the Eddy-viscosity is

$$\nu_T = (C_m\Delta)^2 F_m(\widetilde{\boldsymbol{u}}) \tag{3.33}$$

where $C_m$ is the constant of the model, $\Delta$ the width of the low-pass filter, $F_m$ a differential operator based on the filtered velocity and homogeneous to a frequency, the subscript $m$ corresponding to the model considered. By convention, the square of the constant is usually used and, as for the differential operator, is specific to each model. Among the various

eddy-viscosity models present in the literature, two of them, used in this study have been arbitrarily selected and are described hereafter. They are the dynamic Smagorinsky model and the WALE model.

### 3.4.1 The Smagorinsky model

The first model to be developed was the Smagorinsky model [39] in 1963. It was first implemented and tested in LES simulations 7 years later by Deardoff [40]. This simple model is analogous to the mixing length model in which the characteristic length is the filter width $\Delta$. The simplest term with the dimension of a frequency is the strain rate tensor. The model is then defined as

$$\nu_T = (C_s\Delta)^2 F_s(\widetilde{\boldsymbol{u}}) \tag{3.34}$$

where $F_s(\widetilde{\boldsymbol{u}}) = \left|\widetilde{S}\right| = \sqrt{2\widetilde{S}_{ij}\widetilde{S}_{ij}}$ is the norm of the strain rate tensor. $C_s$ is the so-called Smagorinsky constant, usually taken equal to 0.165 for homogeneous and isotropic turbulence (HIT).

The Smagorinsky model is one of the simplest model to compute, but it suffers from several short-comings. One of the major draw-backs of the Smagorinsky model is its excessive dissipative behavior in laminar regions. Another limitation is that the model doesn't naturally vanish close to the walls and usually requires a damping function.

### 3.4.2 The WALE model

The motivation behind the *Wall Adapting Local Eddy viscosity* (WALE) model [41] is to overcome the problems that have risen from the Smagorinsky model. The main advantage of this model is that it doesn't require any damping function or dynamic procedure to vanish near walls.

The differential operator is built upon the square of the velocity gradient tensor. More precisely, the anisotropic symmetric of the tensor is considered. Let $\widetilde{\mathscr{S}_{ij}}$ be this tensor, it is expressed as

$$\widetilde{\mathscr{S}_{ij}} = \frac{1}{2}\left(\widetilde{g}_{ij} + \widetilde{g}_{ji}\right) - \frac{1}{3}\delta_{ij}\widetilde{g}_{kk}. \tag{3.35}$$

The constant of the model $C_w$ is computed by assuming that the WALE model produces the same subgrid kinetic energy as the Smagorinsky model. The expressions of the model and its constant read

$$\nu_T = (C_w\Delta)^2 F_w(\widetilde{\boldsymbol{u}}), \quad C_w = 0.5 \tag{3.36}$$

where $F_w(\widetilde{\boldsymbol{u}}) = \dfrac{\left(\widetilde{\mathscr{S}_{lm}}\widetilde{\mathscr{S}_{lm}}\right)^{\frac{3}{2}}}{\left(\widetilde{S}_{lm}\widetilde{S}_{lm}\right)^{\frac{5}{2}} + \left(\widetilde{\mathscr{S}_{lm}}\widetilde{\mathscr{S}_{lm}}\right)^{\frac{5}{4}}}$.

With this expression, the WALE model properly decreases as $\mathcal{O}(y^{+3})$ near a wall, with $y^+$ the distance to the wall in wall units.

### 3.4.3 The Germano identity

The models seen above are implemented using an arbitrary constant, empirically defined for each flow configuration. In order to improve the models, one can consider a constant that is not only configuration-dependent, but also space and time-dependent. This constant $C_d$ can be computed with the following dynamic procedure developed by Germano *et al.* [42].

Let's first consider a second filter, called *test* filter, under the notation $\widehat{f}$, of width $\widehat{\Delta} = 2\Delta$, $\Delta$ being the width of the *grid* filter $\overline{f}$. When using the composition of those two filters on the momentum equation, the SGS stress tensor becomes

$$T_{ij} = \widehat{\overline{\rho u_i u_j}} - \frac{1}{\widehat{\overline{\rho}}} \widehat{\overline{\rho u_i}}\, \widehat{\overline{\rho u_j}}. \tag{3.37}$$

This tensor can easily be related to the grid level SGS stress tensor by the following relation

$$T_{ij} = \mathcal{L}_{ij} + \widehat{t}_{ij} \tag{3.38}$$

with

$$\mathcal{L}_{ij} = \widehat{\overline{\rho}\widetilde{u}_i\widetilde{u}_j} - \widehat{\overline{\rho}\widetilde{u}}_i\widehat{\overline{\rho}\widetilde{u}}_j/\widehat{\overline{\rho}}. \tag{3.39}$$

The tensor $\mathcal{L}_{ij}$ is called the resolved turbulent stress tensor, which physically corresponds to the contribution of the largest unresolved motions to the residual stresses. In the specific case where $\widehat{\Delta} = \Delta$, the resolved stress tensor becomes $\mathcal{L}_{ij} = \overline{\overline{\rho}\widetilde{u}_i\widetilde{u}_j} - \overline{\overline{\rho}\widetilde{u}_i}\,\overline{\overline{\rho}\widetilde{u}_j}/\overline{\overline{\rho}}$, which is the modified Leonard stress from Germano's decomposition of the turbulent stress tensor [43]. This second decomposition was proposed as an improved Leonard decomposition to correct the lack of Galilean invariance for the featured terms [44].

$$\begin{gathered} \tau_{ij} = \mathcal{L}_{ij} + \mathcal{C}_{ij} + \mathcal{R}_{ij} \\ \mathcal{L}_{ij} = \widetilde{\widetilde{u}_i\widetilde{u}_j} - \widetilde{\widetilde{u}}_i\widetilde{\widetilde{u}}_j, \quad \mathcal{C}_{ij} = \widetilde{u'_i\widetilde{u}_j} + \widetilde{\widetilde{u}_i u'_j} - \widetilde{u'_i}\widetilde{\widetilde{u}}_j - \widetilde{\widetilde{u}}_i\widetilde{u'_j}, \quad \mathcal{R}_{ij} = \widetilde{u'_i u'_j} - \widetilde{u'_i}\widetilde{u'_j} \end{gathered} \tag{3.40}$$

where $\mathcal{L}_{ij}$ is called the *modified* Leonard stress tensor.

A relation between unknown quantities, the SGS stress tensors $t_{ij}$ and $T_{ij}$, and the resolved stress tensor, which can be explicitly computed, since it only features filtered velocities and density is now given by (3.38). This relation is called the Germano identity and is the core of the dynamic procedure.

The general method to compute those dynamic coefficients is described below. The ratio between the test and the grid filter widths $\alpha$ is taken equal to 2, following the optimal value the original authors have found.

### 3.4.4 Dynamic procedure

The SGS stress tensor at the test level $T_{ij}$ is assumed to be modeled using the same models as for $t_{ij}$ but at the test level, with the same constant. Considering here the eddy-viscosity Smagorinsky model, it follows

$$\begin{aligned} t_{ij} &= -2\overline{\rho}(C_{ds}\Delta)^2 \left|\widetilde{S}\right| \widetilde{S}_{ij} \\ T_{ij} &= -2\widehat{\overline{\rho}}(C_{ds}\widehat{\Delta})^2 \left|\widehat{\widetilde{S}}\right| \widehat{\widetilde{S}}_{ij} \end{aligned} \tag{3.41}$$

where, for the dynamic procedure, the model constant $C_s$ has been replaced by the dynamic constant $C_{ds}$.

The Germano identity (3.38) becomes

$$\begin{aligned} \mathcal{L}_{ij} &= -2C_{ds}^2\widehat{\Delta}^2\widehat{\overline{\rho}}\left|\widehat{\widetilde{S}}\right|\widehat{\widetilde{S}}_{ij} + 2C_{ds}^2\Delta^2\widehat{\left(\overline{\rho}\left|\widetilde{S}\right|\widetilde{S}_{ij}\right)} \\ &= C_{ds}^2 \times \underbrace{2\,([]\,\Delta^2\widehat{\left(\overline{\rho}\left|\widetilde{S}\right|\widetilde{S}_{ij}\right)} - \widehat{\Delta}^2\widehat{\overline{\rho}}\left|\widehat{\widetilde{S}}\right|\widehat{\widetilde{S}}_{ij}]}_{M_{ij}}. \end{aligned} \tag{3.42}$$

The constant $C_{ds}$ can now be fully determined by use of a least squares method [45]:

$$t_{ij} = -2\overline{\rho}(C_{ds}\Delta)^2 \left|\widetilde{S}\right| \widetilde{S}_{ij}, \quad C_{ds}^2 = \frac{\mathcal{L}_{ij}M_{ij}}{M_{ij}M_{ij}} \tag{3.43}$$

In this form and shape, the constant $C_{ds}^2$ can happen to be negative. This would correspond to a reverse energy cascade, also called backscatter. The denominator of $C_{ds}^2$ can also become zero at some locations, and the coefficient infinite. Both of these properties have an important influence on the stability of the model. This is why it is necessary to post-process the constant in order to avoid those complications. The main method to do so is to take the ensemble average of both the numerator and the numerator [45] in the homogeneous directions. The constant now reads

$$C_{ds}^2 = \frac{\langle \mathcal{L}_{ij}M_{ij} \rangle}{\langle M_{ij}M_{ij} \rangle}. \tag{3.44}$$

Note that this process, while it ensures the stability of the model, largely reduces its dynamic and local character.

## 3.5 The MISCOG methodology for turbomachines

The Overset method is utilized for rotor and stator computations, addressing the challenge of rotor/stator coupling in a scenario where two domains are rotating relative to each other. Non-conformal vertices at the interface introduce additional evaluations in each iteration compared to static Domain Decomposition Method. Numerically, various coupling methods exist. The chosen approach involves reconstructing residuals using an overset grid method, exchanging multi-domain conservative variables through interpolation. This method extends geometrical domains with ghost cells, enabling computation of nodal residuals from cell-based residuals of a domain L, geometrically overlapped with another domain R. The interpolation of conservative variables is employed for accurate information exchange between domains.

This approach is preferred for its external implementation and high-order accuracy when used with higher-order interpolation. The interpolation routine employs a Lagrange interpolation operator, compatible with P1 (triangular in 2D and tetra in 3D) and Q1 (quad in 2D and hexa in 3D) elements. For the rotor/stator simulations, external code coupling is favored, coupling multiple instances of the LES solver through the parallel coupler CWIPI [46]. This approach divides the flow domain into static and rotating parts, with efficient distributed search algorithms facilitating information exchange between the rotating and non-rotating units, illustrated in Figure 3.3. Numerical stability and well-posed problems are associated with the overlapped region size and stencil of the schemes. The Lax Wendroff scheme requires one layer of vertices, while TTGC and TTG4A require four layers on each side of the interface. The MISCOG approach has been used with success in numerous research studies and naturally appeared, together with the solver AVBP as the tool of choice for this research endeavor.

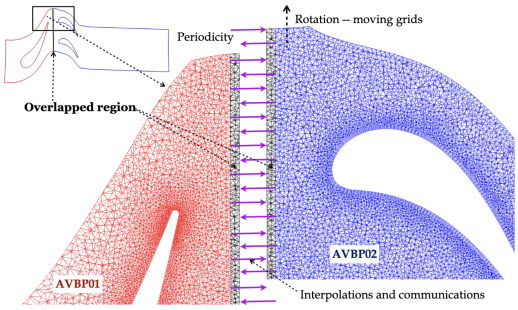


Figure 3.3: Communications framework of coupling rotor/stator interface. (from [2])

# Chapter 4

# Combustion Noise Modeling using Theory and LES

## Contents

## 4.1 Context & Motivations

As the name indicates, combustion noise is a type of noise that is generated by the combustion process. This noise gets emitted when the process of combustion leads directly or indirectly to the creation of unsteady fluctuations of the local density. When that happens, part of this fluctuation translates into a correlated homentropic fluctuation of pressure that starts to propagate at the speed of sound thereby forming acoustic waves. The simple analysis of the perfect gas Equation of State (EoS) illustrates this point. Let's differentiate the relation $P = \rho r T$. This gives the following relation :

$$\frac{\partial P}{P} = \frac{\partial \rho}{\rho} + \frac{\partial r}{r} + \frac{\partial T}{T}.$$

Let us set aside the changes in composition which are related to the term $\frac{\partial r}{r}$ as we recall that even unsteady heat sources without the presence of any flame have long been recognized as potential acoustic sources [47]. In that case the relation simplifies to

$$\frac{\partial P}{P} = \frac{\partial \rho}{\rho} + \frac{\partial T}{T}$$

in which we see that even though the combustion process in itself can be considered isobaric on average, the unsteady fluctuations of temperature do not instantaneously synchronize with that of density. To be more precise, pressure equilibrates at the speed of sound and if one considers a typical flame thickness (0.1mm) and the typical speed of sound in fresh gases (340m/s), the characteristic time scale associated is equal to $\tau_{acou} \approx 300ns$. When the flame front moves at its laminar speed, the associated timescale, equal to the ratio of the flame thickness with the flame speed, is roughly equal to $\tau_{flame} \approx 1ms$. As far as pressure fluctuations are concerned the movement of the flame is therefore quasi-steady with no pressure imbalance being generated. The situation significantly changes when the flame ignites or quenches as the relevant time scale becomes the chemical breakdown time scale. Taking the example of self ignition, the relevant time scale now becomes $\tau_{flame} \approx 10ns$ leading to a pressure imbalance that cannot be relieved in a quasi-steady way and leads to the generation of propagating acoustic waves.
One yet has to keep in mind that the amount of acoustic energy always remains small compared to the overall level of energy present in the system. If we assume that the acoustic power per surface unit emitted by a jet plane during take-off is $10W/m^{-2}$ at 30 meters from the plane then the entire acoustic energy released during the 30s of the take-off can only boil the content of a regular tin can of water. Yet, despite this poor transfer efficiency between mechanical or thermal energy and acoustic energy, acoustics from industrial systems or engines has always been the subject of active research to try to better understand its origins, improve the tools that predict its behavior and ultimately reduce its impact on our lives.

My contributions in the field of combustion noise can be split into three major themes that compose the sections of this chapter. First, in the context of my PhD, I developed a new method to compute the Flame Transfer Function (FTF) from unsteady Large Eddy Simulations (LES) of flames. During the same period I worked on a new formalism for the disturbances energy in reactive flows, a quantity strongly related to the issue of thermo-acoustic instabilities often met by designers when working on a new engine. The newly derived disturbance energy was tested with success five years later in the context of more complex flames through a collaboration with Prof.Brear from Melbourne University. Finally as a research engineer at Onera (2009-2013), I developed a new semi-analytical tool to predict the indirect combustion noise in nozzles. This method, relying only on the knowledge of the geometry and initial amplitude of the temperature fluctuation was extended during the PhD thesis of Jun Zheng (2012-2015) and Ariane Emmanuelli (2016-2019) and opened the field to new techniques for the prediction of indirect combustion noise in turbines.

## 4.2 Flame Transfer Functions for Thermo-acoustic stability maps

### 4.2.1 Context & Motivations

Combustion oscillations are a common occurrence in the development of gas turbine combustion chambers. In the early 2000's, predicting these oscillations during the design stage was not possible, and rectifying them later on highly expensive. To verify the stability of burners, simplified combustion chambers are often used for testing. However, this approach is ambiguous since a burner can exhibit unstable combustion in one chamber but not in another. Gas turbine manufacturers have dedicated substantial efforts to address combustion instability issues and have amassed a significant amount of expertise. Nonetheless, the underlying mechanisms remain incompletely understood, necessitating predictive methods for stability analysis during the design phase. A prevalent approach still involves modeling the combustor's geometry as a network of homogeneous 1D or 2D axisymmetric acoustic elements, where the acoustic problem can be analytically solved. In this model, the flame is assumed to be infinitesimally thin and only appears at an interface between regions of low and high temperatures. Jump relations connect these elements, ensuring pressure continuity and flow rate conservation. The amplitudes of forward and backward acoustic waves in each segment are determined to satisfy the jump relations and boundary conditions. This approach enables the description of a complex system using only a few lumped elements, resulting in a low-order model suitable for pre-design purposes. Advancements have introduced extensions to include azimuthal modes and 1.5D networks [48]. However, this approach has a limitation: it cannot account for the detailed geometry of the combustor and only seeks the first "equivalent" longitudinal or orthoradial modes. Another option is to employ Large Eddy Simulations (LES), which are well-suited for studying the dynamics of turbulent flames. Numerous studies have demonstrated the effectiveness of LES in this matter [49]. However, LES is computationally expensive due to its inherent nature of fully resolving the unsteady Navier-Stokes equations in three dimensions. Furthermore, even if LES confirms combustor instability, it does not provide insights into the causes or methods for control.

A suitable framework for analyzing combustion stability is the wave equation in a reacting flow [50]. Thus, considering the Helmholtz equation, the frequency domain version of the wave equation, provides a way to gain information about the complete set of thermoacoustic modes. The Helmholtz equation can be derived by combining the linearized equation of state with the linear PDEs for each fluctuating quantity. Assuming low Mach number for the mean velocity field, an approximate equation governing pressure perturbation propagation in a reacting flow can be obtained. One example of such inhomogeneous Helmholtz equation can be obtained from the wave equation first proposed by Bergmann in 1946 [51] which writes as follows :

$$\rho(x)\vec{\nabla}.\left(\frac{1}{\rho(x)}\vec{\nabla}P(x,t)\right)-\frac{1}{c(x)^2}\frac{\partial^2 P(x,t)}{\partial t^2}=Q(x,t).$$

Assuming that $P(x,t)=P_s(x,\omega)e^{i\omega t}$ and $Q(x,t)=Q_s(x,\omega)e^{i\omega(t+\Phi(x))}$ are harmonic in time, the Helmholtz counterpart can be derived as

$$\rho(x)\vec{\nabla}.\left(\frac{1}{\rho(x)}\vec{\nabla}P_s(x,\omega)\right)+\frac{\omega^2}{c(x)^2}P_s(x,\omega)=Q_s(x,\omega)e^{i\omega\Phi(x)}.$$

Transforming the initial value problem in the physical domain into an eigenvalue problem, the shape, frequency, and growth rate of the thermoacoustic modes are determined by the eigenfunctions and eigenvalues. In the case of classical acoustics in a homogeneous non-reacting medium, finite element-based methods are often employed to spatially discretize the

Helmholtz equation and convert it into a finite-dimensional eigenvalue problem. However, when combustion is present, the flame-acoustics coupling term introduces nonlinearity to the eigenvalue problem, making classical methods inapplicable. Culick proposed the "linear Galerkin" method [52], which represents the thermoacoustic solution as a linear combination of the acoustic modes of the homogeneous Helmholtz equation (without combustion forcing). Under the assumptions that the eigenvectors of the homogeneous wave equation form an orthogonal basis and that the flame coupling slightly perturbs the acoustic modes, the frequency shift induced by the unsteady heat release can be assessed. The stability of the modes is determined by analyzing the sign of the imaginary part of the frequency shift. In 2007, Nicoud et al. [50] proposed a finite element-based methodology to determine thermoacoustic modes in industrial systems like annular combustors. This method can handle frequency-dependent complex-valued impedance at boundaries, as well as 3D, distributed, and unsteady flames. Yet, as one can see, there remains the issue of the source term $Q_s(x,\omega)e^{i\omega\Phi(x)}$ which represents the Flame Transfer Function (FTF) : the response of the flame to acoustics which in turn (and thanks to the linear response hypothesis) corresponds to the forcing term of the relevant Helmholtz equation.

### 4.2.2 Determine the FTF efficiently

To obtain the source term $Q_s(x,\omega)e^{i\omega\Phi(x)}$ of the Helmholtz equation, only two possibilities existed in the early 2000s. One would either have to rely on models such as the $n-\tau$ model of Crocco [53, 54] which is very easy to implement but only poorly performs in complex 3D reactive environments ; or one would have to perform harmonically forced LES of the configuration to retrieve the forced response of the flame (HF-FFT). Between 2005 and 2008, I therefore build upon the work of Schuermans [55] to propose a new and faster method to obtain the FTF called "White Noise - Wiener-Hopf" (WN-WH). To better grasp the innovative nature of this technique, both methods are described here after.

**HF-FFT method**
The HF-FFT method involves introducing a downstream acoustic wave with a fixed pulsation ($\omega$). It assumes that the response to a harmonic perturbation of the flow results in a harmonic fluctuation of heat release. The overall Flame Transfer Function (FTF) is obtained using the relation $\frac{\hat{Q}'}{\bar{Q}} = F(\omega)\frac{\hat{u}'}{\bar{u}}$, while the local flame transfer function is obtained from $\hat{Q}'(x,y,z) = F_{3D}(x,y,z,\omega)\hat{u}'$. In the local case, the method to retrieve the FTF can be described as follows:

- Harmonically forced Large Eddy Simulations (LES) are performed for a discrete set of excitation frequencies.
- 3D fields of heat release fluctuation and the reference (usually the inlet) velocity fluctuation are extracted.
- By utilizing Fast Fourier Transforms (FFTs) of the time derivative of heat release $Q'(t)$ and velocity fluctuation $u(t)$, 3D fields of $F_3D(\omega)$ are obtained and constructed. $F_3D(\omega)$ provides local information about the flame response's location and phase.

This method requires performing FFTs of $Q'(t)$ at all points of the combustor during its forced operation. The HF-FFT method is computationally expensive as it needs to be repeated for a representative set of discrete frequencies, resulting in multiple forced LES simulations.

**WN-WH method**
The WN-WH method involves forcing the inlet with a filtered white noise signal that includes all frequencies below a specific cut-off frequency. This method leverages the Wiener-Hopf

equation, which relates the autocorrelation matrix Γ of the inlet signal (inlet velocity) and the cross-correlation vector $c : \Gamma = hc$. Here, h represents the impulse response filter, which in this case corresponds to the white-noise response filter. The method to retrieve the FTF (F3D) using the WN-WH method can be described as follows:

- Perform a LES simulation where the inlet is forced with filtered white noise.
- Store the response signal (local heat release) and the reference signal (inlet velocity).
- Determine the autocorrelation matrix Γ using the white noise inlet velocity signal (s).
- With the inlet (velocity) (s) and response (heat release) (r) signals, obtain the cross-correlation vector.
- Invert the equation to obtain h, the filter representing the FTF.
- The FTF is obtained from the filter h.

The size L of the filter is crucial for the validity of the analysis. $\Delta tL$ represents the time memory of the filter, determining the maximum available time delay $\tau_{max} = \Delta tL$. It is important to choose an appropriate value for L to avoid numerical issues during the inversion of the autocorrelation matrix, as its size varies with $L^2$. The main advantage of the WN-WH method is that it provides complete 3D fields of the amplitude and phase response of the flame. Additionally, it can provide response parameters at all frequencies below the specified cut-off frequency using only one forced LES simulation.

**Validation**
Both methods were compared in Giauque et al., AIAA, 2008 [3] on a modified version of a single Siemens hybrid burner used at atmospheric pressure mounted on a sector of an annular combustion chamber as illustrated in Fig 4.1. Figure 4.2 compares the results

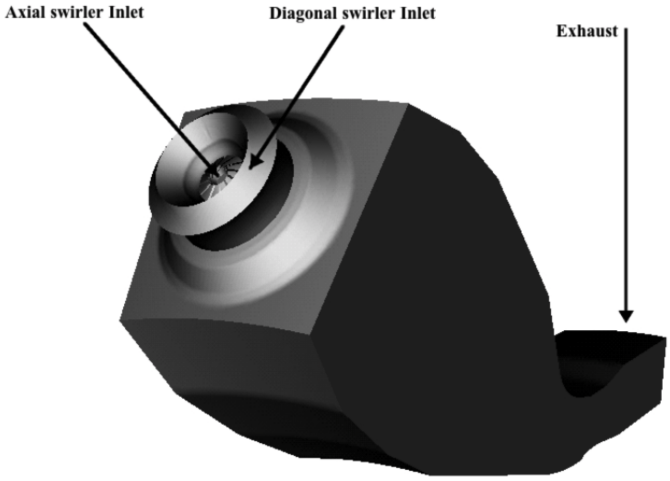


Figure 4.1: A sector of Siemens annular combustion chamber (from [3])

obtained for the amplitude and phase of the FTF using HF-FFT and WN-WH methods. For the WN-WH technique, multiple length for the wiener-hopf filter are compared. For the WN-WH method, all considered lengths provide very similar results except at frequencies beyond 500Hz. Below that frequency, the amplitudes and phases obtained through the two methods are close, validating the single white noise forced LES strategy. It proves particularly useful for configurations where the flame response is not compact compared to

the excitation's characteristic wavelength, such as distributed reacting cases. This study is closely linked to the stability analysis of combustors since FTFs significantly influence the frequency and amplification rates of modes in numerical methods employed for combustor stability.

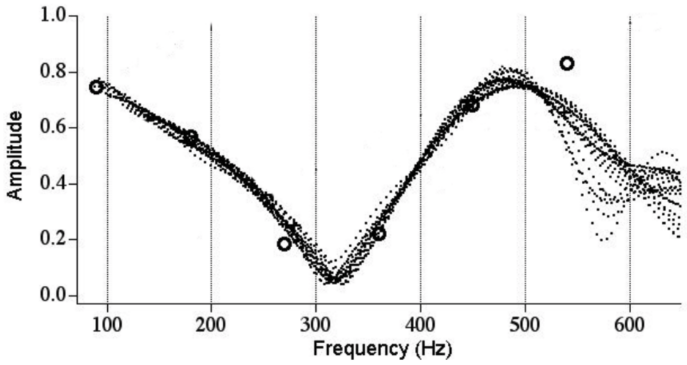


(a)

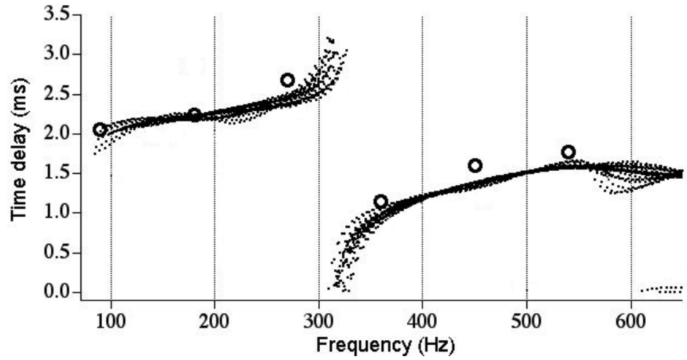


(b)

Figure 4.2: Flame transfer function (FTF) as a function of frequency: ∘ HF-FFT method, ... WN-WH method; a) Amplitude, b) Phase (from [3])

## 4.3 Modeling of indirect combustion noise and optimal design considerations

### 4.3.1 Context & Motivations

It has been known since the 1950's that fluctuations in the mixture ratio in jet engine combustion chambers resulted in masses of gas with non-uniform temperature interacting with the nozzle. Tsien[56] and Crocco [57] investigated this interaction in relation to rocket instability but in 1969, Marble concluded that the convection of gas with non-uniform temperature through the nozzle was also a significant source of low-frequency noise and contributed to the instability of the afterburner. It became apparent in the 1970's that in many technological scenarios, the nozzle could be considered acoustically compact, as demonstrated by Marble [58] for both choked and sub-critical nozzles. This compact analysis approach was later applied by Cumpsty and Marble [59] to examine noise generation in turbines resulting from combustion temperature fluctuations. Ffowcs Williams and Howe [60] theorized the generation of sound by density inhomogeneities. Zukoski [61] conducted experiments to investigate the interaction between entropy waves and nozzles, leading to positive quantitative statements about entropy-generated sound and an extension of the compact analysis to nozzles of finite length. Bohn[62] completed investigations into the response of subsonic nozzles to impinging entropy waves, and the frequency dependence was accurately described by a simple analytical model. Research on the topic almost stopped until the experimental work of Bake on the entropy wave generator (EWG) published in 2009 [63] and subsequent simulations by Mühlbauer [64] and Leyko [65]. Bake et al. demonstrated in their experiment that even though acoustic waves had large enough wavelength to consider the nozzle compact, the same hypothesis could not be made for the entropy wave at the origin of the sound. This lead to a renewed research effort fueled by the development of analytical and semi-analytical models for indirect combustion noise that would be able to match Bake's results.

### 4.3.2 Relaxing the compact hypothesis

The limits of compact models had been pointed out by numerous researchers but no model existed that would provide the full noise emissions resulting from the interaction of an accelerated entropy fluctuation with even a 1D nozzle. At the time of this research project, only compact or semi-compact models existed. Our objective therefore was to obtain a non compact solution in the case of a 1D sub-critical nozzle.
This development begins by rederiving the core equation proposed by Marble and Candel in 1977 [66] and providing a detailed methodology to extend the method to arbitrary nozzles. In the case of a constant acceleration $\Delta = du/dx$ in the nozzle, the set of equations that describe the pressure ($P$) and velocity ($U$) fluctuations in the spectral space write as follows:

$$i\Omega P + 2XP' + 2XU' = 0 \tag{4.1}$$

$$(i\Omega + 2)U + 2XU' - (\gamma - 1)P + (\gamma + 1 - (\gamma - 1)X)P' = \sigma \left(\frac{X}{X_1}\right)^{i\Omega/2} \tag{4.2}$$

where $\Omega = \omega/\Delta$, $X = (\Delta x/c_\star)^2$ and $c_\star$ is the critical speed of sound at the throat. $P'$ and $U'$ are the derivatives with respect to X and $X_1 = (\Delta x/c_\star)^2$, $x_1$ being the location of the inlet of the nozzle. $\sigma$ is the normalized entropy fluctuation source such that

$$\frac{s'}{C_p} = \sigma exp\left[i\omega\left(t - \int^x d\zeta/u(\zeta)\right)\right].$$

Equations 4.1 and 4.2 can be solved analytically as long as the acceleration of the flow $\Delta$ and the acoustic impedances at the inlet and outlet of the nozzle are known. Our derivation

makes use of this exact resolution. The idea is to consider the nozzle as being a collection of elements with constant accelerations. Figure 4.3(a) illustrates the type of simple shape nozzle that can be analytically treated by the model. The specifically interesting feature of these two nozzles is that since the velocity is the same at the inlet and at the outlet, they should not emit any noise according to compact models. In order to be able to describe a subcritical nozzle of arbitrary shape, it may be discretized into elementary units (of index k) in which the velocity is assumed to evolve linearly. It enables to actually take into account the geometrical details of any nozzle. Each element admits homogeneous solutions ($Y_1^k$ ,$Y_2^k$), as well as a particular solution ($Y_p^k$) which are first obtained as a function of the local variable $X_k = (\Delta_k x/c_\star)^2$. As a consequence, if the nozzle is discretized into $n$ elements, $2n$ constants $(A_k, B_k)$ have to be determined. $2(n-1)$ of these conditions are obtained by recognizing that pressure and velocity fluctuations at the boundary between two adjacent elements should be continuous. The last two conditions are provided by the known acoustic impedance coefficients at the boundaries of the nozzle. Figure 4.3 compares the results

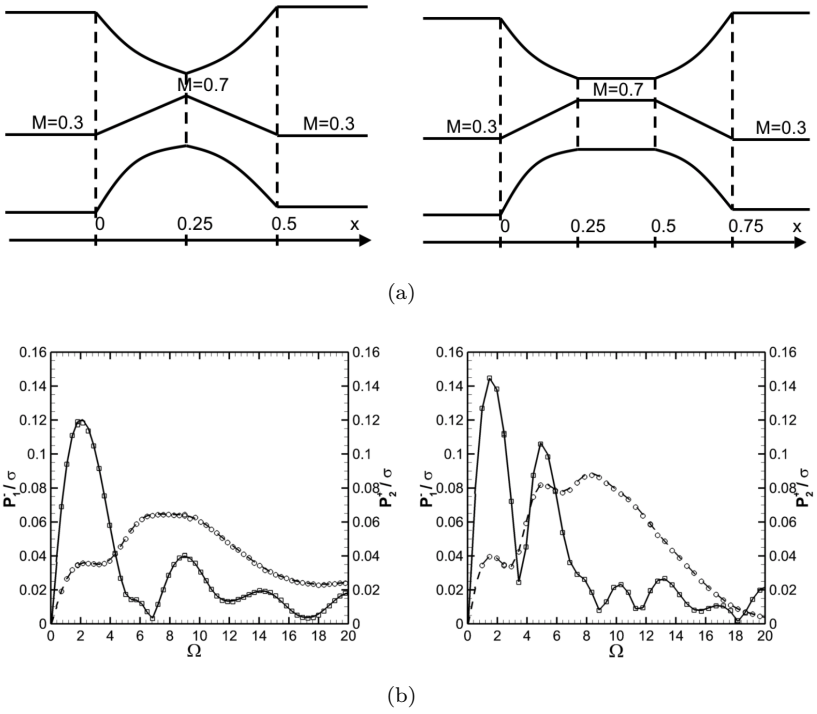


Figure 4.3: a) Left: Converging diverging nozzle; a) right: Converging diverging nozzle with pipe. b) Transfer functions, $P_1^-/\sigma$: – Analytical solution , □ Numerical solution (SUNDAY); $P_2^+/\sigma$: - - Analytical solution, ∘ Numerical solution (SUNDAY); Non-reflective inlet and outlet ($Z_1 = -1$, $Z_2 = 1$) (from [4])

obtained from a quasi-1D nonlinear Euler equations solver [4] to the ones obtained from the proposed model. Both results perfectly match and show that the backward propagating acoustic wave reaches significant levels for $\Omega \approx 2$ in both cases although the asymptotic limit at low frequency is zero.

### 4.3.3 Thermo-acoustic optimization of nozzle shapes

At the time, the non-compact model was not successful in recovering the experimental results from Bake et al. Yet, it opened new perspectives that were explored the next year (2013)[1]. In the context of the DISCERN ANR project lead by Prof. Sebastien Ducruix and Franck Richecoeur at EM2C [67], the goal was to measure experimentally indirect combustion noise generated in nozzles in a very carefully controlled environment. Our team was commissioned with the determination of the nozzle that would generate the most indirect noise given the inlet massflow rate and the overall size available.
To derive this shape, a genetic optimization strategy was followed. The shape of each nozzle is defined through Beziers curves which poles coordinates are the defining features of each evaluated nozzle. These poles coordinates can be made into a numerical genom that can be manipulated in a population of nozzles which can then reproduce and mutate, being subjected to natural selection. The objective function upon which the selection is enforced is the integral of the acoustic spectrum between 0 and 400 Hz. Each individual is evaluated using the Marcan model previously presented. Figure 4.4 illustrates the process. During this study, more than 100000 different nozzle shapes were investigated using parallel computing (illustrated in Fig 4.5).
The results of this optimization procedure support the findings described by Bloy [68], further confirming the significant influence of nozzle shape on indirect combustion noise, even when the operating conditions are kept constant. It is observed that the quietest nozzle profile exhibits a nearly linear evolution along its converging and diverging sections, resulting in a squared variation of the cross-sectional area (see Figure 4.6).

To gain insight into the underlying physical cause of the noise emission difference between two extreme nozzle designs, the integral value of the source term in the equation describing the behavior of acoustic pressure within the nozzle is examined. The study reveals that the frequency-dependent evolution of the source term is related to the overall acoustic emission. Strong evidence suggests that noise emission increases when the compensating effect of the source term in the converging and diverging parts becomes less pronounced. an important achievement of this research is the proposal of an Acoustic Emission Factor (AEF), which can serve as a surrogate for the complex determination of exact acoustic levels in nozzle flows during thermoacoustic shape optimization. The AEF writes as

$$AEF = \frac{\int_{x_1}^{x_2} \left( \frac{du}{dx}(x) e^{-i\omega_0 \int_{x_1}^{x} \left( \frac{1}{u(\zeta)} d\zeta \right)} \right) dx}{\sigma(x_2 - x_1) \overline{du/dx}_{conv}} \tag{4.3}$$

where $x_1$ and $x_2$ respectively refer to the inlet and outlet coordinates of the nozzle, $\overline{du/dx}_{conv}$ is the average acceleration in the converging part of the nozzle and $\omega_0$ is the angular frequency corresponding to the maximum frequency considered in this optimization (here $f_0 = 400$Hz). This Acoustic Emission Factor can be computed much more quickly and only requires knowledge of the cross-sectional area evolution, as well as the inlet thermodynamic and velocity characteristics. Figure 4.7 presents the clear correlation that exists between the AEF and the complex objective function used in this study.

[1] It is suspected that the reason also lies in the experimental setup in which the genereration of the entropy wave also creates additional acoustics that is not taken into account

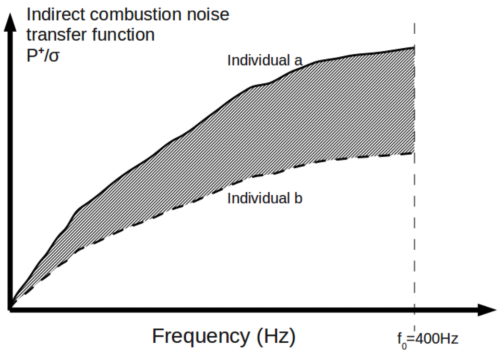


(a)

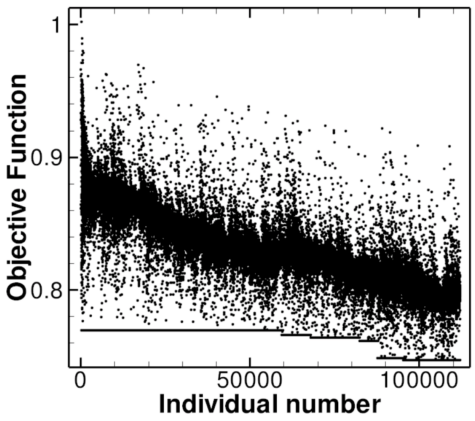


(b)

Figure 4.4: a) Illustration of the objective function, b) evolution of the population with respect to the objective function (from [5])

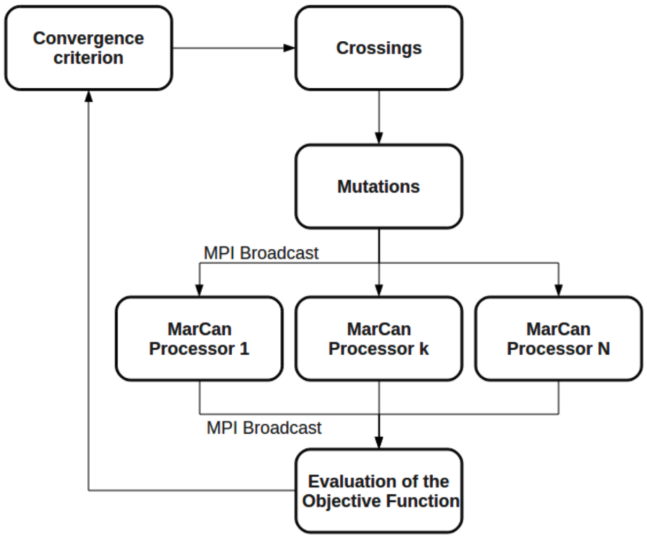


Figure 4.5: Structure of the optimization procedure

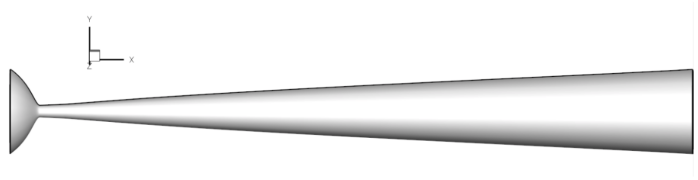

(a)

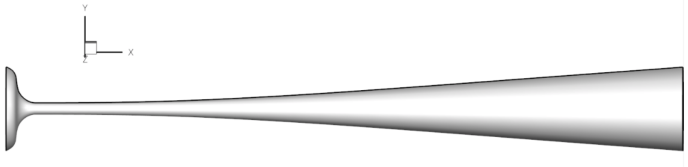

(b)

Figure 4.6: Optimal nozzle shapes: a) quietest, b) noisiest (from [5])

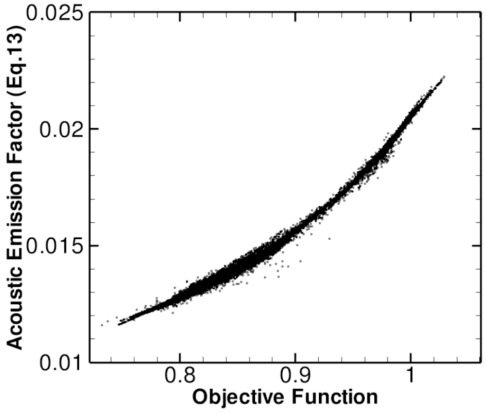


Figure 4.7: Correlation between the AEF and the objective function (from [5])

### 4.3.4 Relax the 1D hypothesis for the velocity field

To further improve the results, it was soon realized that the deformation of the entropy waves due to the 2D nature of the flow as illustrated in Fig 4.8 was to be taken into account. This lead to the theoretical developments made during the PhD thesis of Jun Zheng (2016) [69] and Ariane Emmanuelli (2019) [70].

This study introduces a novel 2D-axisymmetric model that estimates the indirect combus-

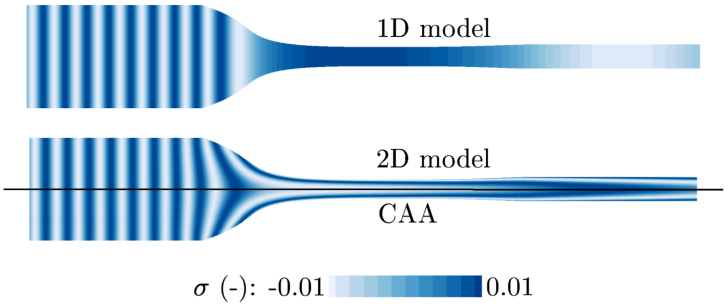


Figure 4.8: Illustration of the deformation of entropy waves during their transport (from [6])

tion noise produced by the acceleration of non-uniform temperature regions as they pass through a subcritical nozzle. The model expands upon the 1D models proposed by our team in Giauque et al. [4] and by Duran & Moreau [71] by considering the radial deformation of fluctuating entropy fronts during their convection through the nozzle. CHEOPS-Nozzle, a semi-analytical model for entropy noise in subsonic nozzle flow, is introduced. This model for indirect combustion noise in nozzles makes use of the following hypothesis:

- all viscous terms are neglected, verifying the Euler equations,
- pressure and velocity fluctuations are solely due to acoustics, thereby neglecting vorticity fluctuations,
- the mean flow is considered 2D-axisymmetric, with variations in the axial and radial directions,
- acoustic waves are considered one-dimensional throughout the domain, as radial modes are cut-off by the duct and azimuthal modes are neglected, assuming all fields are 2D-axisymmetric,
- perturbations are small, allowing the linearisation of equations.

The first step of the semi-analytical methodology is to obtain the 2D field (x,r) followed by the axial velocity in the nozzle. This can be achieved using RANS for example. One then splits the flow in streamtubes as illustrated in Fig 4.9. In the next step, the entropy fluctuations are transported numerically using the mean velocity by integration along each streamtube. A sufficient number of streamtubes is required to accurately capture the radial variation of the entropy perturbations. The mesh must also be discretized enough in the axial direction to prevent entropy wave dispersion errors. Once the transported entropy fluctuation and the mean velocity fields are known, they can be averaged in each section. Equations that provide for each axial element of the nozzle the pressure and velocity fluctuations in the spectral space can then be solved. These equations, at the core of the method are the following:

$$\left(A\overline{\left(\frac{1}{c_0^2}\right)}i\omega + \frac{d}{dx}\left[A\overline{\left(\frac{u_{0x}}{c_0^2}\right)}\right]\right)P + \left[A\overline{\left(\frac{u_{0x}}{c_0^2}\right)}\right]P' + \frac{dA\overline{\rho_0}}{dx}U + A\overline{\rho_0}U' = \frac{d}{dx}\left[A\overline{\rho_0 u_{0x}\sigma}\right] + Ai\omega\overline{\rho_0\sigma} \quad (4.4)$$

$$\left[\overline{\frac{u_{0x}}{\gamma p_0}\frac{\partial u_{x0}}{\partial x}} + \overline{\frac{u_{0r}}{\gamma p_0}\frac{\partial u_{x0}}{\partial r}}\right]P + \overline{\left(\frac{1}{\rho_0}\right)}P' + \left[i\omega + \overline{\left(\frac{\partial u_{x0}}{\partial x}\right)}\right]U + \overline{u_{0x}}U' = \overline{\left[u_{0x}\frac{\partial u_{x0}}{\partial x} + u_{0r}\frac{\partial u_{x0}}{\partial r}\right]\sigma} \quad (4.5)$$

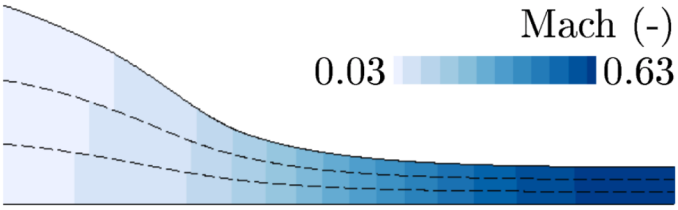


Figure 4.9: Decomposition of the flow in streamtubes (from [6])

where $P$ and $U$ are the amplitude of the pressure and velocity fluctuations in the spectral space. $P'$ and $U'$ are the derivative of those with respect to x. The operator $\overline{(.)}$ refers to the operation of sectional averaging and $(.)_0$ refers to the mean field variables. $A(x)$ is the sectional area. If one compares Eqs 4.4-4.5 to Eqs 4.1- 4.2, the main differences comes from (i) the presence of sectional averages both on the l.h.s. and r.h.s. and (ii) new terms related to the radial derivative of the axial velocity that modify both the transport and source terms.
The nozzle is finally split into lumped elements of finite axial length connected to each other through the continuity of the pressure and velocity fluctuations. Additionally using the inlet and outlet acoustic impedances, a system is solved that provides the amplitudes of the forward propagating wave ($P^+$) at the outlet and backward propagating wave ($P^-$) at the inlet as a function of frequency. The general structure of the resolution is recalled in Fig 4.10

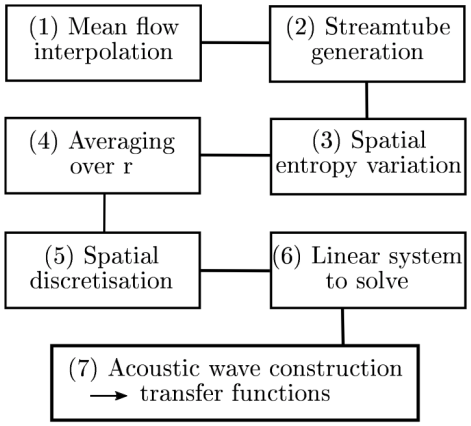


Figure 4.10: 2-D arbitrary shape ICN model : general procedure (from [6])

To validate the accuracy of the model, it is compared to a reference case generated using a novel Computational Aeroacoustics (CAA) approach, which also relies on the Euler equations but differs in two key aspects: it considers non-one-dimensional acoustics and does not neglect vorticity. Numerical analysis (partly displayed in Fig 4.11) confirms the validity of the first assumption. The agreement between the noise levels predicted by the model and the CAA method suggests that the assumption of negligible vorticity is also applicable. The model exhibits good agreement for all three types of excitation: entropic, upstream acoustic, and downstream acoustic. Furthermore, these results align with Marble and Candel's compact solution at low frequencies.
This study sheds light on the importance of 2D effects on entropy noise, attributed to the

deformation of the entropy wave and subsequent decorrelation of acoustic sources along the nozzle.

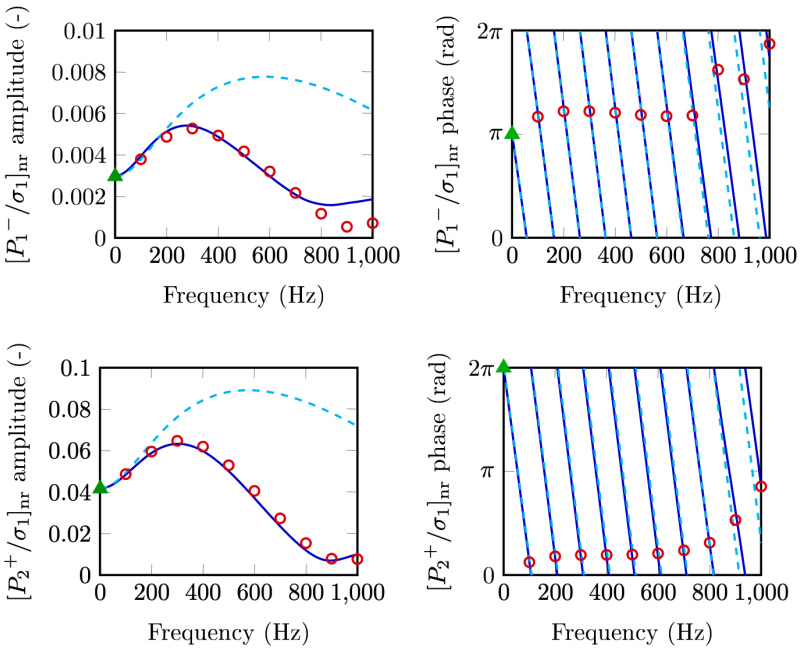


Figure 4.11: Indirect combustion noise transfer functions: Comparison between - - 1-D arbitrary shape model, – 2-D arbitrary shape model, ∘ CAA and △ compact model. (from [6])

## 4.4 Disturbance energies in reacting flows

### 4.4.1 Context & Motivations

In thermoacoustic systems, such as flames in combustors, heat release oscillations interact with acoustic pressure oscillations. When the phase relationship between heat release and pressure is favorable, these oscillations can amplify, leading to potentially catastrophic consequences. This phenomenon has been formulated by Rayleigh [47] and is know since then as the Rayleigh criterion

$$\int_t \int_v p'(x,t)\omega'_T(x,t)dvdt > 0.$$

Thermoacoustic instabilities remain one of the most daunting challenges in the realms of gas turbine and rocket motor manufacturing. As said, when these arise, the fluctuations of pressure and velocity within the combustor increase in amplitude. Without prejudice to the generality of the statement, one can say that the disturbance energy (regardless of its precise definition) also increases in the process. In flows involving combustion, any equation that addresses the conservation of disturbance energy must begin with equations of motion that incorporate non-zero mean flow quantities and entropy variation. Neglecting either the mean flow or entropy variation leads to conceptual issues. It seems that only the energies defined by Morfey and Myers [72, 73] accomplish this requirement. While viscous dissipation and heat conduction are considered in their works, they are not essential and typically have negligible effects. in 2005, Nicoud and Poinsot revisited Chu's fluctuating energy equation [74] and argued that the Rayleigh criterion alone does not provide a complete description of the significant sources of "disturbance" energy in combustion. In the case of small disturbance amplitudes, a source term proportional to $T_1\omega_{T1}$ was discovered, where $\omega_{T1}$ and $T_1$ represent the first terms in the asymptotic expansions of heat release and static temperature. This term bears some resemblance to the "Rayleigh term", but it is significantly different. Additionally, disturbances in entropy throughout the flame are believed to be a significant source of disturbance energy. Bloxsidge and Dowling [75] also demonstrate the existence of terms other than the Rayleigh term in their alternative definition of the acoustic energy equation, but they argue that these terms are usually negligible in practice. The divergence of opinions on this fundamental and practically important problem requires resolution.

In this section we present the contributions of the author to this controverse. This can be accomplished by first deriving a comprehensive equation for a disturbance energy and then numerically studying the magnitudes of all identified source terms. The fundamental equation should not be linear, as is often the case in acoustics. In fact, temperature, entropy, and velocity disturbances, particularly within flames, can be substantial, and nonlinear effects have already been recognized as significant in the analysis of acoustic energy in solid rocket combustion. Myers' work [73] also justifies the inclusion of entropy disturbances in the energy density and flux terms. Significant entropy or pressure disturbances can be accompanied by propagating disturbances in the pressure and entropy fields, respectively, through convection or sonic effects. Therefore, a useful disturbance energy formulation should encompass pressure, velocity, and entropy disturbances for nonlinear investigations. To determine the main source terms of this energy, one must examine the balance closure of conservation equations for various disturbance energies that can be defined in reacting flows. In a second part, the question of which stability criteria can be derived from these disturbance energies can be explored. For this purpose, but only at that stage, the nonlinear transport equations for these energies can be linearized to investigate whether or not simple stability criteria can be derived.
In the following, the whole theoretical derivation won't be reproduced. Instead, the author focuses on the elements that appear the most important almost a decade after the facts.

### 4.4.2 Disturbance energies

Computed from the non-linear equation that can be derived from pressure and velocity fluctuations, the minimal linear acoustic energy transport equation (**AE**) can be written as

$$\frac{D_0}{Dt}\left(\frac{p_1^2}{2\gamma_0 p_0}+\frac{\rho_0 u_1^2}{2}\right)=-\vec{\nabla}.\left(p_1\vec{u}_1\right)+\frac{\gamma_0-1}{\gamma_0 p_0}p_1\left(\omega_{T1}-\vec{q}_1\right)+\frac{\gamma_1 p_1}{\gamma_0 p_0}\left(\omega_{T0}-\vec{q}_0-\vec{\nabla}.\vec{u}_0\right)+\vec{u}_1:\vec{\nabla}\bar{\bar{\tau}}_1 \tag{4.6}$$

In comparison to the simpler version of this equation usually derived, numerous additional terms appear that are related to the mean heat release, heat flux and velocity. The associated energy $\frac{p_1^2}{2\gamma_0 p_0}+\frac{\rho_0 u_1^2}{2}$ relates to the classical acoustic energy but as pointed out by Poinsot and Nicoud [74] does not include entropy fluctuations which are a major source of fluctuations in reactive cases.
A nonlinear transport equation for the disturbance energy related to entropy (**SE**) can be derived. When linearized it writes

$$\begin{aligned}\frac{D_0}{Dt}\left(\frac{p_0 s_1^2}{2r_0 C_{p0}}\right)&=-\frac{p_0 s_1}{r_0 C_{p0}}\vec{u}_1.\vec{\nabla}s_0+\frac{s_1}{C_{p0}}\left[\omega_{T1}+\phi_1-\vec{\nabla}.\vec{q}_1\right]\\ -\frac{s_1}{C_{p0}}&\left[\left(\frac{\rho_1}{\rho_0}+\frac{T_1}{T_0}\right)\left(\omega_{T0}+\phi_0-\vec{\nabla}.\vec{q}_0\right)\right]+\text{Species mass fractions related terms}\end{aligned} \tag{4.7}$$

Yet as it will be shown latter, even though the original idea was to add the usual acoustic energy to the disturbance energy of entropic origin, this cannot be done due to the impossibility of linearizing the disturbance energy equation arising from entropy fluctuations. This leads to the development of a nonlinear disturbance energy (**NLE**) definition together with its transport equation that contains entropy fluctuations. Extending the work of Myers [73], one obtains

$$\begin{aligned}\frac{\partial Ed}{\partial t}+\vec{\nabla}.\vec{W} &= D \\ \text{where}\quad Ed &= \rho(H_1-T_0 s_1)-(\rho\vec{u})_0.\vec{u}_1-p_1-\rho\sum_{k=1}^{n-1}g_{sk0}Y_{k1} \\ \text{and}\quad \vec{W} &= (\rho\vec{u})_1(H_1-T_0 s_1)+(\rho\vec{u})_0 T_1 s_1\end{aligned} \tag{4.8}$$

The reader is referred to the original text for the detailed definition of the source term $D$.

### 4.4.3 Test case and main results

To validate the previous theoretical developments, a simple laminar 2D-axisymmetrical CH4/air premixed flame is considered [76] as illustrated in Figure 4.12. To investigate Eqs 4.6, 4.7 and 4.8, a numerical experiment is devised. First, using the NSCBC boundary condition model [77] the acoustic impedance at the outlet is modified to be more reflective. It leads to the appearance and development of a thermo-acoustic instability which then reaches a limit cycle. In a second part of the experiment, the impedance is modified again to restore the original non-reflective behavior. In presence of the thermo-acoustic instability, pressure, velocities and heat release fluctuate so that the flame in Fig 4.12 moves in an oscillating manner from left to right. First the closure of the balance equation 4.6 integrated over the entire domain with respect to time is checked in Figures 4.13 that presents the evolution of the integrated time derivative of the AE compared to the volume integral of the r.h.s. of Equation 4.6. Both parts perfectly match and the identified source terms are indeed the ones responsible for the evolution of AE. It is interesting to see that even though the instability is self sustained, it is not harmonic in time but includes at least two distinct modes. The closure of the balance equation 4.7 for the disturbance energy related to entropy (SE) is checked in Figure 4.14. It appears that this budget does not close meaning that as previously mentioned

Figure 4.12: Illustration of the 2D axisymmetrical flame used in this study. Left: mean density, Right: mean heat release (from [7])

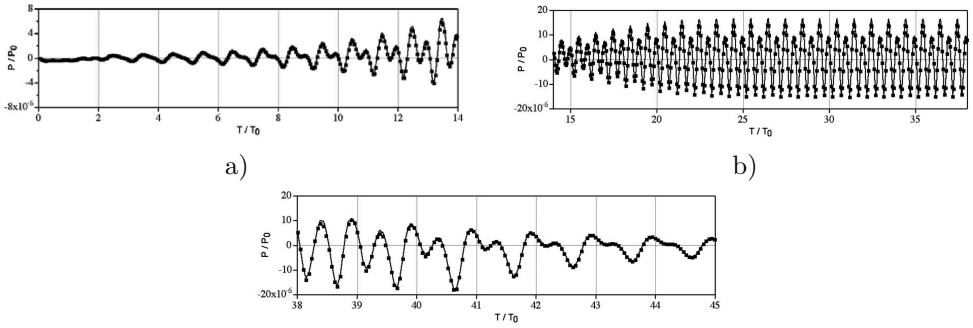


Figure 4.13: Budget of Eq 4.6 (AE) during the numerical experiment. – r.h.s., ■ temporal derivative of disturbance energy. a) instability onset, b) limit cycle, c) relaxation phase. (from [7])

the equation cannot be linearized. The core reason is that the term $\frac{1}{T'}$ cannot be linearized as $-\frac{T_1}{T_0}$ because of the strong gradients of temperature though the flame front. The closure of the nonlinear disturbance energy (NLE) transport equation 4.8 originally developed in this study is verified in Figure 4.15. It shows that this disturbance energy possesses the two main researched qualities for the problem at hand: (i) It is a disturbance energy that both contains acoustic and entropy fluctuations and (ii) its conservation equation is a transport equation that clearly states the fluxes and source terms.

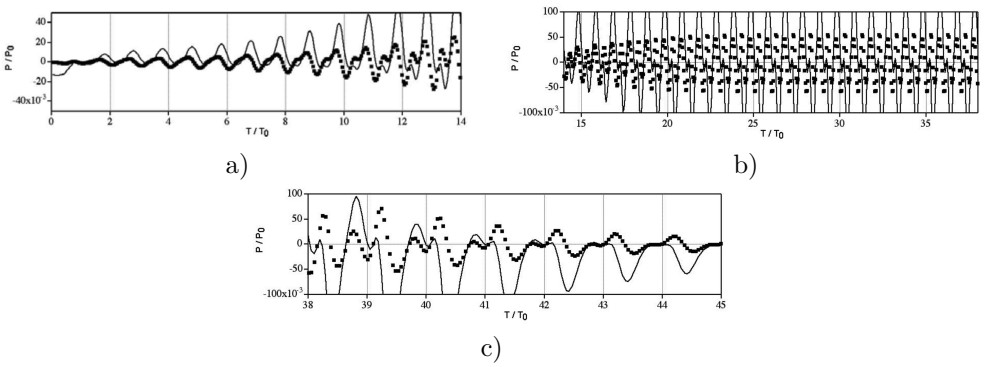


Figure 4.14: Budget of Eq 4.7 (SE) during the numerical experiment. – r.h.s., ■ temporal derivative of disturbance energy. a) instability onset, b) limit cycle, c) relaxation phase. (from [7])

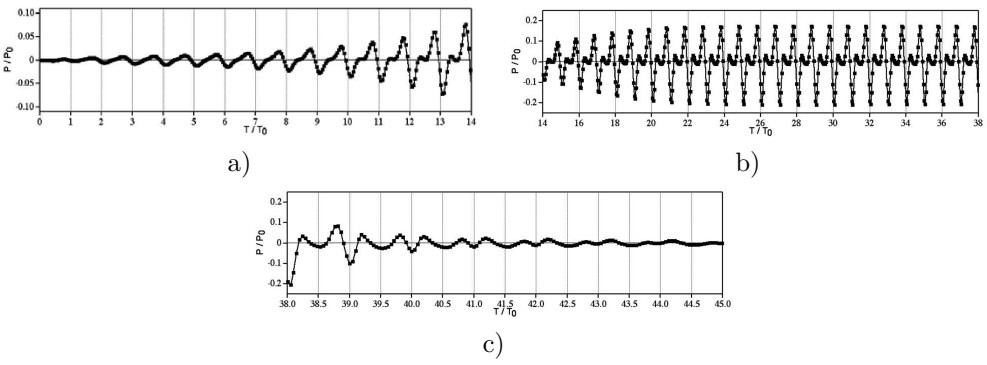


Figure 4.15: Budget of Eq 4.8 (NLE) during the numerical experiment. – r.h.s., ■ temporal derivative of disturbance energy. a) instability onset, b) limit cycle, c) relaxation phase. (from [7])

### 4.4.4 Stability criteria

The Acoustic energy (AE) on one hand and the nonlinear disturbance energy (NLE) on the other can be integrated in time over a period of oscillation that represents the main frequency in the problem. Doing so, the growth and decrease of disturbance energies can be related to the equivalently integrated r.h.s. of their respective equations. It leads to the derivation of new stability criteria that expand the one of Rayleigh. For the AE, it is observed that when

$$\int_{T_0}\left[\int_V\left(\frac{\gamma_0-1}{\gamma_0 p_0}p_1\left(\omega_{T1}-\vec{q}_1\right)\right)dv-\int_S\left(p_1\vec{u}_1.\vec{n}\right)dS\right]dt>0$$

the flame is instable. This criterion although close to the Rayleigh criterion also involves the acoustic fluxes at the boundaries and the source/damping effect of the correlation between the pressure fluctuations and the heat fluxes.

The NLE leads to a different criterion that writes

$$\int_{T_0}\left[\int_V\left(-s_1\left(\rho\vec{u}\right)_1.\vec{\nabla}T_0+s_1\left(\rho\vec{u}\right)_0.\vec{\nabla}T_1+T_1\omega_{T1}\right)dv\right]dt>0.$$

A first observation is that no flux term appear which is probably strongly linked with the case at hand. One possible interpretation is that the NLE since it contains entropy fluctuations has at least partly a convective behavior. Because of the size of the domain and the location of entropy fluctuations, it is not so surprising that no flux term is required to form a stability criterion. Instead of the usual $p_1\omega_{T1}$ term, three correlations interplay to lead to the instability $s_1\left(\rho\vec{u}\right)_1$, $s_1\vec{\nabla}T_1$, and $T_1\omega_{T1}$. It is interesting to see that one recovers the main source term obtained by Chu [78] connecting fluctuations of the temperature with that of heat release.

### 4.4.5 Further discussion

**Influence of mean Mach number terms**
The provided equations 4.6, 4.7 and 4.8, represent the minimum equations, including terms associated with the mean Mach number. It is important to note that the mean Mach number in the numerical experiment is 0.01. If the mean velocity is zero, it is not possible to sustain any mean heat release in a combustor. Consequently, the presence of terms related to the mean heat release in equations 4.6, 4.7 and 4.8 indicates the influence of the mean velocity field on the magnitude of disturbance energies.

In the minimum linear equation 4.6, there is a term associated with the mean Mach number. The ratio $\frac{\gamma_1 p_1}{\gamma_0 p_0}$ is very small, but its impact on AE can be determined by multiplying it with the mean heat release. In this particular case, the product of these two factors yields a maximum value per unit volume, which accounts for 60% of the maximum power of the disturbance energy per unit volume.

The minimum equation 4.8, which deals with nonlinear disturbance energy, incorporates a term directly linked to the mean Mach number: $\overline{\vec{m}}s_1\vec{\nabla}T_1$. This term signifies that a fluctuation in entropy, positively correlated with a fluctuation in the temperature gradient, can generate nonlinear disturbance energy, as long as the mean Mach number is not zero.

**Nonlinearization of SE (Eq.4.7)**
The matter of linearization applies solely to Equations 4.6 and 4.7 when describing the evolution of disturbance energies. The linearization of Equation 4.7 becomes impossible once the flame front is perturbed. This finding suggests that the linearization could also pose difficulties in more realistic and turbulent cases. The reason behind this lies in the fact

that the nonlinear version of SE equation directly involves terms like $\left[\frac{\dot{\omega}_T}{\rho T}\right]'$, which cannot be linearized in the form $\left[\frac{\dot{\omega}_{T1}}{\rho_0 T_0}\right] - \dot{\omega}_{T0}\left[\frac{\rho_1}{\rho_0^2 T_0} + \frac{T_1}{\rho_0 T_0^2}\right]$.

### 4.4.6 On the linearization of NLE

A question that remained unanswered at the time was the following: Far away from the flame, the NLE should degenerate to AE for no further fluctuations of entropy are present. Yet at what distance with respect to the flame front this transition occurs? In other words, beyond which distance is the flux of NLE becoming linear? To answer this question, I was involved in a new numerical experiment lead by Prof. Brear at Melbourne University in 2012 [8]. This study was conducted to analyze the energy carried by disturbances in gaseous combustion, expanding upon the previous work of Myers [73] by incorporating multiple species and finite-rate chemical reactions. As a result, exact and second-order equations describing the energy transport in gaseous combustion were derived. The nonlinear disturbance energy definition and transport equation is provided by Eq 4.8. The second order equation writes as

$$\frac{\partial E_2}{\partial t} + \vec{\nabla}.\vec{W}_2 = D_2 \tag{4.9}$$

$$\text{where} \quad E_2 = \frac{p_1^2}{2\rho_0 c_0^2} + \frac{1}{2}\rho_0 u_1^2 + \rho_1 \vec{u_0}.\vec{u_1} + \frac{\rho_0 T_0 s_1^2}{2C_{p0}}$$

$$\text{and} \quad \vec{W}_2 = (p_1 + \rho_0 \vec{u}_0.\vec{u}_1)\left(\vec{u}_1 + \frac{\rho_1}{\rho_0}\vec{u_0}\right) + (\rho\vec{u})_0 T_1 s_1$$

$$D_2 = (\rho\vec{u})_1 .\vec{\zeta}_1 - s_1 (\rho\vec{u})_1 .\vec{\nabla}T_0 + s_1 (\rho\vec{u})_0 .\vec{\nabla}T_1 + \left(\frac{\omega_{T1}T_1}{T_0} - \frac{\omega_{T0}T_1^2}{T_0^2}\right)$$

In "classical" thermoacoustics, the "Rayleigh source term," which represents the acoustic source term, is derived from general equations of combusting gas motion. It was observed that this term becomes the sole acoustic source term in cases where the flows exhibit small irrotational disturbances, are non-diffusive (in terms of species, momentum, and energy), homentropic, without mean flow, and at chemical equilibrium. Under these conditions, the energy density and flux terms follow their classical (zero mean flow) formulations.
Furthermore, for non-diffusive flows with non-zero mean flows at chemical equilibrium, a second-order source term proportional to the mean heat release was identified in this study. This term has the potential to interfere destructively with the Rayleigh term. Building upon the approach proposed by Doak [79], the extended conservation equation for disturbance energy was employed to establish a relationship between the time-averaged far-field sound from a jet flow and the volume integral of the time-averaged disturbance energy source terms. It was argued that a reasonable definition of the far-field is one where disturbances in entropy and mass fraction can be neglected. In such cases, the relative contributions of each source term to the averaged far-field sound can be compared, assuming complete knowledge of the source region. This approach complements the more common analytical methods used in aeroacoustics that rely on acoustic analogies.

The exact and second-order energy budgets were then evaluated using a series of aeroacoustic Direct Numerical Simulations (DNS) of a forced, low Mach number, laminar, premixed flame illustrated in Fig. 4.16. These evaluations demonstrated the significance of several source terms, including those related to mean flow effects and the entropy field. It was concluded that understanding sound generation energetics requires considering not only the Rayleigh source term but also other significant terms. It was also shown (as illustrated in Fig 4.17) that the nonlinear flux simplifies to the linear second order one ($\vec{W} \approx \vec{W}_2$) as soon as the integration surface is outside of the reactive region in all directions.

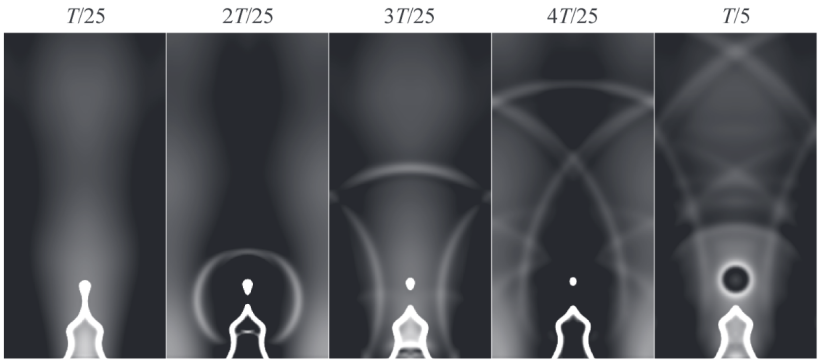


Figure 4.16: Illustration of the numerical experiment. The flame is acoustically forced at $S_T = 0.02$ (from [8])

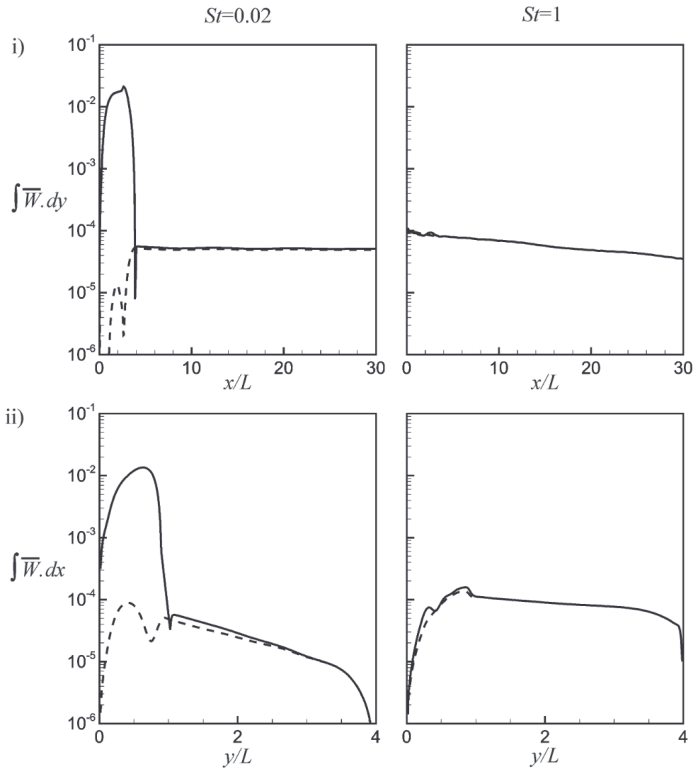


Figure 4.17: Comparison between the surface integrals of : – nonlinear disturbance energy flux and - - its second order counterpart (from [8])

## 4.5 Conclusion

My contributions to the field of combustion noise can be categorized into three main themes. Firstly, I pioneered the development of a novel and efficient method for computing the Flame Transfer Function (FTF) from unsteady Large Eddy Simulations (LES) of flames, employing the Wiener-Hopf signal processing technique.
Secondly, I formulated a new framework for quantifying disturbances energy in reactive flows, a crucial parameter linked to the challenge of thermo-acoustic instabilities frequently encountered by engine designers. The effectiveness of this newly derived disturbance energy measure was successfully validated within the context of more intricate flame scenarios.
Lastly, I devised a novel semi-analytical 1D tool designed to predict indirect combustion noise in nozzles. Utilizing this tool facilitated the resolution of shape optimization problems devoted to the experimental study of indirect combustion noise. This method, which relies solely on knowledge of geometry and initial amplitude of temperature fluctuations, was subsequently expanded to turbine flows, introducing innovative approaches for predicting indirect combustion noise in gas turbines.

## 4.6 Summary of contributions and collaborations

We conclude this chapter by summarizing the key communications regarding combustion noise and the collaborations at their origins.

| Topic | articles | people | status | place |
|---|---|---|---|---|
| Flame Transfer Functions for Thermo-acoustic stability maps | [80, 7] [3] | Thierry Poinsot<br>Laurent Selle<br>Franck Nicoud | PhD director<br>Collaborator<br>Collaborator | CERFACS<br>CERFACS<br>Univ. Montpellier |
| Modeling of indirect combustion noise and optimal design considerations | [4, 5, 81] [70, 6] [82, 69] | Maxime Huet<br>Sebastien Ducruix<br>Marien Simeni<br>Jun Zheng<br>Ariane Emmanuelli | Collaborator<br>Collaborator<br>M2 student<br>PhD student<br>PhD student | ONERA<br>Centrale Supelec<br>ONERA<br>ONERA<br>ONERA |
| Disturbance energies in reacting flows | [7, 83] [84, 8] | Franck Nicoud<br>Thierry Poinsot<br>Michael Brear | Collaborator<br>PhD Director<br>Collaborator | Univ. Montpellier<br>CERFACS<br>Melbourne Univ. |

Table 4.1: Combustion Noise: key publications and their context

# Chapter 5

# Broadband Rotor Noise Modeling using LES

## Contents

## 5.1 Context & Motivations

The aviation industry is currently facing a significant (if not deadly) challenge of balancing the growth in air traffic with a decrease in CO2 emissions. As the demand for air travel continues to rise, it becomes crucial to find sustainable solutions that minimize the environmental impact of the industry [85].
On top of the breakthrough technology related to electric propulsion, one of the short to mid-term technological solutions being explored is the modification of engine architecture. Specifically, the development of Ultra-High Bypass Ratio (UHBR) and Open Fan configurations has been known as an effective solution for almost thirty years [86]. The UHBR architecture focuses on increasing the bypass ratio of the engine beyond 15, which refers to the ratio of the amount of air bypassing the engine core to the amount of air passing through the core and being burned with fuel. This results in higher efficiency and reduced fuel consumption (≈10%) compared to traditional engines. By incorporating advanced materials, optimized aerodynamics, and improved combustion technologies, UHBR engines aim to achieve significant reductions in CO2 emissions.

However, a major concern associated with modern engine architectures, including UHBR, is the increase in noise emissions. Aeronautical engine noise has been a concern since the 1940s and the origin of modern research on the topic can be traced back to the Aeronautical Research council report of 1950 [87] from Goldstein and Lighthill. Significant theoretical progress are made in the 1950s (among those the Lighthill acoustic analogy [88]) and the very first model for blade noise is proposed in 1959 by Allan Powell [89, 90]. Yet, in their article from 1986, Fukano et al. stated in introduction [91, 92] :
*It is an urgent necessity to establish general countermeasures for reducing the sound pressure level of fan noise. It seems to be very hard to solve this problem because the mechanisms of the noise generation have not yet been fully understood and the parameters relevant to the noise generation seem to be manifold.*

For modern UHBR engines, the decrease of the nacelle shielding effect along with the increased aerodynamic load at the blade tip rotating at near sound speed results in elevated noise levels. Noise pollution is a significant environmental and social issue that affects both airport communities and the overall public perception of the aviation industry. To address this issue, noise regulations have evolved over time to limit the impact of aircraft noise. The International Civil Aviation Organization (ICAO), along with regional aviation authorities, has implemented stringent noise standards for aircraft [93]. These standards set maximum noise limits that aircraft must comply with during certification and operation. Aircraft manufacturers and engine developers are investing in research and development to find innovative solutions for noise reduction. This includes the development of advanced noise reduction technologies, such as active noise control systems, improved acoustic treatments, and optimized engine designs. To really foster innovation, two aspects need to be improved in priority.

- The first one relates to the deep understanding of the noise sources in such systems. It will be made clear in the following that gaps still exist in our comprehension (despite almost 75 years of research). For example, the links that exist between secondary flows in fan, leading to the generation of turbulence and organized dissipative structures in the flow and their respective acoustic signatures still need further research.
- The second aspect is strongly linked with the enormous increase in our numerical simulation capabilities that occurred during the last decades. With massively parallel simulations, our numerical modeling tools now make possible the unsteady modeling of such flows in almost all their complexity. This will most certainly lead to better

low-order models empowering engineers when they develop and optimize these architectures during the preliminary design phases.

The objectives of this chapter is to present the research initiative I launched in 2017 together with Jérome Boudet and Vincent Clair to tackle these challenges. A significant part of this chapter (if not all of it!) presents the results obtained by Jean Al Am during his PhD thesis between 2019 and 2022, and his subsequent postdoc in 2023. His research were funded by the ARENA industrial chair financed by ANR and SAFRAN. We will see that this work was made possible thanks to the CATANA research initiative and the PHARE project lead by Christoph Brandstetter and Xavier Ottavy at LMFA [94]. These projects aim at designing and testing a UHBR fan at the LMFA laboratory hosted by Ecole Centrale de Lyon. The innovative fan itself is called ECL5 and is an open configuration which geometry is already shared with multiple academic partners. This project is a flagship project for LMFA most especially regarding the experimental aspects. Our goal in ARENA therefore was to show that the same level of expertise could be reached using a numerical approach for the modeling of such flows. This initiative is consequently a tightly joined research effort between the turbomachinery and acoustics groups at LMFA.

## 5.2 Fan noise sources

Figure 5.1 illustrates the typical sound power spectra produced by turboengines at two operating conditions: approach and take-off. The fan stage emits both tonal and broadband noise components. Tonal noise stems from periodic phenomena and manifests as discrete frequencies. In contrast, broadband noise (BBN) arises from random fluctuations related to turbulent flow and spans the full frequency range continuously [95]. At approach, where

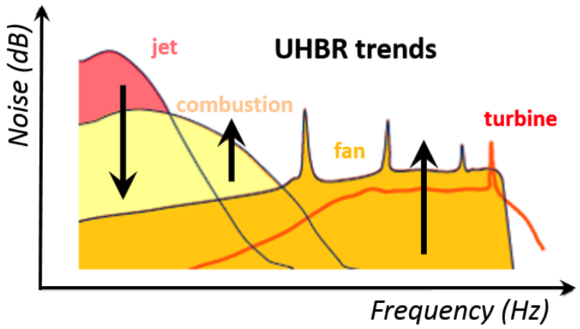


Figure 5.1: Typical turboengine spectrum and future trends for UHBR architectures. (from [9])

the flow stays subsonic along the blade, tonal noise primarily originates from the periodic interaction of fan wakes with outlet guide vanes (OGVs). This produces tones at the blade passing frequency (BPF) and its harmonics [96]. However, at take-off, the flow becomes transonic at the rotor tip, generating shock waves and additional tones in the acoustic spectrum. These are called multiple pure tones, responsible for the characteristic "buzz saw noise" of transonic regimes [96]. Extensive research has targeted reducing tonal noise from the fan-OGV stage. For example, specially designed nacelles and acoustic liners at the duct exhaust can dampen propagating tones [96]. Also, optimizing the fan and OGV counts can exploit duct filtering to attenuate the BPF [97].
In contrast, Broad-Band Noise (BBN) from the fan/OGV stage is less explored due to its stochastic nature arising from fine turbulence structures in the blade and vane boundary layers and fan wakes. This noise is difficult to mitigate given the many cut-on modes [96]. BBN has several origins:

- (i) Inlet turbulence interacting with rotor blades [91].
- (ii) Fan tip gap noise from highly unsteady flow through the blade/casing gap [98].
- (iii) Trailing edge noise generated when turbulence hits the blade or vane trailing edge [99].
- (iv) Rotor-stator Interaction (RSI) noise from wake turbulence interacting with the stator leading edge, inducing unsteady vane loading [96]. RSI noise often dominates in a fan stage at approach [96].

Controlling BBN is challenging given its multifaceted origins. Thus, researchers and engineers must explore innovative solutions to enable low-noise, environmentally friendly aircraft engines. Additionally, further computational and experimental advancements are required to comprehensively understand BBN and its implications for noise reduction in future engine designs.
Before focusing on the precise contributions of the author to the field, one should first describe with more details the different sources of noise briefly introduced above. Figure 5.2 illustrates these different noise sources. Tonal noise sources are in green and BBN sources are in blue.

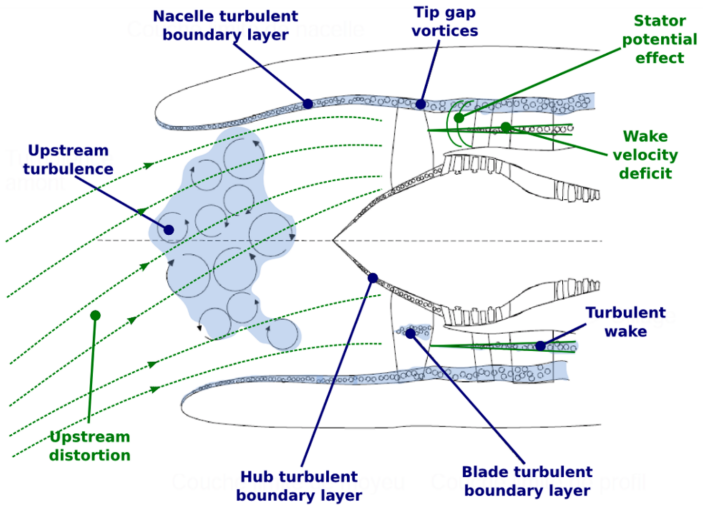


Figure 5.2: Sketch of turbofan noise sources. (from [9])

### 5.2.1 Tonal noise

The primary noise mechanisms generating tonal sources are illustrated in Figure 5.2 and described below [96]:

- Shock wave noise: At take-off, the flow becomes supersonic at the blade tip, forming shock waves. Small blade-to-blade angle variations lead to shock wave detachment, propagating upstream and causing tones at multiples of the rotational frequency rather than the BPF and harmonics linked to buzz saw noise [100].
- Rotor-stator interaction noise: At subsonic speeds, fan noise mainly arises from the periodic rotor wake velocity deficit impacting stator vanes. From the stator frame, the rotating wakes occur at the blade passing frequency (BPF), inducing periodic stator

loading variations. This interaction produces noise at BPF harmonics $\omega = nBN$, where $n$ is the harmonic order, $B$ the blade count and $N$ is the rotational speed [96]. The Tyler and Sofrin rule gives the azimuthal orders $m$ of the generated acoustic duct modes as $m = nB - kV$, with $k$ an integer and $V$ the vane count [101]. The tonal nature causes narrow spectrum peaks. This mechanism has been substantially reduced over decades [96].

- Inlet distortions/rotor interaction noise: At subsonic speeds, this arises when steady inlet distortions from installation or ground effects interact with rotor blades, generating tones at the BPF and harmonics [100].

- Potential interaction noise: The stator vanes induce steady streamline distortions, fluctuating rotor blade pressures. This effect rapidly decays upstream and is negligible beyond 0.3 chord lengths. For future tighter rotor-stator spacing, this mechanism may become important, with the rotor trailing edge encountering the stator's periodic potential field, fluctuating blade loads converted to BPF tone harmonics. The Tyler-Sofrin rule applies, but the source order equals the vane count multiple $kV$.

Overall, extensive research has targeted tonal noise reduction, with considerable success over decades. However, further work is needed on emerging mechanisms with tighter future engine spacing.

### 5.2.2 Broadband noise

At subsonic operating conditions, the broadband noise component, which is related to the turbulent flow, becomes a significant contributor to the total noise emissions. The different BBN noise mechanisms are described as follows:

- Blade/Vane self-noise: The self-noise is associated with the turbulent flow that develops in the boundary layers of the blades and vanes, all along their span. When the flow remains attached along the surface of an airfoil with a sharp trailing edge, the turbulent eddies developing in the boundary layer are diffracted when passing the trailing edge and generate noise. This mechanism is referred as Trailing Edge noise (TE noise) and is mostly present in the case of a fan stage at its nominal operating regime. Experimental and computational studies have been conducted to characterize TE noise and develop noise reduction strategies, such as serrated trailing edges [102, 103]. If the fan operates at a lower regime, for example at approach conditions, a separation region may appear in the vicinity of the fan blades leading edge, which leads to the formation of a recirculation bubble in that region. This phenomenon and its contribution to self-noise have been studied experimentally using microphone arrays [104] and computationally using large eddy simulations [105].

- Rotor/Stator interaction noise: Also known as turbulence interaction noise or leading edge noise, this noise is produced when the turbulent flow in the wakes of the fan blades, formed by the mixing of both the suction and pressure side boundary layers at the trailing edge, impinge on the OGVs. The coherent and periodic components of the wakes give rise to tonal noise at the blade passing frequency, whereas the stochastic part of the wakes turbulent flow generate a broadband component. Hot-wire measurements [106] and computational fluid dynamics [107, 108] have been used to study this noise source, identified as one of the major contributors to the broadband noise radiated by modern aircraft engines.

- Upstream turbulence/rotor interaction noise: The interaction of the atmospheric upstream turbulence with the rotor leading edge can also be considered as a BBN source. Wind tunnel experiments with turbulence grids have examined this noise mechanism [109].

- Boundary layers/rotor interaction noise: The interaction of the turbulent boundary layers on the shroud and the hub with the rotor blades generates BBN. At the shroud, the boundary layer is thick and interacts with the tip gap of the blade. This may lead to the formation of a horse shoe vortex at the blade leading edge at the tip. At the hub, the boundary layer interacts with the blade and leads to the formation of a corner vortex. Detailed flow measurements have elucidated these interactions and their noise generation [108].

- Tip gap noise: The tip gap of the rotor blade leads to aerodynamic losses and noise generation. The pressure gradient between the pressure and suction side on the blade tip generates a tip clearance flow. This region is characterized by a high speed and turbulent flow, that exists in the gap as a cross-flow jet and interacts with the surrounding flow. Consequently, two main vortices are generally formed, (i) the tip leakage vortex (TLV), generated at the leading edge of the rotor, and (ii) the tip separation vortex (TSV), formed at mid-chord. These vortices interact with the outer flow and the surrounding walls of the blades and the shroud. Such interactions generate two highly turbulent pressure fluctuation zones, leading to broadband self-noise production.

  – The first zone corresponds to a jet-like flow, that generates a quadrupolar noise source when leaving the clearance region, directly and by interacting with the blade tip edge.
  – The second zone corresponds to the tip vortices, the TLV and TSV, that induce loading fluctuations when interacting with the suction side of the blade they originated from or the pressure side of the neighboring blades. The tip vortices are also diffracted at the TE and contribute to the TE noise, thus forming a local dipole source that is much more coherent than the distributed TE noise.

  The tip noise is usually characterized by large broadband humps in the acoustic spectra. These humps occur at frequencies independent from the BPF and its harmonics and correspond to quasi-tonal spectral features. These features result from the mixing of highly coherent flow structures (the tip leakage vortex) with uncorrelated flow structures (the turbulent flow), which leads to the spectral humps. The tip vortices may also interact with the stator vanes with a noise signature at the BPF harmonics, thus contributing to the RSI noise. Detailed experimental [109] and high-fidelity computational [110] studies have provided significant insight into tip gap noise generation.

## 5.3 LMFA testing facility and The ECL5 Fan/OGV stage configuration

### 5.3.1 Testing facility at LMFA

The ECL-B3 test facility, utilized for open-test-case investigations, is a newly established platform resulting from a collaborative effort between École Centrale de Lyon and Safran Aircraft Engines under the ANR EQUIPEX program. Commissioned in 2017, it has proven successful in examining a cutting-edge fan stage derived from the CFM International LEAP engine [10]. The purpose-built structure, inaugurated around the test cell, ensures minimal inflow disturbances, facilitating precise aerodynamic and acoustic characterizations of the test vehicle. Illustrated in Figure 5.3, the test cell comprises a rotor driven by an acoustically isolated electric motor with a maximum shaft power of 3000 kW at around 16,000 rpm. A torque meter measures applied power, while electronic control systems enable accurate transient investigations, providing autonomy from ambient conditions via active control of cooling and lubrication fluids. Operation oversight occurs from a separate control room, ensuring a clear distinction from the test cell and machine room. Operating in an open cycle, air is drawn in through silencers from the roof, passing through the anechoic chamber

housing the machine. Post fan stage, compressed air traverses an axisymmetric cone throttle for precise mass flow control. A Venturi nozzle after a 25 m long circular tube section measures mass flow. Exiting through a diffuser and additional silencers, the air is released to the ambient environment. Within the anechoic test chamber, a movable microphone array facilitates the localization and quantification of noise sources in the machine (Figure 5.4). To manage inflow turbulence, a spherical set of screens can be applied to the machine inlet (turbulence control system). The machine core comprises annular modules with variable instrumentation, allowing individual traversal for detailed flow field measurements. Mounted on purpose-designed rails and support systems, the core permits rapid module exchange during measurement campaigns, ensuring reproducible positioning. Emphasis has been placed on providing extensive instrumentation access to the flow channel, including optical access to the rotor section for planned laser-optical investigations.

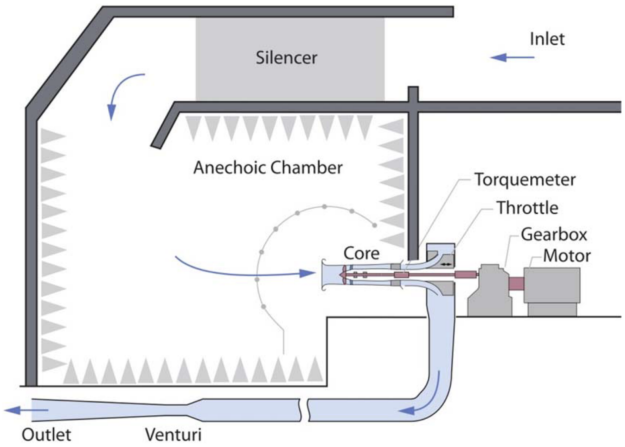


Figure 5.3: Test cell schematic. (from [10])

Figure 5.4: Test cell with traversable microphone antenna. (from [10])

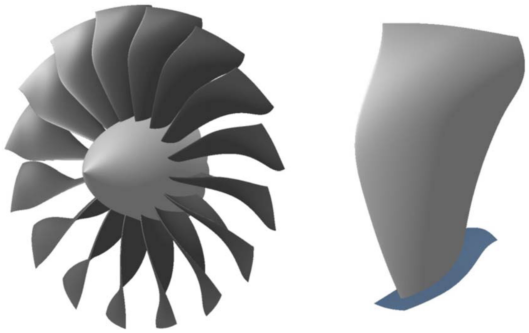

Figure 5.5: ECL5 rotor design. (from [10])

### 5.3.2 The ECL5 configuration and the geometry used for LES

The configuration of interest in this chapter features the ECL5 fan stage, a design originating from Ecole Centrale de Lyon [94], adhering to the technical specifications of a mid-range commercial aircraft. Serving as a novel open test case [111, 112], the ECL5 corresponds to an Ultra High Bypass Ratio (UHBR) aero-engine model characterized by a low rotational speed and the absence of core flow. This cutting-edge experiment has already contributed to investigations on blade vibrations [113] and the stability of turbomachinery flow [114]. Comprising 16 fan blades (B) and 31 Outlet Guide Vanes (OGVs) (V), the ECL5 fan stage serves as the basis for both the 360° and periodic sector geometries, as illustrated in Figure 5.5. In the context of periodic angular simulations, it is crucial to ensure consistency in the angular extent between the rotor and stator domains for the flow solver [29], which requires augmenting the vane count to 32 in the periodic sector configuration. This adjustment ensures a $2\pi/16$ (22.5°) angular periodicity. In this scenario, the OGV chord length is modified while preserving solidity, defined as the ratio of chord length to inter-vane spacing, to uphold stage performance [115]. In this chapter that focuses on the analysis of LES results obtained for this configuration, the computational domain spans from 3.75 fan chord lengths ($c_r$) upstream of the fan leading edge to 4.25 vane chord lengths ($c_s$) downstream of the OGV trailing edge. The upstream distance from the fan is chosen to ensure a well-developed boundary layer on the outer casing. Tip clearance is set at 0.965 mm at the leading edge and 1.27 mm at the trailing edge of the fan blade. The simulations are conducted under approach conditions, with a rotational speed ($\Omega$) of 6050 RPM, corresponding to 55% of the nominal rotational speed ($\Omega_n$), utilizing the fan hot shape. Figure 5.6 illustrates both the 360° and periodic sector computational domains.

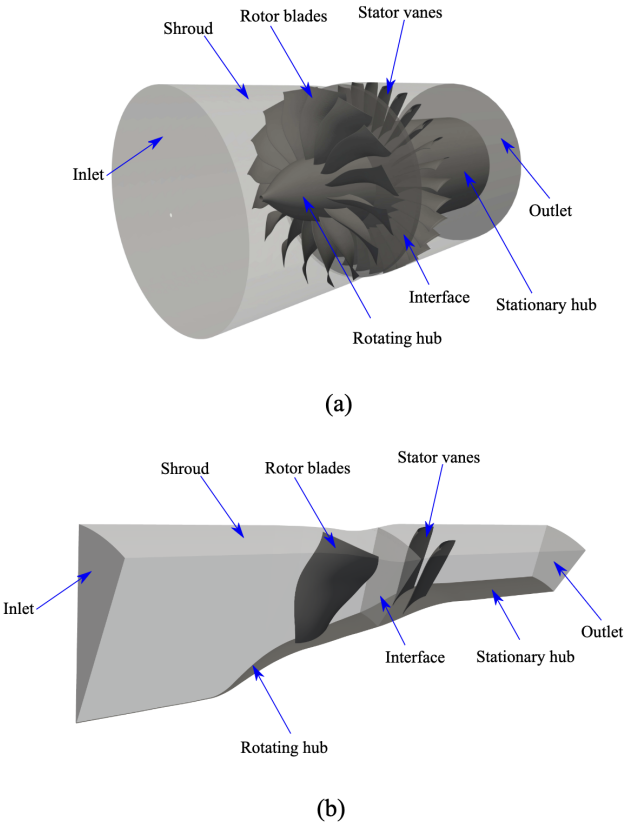


Figure 5.6: Computational domains of (a) the 360° and (b) the periodic sector ECL5 fan stage (from [11])

## 5.4 Numerical setup for BroadBand Noise LES

### 5.4.1 LES

This research initiative was accomplished by solving the governing equations of Large Eddy Simulations (LES) using the AVBP solver [29], an explicit, unstructured, fully compressible LES solver developed by CERFACS [29]. The rotor and stator domains are connected through CWIPI, employing an overlapping grid method [2]. The rotor domain accommodates the fan blades, while the stator domain contains the Outlet Guide Vanes (OGVs). A Two Steps Taylor Galerkin Convective (TTGC) scheme, a third-order finite-volume convective scheme, is utilized to address the filtered Navier-Stokes equations [116]. The sub-grid scale turbulence is modeled using the SIGMA sub-grid scale model [117]. Non-reflecting Navier-Stokes Characteristic Boundary Conditions (NSCBC) [118] are applied at the inlet and outlet sections, where a uniform mean flow is introduced axially with a total pressure of $P_0 = 101325$ Pa and a total temperature of $T_0 = 300$ K. The static pressure at the outlet section is adjusted to achieve the desired mass flow rate in the fan stage. For the periodic sector configuration, periodic boundary conditions are imposed on the azimuthal boundaries of the computational domain. On the surfaces of blades, vanes, shroud, and hub, a no-slip boundary condition is implemented. A wall law [119] captures the inner part of the boundary layer, with the dimensionless velocity relative to the wall $u^+ = \frac{1}{\kappa}\ln(Ay^+)$ for $y^+ > 11.45$, where $\kappa = 0.41$ and $A = 9.2$. Below $y^+ = 11.45$, a linear wall law is enforced. For the simulations presented in this chapter, the time step is set at $\Delta t = 2.8 \times 10^8 s$, and the computational cost is around $10^5$ CPUh per rotation for the periodic sector configura-

tion and $1.7 \times 10^6$ CPUh per rotation for the 360° configuration. The simulations involved two complete fan rotations for numerical convergence and a minimum of an additional four rotations for post-processing and acoustic data collection.

### 5.4.2 A priori setup for Direct Noise predictions using Large Eddy Simulation

Directly predicting noise using LES imposes stringent constraints on the solver and mesh, demanding a substantial amount of CPU hours, necessitating careful pre-evaluation. The interplay of these constraints complicates obtaining essential simulation variables, particularly for 360° simulations. Influential factors such as the convective scheme's order, wall mesh resolution, and the acoustic cut-off frequency, generated by acoustic wave propagation, are challenging to assess beforehand. Addressing these challenges, Jean Al Am conducted numerous simplified simulations as part of a multi-parameter analysis during his PhD. The specifics of this analysis are detailed in Jean Al Am's PhD thesis, with some key findings highlighted here:

- In order to provide good statistics for the boundary layer development on the blades, one should have a reasonable grid spacing at the wall no larger than $y^+|_{wall} <= 50$. Values for $x^+|_{wall}$ and $z^+|_{wall}$ should be chosen accordingly such that $x^+|_{wall} <= 150$ and $z^+|_{wall} < 150$.
- Away from the walls, two phenomena need to be properly captured by the LES, namely the acoustic waves and the turbulent structures.
  - For the former, the quantity of interest is the apparent wavelength, directly linked with the frequency and the Mach number. It is shown that 13 points per apparent wavelength is enough to accurately propagate the acoustic waves up to a frequency of 20 kHz.
  - For the latter, the quantities of interest are the Turbulent integral scale and the Taylor micro-scale. The resolution of the LES should lie between those two scales so that the LES cut-off frequency remains in the inertial region of the turbulent spectrum. It has been shown that a grid spacing as close as possible from the Taylor micro-scale provides good results.

  Depending on the Mach and Reynolds numbers, the smallest size should be used to properly design the mesh away from the walls.

Armed with this knowledge, we can overcome the inherent challenge of determining the physical qualities influenced by a specific mesh and numerical setup before executing LES. To harness this insight, we developed LESCOTT, an acronym for "Large Eddy Simulations COnfiguration Tool for Turbomachinery,", a pre-dimensioning tool for LES setups in turbomachinery applications, initiated by Jérôme Boudet and notably enhanced during Jean Al Am's PhD. On top of the above recommandations regarding the grid spacing, LESCOTT is equipped with the knowledge of the computational CPU-hour cost per time-step per million element that changes depending on the HPC cluster used and the numerical scheme at hand. introducing the statistical requirements for temporal convergence and the geometry within LESCOTT, the overall cost of LES studies using AVBP can be asserted prior to the computation within less than 10% error margin.

## 5.5 Description and Impact of Recirculation Bubbles on Fan Noise

In the course of Jean Al Am PhD thesis, the first LES that was made was the one of a spanwise strip of the full ECL5 configuration as illustrated in Figure 5.7. This simplified

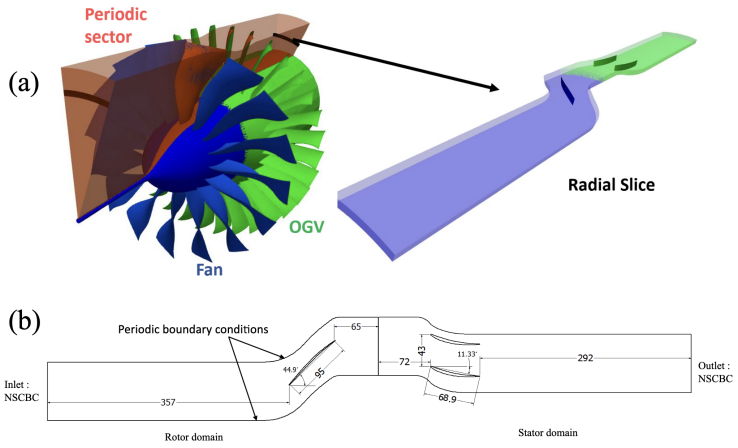


Figure 5.7: (a) Radial slice sector of the Fan/OGV stage. (b) Blade-to-blade view of the ECL5 fan/OGV configuration at 80% of the span. Dimensions are given in mm. Angles are given in degrees. (from [12])

configuration proved useful to prepare for the next steps of this investigation but also revealed some very interesting phenomena. Among those, a recirculation bubble was found at partial rotational speed on the suction side of the rotor blades which acoustic emissions proved to be significant. This led us to devote some significant efforts and try to better understand the structure and noise emission mechanisms of this bubble. All the details of this study have been published in *Al Am et al., On the effects of a separation bubble on fan noise, Journal of Sound and Vibration (537), 2022.* The objective of this section is to provide the reader with its main conclusions and findings.

It should be first mentioned that separation bubbles as being responsible for BBN emissions in turbomachinery is not new and has been explored by numerous authors. For low fan speeds, such as during approach conditions, a region of flow separation near the leading edge (LE) of the fan blades may emerge, potentially generating a recirculation bubble. This occurrence and its impact on self-noise have been thoroughly investigated both experimentally [120, 121, 122, 123] and numerically [124, 125, 126, 127, 128, 129] using a single airfoil configuration.
Michelis et al. [122] show a dominant broadband peak in the Power Spectral Density (PSD) of the velocity fluctuations in the bubble region, which is related to Kelvin-Helmholtz instabilities. Yet these analyses involve single profiles and a detailed analysis in a realistic fan/OGV context was missing.
As often in this type of studies, we first started with an observation, the observation that the Power Spectral Density of pressure fluctuations showed significant additional peaks when compared to our expectations for the target mass flow rate of 21 kg/s. Figure 5.8 shows the comparison of the PSD of pressure fluctuations in two simulations. The first one comprises both the rotor and stator stages whereas the second one only contains the rotor stage. It shows that if the peaks correlated to the Vane Passing Frequency (VPF) vanish in the rotating frame of reference, some High Frequency Peaks (HFP) remain even in presence of the rotor alone. It shows that these peaks find their source on the rotor. By varying

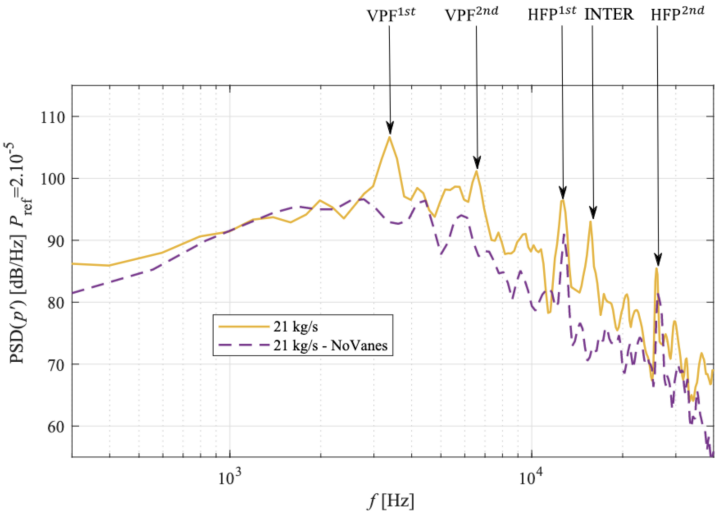


Figure 5.8: PSD of the pressure fluctuations from a monitor point in the normal direction to the rotor surface at one chord length from the rotor LE. Comparison between rotor-stator and rotor-alone simulations at $\dot{m} = 21$ kg/s. (from [12])

the mass flow rate, a change in the acoustic emission pattern can be observed. Of course, at the same time, as one modifies the fan blade attack angle a separation bubble appears and strengthens with the decreasing mass flow rate as illustrated in Figure 5.9. The bubble becomes very significant below $\dot{m} = 21$ kg/s and produces a clear signature on the turbulent kinetic energy contour. Some statistical aspects of the turbulent boundary layer forming on

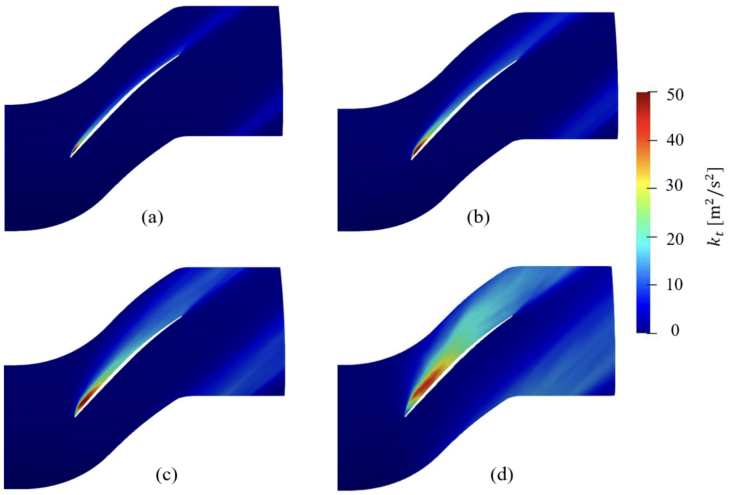


Figure 5.9: Contours of turbulent kinetic energy kt around the rotor blade, for various mass flow rates, (a) $\dot{m} = 22$ kg/s, (b) $\dot{m} = 21$ kg/s, (c) $\dot{m} = 20$ kg/s and (d) $\dot{m} = 19$ kg/s. (from [12])

the suction side are provided in Figures 5.10 and 5.11. They clearly show the extent of a separation bubble that perturbs the development of the boundary layer on the suction side. The displacement thickness at the trailing edge is significantly influenced by the presence of the bubble. Looking at the shape factor of the turbulent boundary layer one sees that it reattaches behind the bubble and is turbulent in nature. In fact the bubble almost acts as

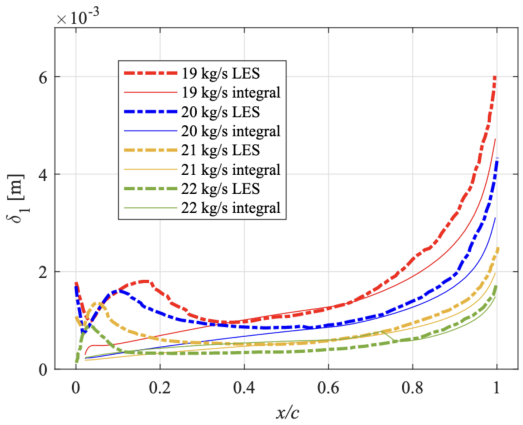


Figure 5.10: Comparison of boundary layer parameters on the suction side of the rotor blade for various mass flow rates. Boundary layer displacement thickness $\delta 1$ (from [12])

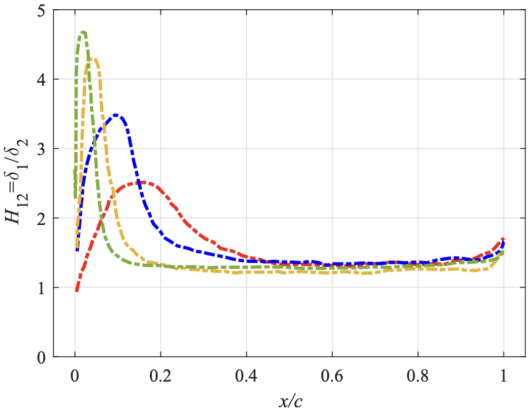


Figure 5.11: Comparison of boundary layer parameters on the suction side of the rotor blade for various mass flow rates. Shape factor $H_{12}$. (from [12])

a solid object that would induce the transition to turbulence of the boundary layer. This is illustrated by fine lines in Figure 5.10 which show the growth of a regular turbulent boundary layer taking into account its initial thickness to be the one computed just behind the bubble.
As illustrated in Figure 5.12, the effective thickness of the boundary layer also has downstream a strong impact on the width and strength of the rotor wake with the largest bubble leading in the context of an also larger angle of attack to a more pronounced wake. Coming back to the pressure fluctuation PSD in Figure 5.13, this can explain why the change of the angle of attack both modifies the peaks and the broadband content of the PSD. Tonal noise also is influenced through the modification of the rotor wake that downstream hits the vane leading edges. This is particularly visible at frequencies below 4000Hz for which one can rank the spectra using the mass flow rate information only. However, if the VPF peak and its harmonics more or less follow an expected behaviour in Figure 5.13, it is not the case of the HFP and the peak denoted INTER. Their frequency increases with the mass flow rate when they exist. To better grasp the difference in nature between those acoustic signatures, a DMT technique [130] was used to filter the density at the VPF and at the HFP frequency. Both blade-to-blade views are shown in Figure 5.14. These fields undoubtedly show that the separation bubble is at the origin of the HFP. A closer inspection of the Q criterion field on top of the suction side presented in Figure 5.15 shows the presence of large

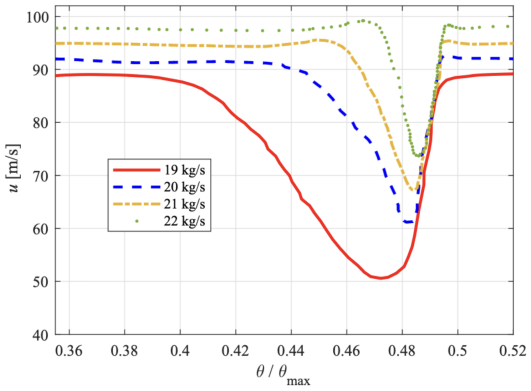


Figure 5.12: Comparison of the streamwise velocity component $u$ profiles in the wake of the rotor blade, at one chord length from the TE. (from [12])

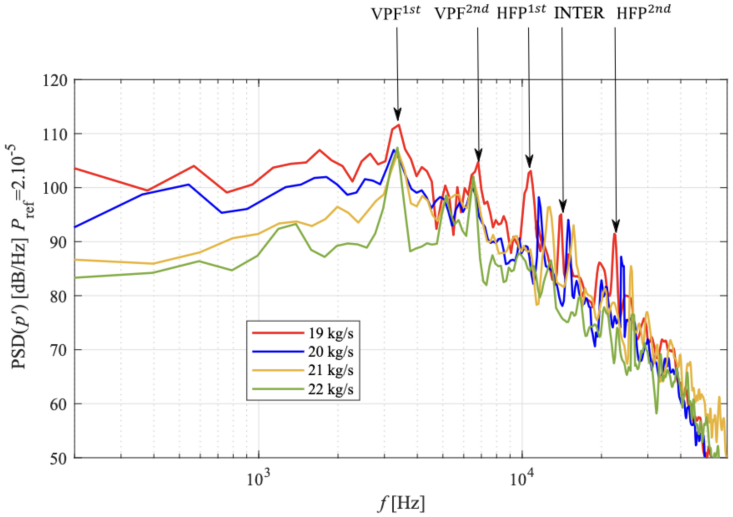


Figure 5.13: PSD of the pressure fluctuations from a monitor point in the normal direction to the rotor surface at one chord length from the rotor LE. Rotor-stator simulations at various mass flow rates (from [12])

spanwise vortical structures in the vicinity of the separation bubble, particularly visible for the smallest mass flow rate. Using the DMT results at the HFP frequency peak, one can reconstruct the band-filtered Q criterion. As shown in Figure 5.16 the scalar iso-surface even more clearly reveals the spanwise structures hinted at by Figure 5.15. Their spacing is regular and their organisation is strongly reminiscent of that observed behind a bluff body. By analogy, one can associate the size of the obstacle to the displacement thickness computed in the separation region. Together with the freestream velocity and the HFP frequency, one can form a Strouhal number. Figure 5.17 provides the result of this analysis. It shows that regardless of the operating conditions at hand, the noise associated to the HFP can be linked to a periodic vortex release mechanism unaware of the turbomachinery context in which it occurs. This result and the simple relations to which it leads is believed to be of significant importance for further research which will aim at modeling this acoustic source, particularly significant at low mass flow rates. To this respect, it is interesting to note that the RSI tones and the bubble tones can interact and lead to mixed modes such as the one denoted INTER in this study.

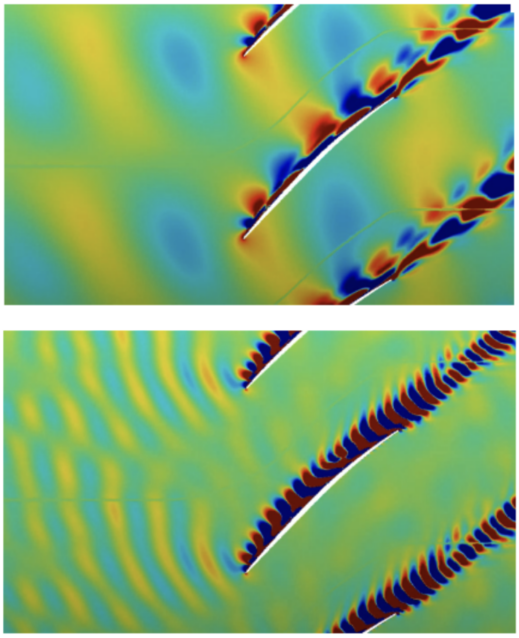

Figure 5.14: Spatial distribution of the density modes using the DMT technique. Frequency : $VPF^{1st}$ (top), $HFP^{1st}$ (bottom) . (from [12])

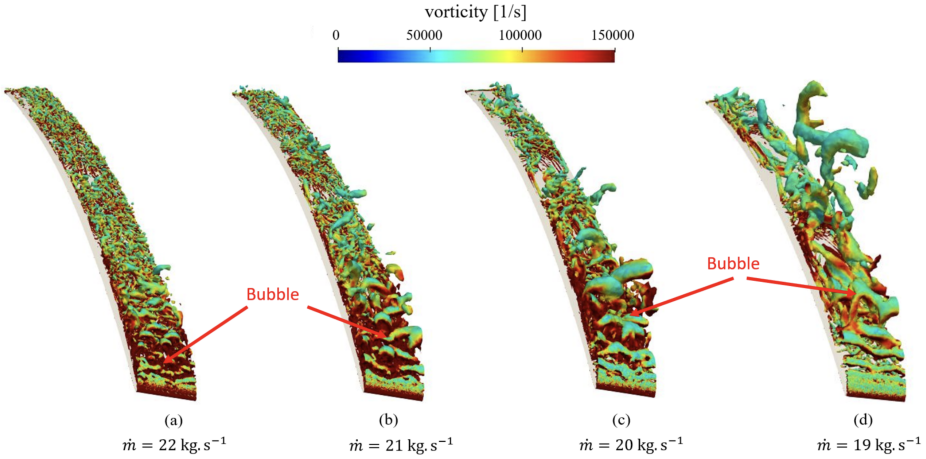


Figure 5.15: Iso-surfaces of Q-criterion ($Qc^2/U_0^2 = 1500$), colored by the vorticity magnitude, for the different mass flow rates. The cases are shown by decreasing mass flow rate, and increasing the angle of attack of the fan blade. (from [12])

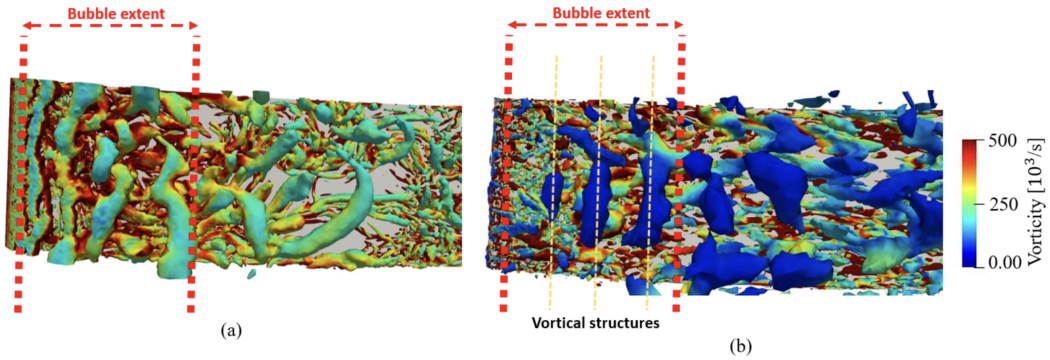


Figure 5.16: so-surfaces of Q-criterion ($Qc^2/U_0^2 = 5000$), colored by the vorticity magnitude, for the mass flow rate $\dot{m} = 20$ kg/s. (a) Instantaneous flow field. (b) Mode using the DMT technique at $HFP^{1st}$. (from [12])

| $\dot{m}$ [kg/s] | $U_0$ [m/s] | $\delta_{1,\text{bubble}}$ [mm] | HFP$^{1st}$ frequency [kHz] | $St$ |
|---|---|---|---|---|
| 19 | 80 | 1.81 | 10.5 | 0.237 |
| 20 | 84 | 1.61 | 11.6 | 0.222 |
| 21 | 88 | 1.38 | 12.8 | 0.201 |

Figure 5.17: Strouhal number $St$ parameters for various mass flow rates. $\delta_{1,bubble}$ corresponds to the local maximum of the boundary layer displacement thickness $\delta_1$ in the separation region. (from [12])

## 5.6 Influence of Tip-Gap Flow Mechanisms on Fan/OGV Broadband Noise

Progressing into our understanding of the broadband noise emission mechanisms at play in the ECL5 configuration, we now turn our attention to the tip-leakage flow. This region is of a particular interest because of the complexity of the flow structures it harbors.

Numerous experimental investigations [131, 132] and numerical analyses [133, 134, 135, 136] have delved into the nuances of the tip-leakage flow, focusing predominantly on isolated airfoil configurations. These studies have aimed to dissect the tip-leakage flow's intricacies, free from additional aerodynamic complexities and fan noise sources typical in rotating setups. Grilliat et al. [131] conducted a parametric examination on a NACA 5510 airfoil positioned between two side plates. They explored the effects of flow speed, angle of attack, and tip-gap size variations on the tip-leakage flow topology and noise emissions. Notably, while flow speed exhibited minimal influence, angle of attack and tip-gap size significantly shaped the flow dynamics. Acoustic analysis identified two primary noise sources in the far-field spectrum: the first, occurring at frequencies between 0.7 kHz and 3.5 kHz, emanated from turbulent structures in the tip-gap region convected past the trailing edge. The second noise source, predominant between 4 kHz and 7 kHz, stemmed from vortices within the tip-leakage flow's shear layers. Various numerical methodologies, including large-eddy simulation (LES), zonal LES, and lattice Boltzmann methods, have corroborated these findings, pinpointing the main noise source near the airfoil tip. Additionally, studies have shifted focus to rectilinear compressor cascades to explore the tip-leakage flow's complexities and noise mechanisms further. Kang and Hirsh [137] conducted experimental investigations on a cascade of NACA 65-1810 airfoils, identifying multiple types of tip vortices and their interactions. Numerical simulations, such as those by You et al. [138], elucidated the flow characteristics and noise generation mechanisms within compressor cascades, corroborating experimental findings. To capture realistic turbomachinery configurations, both experimental and numerical studies have employed scale model fan stages, such as the NASA source diagnostic test (SDT) configuration. These investigations have enabled a comprehensive understanding of tip-leakage flow dynamics and noise emissions in contemporary fan stages designed for transonic operation.

As already observed in previous studies on other geometries and devoted to the analysis of the tip-leakage flow and its acoustic emissions, the organisation of the flow in the tip region of the ECL5 rotor is quite complex. In order to gain some understanding, Figure 5.18 presents an iso-surface of the Q-criterion based on the time-averaged flow field. A complex flow pattern emerges within the tip-gap region, characterized by the presence of multiple tip vortices. These include a horseshoe vortex (HSV) near the leading edge of the blade, a first tip-leakage vortex (TLV1) forming approximately 0.25 chord lengths from the leading edge, and a tip separation vortex (TSV) along with a second tip-leakage vortex (TLV2) and an induced vortex (IV) at around 0.7 chord lengths. This wealth in terms of vortical structures at the tip-gap is somewhat unusual in the sense that usually only one tip-leakage vortex is observed. It is thought that the profile's shape at the tip (visible in Figure 5.19 (f)) adapted to transonic flows and which presents a double curvature explains the creation of this additional tip-leakage vortex. Figure 5.19 illustrates the complexity of the flow at the tip with fluctuations of the velocity encompassing the entire blade-to-blade region near the trailing edge.

Figure 5.20 further shows the structures in the tip-leakage flow and different iso-surfaces of the Q-criterion, for which a growing value of the threshold is chosen. It enables to better understand the hierarchy of the vortical structures. This comparison is summarized in Figure 5.21. It reveals that the tip separation vortex also denoted as the second tip leakage

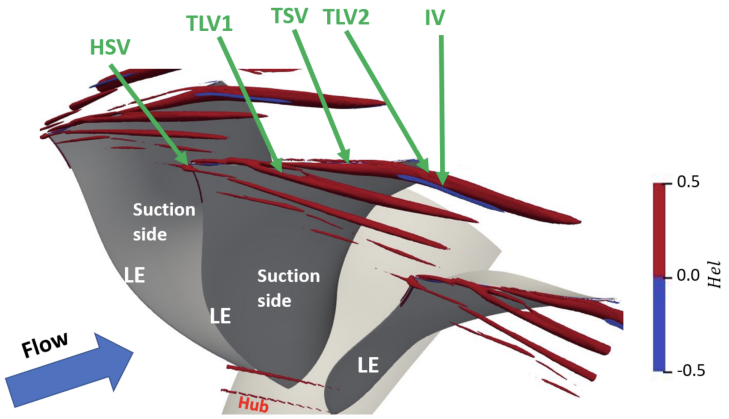


Figure 5.18: Averaged iso-surface of Q-criterion ($Qc_r^2/U_0^2 = 500$), where $U_0$ is the free-stream velocity magnitude) in the tip-gap region, colored by the normalized helicity. (from [13])

vortex is the strongest. Yet this comparison also reveals the path taken by each of the vortical structures in the flow. For example, the HSV, generated somewhat in front of the leading-edge of the blade impacts the next blade at a location in % of the chord which is close to the one where the TLV1 finds its origin (see in particular Figure 5.20 (a) ).

The instantaneous contour of the dilatation rate shown in Figure 5.22 enables to better understand the intrinsic turbulent nature of the flow in the tip-gap. If the HSV and TLV1 can clearly be identified, this not really the case of the TVL2/TSV and IV which are only emerging structures from the temporal averaging procedure. In practice, a large complex turbulent zone follows a trajectory that leads it to impact the next blade at the trailing edge, with numerous additional smaller structures generated by the main vortical motion.

To get a first glimpse at the acoustic emissions related to the flow structures in the ECL5 configuration, Figure 5.23 shows the instantaneous contours of the dilatation and iso-surfaces of the Q-criterion at two spanwise locations. At 80% of the entire span, acoustic wave are clearly visible and seem to originate from the trailing edge of the blade. At 98%, the picture becomes more complex and if the trailing edge still remains among the possible emission regions, other acoustic waves seem to be emitted at other locations along the chord.

To better grasp the potential influence of the tip-gap flow on the acoustic emission, we now turn our attention to the Wall Pressure Spectra (WPS) on the rotor blade at different locations in span and chord. Figure 5.24 (a) shows a comparison of the WPS at 80% of the entire blade span. This comparison reveals that between $10^3$ and $10^4$ Hz, the WPS follows the theoretical trend but also that above $10^4$ Hz, a hump is visible in the spectrum at larger values of the chord. This is further evidenced when one analyses the same comparison at 98% of the span. At that location in span, the signal almost becomes flat between $5 \times 10^3$ and $3 \times 10^4$ Hz for the most downstream location. Since this location completely lies within the tip-gap flow zone of influence, it is consistent to assume that the observed increase in the WPS is related to the additional pressure fluctuations induced by the turbulent structures identified earlier.

Figure 5.25 further explores the WPS at the tip gap itself as a function of the location along the chord. A general picture emerges in which the WPS globally increases as one moves downstream. Since it has been observed that the intensity of the turbulence increases in this direction, this result is not that surprising. Yet it also becomes apparent that the entire

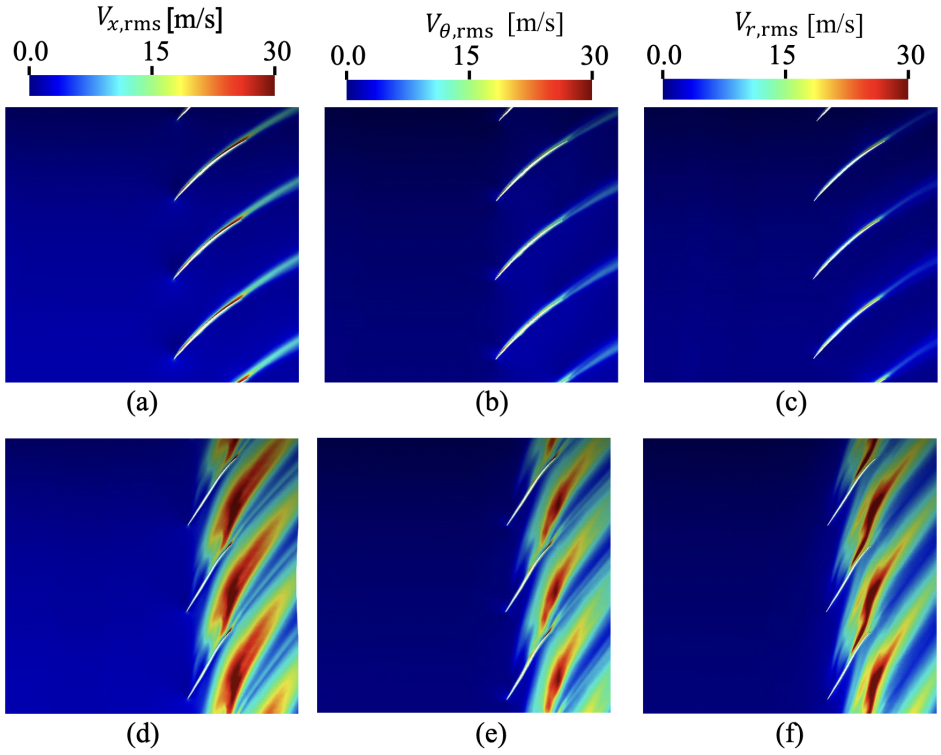


Figure 5.19: Contours of the components of the RMS velocity fluctuations, around the rotor blade, at two spanwise positions, (a,b,c) 80%, (d,e,f) 99% (from [13])

WPS is not influenced in the same way depending on the specific frequency of interest. Between 30% and 50% of the chord the increase mostly occurs beyond $10^4$ Hz. Between 50% and 70%, the entire spectrum increases and again the region in the spectrum that lies beyond $10^4$ Hz appears to be the most influenced. The comparison of the WPS between 70% and 90% of the chord interestingly shows a different evolution. The increase of the WPS is limited to the region in the spectrum below $10^4$ Hz and a decrease is observed beyond. From this analysis one gets the idea that two main mechanisms are at play that explain the evolution of the WPS. The first one mostly occurs between 30% and 70% of the chord and impacts the WPS at high frequencies (beyond $10^4$ Hz) and a second mechanism mostly occurs close to the trailing edge and influences the WPS at frequencies lower than $10^4$ Hz.

To try to prove this hypothesis, a coherence analysis between the pressure fluctuations is made between points in the tip-gap flow that are represented in Figure 5.26 (b). Figure 5.27 (a) reveals that pressure fluctuations at "A" and "D" are particularly correlated for frequencies lower than $10^4$ Hz. This results advocates in favor of the pressure fluctuation at the trailing edge being generated by the diffraction of vortical structures at the trailing edge of the blade originating from the TLV1. Figure 5.27 (b) shows a strong correlation between "B" and "C" mostly localized at high frequencies.

Of course one should not confuse the WPS with the actual acoustic emission, especially in this highly turbulent context. To gain some better understanding in this regard, Figure 5.28 proposes a comparison of the SWL spectra from the FWH analogy for the full rotor blade, the lower part of the blade (below 80% of the entire span), the tip-gap region and the cross-correlation between them in the upstream and downstream directions. This analysis reveals that regardless of the direction, the blade is the main source of noise at low frequencies

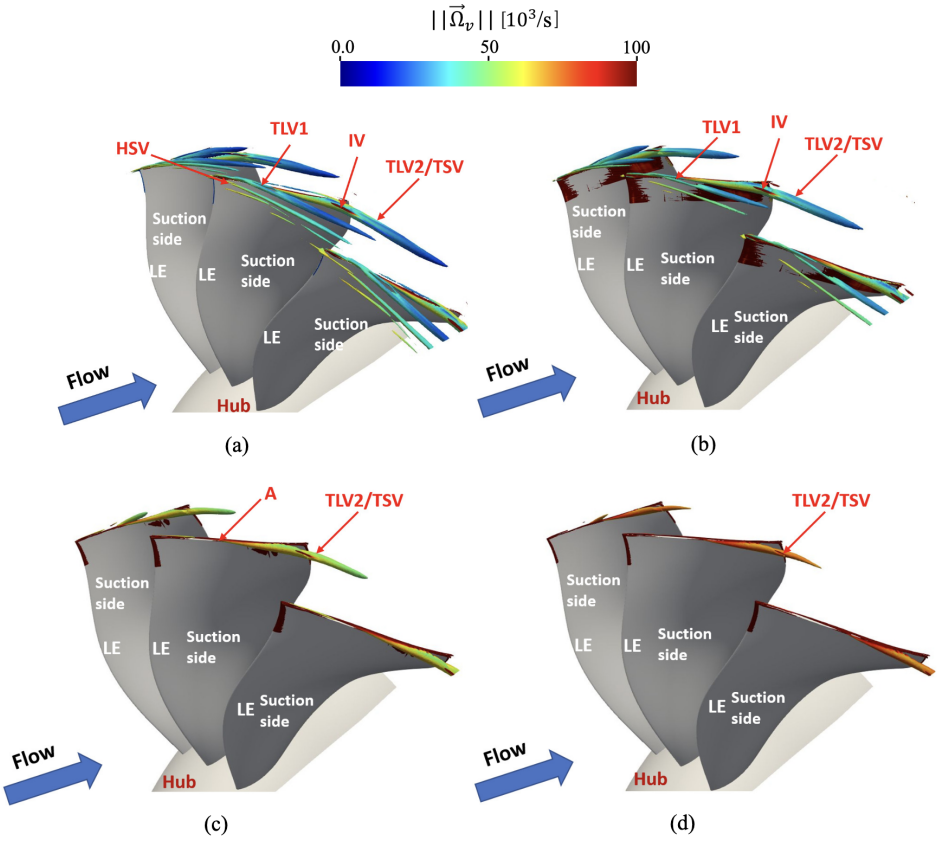


Figure 5.20: Averaged Q-criterion in the tip-gap region, colored by the vorticity magnitude, for different iso-surface values, (a) $Qc_r^2/U_0^2 = 500$, (b)$Qc_r^2/U_0^2 = 750$ , (c)$Qc_r^2/U_0^2 = 1000$ , and (d)$Qc_r^2/U_0^2 = 1250$ . (from [13])

(below $2 \times 10^3$ Hz). Beyond this value, the two regions are responsible for the acoustic emission at equal shares, especially in the upstream direction. Beyond $10^4$ Hz, the tip-gap region even becomes the main acoustic source region in the upstream direction and is responsible for the entire spectrum very slow decay at high frequencies.

| Type of vortex | Onset at fan tip | Rotation | Relative intensity | Inter-adj | Inter-same |
|---|---|---|---|---|---|
| HSV | leading edge | CW | + | yes | no |
| TLV1 | $0.25c_r$ | CW | ++ | yes | no |
| TSV | $0.70c_r$ | CW | ++++ | no | yes |
| TLV2 | $0.75c_r$ | CW | ++++ | no | yes |
| IV | $0.75c_r$ | CCW | +++ | no | yes |

Figure 5.21: Summary of the main characteristics estimated for the different tip-leakage vortices. (from [13])

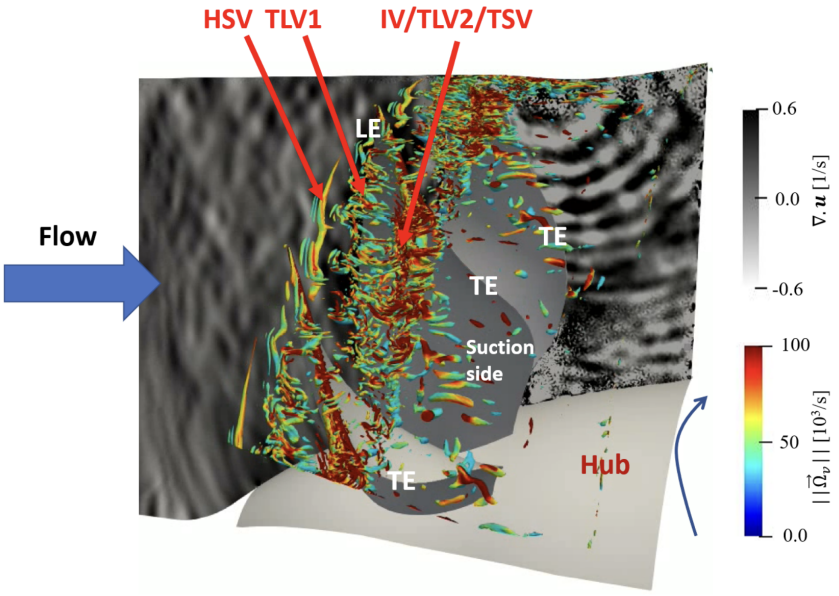


Figure 5.22: Instantaneous contours of dilatation rate in a cross-section that intersects the rotor blade, and iso-surfaces of Q-criterion ($Qc_r^2/U_0^2 = 100$) colored by the vorticity magnitude in the tip-gap region. "LE" refers to the leading edge and "TE" refers to the trailing edge. (from [13])

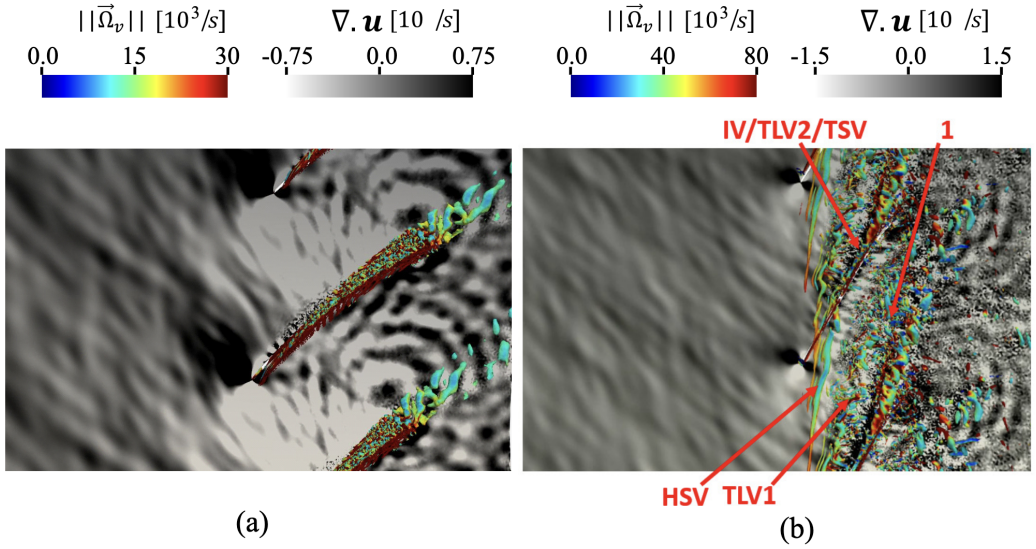


Figure 5.23: Instantaneous contours of dilatation rate and iso-surfaces of Q-criterion ($Qc_r^2/U_0^2 = 100$) colored by the vorticity magnitude, around the rotor blades, at two spanwise positions, (a) 80% and (b) 98%. (from [13])

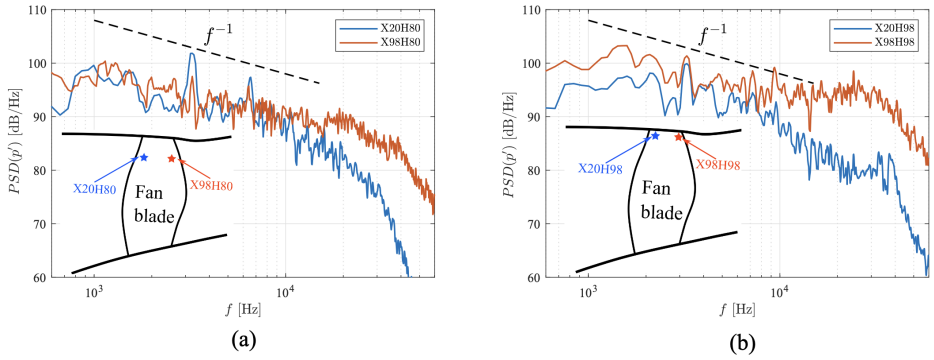


Figure 5.24: WPS on the suction surface of the rotor blade, at several positions (a) 80% and (b) 98% of the rotor span. p' corresponds to the pressure fluctuation. The reference pressure is $P_{ref} = 2 \times 10^5$ Pa. (from [13])

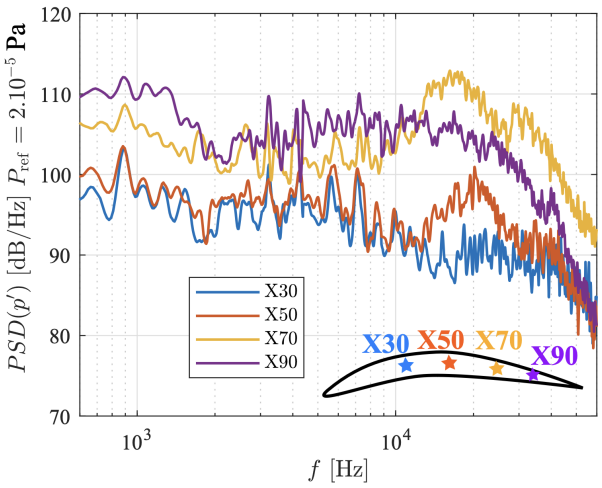


Figure 5.25: WPS on the surface of the blade tip, at four different chordwise positions. (from [13])

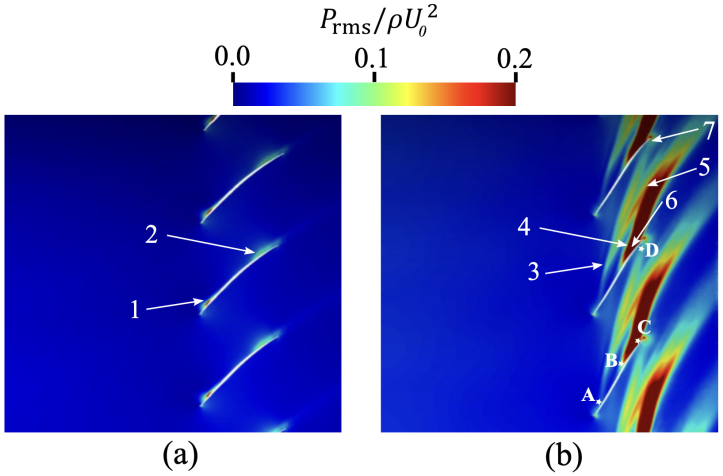


Figure 5.26: Contours of RMS pressure fluctuations around the rotor blade, at two spanwise positions, (a) 80%, (b) 99%. The star symbols show the positions of the monitor points, "A", "B", "C" and "D", used for the computation of the coherence in the tip-gap region. (from [13])

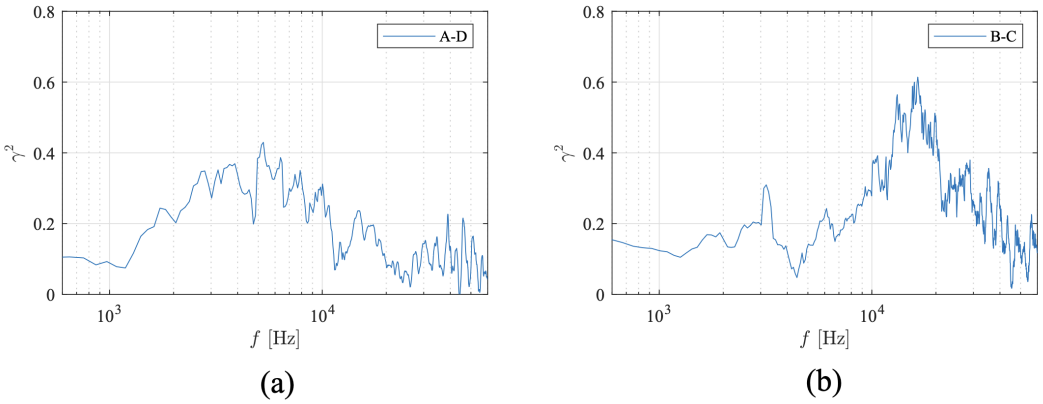


Figure 5.27: Coherence between the pressure fluctuations at the monitor points "A" and "D" (a), and the monitor points "B" and "C" (b). (from [13])

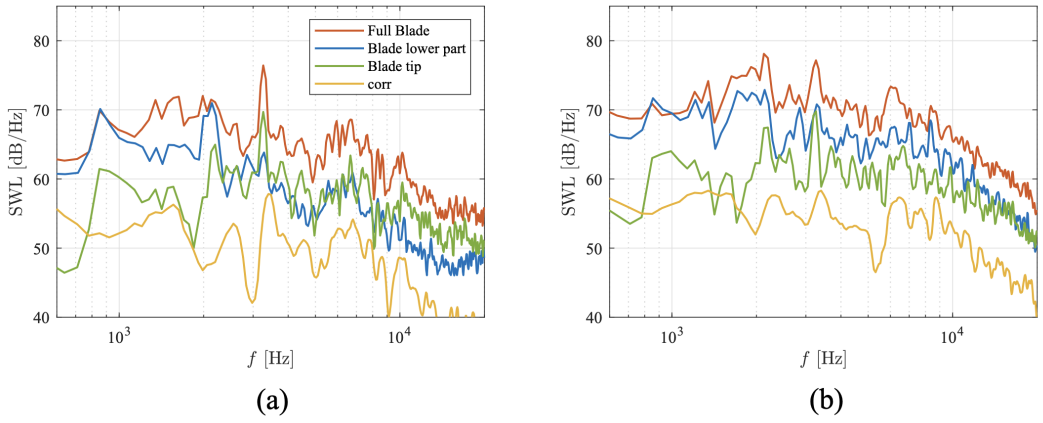


Figure 5.28: SWL spectra from the FWH analogy[14] for the full blade (denoted "Full Blade"), the tip-gap region (denoted "Blade tip"), the lower part of the blade (denoted "Blade lower part") and the cross-correlation between them (denoted "corr"). (a) Upstream direction. (b) Downstream direction. (from [13])

## 5.7 360° Direct Noise Predictions and Experimental Validation

This last result section in this chapter concentrates on the acoustic results obtained through direct propagation of the sound waves in the LES for two different instances of the ECL5 Fan/OGV case. As already mentioned a periodic case is considered in which the number of vanes is adapted to satisfy this angular periodicity condition. This LES has been performed on the HPC cluster OCCIGEN using CPUh allocated through the DARI-GENCI annual call process. The second computation, much more computationally intensive considers the full ECL5 geometry representing 360° of the machine. It has been performed on the cluster IRENE using CPUh allocated through the EuroHPC-PRACE call process. The two LES have been compared in a recent paper [11] which reveals that only the 360° provides a full picture of the acoustic emission in this flow. The following results, still somewhat preliminary, will be compared in the near future with experimental findings. As a first step towards this comparison, Figure 5.29 provides a comparison between the LES, RANS and experimental results of the radial profiles of the (a) total pressure, (b) relative flow angle, and (c) total temperature. It appears that the LES is able to reproduce these radial profiles with a very good accuracy, especially at the tip. This encouraging result suggests that further acoustic analysis can be done using the results from both the periodic and 360° LES results.

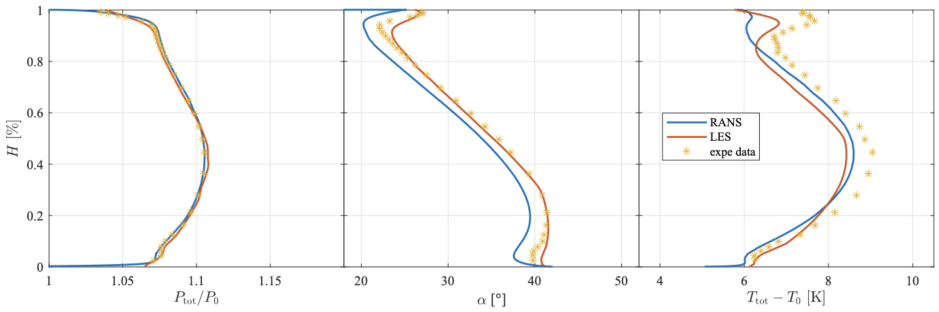


Figure 5.29: Comparison between the LES, RANS and experimental results of the radial profiles of the (a) total pressure, (b) relative flow angle, and (c) total temperature. (from [11])

Figure 5.30 illustrates the two LES results. One can see the rotor and OGV wheels surrounded by an iso-surface of the Q-criterion revealing the vortical structures developing in the flow especially along the walls and in the wakes. Additionally, the dilatation is shown at 99% of the full span. It reveals very strong signatures in the turbulent region of the tip gap but also significant levels most probably related to acoustic waves upstream of the rotor.

The next two Figures compare the azimuthal modal decompositions at the inlet and outlet of the LES with experimental results upstream of the rotor and downstream of the stator. At the inlet, a modal decomposition in the azimuthal direction is done which shows in Figure 5.31 that co-rotating modes have much stronger levels. This corroborates theoretical results related to the preferred emission directivity of the emitting dipoles at the leading edges of the stator blades. In Figure 5.31, white lines are added to represent the Tyler&Sofrin cut-off limit [101] and azimuthal modes at the inlet are indeed found to be cut-on with only small levels beyond the limit. The comparison between numerical and experimental results shows that the overall distribution of the modal content is very well captured by the LES. They both share the same distorsion leading to positive azimuthal modes having larger amplitude and for example they also share the same groups of modes having larger amplitudes between BPF1 and BPF3, localized on the positive side and at the

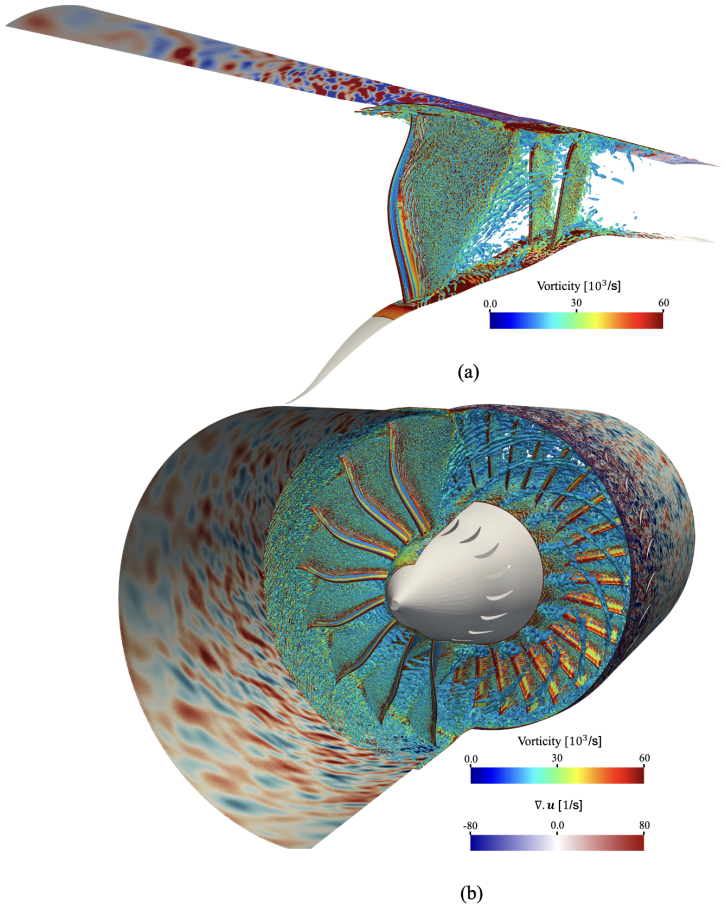


Figure 5.30: Iso-contours of Q-criterion colored by vorticity magnitude in the fan stage and instantaneous contours of dilatation rate at 99% of the span. (a) Periodic sector LES. (b) 360° LES. (from [11])

same distance from the cut-off limit.
Figure 5.32 presents the azimuthal mode decomposition at the outlet, no difference if found between co-rotating and counter-rotating modes. The diagram is therefore symmetric. Dotted curves correspond to the cut-on limits of increasing radial order modes and concentrate the most significant levels. Here again, the qualitative agreement between LES and experiment is very good, although maybe not as good as for the inlet. Yet, significant modes seem to be localized symmetrically with respect to order 0. The distributions also seem to share the same type of increase as additional radial numbers become cut-on. Figure 5.33 further explores the acoustic modes emitted by the ECL5 at 55Nn by providing for each harmonic of the BPF, the azimuthal and radial mode decomposition. It appears that for BPF1 and because of the short distance between the stator trailing edge and the outlet surface, modes $m = -15$ and $m = 16$ are not entirely cut-off and represent the dominant modes. Yet, for all other frequencies and directions, only cut-on modes dominate. One again finds that upstream the co-rotating modes are favored. The most important modes are $m = 1$ for the first harmonic of the BPF, $m = 17$ for the second harmonic and $m = 2$ and $m = 33$ for the third harmonic. Downstream, the dominating modes are $m = 1$ for the first harmonic of the BPF, $m = -14$ and $m = 17$ for the second harmonic and $m = 2$, $m = -29$ and $m = 33$ for the third harmonic.
Upstream and for the BPF and its first harmonic, only the radial modes with order $n = 0$

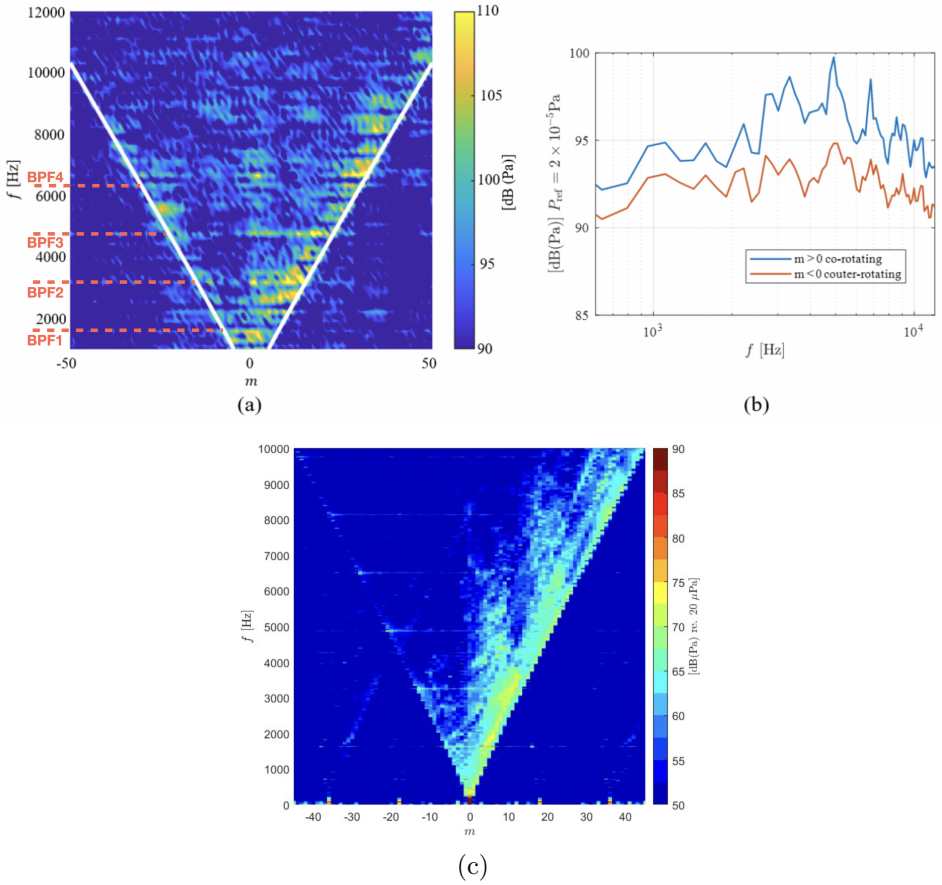


Figure 5.31: Azimuthal mode detection plots at the intake section. (a) 360° **LES:** The frequency is plotted against the azimuthal mode order m, and the modes are colored by their amplitude. (b) Integrated mode spectra over co-rotating (m > 0) and counter-rotating (m < 0) modes, (c) **Experiment:** The frequency is plotted against the azimuthal mode order m (from [11])

concur to the observed azimuthal modes. Yet at larger frequencies, radial modes of order $n = 1$ start to emerge. (see for example mode $m = 1$ for BPF3). For some modes, higher radial mode orders even become predominant. For example, for the third harmonic of the BPF (BPF4), the azimuthal mode $m = 2$ is mostly composed of radial modes with order larger than 1. Downstream, the lower number of azimuthal modes dominating the emitted acoustic signal makes the analysis slightly simpler. Interestingly, higher radial mode orders often dominate over the radial mode $n = 0$. This is the case at all frequencies; see for example the azimuthal mode $m = 16$ which is mostly composed of radial modes $n = 1$ and $n = 2$.

To gain some deeper understanding of this modal content, Figure 5.34 presents the spatial distribution of the density modes using the DMT technique [130] at the BPF and its first three harmonics. The general impression is that higher orders (that correspond spatially to smaller structures) are much more present downstream in comparison to what is observed at the inlet.

Upstream and for the first harmonic (BPF2), the first azimuthal mode is clearly visible. It is also mostly composed of the radial mode of order 0. Downstream and for the BPF, azimuthal mode $m = 16$ is clearly visible especially close to the hub which translates into a radial mode order equal or larger than $n = 1$.

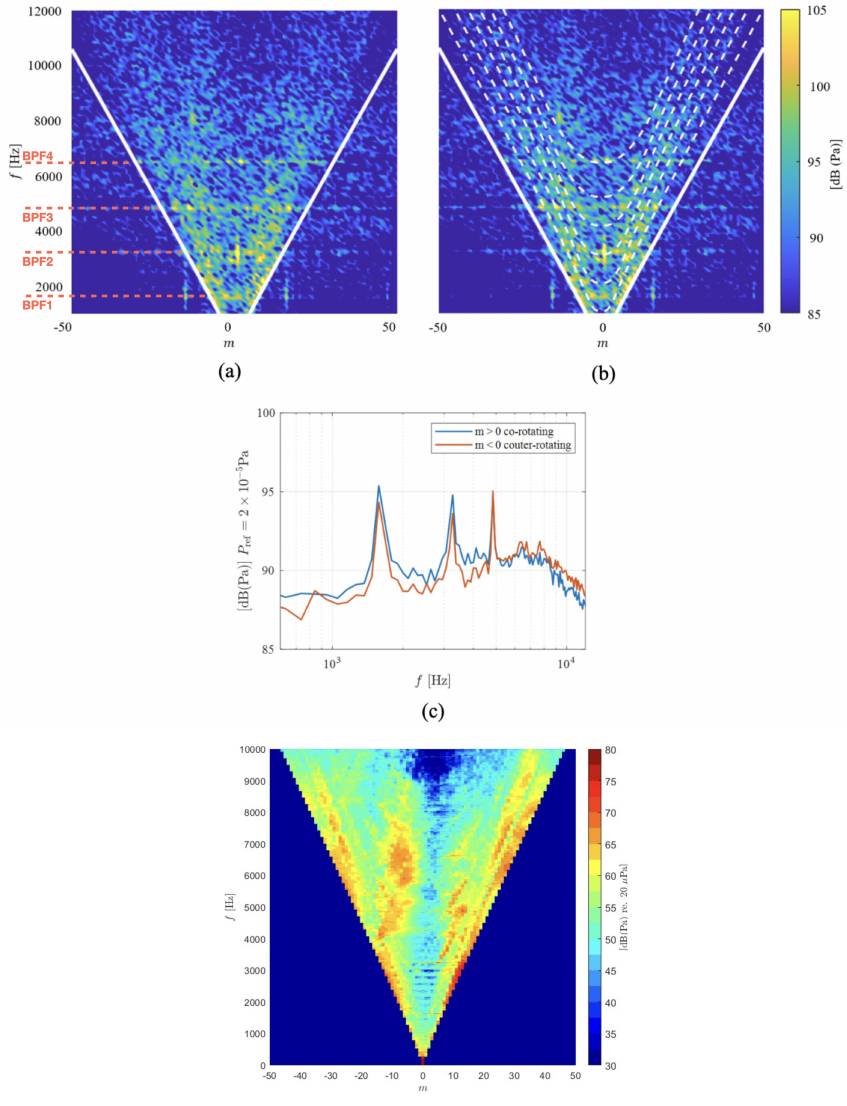


Figure 5.32: Azimuthal mode detection plots at the exhaust section. (a,b) 360° **LES:** The frequency is plotted against the azimuthal mode order m, and the modes are colored by their amplitude. (c) Integrated mode spectra over co-rotating (m > 0) and counter-rotating (m < 0) modes, (d) **Experiment:** The frequency is plotted against the azimuthal mode order m (from [11])

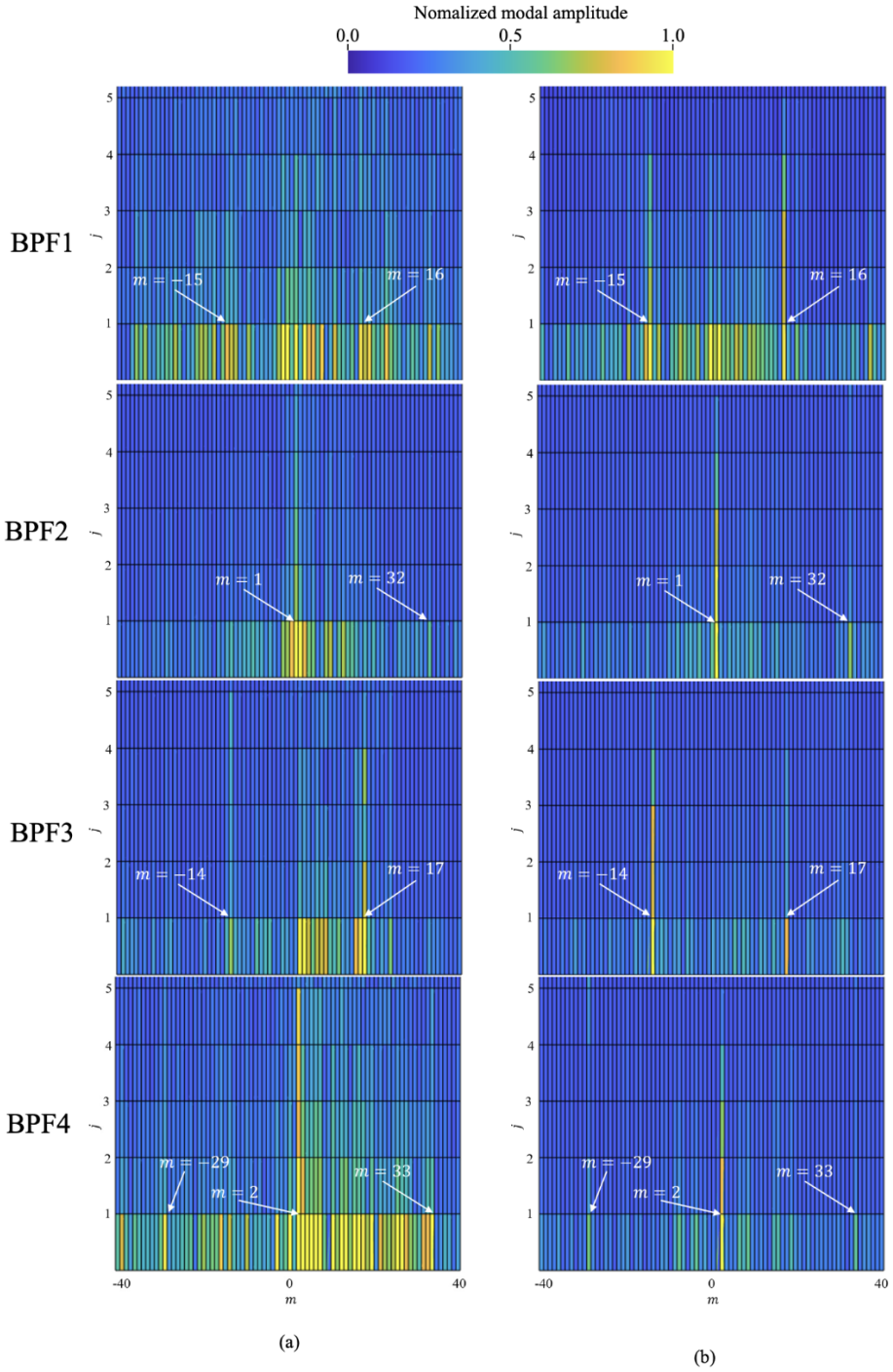


Figure 5.33: Modal content obtained by an azimuthal and a radial decomposition at (a) inlet and (b) exhaust sections for the first four BPF. (from [11])

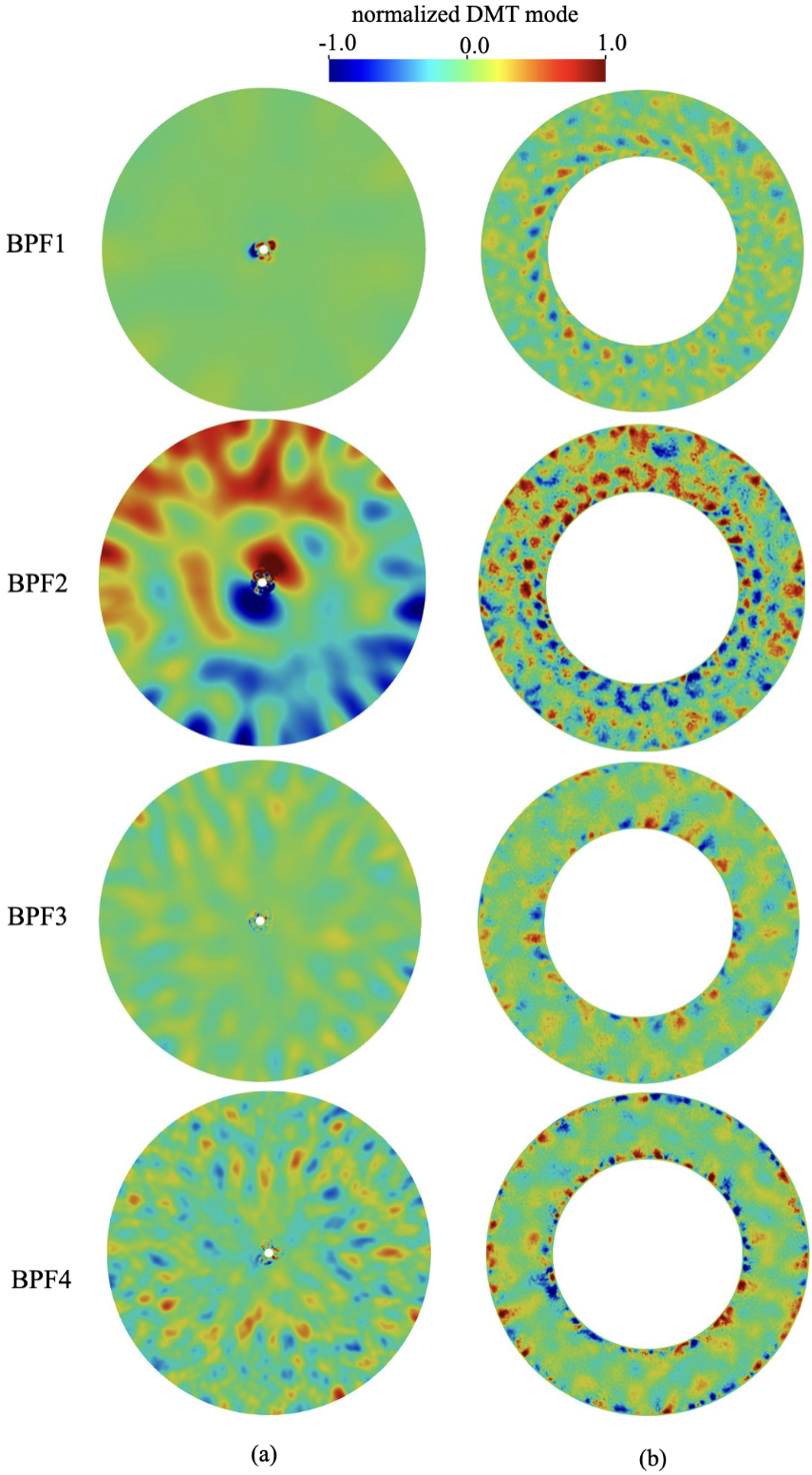


Figure 5.34: Spatial distribution of the density modes using the DMT technique at the first four BPF. (a) intake section. (b) exhaust section. (from [11])

## 5.8 Conclusion and future directions

### 5.8.1 Conclusion

The presence of a separation bubble significantly influences the characteristics of pressure fluctuations in turbomachinery. Our work demonstrates that variations in mass flow rate and fan blade attack angle affect the acoustic emission pattern and lead to changes in the turbulent boundary layer and wake characteristics downstream. Furthermore, the study reveals that the separation bubble generates high-frequency peaks (HFP) in the pressure spectrum, with their frequency increasing with the mass flow rate. These HFPs are attributed to the presence of large spanwise vortical structures near the separation bubble, which act as a source of periodic vortex release, contributing to tonal noise in the system. This finding is considered significant for further research in modeling this acoustic source, especially at low mass flow rates, as it provides insights into the mechanisms underlying acoustic emissions in turbomachinery.

The organization of the flow in the tip region of the ECL5 rotor is complex, characterized by multiple vortical structures including a horseshoe vortex (HSV), first and second tip-leakage vortices (TLV1 and TLV2), a tip separation vortex (TSV), and an induced vortex (IV). The HSV impacts the next blade at a location similar to where TLV1 originates, suggesting a relationship between these vortices. Two main mechanisms explain the evolution of the Wall Pressure Spectra (WPS). The first mechanism, occurring between 30% and 70% of the chord, affects WPS at high frequencies ($> 10^4$ Hz), while the second mechanism, closer to the trailing edge, influences WPS at lower frequencies ($< 10^4$ Hz). This is supported by coherence analysis showing correlations between pressure fluctuations in the tip-gap flow. Regardless of direction, the blade is the primary noise source at low frequencies ($< 2 \times 10^3$ Hz). At higher frequencies, both the blade and tip-gap region contribute equally, with the tip-gap region becoming the main acoustic source region in the upstream direction beyond $10^4$ Hz. These findings highlight the complex interactions between flow structures and acoustic emissions in the tip-gap region of the rotor, with implications for understanding and mitigating noise in turbomachinery systems.

Acoustic results obtained through direct propagation of sound waves in Large Eddy Simulations (LES) for two instances of the ECL5 Fan/OGV case are compared. The LES performed on the full ECL5 geometry provides a more comprehensive understanding of acoustic emissions compared to periodic LES. The LES accurately reproduces radial profiles of total pressure, relative flow angle, and total temperature, particularly at the tip of the rotor. The LES reveals vortical structures in the flow, especially along walls and in wakes. Strong signatures in turbulent regions of the tip gap and significant acoustic waves upstream of the rotor are observed. Comparison between LES and experimental results shows good agreement in the distribution of azimuthal modal content at both inlet and outlet. Upstream, co-rotating modes have stronger levels, consistent with emission directivity theories. The overall distribution of modal content is well captured by LES, with positive azimuthal modes having larger amplitudes. Downstream, no difference is found between co-rotating and counter-rotating modes, indicating symmetry in the diagram. The qualitative agreement between LES and experiment is good, with significant modes symmetrically distributed. These findings provide valuable insights into the acoustic emissions and modal content of the ECL5 Fan/OGV configuration, laying the groundwork for further comparisons with experimental data and enhancing understanding of acoustic propagation in turbomachinery systems.

### 5.8.2 Future directions

Overall, it is now understood that the LES analysis methodology is mature enough to address in detail complex flows involving broadband acoustic sources in turbomachinery in realistic conditions. The next steps involve applying this research methodology to:

- **Understand the physical mechanisms behind broadband acoustic sources when the fan operates at its nominal speed:**
  In this case, the relative flow at the leading edge becomes supersonic, leading to the formation of a supersonic pocket at the blade's leading edge. The associated shock prevents acoustic waves from freely propagating upstream. As illustrated in Figure 5.35, the directivity and local intensity of the broadband noise resulting from the rotor-stator interaction are significantly altered. This preliminary result, obtained from a calculation on a single radial slice of the complete stage, seems to indicate the potential value of a specific case study. This research is currently being conducted by Allan Beurville as part of his thesis, which began in November 2022.

- **Understand the physical mechanisms behind broadband acoustic sources in the case of unducted fans:**
  To achieve a significant increase in dilution rates, manufacturers, particularly SAFRAN, are leaning toward unducted propulsion architectures. An example is the RISE configuration currently under study at SAFRAN [139]. This research has just begun at LMFA (in December 2023) as part of Pierre-Louis Pape's doctoral thesis (directed by Marc Jacob (LMFA) and co-supervized with Jérôme Boudet) which is part of the European project PANDORA aimed at improving the design and modeling of unducted fan architectures.

- **Develop new low-order models for the broadband noise** emitted by (i) the recirculating bubble that forms at partial load, (ii) the tip-gap complex vortical structures, (iii) the shock wave that develops at nominal speed above the suction side of the rotor blade. This work will be part of both Allan Beurville and Pierre-Louis Pape PhD thesis.
  This research which will be pursued in collaboration with the acoustic group will lead to the development of a tool capable of describing noise emissions from fans (including BBN) with very small turnover times. This brick is essential for the optimization of fan/OGV stage architectures in future engine configurations.

- **Assess new noise mitigation techniques** such as the one described in a patent application recently filed by the author.

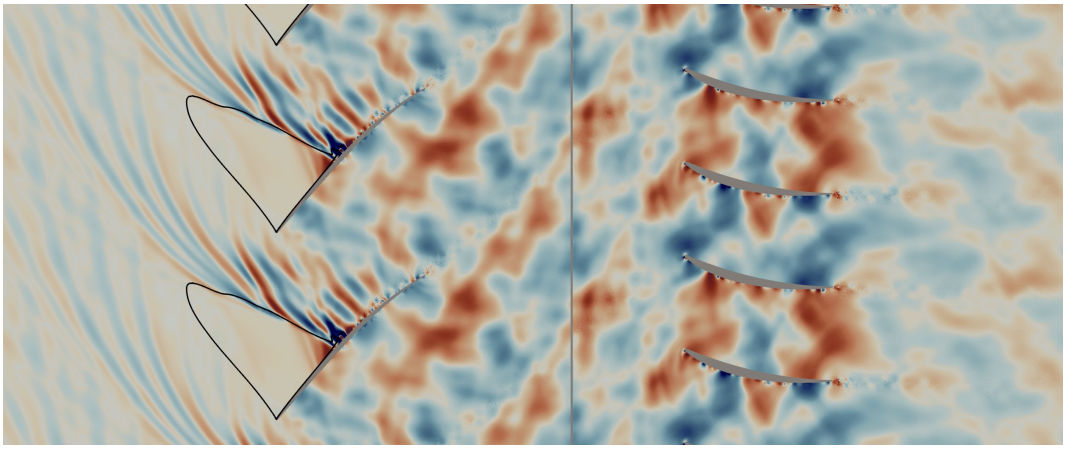

Figure 5.35: Blade-to-blade view of the pressure fluctuation. Black lines mark the locations of $M_r = 1$ (Source: Allan Beurville [15])

## 5.9 Summary of contributions and collaborations

We conclude this chapter by summarizing the key communications regarding broadband noise and the collaborations at their origins.

| Topic | articles | people | status | place |
|---|---|---|---|---|
| Broadband noise analysis in turbomachines using Large Eddy Simulation | [140, 141] | Jean Al Am | PhD student | LMFA |
| | [142, 12] | Allan Beurville | PhD student | LMFA |
| | [143, 144] | Jérôme Boudet | Collaborator | LMFA |
| | [13, 145] | Vincent Clair | Collaborator | LMFA |
| | [11, 15] | Fernando Gea-Aguilera | Collaborator | SAFRAN |

Table 5.1: key research elements and their context

# Chapter 6

# Turbulence Modeling in Dense Gas Flows using DNS, LES and Machine Learning

## Contents

## 6.1 Context & Motivations

Humanity faces today the most dramatic events the species has ever encountered. Climate change and scarcity of conventional energy resources in a context of growing population are two major challenges that need to be addressed with determined actions involving both industry and research. Because humans have started to significantly change the environment in which they live in at the Earth scale, geophysicists are actively debating the fact that the planet has now entered into a new geological epoch called Anthropocene [146]. This very short period of time will be visible to future scientists as a bedrock layer containing radioactive nuclei, rare earth elements, burnt gases residue and fertilizer chemicals in large concentrations. As stated by the philosopher of science Etienne Klein, energy exchanges directly measure our ability to transform things around us. As the size of the population grows, humanity requires more energy to fulfill its needs. In 2021, the International Energy Agency has estimated that approximately 14.7 (13 in 2013) Billion Tons-Oil-Equivalent have been used which represent a consumed power of 2.5kW (2.3kW in 2013) per earth inhabitant at each instant. At the same time and for decades, our modern civilizations have been organized around coal, liquid oil or gaseous fuel, a list to which nuclear energy should be added for the specific case of France. Today, only 5.2% (3.5% in 2013) of the entire energy consumption in the world comes from renewable sources (hydro, solar, wind, geothermy,...). This model is not sustainable and will eventually change for two reasons.

The first reason comes from the energy resources themselves. Oil production is hitting its maximum in volume around 94 Million barrels per day (86 Million in 2013) even when taking into account the new unconventional type of oil obtained from sands in Alaska or other regions of the world[1]. Gaseous fuel production is expected to reach its maximum around 2030 (today 4 Tera $m^3$ per year) and coal will encounter a production peak sometimes later during this century (today 8 Billion Tons per year). Even uranium is only available in limited quantities and will not support our economic model indefinitely. This reason alone represents a strong incentive for the development of technologies designed to (a) reduce energy consumption and (b) harvest to a much more significant scale renewable energies. Policy makers, companies and researchers are now actively pursuing this goal and this project should be considered as taking part of this effort at its own measure.

Yet, although already a great challenge, scarcity of resources might not be the main problem as far as humanity is concerned. The main issue is our climate, changing so fast that resilience and adaptability of humans will be stretched to their limits. Measurements of $CO_2$ concentrations in the atmosphere all around the world (see for example the oldest recordings in Hawaii[2]) all show the same trend. Concentrations have already reached levels (above 420ppm) that have never been seen since the Pliocene epoch, 3 million years ago[3]. Using simple thermodynamic models it is shown that this high level of CO2 explains a large part of the already observed increase in temperature on Earth today, estimated at $1.2°C$ above the average temperature observed during the first half of the 20th century. Conferences Of Parties (COPs) on the topic have confirmed thanks to the analysis of the researchers of GIEC that political decisions should be taken now if we want to limit the rise in temperature to a mere $2°C$.

Part of the technical solution to both challenges is known for 50 years and is called by the thermodynamic cycle it uses, namely the Organic Rankine Cycle. It is different from the classical Rankine cycle which uses water because the working fluid is in this case an organic fluid. This working fluid has specific properties among which a preferably low boil-

[1] http://www.iea.org
[2] https://gml.noaa.gov/ccgg/trends
[3] https://www.rmets.org/event/pliocene-last-time-earth-had-400-ppm-atmospheric-co2

ing temperature, a large gas density and a large specific heat. All those properties which as we will see in the following are present in dense gases, make them especially useful for both solar concentration and fatal (lost) heat recovery applications using ORCs. The first ORCs have been built during the early 1960's by Tabor and Bronicki and commercially developed in Israel and Italy in the 1980's. Unfortunately, because of the low price of oil, it has remained somewhat confidential at the industrial scale until the late 1990's. Today, the general evolution of energy prices help a French industrial sector to flourish around small companies such as Enogia or Enertime. In order for them to propose the most innovative and cost effective systems, challenges are still numerous and the research topic presented in this chapter aims at facing some of them. When Organic Rankine Cycle (ORCs) are used to recover lost heat, the temperatures of both the hot and cold sources are known and cannot be modified so that the efficiency is often bounded by relatively low Carnot efficiencies ($\eta = 1 - \frac{T_{cold}}{T_{hot}}$). In this case, the most important challenge is the increase of the overall efficiency in order to approach as close as possible this Carnot limit. This overall efficiency is logically the collective result of all sub-elements composing the ORC. Among them is the necessary expanding system (often a turbine for powers above 10kW). To obtain efficient turbomachinery systems, numerous prototypes are designed on the basis of computer simulations before being tested.

The working fluids in ORCs are often of a high molecular complexity (HMC). These fluids are particularly suitable because of their large heat capacity and low boiling temperature. They also often exhibit strong non-ideal behaviors when their thermodynamic state is close to the critical point [147]. In this region of the $p-v$ diagram, the fundamental derivative of gas dynamics becomes lower than unity ($\Gamma < 1$)[148]. The term "fundamental" emphasizes the importance of $\Gamma$ in the determination of the non-linear behaviour of dense gases. The fundamental derivative of gas dynamics was introduced by Hayes (1958) [149], and then rewritten by Thompson (1971) [148] as:

$$\Gamma = \frac{v^3}{2c^2}\frac{\partial^2 p}{\partial v^2}\bigg|_s = \frac{c^4}{2v^3}\frac{\partial^2 v}{\partial p^2}\bigg|_s = 1 + \frac{\rho}{c}\frac{\partial c}{\partial \rho}\bigg|_s \tag{6.1}$$

where $v$ is the specific volume, $\rho$ the density, $c = \sqrt{\partial p/\partial \rho|_s}$ the speed of sound, $p$ the pressure and $s$ the entropy. This physical quantity is a measure of the speed of sound rate of change in an isentropic transformation. It is directly related to the curvature of isentropic curves in the $p-v$ diagram $\left(\partial^2 p/\partial v^2\big|_s\right)$.
There are three main regimes depending on the value of the fundamental derivative:

- $\Gamma > 1$ corresponds to the classical ideal gas behaviour. For thermally and calorically perfect gases, the fundamental derivative is constant and given by: $\Gamma = (\gamma + 1)/2$.

- $0 < \Gamma < 1$ corresponds to the classical non-ideal gas behaviour. In this regime, the speed of sound decreases in isentropic compressions $\left(\partial c/\partial \rho\big|_s < 0\right)$.

- $\Gamma < 0$ corresponds to the non-classical behaviour referred to as Bethe-Zel'dovich-Thompson (BZT) effect. The name BZT was given by Cramer [150] to acknowledge the pioneering works of Bethe [151], Zel'dovich [152] and Thompson [148] on these gases which are also widely used in industry. Examples of BZT gases include hydrocarbons, per-fluorocarbons and siloxanes. It is a narrow region in the $p-v$ diagram. In that zone, because of the negative sign of the fundamental derivative, rarefaction shock-waves can occur.

The study by Dura Galiana et al. [153] indicates that in an ORC turbine stage using a dense gas, the losses due to viscous effects are a significant contributor to the total losses.

Since turbulence models determine the accurate prediction of friction losses at the walls and in the blades' wakes, it is essential to assess their relevance in the framework of dense gas flows and to revisit them if necessary. This chapter therefore describes the research initiative launched together with Christophe Corre in 2015 to address this question.

We proposed to investigate turbulence in the field of dense gas flows through the introduction of Large Eddy Simulation (LES) and improvement of Reynolds Averaged Navier-Stokes (RANS) CFD techniques. To accomplish this general goal, scientific and technical barriers had to be overcome. They mostly come from the fact that a decade ago, CFD computations of industrial applications had to consider at best only marginally compressible turbulence. This can be easily understood taking into account perfect gas thermodynamic relations. Indeed, if one considers that the representative turbulent velocity in a realistic air flow is at most 10% of the bulk velocity, one needs a bulk velocity larger than ten times the speed of sound to have a unity Turbulent Mach number. This kind of flow is only seen in atmospheric reentry applications or the study of supernova explosion flows [154]. Yet, dense gas flows as seen in ORC have much smaller sound speeds for the practical thermodynamic conditions we focus on. For example, in FC-70 flows (a specific type of dense gas), the sound speed can drop down to 15 m/s close to the critical thermodynamic conditions and a unity turbulent Mach number can be reached by flows having realistic bulk velocities around 150m/s.

In highly compressible turbulence, additional phenomena appear when compared to the incompressible case. The first phenomenon is the coupling of the solenoidal and dilatational components of the velocity above a turbulent Mach number of 0.3. The viscous dissipation is thereby modified down to the sub-grid scale for LES. Many authors have explored the implications and proposed new subgrid-scale models since the late 1980's [155, 156]. Yet, above turbulent Mach numbers of 0.5 shocklets are formed that also modify the local balance of energy. These very thin discontinuous structures arise from the relaxation of the kinetic energy contained in supersonic eddies. Although very difficult to observe experimentally, they have been analyzed numerically in isotropic turbulent configurations for thirty years [157]. Those structures strongly influence turbulent kinetic energy at very small scales and are expected to modify the losses in supersonic turbomachinery flows. Yet, even if some propositions have been made to directly take shocklets into account at the sub-grid level for LES [158], they are not explicitly present in most available turbulent models. Because of this, one of the main motivations behind this research topic at the time was that available RANS and LES turbulence closure models might not be accurate enough to handle properly highly compressible turbulent dense gas flows. It was therefore proposed to revisit the entire methodology developed for the modeling of incompressible turbulence and apply it to the development and validation of new turbulence closure models directly applicable to turbulent dense gas flows used in ORC expansion systems.

## 6.2 Brief Introduction to dense gas flows, their properties and open questions

To better understand the type of fluids we are interested in, this section, strongly inspired by the introduction of the recent review article published by Guardone et al. [147], presents the main characteristics of dense gases.

In contrast to the behavior observed in incompressible fluid flows, the evolution of compressible flows is notably influenced by the thermodynamic state of the fluid. For instance, the speed of sound, which dictates the propagation velocity of small-amplitude pressure disturbances within the flow, is a thermodynamic property defined as $c^2 = (\partial P/\partial \rho)_s$, where $P$ represents pressure, $\rho$ denotes density, and $s$ signifies entropy per unit mass. In the realm

of gas dynamics studies, the thermodynamic properties of the fluid are typically computed utilizing the polytropic ideal gas model. The expression for the ideal gas sound speed, while straightforward, underscores the influence of fluid properties on the speed of sound. The gas constant $r$ is inversely proportional to the molar mass of the substance, resulting in a lower speed of sound for compounds composed of heavier molecules. The specific heat $c_v$ in the dilute gas limit is correlated with the number $N$ of active degrees of freedom of a molecule, as per the energy equipartition principle. For a polytropic ideal gas, $\gamma = c_p/c_v = (1 + 2N)$, where $c_v$ and $c_p$ represent the isochoric and isobaric specific heats, respectively. Consequently, $c^2 = \gamma rT = (1 + 2N)rT$. The number of active degrees of freedom of a molecule $N$ is a proxy for molecular complexity, with increasing $N$ values indicating more complex molecular arrangements, as discussed by Colonna & Guardone (2006) [159]. The ideal gas or dilute gas region encompasses states with $Z = 1$ at low pressure. Here, $Z$, the compressibility factor, equals $P/(\rho rT)$ and is unity for a fluid in the ideal gas state. States are classified as supercritical if both pressure and temperature exceed the vapor-liquid critical values $P > P_c$ and $T > T_c$, or subcritical for lower pressure or temperature values.

The dense vapor region comprises vapor states at subcritical pressure featuring $Z < 1$. Departure from the ideal gas sound speed increases with the molecular complexity of the fluid, often leading to the misconception that nonideal compressible fluid dynamic (NICFD) phenomena solely affect the flows of molecularly complex fluids. However, non-ideal gas dynamic phenomena influence the flows of all fluids if their thermodynamic states fall within the nonideal thermodynamic region, even those composed of the simplest molecules. Nevertheless, nonideal effects are more pronounced for molecularly complex fluids, such as heavy hydrocarbons or fluorinated compounds used in organic Rankine cycle (ORC) engines or refrigeration systems. The higher the molecular complexity of the fluid, the stronger the nonideal gas dynamic effects in the flow, potentially resulting in qualitatively different flow phenomena, such as nonclassical rarefaction shock waves. Another instance of a nonideal effect is the non-monotonic variation of the Mach number in steady isentropic expansions, as opposed to the well-known monotonic increase occurring for ideal gas flows through converging-diverging nozzles, like those of rocket engines.

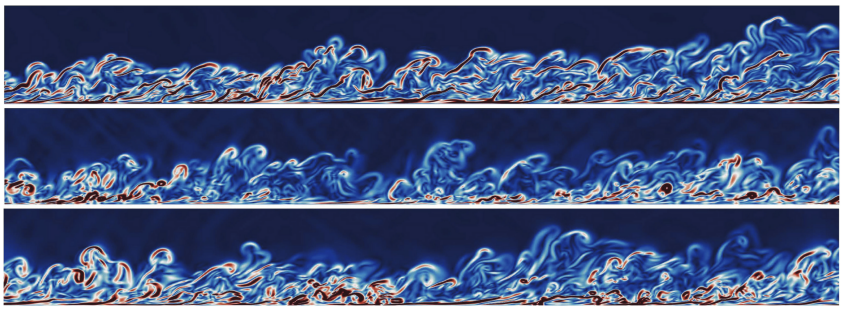

Figure 6.1: Velocity fluctuations within the zero-pressure gradient turbulent boundary layer over a flat plate for air (top) and siloxane hexamethyldisiloxane in ideal (middle) and nonideal (bottom) thermodynamic conditions. The calculations were performed with a direct numerical simulation solver (Tosto 2023). (from [16])

The kinematics and dynamics of turbulence in compressible flows are significantly influenced by variations in fluid thermophysical properties such as dynamic viscosity, density, and the speed of sound [160]. As a result, turbulence characteristics are contingent upon the specific fluid class and thermodynamic state [16] (See Figure 6.1). For instance, the dissipation of turbulent kinetic energy (TKE) at the smallest scales generates thermal energy input, which has a more pronounced impact on thermophysical properties in low molecu-

lar complexity (LMC) fluids compared to high molecular complexity (HMC) compounds. Consequently, the most notable disparities in turbulence arise between dilute gas and dense-vapor flows when the fluid consists of simple molecules. When examining turbulence within the realm of nonideal compressible fluid dynamics (NICFD), it is crucial to differentiate between effects stemming from fluid molecular complexity and those arising from the nonideal thermodynamic state. Sciacovelli et al. (2017) [35] and Duan et al. (2021) [161] investigated the effects of dense vapor on the largest and smallest structures of homogeneous isotropic turbulence for an HMC fluid using direct numerical simulation (DNS). They observed that turbulence dynamics are primarily influenced by effects related to molecular complexity, while local variations of the speed of sound significantly impact small-scale dynamics.

## 6.3 Initial results analyzing decaying Homogeneous Isotropic Turbulence (HIT)

When we started this research program in 2016, little was known about turbulence in dense gas flows and the logical first step was to consider the academic case of the decaying homogeneous isotropic turbulence using DNS.
In this study, the first meshes we used did not consider that many elements (we went up to $400^3$ elements corresponding to a turbulent Reynolds number based on the Taylor scale equal to 75) but this eventually enabled us to gain some understanding of the problem. These first DNS of decaying homogeneous isotropic turbulence are detailed in Giauque et al. [17]. We compared the evolution of compressible turbulence (turbulent Mach number of 0.8) for a perfect gas and for a dense gas, namely FC-70. It soon appeared that the local structure of vortices is deeply influenced by the nature of the fluid. Figure 6.2 presents a 2D cut of the entire 3D domain after one non-dimensional time. Compression shocklets, corresponding to localized regions of very large negative values of the velocity divergence are found in the perfect gas. Yet, in the dense gas, if those structures are also present they live together with regions of space having very large positive values of the velocity divergence. Even though by itself this result is not enough to prove their existence, these structures seemed to be expansion shocklets that required more investigation.

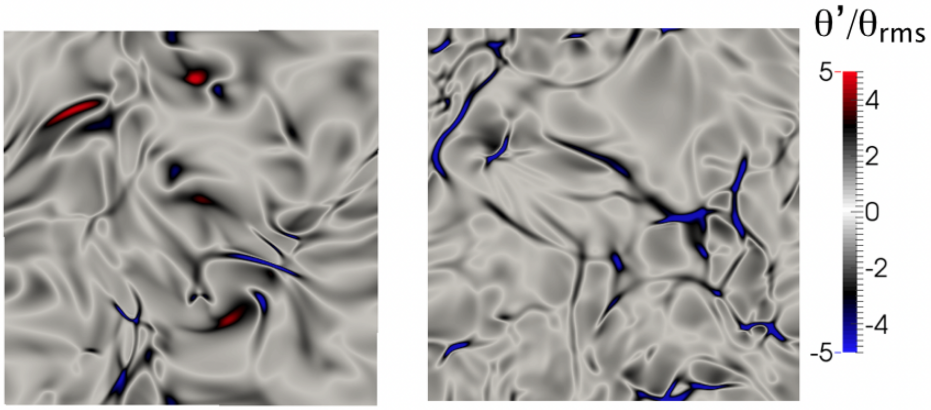


Figure 6.2: Sectional cut of the flow colored by the local divergence divided by its spatial r-m-s value at time $\tau = 1$. Left: Dense gas, Right: Perfect gas. (from [17])

To be sure to observe specific dense gas effects, the simulations with FC-70 were initialized with constant pressure and density in the thermodynamic inversion region as illustrated

in Figure 6.3. One can see that at $t/\tau = 3$, the thermodynamic states have spread along an adiabatic curve way beyond the inversion region. Yet, as time evolves the distribution of thermodynamic states reverts back to its original location and a large number of cells in the DNS again lie in the inversion region. Because of this wealth of physical states, the temporal evolution of the Turbulent Kinetic Energy (TKE) is interesting to further analyze.

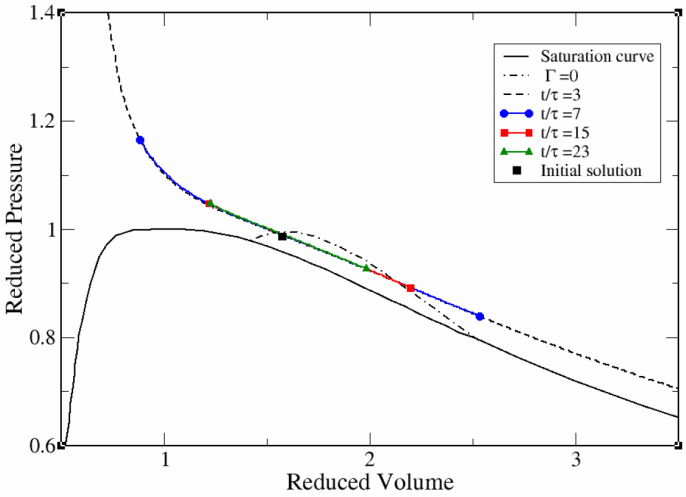


Figure 6.3: Distribution of the thermodynamic states in the $Pr - Vr$ diagram in the Dense gas case at different instants in time. (from [17])

Figure 6.4 presents the temporal evolution of the TKE in the two fluids. One observes that the rate of decay of the TKE is different between the dense gas and the perfect gas. In the latter, TKE decays at a slightly faster rate. Also very insightful is the analysis of the capability of LES to capture this decay in both cases. We show (not presented here) that when the turbulent Mach number is low enough, thermodynamics does not significantly influence turbulence. In these cases, the standard dynamic Smagorinsky subgrid-scale model is good enough to study turbulent dense gas flows using LES. For this condition to be verified though, the turbulent velocity needs to be small enough compared to the speed of sound. This is where the thermodynamic inversion region plays a key role. Indeed, when the average thermodynamic state lies within this inversion region, the speed of sound is drastically decreased and the same turbulent speed (here 20 m/s) leads to a highly compressible evolution of the turbulence. As it can be seen in Figure 6.4 for the dense gas case, both LES simulations cannot capture the right evolution of the kinetic energy. One can first note that no oscillations of the kinetic energy are visible for the realistic resolution of $16^3$. This is coherent with the fact that these fluctuations relate to length scales smaller than 5 Kolmogorov length scales as suspected from the time evolution of the spectra (not shown).

More importantly, even for the $32^3$ resolution, LES fails to capture the right slope of the curve of the kinetic energy in the dense gas case. For the perfect gas case, one can see that kinetic energy oscillations also disappear for the resolution comprising $16^3$ elements. Yet, in the perfect gas, LES results are much closer to DNS once the initial highly compressible phase of the simulation is over. After this transitional phase, perfect gas LES seems to correctly predict the slope of the curve of the kinetic energy in contrast with what is observed for the dense gas case. One can mention that in the perfect gas, the oscillations of the TKE have already been observed by Kida & Orszag [157] and are related to a periodic exchange between the internal and kinetic energies through the pressure gradient term.

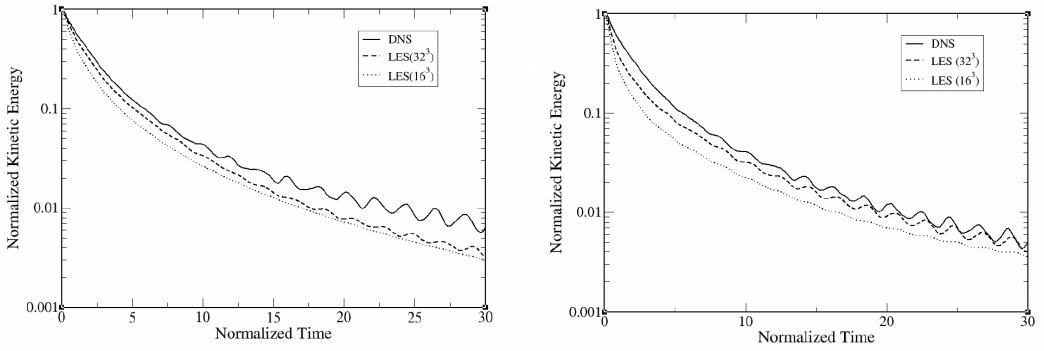


Figure 6.4: Evolution of the normalized kinetic energy with time with comparison between LES and DNS in the Dense Gas case (left) and Perfect Gas case (right). (from [17])

## 6.4 DNS of forced compressible homogeneous isotropic turbulence and mixing layer – *Building a database for the modellng of turbulence in dense gas flows*

Results obtained from the DNS of Decaying Homogeneous Isotropic Turbulence led us to think that turbulence might indeed be strongly influenced by the nature of the fluid at hand. We therefore launched a series of DNS systematically comparing the behavior of BZT-dense gas (High Molecular Complexity fluid in the thermodynamic inversion region) against that of perfect gas. Two academic flows were particularly explored. The first one is the forced Homogeneous Isotropic Turbulence and the second one is the mixing layer. Right from the start, our motivation was two-fold. On the one hand, we aimed at better understanding the peculiar behavior of turbulence in dense gas flows and in the other hand we planned to gather enough high-fidelity results to stem the development of new turbulence models dedicated to this type of flows.

### 6.4.1 Forced compressible Homogeneous Isotropic Turbulence (HIT) in a dense gas

DNS of a compressible HIT with initial turbulent Mach number $M_t = 0.8$ are performed for a perfect gas and for a (BZT) dense gas. The dense gas used in this study is perfluorotripentylamine (FC-70, $C_{15}F_{33}N$)). It is the same dense gas used by Fergason et al. [162] in order to simulate rarefaction shock-waves in a shock tube. It is in particular used as heat transfer fluid, is almost not toxic and has been evaluated as synthetic blood [163]. Physical parameters useful for the thermodynamic description of FC-70 are given in table 6.1, as extracted from Cramer et al. [26].

Setting the initial conditions of the forced HIT requires the choice of the initial operating thermodynamic point in the $p - v$ diagram. This initial thermodynamic state is defined by the reduced pressure $p_r^{init} = p^{init}/p_c = 0.9866$ and the reduced specific volume $v_r^{init} = v^{init}/v_c = 1.5733$. This initial state is selected inside the inversion zone of FC-70 ($\Gamma < 0$), in order to favor the occurrence of expansion shocklets and to maximize dense gas effects on turbulence. It is also in that region of inversion that compressibility effects are the largest since the sound speed is reduced [164], which maximizes the turbulent Mach number.

The main non-dimensional characteristic numbers of the compressible HIT are the Taylor

Table 6.1: Physical parameters of FC-70 [26]. The critical pressure $p_c$, the critical temperature $T_c$, the boiling temperature $T_b$ and the compressibility factor $Z_c = p_c v_c/(RT_c)$ are the input data for the Martin-Hou equation of State. The critical specific volume $v_c$ is deduced from the aforementioned parameters. The exponent $n$ and the $c_v(T_c)/R$ ratio are used to compute the heat capacity $c_v(T)$ (with $R = \mathcal{R}/M$, the specific gas constant computed from the universal gas constant $\mathcal{R}$ and the molar mass $M$).

| | $M$ (kg/mol) | $T_c$ (K) | $p_c$ (atm) | $Z_c$ | $T_b$ (K) | $m$ $(= c_v(T_c)/R)$ | $n$ |
|---|---|---|---|---|---|---|---|
| FC-70 | 0.821 | 608.2 | 10.2 | 0.270 | 488.2 | 118.7 | 0.493 |

Reynolds number $Re_\lambda$ based on the Taylor scale $\lambda$:

$$Re_\lambda = \frac{\lambda\sqrt{<u_i' u_i'/3>}}{<\nu>} \quad \text{with} \quad \lambda = \sqrt{2\frac{<u_i' u_i'/3>}{<\left(\frac{\partial u_1'}{\partial x_1}\right)^2>}} \tag{6.2}$$

and the turbulent Mach number:

$$M_t = \frac{\sqrt{< u_i' u_i' >}}{< c >} \tag{6.3}$$

where Einstein implicit summation is used. Operator $< \cdot >$ represents the space averaging operator, $u_i'$ denotes the fluctuating velocity in direction $x_i$, $\nu$ is the kinematic viscosity and $c$ the speed of sound.
The flow domain is a cube with edge length $L$ (the value of $L$ depends on the EoS). Periodic boundary conditions are applied in the three space directions $x_1$, $x_2$, $x_3$ (or equivalently $x$, $y$, $z$). The initial Taylor Reynolds number is set equal to 100 for all simulations, which are initialized using an incompressible homogeneous isotropic turbulent velocity field following the Passot-Pouquet spectrum:

$$E(k) = (k/k_e)^4 exp(-2(k/k_e)^2) \tag{6.4}$$

with $k_e$ the wavenumber of maximum initial kinetic energy set to $k_e = L/4$.
Given the low speed of sound obtained using the Martin & Hou (MH) EoS [27] for the chosen initial thermodynamic point, a 20 m/s turbulent velocity translates into a turbulent Mach number equal to 0.8. For the computations using the Perfect Gas (PG) EoS, a 63 m/s turbulent velocity has to be imposed in order to reach the same turbulent Mach number. Five computations are performed in this study, as summarized in Table 6.2. The $540^3$, $675^3$ and $800^3$ resolutions correspond respectively to discretizations of the Kolmogorov length scale with 2, 2.5 and 3 points respectively.

Table 6.2: Key features of the numerical test cases. The characteristic turnover time $\tau$ is defined as the ratio of the integral length scale $\ell$ and the turbulent velocity $\sqrt{< u_i' u_i' >}$ at $t = 0$.

| Case name | EoS | Mesh size (nb of cells) | Turbulent velocity (m/s) | Viscosity and Conductivity | Domain size L (m) | Kolmogorov length (m) at $\tau = 15$ |
|---|---|---|---|---|---|---|
| MH1 | MH | $540^3$ | 20 | Chung | 4.58727e-06 | 1.84e-8 |
| MH2 | MH | $675^3$ | 20 | Chung. | 4.58727e-06 | 1.72e-8 |
| MH3 | MH | $800^3$ | 20 | Chung | 4.58727e-06 | 1.7e-8 |
| PG1 | PG | $540^3$ | 63 | Suth. | 4e-6 | 2.2e-8 |
| PG2 | PG | $675^3$ | 63 | Suth. | 4e-6 | 2.15e-8 |

#### 6.4.1.1 Forcing methodology

Forcing turbulence in order to reach statistical stationarity is an entire research topic *per se* and it is not the objective of this section to give a full review on the subject. Because

the numerical tool used in this work is a temporal solver, the linear forcing model proposed by Lundgren [165] and studied by Rosales and Meneveau [166] is used. The linear forcing scheme for incompressible turbulence has been since analyzed in the compressible context by Petersen and Livescu [167] and is similar to the natural Reynolds shear stress production mechanism in the turbulent kinetic energy equation.
One of its major advantages is its straightforward implementation in physical-space numerical solvers using only the knowledge of the instantaneous momentum in the turbulent flow. Yet, in its original formulation, such as proposed by Lundgren [165] :

$$\vec{F} = \underbrace{\frac{- < \vec{u}.[\vec{\nabla}.(\mu\bar{\bar{S}})] > + < \vec{u}.\vec{\nabla}p >}{< \rho\vec{u}.\vec{u} >}}_{B} \rho\vec{u} \tag{6.5}$$

with $< \cdot >$ representing the space averaging operator, and $\bar{\bar{S}}$ the strain rate tensor, all wavelengths are equally affected by the forcing, which might significantly impact the way turbulent kinetic energy is transferred from one scale to another. To prevent such undesirable phenomenon, only large wavelengths are forced in the present study. This is achieved by first interpolating the momentum field onto a coarse mesh ($8 \times 8 \times 8$ cells), before using it in the linear forcing model :

$$\vec{F_8} = B(\rho\vec{u})_8 * \left(1 - \frac{< \rho\vec{u}.\vec{u} > - < \rho\vec{u}.\vec{u} >_{init}}{< \rho\vec{u}.\vec{u} >_{init}}\right) \tag{6.6}$$

where $(\cdot)_8$ represents the interpolation of the variable $(\cdot)$ onto the $8 \times 8 \times 8$ cells coarse mesh, and $< \cdot >_{init}$ the space averaging operator applied at the initial time. Because of the Nyquist-Shannon theorem, only wavelengths larger than a fourth of the entire computational domain are impacted in this way by a non-negligible source term. Contrary to the original model (6.5), the modified implementation (6.6) for $\vec{F}$ does not ensure the conservation of the TKE. This is achieved by modulating the amplitude of the forcing term so that the overall turbulent kinetic energy remains constant using a simple relaxation technique. To remove the additional energy introduced by the forcing and enable the flow to reach a statistically stable state, a sink term $F_e = - < \vec{F_8}.\vec{u} >$, variable in time but constant in space, is added to the total energy equation.

#### 6.4.1.2 Physical analysis

**Dense Gas (DG) cases: PDF of thermodynamic states**
In the DG cases, during the period of statistical stationarity of the flow between $t = 12\tau$ and $t = 22\tau$, the probability density function (PDF) of thermodynamic states remains nearly constant. In Figure 6.5, the joint PDF of the reduced pressure ($p_r = p/p_c$) and reduced specific volume ($v_r = v/v_c$) in the case MH2 at $t = 15\tau$ is illustrated. Due to (a) the constant removal of energy introduced by the forcing and (b) the constant space-averaged Turbulent Kinetic Energy (TKE) over time, the thermodynamic states closely follow the adiabatic curve passing through the initial state. Additionally, the isothermal curve passing through the initial state is included in Figure 6.5 to demonstrate that the difference between this curve and the adiabatic one becomes significant only when the fluid is in a supercritical state. From the analysis of the distribution itself, it is observed that approximately 30% of the flow volume remains in a thermodynamic state located inside the inversion zone. Simultaneously, 37% of the flow volume is in a supercritical state.

**Comparison of TKE spectra**
When studying largely compressible turbulence, Kritsuk et al. [168] demonstrate that Kolmogorov's cascade phenomenology, leading to the well-known $-5/3$ decay of the Total Kinetic Energy (TKE) spectrum with the wavenumber, requires correction to account

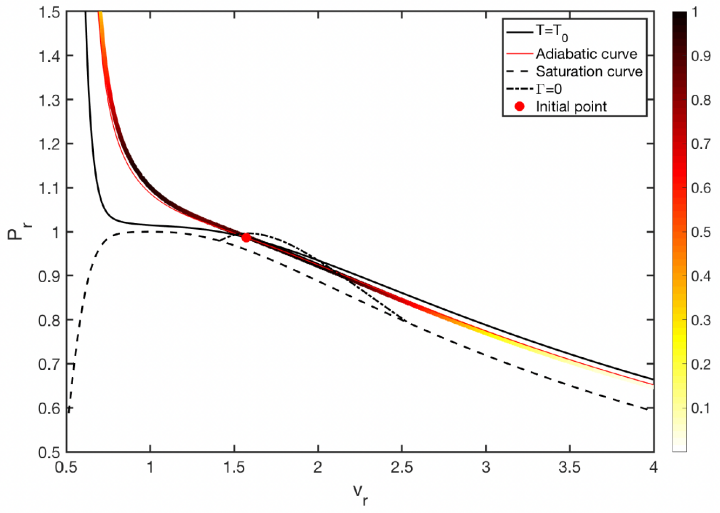


Figure 6.5: Joint PDF of the reduced pressure ($p_r$) and reduced specific volume $v_r$ in the case MH2 at $t = 15\tau$. The resolution of a given thermodynamic state is 0.01 for $p_r$ and 0.01 for $v_r$. (from [18])

for compressibility. For a turbulent Mach number equal to 6, the velocity power spectrum, defined as $< (\mathcal{F}(u_i')^2/2)(k) >$, follows a -2 slope. The TKE spectrum, defined as $< (\mathcal{F}\left[\sqrt{\rho}u_i'\right]^2/2)(k) >$, follows a -3/2 slope. Their study infers that as the turbulent Mach number increases, the deviation between the velocity power spectrum and the TKE spectra reveals the influence of compressibility on turbulence. As will become clearer in the section dedicated to the analysis of the filtered TKE, the inertial range is confined to a narrow region in the spectral space between $k = 4k_0$ and $k = 20k_0$. This limitation is attributed to the moderate Taylor Reynolds number reached in the presented cases. Figure 6.6 also includes a closer view focused on this region. In this region, the velocity power spectrum computed using the MH EoS deviates only slightly from the TKE spectrum. It indicates that, unlike the perfect gas case, compressibility effects have less influence on dense gas flow turbulence. Additionally, both spectra in the inertial range follow a slope close to $-5/3$, corresponding to the incompressible case. In the PG case, the spectra followed by the velocity power and TKE are more significantly separated. The velocity power spectrum slope is close to $-2$, while the TKE spectrum follows a $-5/3$ slope. At this stage, results indicate that compressibility does not significantly impact the turbulent cascade in dense gas flow, at least for the turbulent Mach and Taylor Reynolds numbers under consideration.
However, the dissipation region reveals an interesting difference between the turbulent flows modeled using the PG EoS or the MH EoS. Although the spectra follow an almost constant slope in the dense gas case, they initially decrease less significantly in the PG case but then follow a steeper slope as one approaches the Kolmogorov wavenumber (beyond $k = 100k_0$). Studied in more detail in the following, this difference is believed to be due at least in part to the departure in the shocklets behavior between the two types of flows.

**Shocklets analysis**
The analysis of the shocklets in this compressible configuration follows two goals:

- Firstly, relationships between pressure and density jumps across compressible shocklets are compared both in the PG and DG cases. The entropy jump through compressible shocklets is also studied because one of the interesting features of dense gases for turbomachinery applications is that much weaker compression shocks are expected, leading to reduced entropy losses.

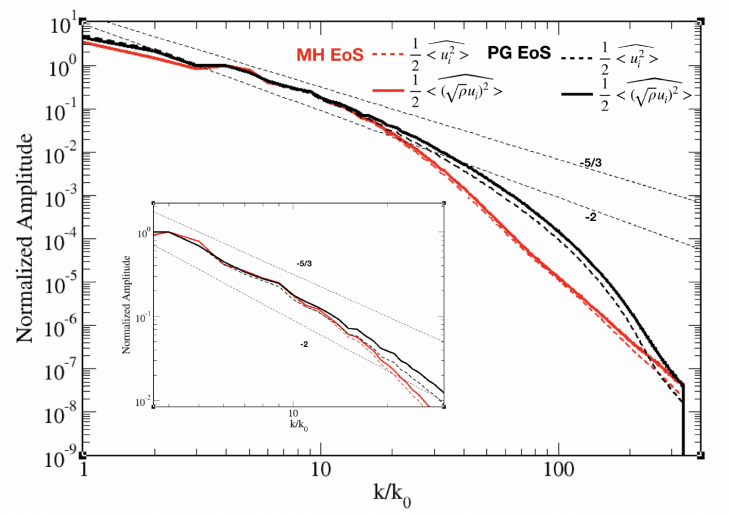


Figure 6.6: TKE and velocity power spectra at $t = 15\tau$ in case MH2 and case PG2 (from [18])

- Secondly, since the dense gas computation using the MH EoS is performed with an initial mean thermodynamic state located in the inversion region where the fundamental derivative $\Gamma$ is negative, the occurrence of expansion shocklets for the dense gas simulation is also assessed.

In order to analyze both PG and DG compression shocklets and possibly DG expansion shocklets, the marching cube algorithm proposed by Samtaney et al [169] is implemented. It consists in detecting in the flow the iso-surfaces of zero density Laplacian ($\Delta\rho = 0$). In order to only keep iso-surfaces corresponding to actual shocklets, the generalized Rankine-Hugoniot condition across the shocklet:

$$2(h_2 - h_1) = (p_2 - p_1)\left(\frac{1}{\rho_1} + \frac{1}{\rho_2}\right) \tag{6.7}$$

is verified between left and right states on each side of the presumed shocklet. The verification is performed on a distance set to $4\Delta x$ in the direction normal to the discontinuity since it is known from previous studies [170] that the shock is numerically spread over four cells. Jumps verifying relation (6.7) within 10% of the mean enthalpy are kept as (6.7) is only strictly valid in the inviscid context. The interesting feature of the generalized Rankine-Hugoniot relation is that it retains its validity regardless of the velocity of the shocklet itself, which can be complex to compute. Finally, in order to ensure the detected region corresponds to an actual shocklet, it is also requested the selected candidate iso-surface is associated to a local value of the velocity divergence large enough when compared to the rms value of the velocity divergence in the turbulent flow. For compressible shocklets, this threshold value is set to $-3$ and for expansion ones to 3.
When applied with the perfect gas EoS, $h_{pg} = \frac{\gamma}{\gamma-1}\frac{p}{\rho}$ so that (6.7) can be simplified into:

$$\frac{\rho_2}{\rho_1} = \frac{(\gamma+1)p_2/p_1 + \gamma - 1}{(\gamma-1)p_2/p_1 + \gamma + 1} \tag{6.8}$$

Because for FC-70 described using the PG EoS the value of $\gamma$ is very close to unity ($\gamma = 1.0084$), the density and pressure jumps are expected to be almost the same for the perfect gas flow.
When modeled using the perfect gas EoS, the entropy difference between the upstream and

downstream states through a shocklet is given by the following equation:

$$s_2 - s_1 = c_v \left[ \ln\left(\frac{p_2}{p_1}\right) - \gamma \ln\left(\frac{\rho_2}{\rho_1}\right) \right] \tag{6.9}$$

Since $\gamma = 1 + \epsilon$ with $\epsilon = 8.4\ 10^{-3}$ for FC-70 described as a perfect gas, the following relation can be derived to describe the evolution of the entropy increase through the shocklet with respect to the pressure ratio:

$$s_2 - s_1 = c_v \left[ \ln\left(\frac{p_2}{p_1}\right) - \gamma \ln\left(\frac{2\frac{p_2}{p_1} + \epsilon}{\epsilon\frac{p_2}{p_1} + 2}\right) \right] \tag{6.10}$$

Figure 6.7 displays the distribution of the density and entropy jumps as a function of the pressure jump across shocklets in case PG2. It confirms that $\rho_2/\rho_1 \approx p_2/p_1$ and also shows that very strong compression shocklets are observed in case PG2 up to $\rho_2/\rho_1 = 45$. This is only possible because when the Mach number upstream of the shocklet increases, the jump in density evolves asymptotically towards $\frac{\gamma+1}{\gamma-1} = 239.1$ which is very large in case PG1 and PG2. Figure 6.7 finally shows that the entropy increase through the compression shocklet follows indeed quite closely (6.10) leading to strong entropy jumps as the pressure ratio through the shocklet increases.

Compression shocklets are also observed in the dense gas case (MH2), as shown in Figure 6.8. The dissipative structures observed at $t = 15\tau$ are intricate and form a dense net. At the center of each structure, the velocity divergence is strongly negative, which corresponds to the focal point of compression. Values as large as ten times the rms velocity divergence are observed. As shown in Fig 6.9, the density and pressure jumps related to compression shocklets are significantly reduced in the dense gas. The largest jump in pressure is more than one order of magnitude smaller when compared to the PG case. The density ratio is no longer coupled to the pressure ratio through (6.8) and is observed to be much larger in average for a given pressure jump, with respect to the PG case. The maximum density ratio reached for a given pressure ratio almost follows the relation $\frac{\rho_2}{\rho_1} = \left(\frac{p_2}{p_1}\right)^2$. Following both the decrease in density and pressure jumps on one hand and the decrease of the fundamental derivative on the other, the entropy increase across compression shocklets in the dense gas is significantly reduced and much more scattered.

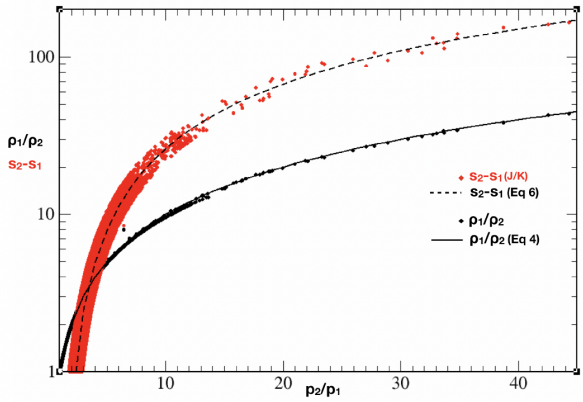


Figure 6.7: Evolution of the density jump and the entropy increase in compression shocklets in case PG2 at $t = 15\tau$. (from [18])

When applying the detection algorithm in search of expansion shocklets, none are found in the perfect gas case, as physically expected. In the dense gas case however, some structures are identified (see Figure 6.10), which are quite different in shape and size when compared

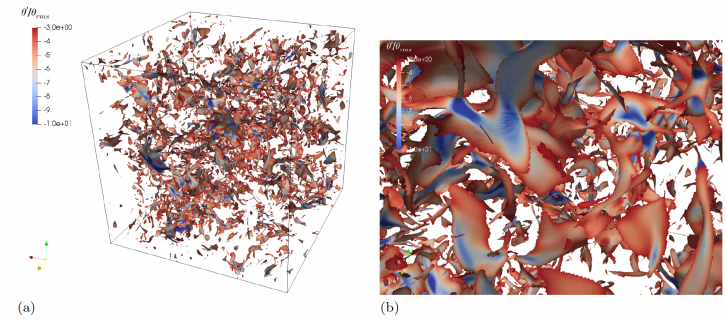


Figure 6.8: Compression shocklets colored by the velocity divergence in case MH2 at $t = 15\tau$ and closer view. (from [18])

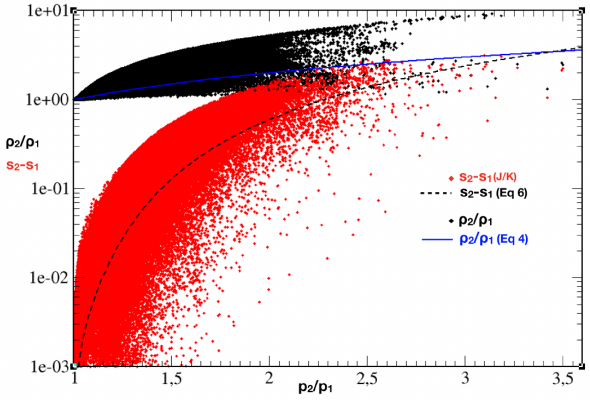


Figure 6.9: Evolution of the density jump and the entropy increase in compression shocklets for case MH2 at $t = 15\tau$. (from [18])

to compression shocklets. They are much smaller and all of them are curved in a spoonlike manner. Figure 6.11 shows the relation between the density ratio and entropy increase with the pressure jump. In order to qualitatively compare the jump relations between compression and expansion shocklets, partial distributions for compression shocklets are inserted at the bottom right in Figure6.11 for the same range of pressure ratio. The distributions of density ratio and entropy increase in the compression and expansion cases look quite similar, confirming that the fundamental conservation relations though the shocklet are the same regardless of its compression/expansion type. The pressure and density ratio are significantly smaller when expansion shocklets are considered. The maximum pressure ratio reached at time $t = 15\tau$ is equal to 1.52. Accordingly, the entropy increase though the expansion shocklets is also very small and remains below $1\,J/K$.

**Filtered TKE spectral analysis**

In order to more clearly understand the influence of the EoS on turbulence, the filtered compressible TKE equation is analyzed as proposed by Aluie et al. [171, 172, 173]. The transport equation for the large-scale turbulent kinetic energy can be written as follows:

$$\frac{\partial}{\partial t}\left(\bar{\rho}\frac{\widetilde{u_i}^2}{2}\right) + J_l = \Pi_l + \Lambda_l + PD_l + D_l + e_l^{inj} \tag{6.11}$$

with the filtering operators applied to a flowfield $\varphi$ defined as $\overline{(\varphi)} = (\mathcal{F}^{-1}_{k\leq 2\pi/l}(\mathcal{F}\varphi))(\vec{x})$ and

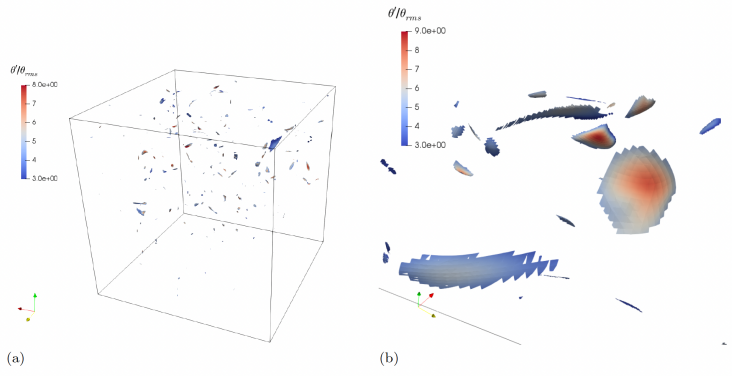


Figure 6.10: Expansion shocklets colored by the velocity divergence in case MH2 at $t = 15\tau$ and closer view. (from [18])

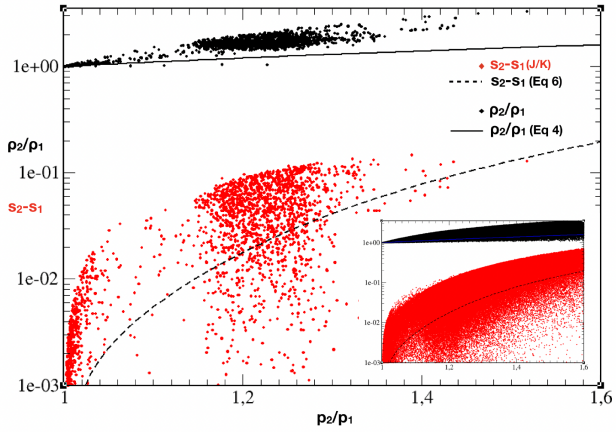


Figure 6.11: Evolution of the density jump and the entropy increase in expansion shocklets in case MH2 at $t = 15\tau$. Bottom-right window: evolution of density and entropy jump in compression shocklets for the same configuration and in the same range of pressure jump. (from [18])

$\widetilde{(\varphi)} = \overline{(\rho\ \varphi)}/\overline{\rho}$. These filtering operators at scale $l$ are such that only spatial fluctuations larger than $l$ are conserved in the field. The various terms appearing in (6.11) are respectively defined as:

$$
\begin{aligned}
\Pi_l &= \overline{\rho}\widetilde{\tau_{ij}}\frac{\partial \widetilde{u_i}}{\partial x_j}, \\
\Lambda_l &= -\frac{1}{\overline{\rho}}\bar{\tau}_j\frac{\partial \overline{p}}{\partial x_j}, \\
PD_l &= \overline{p}\frac{\partial \overline{u_i}}{\partial x_i}, \\
D_l &= -\overline{\sigma_{ij}}\frac{\partial \widetilde{u_i}}{\partial x_j}, \\
e_l^{inj} &= \widetilde{u_i}\overline{\rho}\widetilde{F_i}, \\
J_l &= \frac{\partial}{\partial x_j}\left(\frac{1}{2}\overline{\rho}\widetilde{u_i}^2\widetilde{u_j} + \overline{p}\overline{u_j} + \overline{\rho}\widetilde{\tau_{ij}}\widetilde{u_i} - \widetilde{u_i}\overline{\sigma_{ij}}\right),
\end{aligned}
$$

where $\widetilde{\tau_{ij}} = \widetilde{u_i u_j} - \widetilde{u_i}\widetilde{u_j}$, $\bar{\tau}_j = \overline{\rho u_j} - \overline{\rho}\overline{u_j}$, $\overline{\sigma_{ij}} = \overline{\mu\left(\frac{\partial u_i}{\partial x_j} + \frac{\partial u_j}{\partial x_i}\right) - \frac{2}{3}\mu\frac{\partial u_k}{\partial x_k}\delta_{ij}}$, and $F_i$ is provided

by Equation 6.6.
In order to compare the dense and perfect gas cases, at any given time, the space averaged $< \cdot >$ of (6.11) is considered. Because of the periodicity of the forced THI configuration, the equation simplifies to:

$$\left\langle \frac{\partial}{\partial t}\left(\bar{\rho}\frac{\widetilde{u_i}^2}{2}\right)\right\rangle =< \Pi_l > + < \Lambda_l > + < PD_l > + < D_l > + < e_l^{inj} > \tag{6.12}$$

Equation (6.12) shows that in the inertial region of the spectrum (where both forcing $< e_l^{inj} >$ and dissipation $< D_l >$ are negligible), the temporal evolution of the filtered TKE is driven by the equilibrium between the three terms $< \Pi_l >$, $< \Lambda_l >$, and $< PD_l >$, respectively representing the SGS deformation work, the SGS baropycnal work and the pressure dilatation term.
Figure 6.12 presents the evolution of these three terms with respect to the filtering length scale at $t = 15\tau$ for cases PG2 and MH2. All terms are normalized by the initial TKE dissipation computed as $\epsilon_0 = \left\langle \bar{\rho}\frac{\widetilde{u_i}^2}{2}\right\rangle_{t=0}/\tau$.
In order to link the filtered terms to the overall evolution of the TKE spectrum shown in Fig 6.6, the three identified regions (forcing, inertial and dissipation) are recalled. One can observe that the most important term regardless of the EoS is the SGS deformation work which transfers TKE from large scales to smaller ones following the usual cascade behavior. In the spectral region identified as inertial, this term has a constant amplitude which is the same in the PG and DG cases. As dissipation sets in, it decreases to zero as expected.
In both the PG and DG cases, the baropycnal work ($< \Lambda_l >$) brings TKE from the small to the large scales and the resolved pressure dilatation term ($< PD_l >$) transforms TKE into internal energy therefore appearing here as a sink term. Regardless of the EoS, $< \Lambda_l >$ and $< PD_l >$ almost cancel out each other in the inertial region. These results present a significant difference with Aluie's findings. In Aluie et al. [172], the pressure dilatation term is often large (at least comparable in amplitude to the SGS deformation work). Aluie et al. therefore rightfully condition the existence of an inertial range to $< PD_l >$ being constant in this region of the spectrum. Using FC-70 as a fluid, the pressure dilatation amplitude evolves significantly in the identified inertial range but remains small enough when compared to the SGS deformation work (its amplitude is approximately 1% of the SGS deformation work) so that this region still exists. Finally, even though $< \Lambda_l >$ and $< PD_l >$ do not significantly influence the behavior of the TKE, it should be noted that their amplitude is two times smaller in the DG case when compared to the PG case.

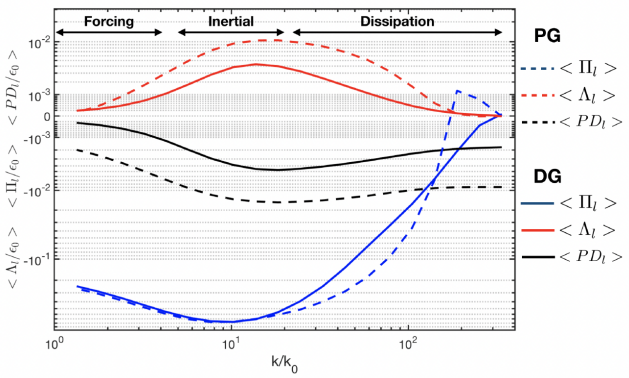


Figure 6.12: Spectral evolution of $< \Pi_l >$, $< \Lambda_l >$ and $< PD_l >$ in cases PG2 and MH2 at $t = 15\tau$ (from [18])

**Total energy conservation equation analysis**

When computing any compressible turbulent flow, the total energy per unit volume $\rho E$ is often transported using the conservative equation
In order to prepare future work focusing on the modeling of sub-grid terms for LES and RANS techniques using the DNS database, it is interesting to compare the PDF of the terms on the right-hand side of this equation when using the PG EoS or the MH EoS. The underlying idea is that any difference in the statistics of the fluctuations of those terms would be a sign of the influence of the EoS. It is shown above that during the simulation, the thermodynamic variables remain along the adiabatic curve passing through the initial conditions in the p-v diagram. In this context, it is found that the PDF of the pressure term is strongly influenced by the dense gas EoS (See Figure 6.13). Interestingly, in the PG case, the distribution obtained by regression fits quite nicely. Only a small additional skewness is observed leading to slightly more probable large positive terms. In the DG case however, the distribution of the pressure term displays much more skewness. The distribution of negative values follows a Laplace distribution, whereas for large positive values it is close to the PG case. This last observation indicates that the pressure term $\frac{\partial p u_i}{\partial x_i}$ is indeed sensitive to the EoS and needs to be further analyzed.

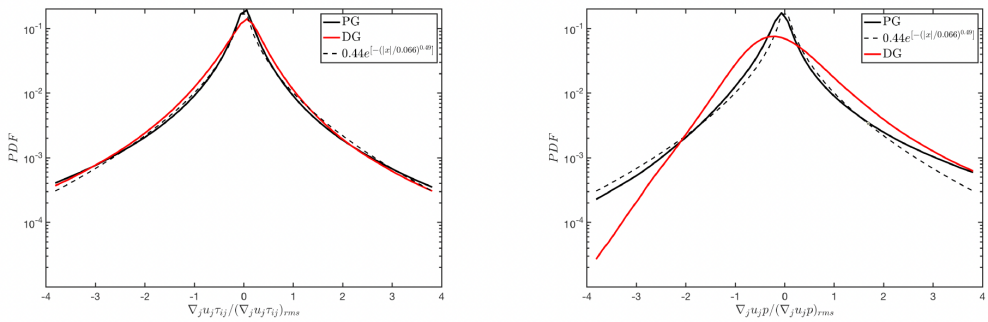


(a) Viscous term $\frac{\partial \tau_{ij} u_i}{\partial x_j}$

(b) Pressure term $\frac{\partial p u_i}{\partial x_i}$

Figure 6.13: PDF of RHS terms of the total energy equation in cases PG2 (PG) and MH2 (DG) at $t = 15\tau$. (from [18])

### 6.4.2 Mixing layer in a dense gas

The temporal mixing layer consists of two streams flowing in opposite directions. The velocity in the upper part of the domain $U_1$ is set equal to $-\Delta u/2$, whereas $U_2$ is set to $\Delta u/2$. A representation of the computational domain is provided in figure 6.14. A snapshot of the velocity magnitude is also plotted for the DG DNS at $M_c = 2.2$. Periodic boundary conditions are imposed in the $x$ and $z$ directions and non-reflective conditions are set in the $y$ directions using the NSCBC model proposed by Poinsot & Lele [118].

The streamwise velocity field is initialized using an hyperbolic tangent profile:

$$\bar{u}_x(y) = \frac{\Delta u}{2} \tanh\left(-\frac{y}{2\delta_{\theta,0}}\right) \tag{6.13}$$

The complete streamwise velocity field is obtained by adding fluctuations to the average velocity. For the $y$ and $z$ components, the average velocity is set equal to zero. A Passot-Pouquet spectrum is imposed for initial velocity fluctuations:

$$E(k) = (k/k_0)^4 exp(-2(k/k_0)^2) \tag{6.14}$$

where $k$ denotes the wavenumber. The peak wavenumber $k_0$ controls the size of the initial turbulent structures. Its value only influences the initial unstable growth regime. It has been

noted that a larger value of $k_0$ accelerates the transition to the unstable growth. The velocity field is then filtered to initialize turbulence only inside the initial momentum thickness.

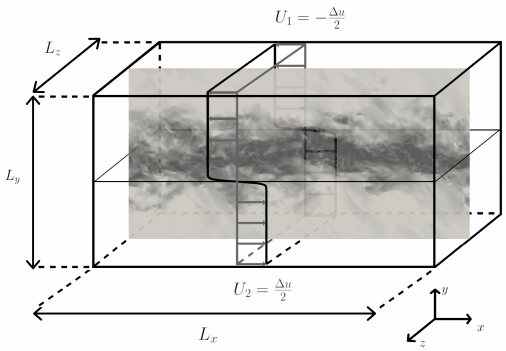


Figure 6.14: Configuration of the temporal mixing layer. The velocity magnitude is plotted for the DG DNS at $M_c = 2.2$ at $\tau = 4000$. (from [19])

#### 6.4.2.1 Comparison with perfect gas over the self-similar period

Self-similar periods have been identified for both gas types, enabling the depiction of self-similar growth rates as a function of the convective Mach number. Typically, slopes are standardized using an incompressible reference scenario at very low convective Mach numbers, where compressibility effects are negligible, with DNS at $M_c = 0.1$ serving as the reference incompressible case. For instance, Pantano & Sarkar [174] utilize a simulation at $M_c = 0.3$ as a reference scenario, reflecting the lack of consensus on this selection, contributing to the divergence of PG results as depicted in Figure 6.15. Dense gas (DG) mixing layer outcomes are illustrated with black error bars, indicating the standard deviation of the normalized growth rate across the self-similar range. In contrast to the PG mixing layer, which exhibits a relatively sharp decline in growth rate as $M_c$ rises, the DG mixing layer appears to be less affected by compressibility effects as $M_c$ surpasses 1.1. The substantial differences between DG and PG mixing layers, compared to the standard deviations, suggest that turbulent development is notably influenced by dense gas effects in mixing layer flows. Figure 6.15 shows a comparison between current PG results and available numerical [175, 174, 176, 177, 178, 179, 180] and experimental results [20] from the literature. The current DNS results align with the trend documented in existing literature: the well-established decrease in momentum thickness growth rate with increasing convective Mach number ($M_c$) due to compressibility effects. The growth rate of the mixing layer decreases by approximately fivefold from the incompressible case to $M_c = 2.2$. Standard deviations have been calculated and are depicted on the plot, representing around 5% of the computed growth rates. Mitigating this uncertainty proves challenging due to difficulties in achieving perfect self-similarity, as evidenced by the dispersion of literature findings, potentially stemming from this issue. Furthermore, the scarcity of numerical data in highly compressible regimes complicates the validation process.

To examine the influence of compressibility effects, Pantano & Sarkar [174] investigate the turbulent kinetic energy (TKE) equation, focusing on the significance of the turbulent production term. They observe a proportional decrease in this term with the growth rate as the convective Mach number increases. Calculating the TKE equation terms necessitates statistical averaging, feasible only during the self-similar period when both mixing layers attain statistical stability. Figure 6.16 presents a comparison between dense gas (DG) and perfect gas (PG) mixing layers of the normalized primary terms of the TKE equation across

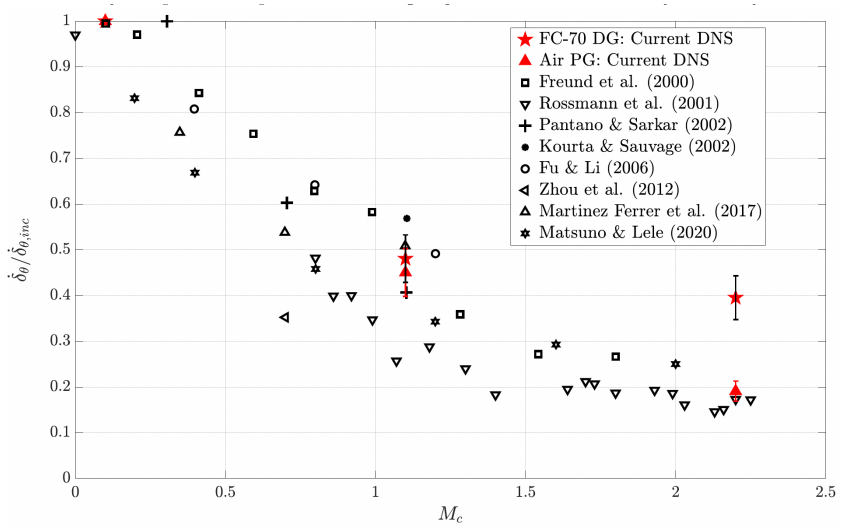


Figure 6.15: Evolution of the mixing layer growth rate over the convective Mach number for air and for FC-70. Comparison is made with available DNS results in literature and experimental results in Rossmann et al.[20]. (from [19])

the non-dimensional cross-stream direction $y/\delta_\theta(t)$. These terms, including production ($P$), viscous dissipation ($D$), and transport ($T$), are averaged over corresponding self-similar ranges. The production term, responsible for mixing layer growth, remains positive, while viscous dissipation counteracts it, and the transport term facilitates TKE propagation from the center to the edges of the mixing layer. In line with the comparison of slopes between DG and PG flows, all primary terms, particularly the production term, are approximately two to three times larger for DG.
A notable observation previously emphasized in the analysis at $M_c = 1.1$ [181] is reaffirmed: the curves exhibit greater width for the perfect gas (PG) mixing layer compared to the dense gas (DG) mixing layer. In the case of the DG mixing layer, turbulent kinetic energy (TKE) is more concentrated at the center, a characteristic directly influenced by the wider thermodynamic profiles observed in the PG mixing layer. Regarding other terms within the TKE equation, including compressible dissipation, mass-flux coupling, convective derivative of TKE, and pressure dilatation, they are deemed negligible for both gas types.

Figure 6.17 illustrates the comparison of streamwise specific turbulent kinetic energy spectra between perfect gas (PG) and dense gas (DG) computed along the centerline. Spectra are normalized by $(\Delta u)^2\delta_\theta(t)$, following the methodology of Pirozzoli et al.[182], and averaged over the self-similar period. Additionally, the longitudinal Taylor microscale $\lambda_x$ is indicated for each gas in Figure 6.17, with its notably larger value for DG flow consistent with Reynolds numbers derived from Taylor microscales. Consequently, the inertial phase is considerably reduced for PG flow, with dissipation occurring at much larger scales, complicating the comparison between inertial phase slopes. Nonetheless, the spectra confirm previous findings observed at $M_c = 1.1$ [181]: dense gas effects tend to enhance energy at small scales, with a notable reduction in the dissipation term, the predominant term at these scales. These results underscore the necessity for specific sub-grid scale modeling of dense gas flows, given the significant modification of small-scale dynamics compared to perfect gas flows.

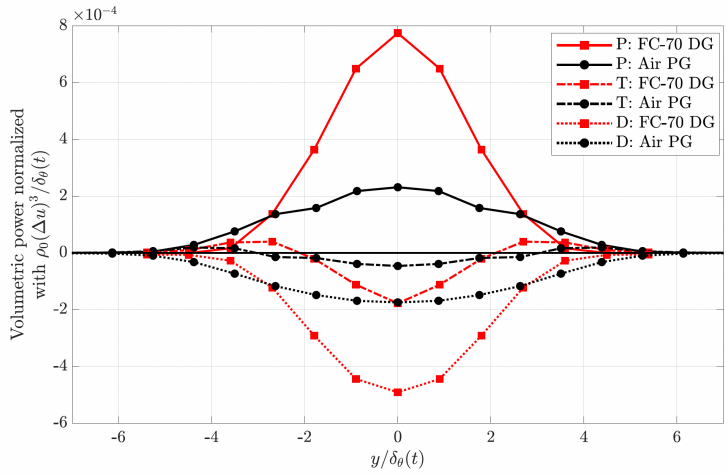


Figure 6.16: Distribution of the volumetric normalized powers over the non-dimensional cross-stream direction $y/\delta_\theta(t)$ at $M_c = 2.2$. P: Production, D: Dissipation and T: Transport are normalized by $\rho_0(\Delta u)^3/\delta_\theta(t)$. Distributions have been averaged between the upper and the lower stream to get perfectly symmetrical distributions. (from [19])

#### 6.4.2.2 Additional simulations varying the initial thermodynamic operating point

To address discrepancies observed between dense gas (DG) and perfect gas (PG) flows, additional DNS simulations are conducted, varying the initial thermodynamic operating point. Figure 6.18 illustrates the four selected operating points. The initial operating point for simulation DGA corresponds to the reference scenario analyzed thus far, situated within the inversion zone, also known as the BZT region. For the second simulation, DGB, the operating point is deliberately positioned outside the inversion region and within the dense gas zone, allowing for an examination of the impact of BZT effects on mixing layer growth. Lastly, for simulations DGC and DGD, initial operating points are situated on the same adiabatic curves as DGB and DGA, respectively, but outside the dense gas zone. This diversity in targeted thermodynamic regions aims to offer a comprehensive understanding of the effects of dense gas on shear layer growth.

Concerning the decline in growth rate relative to the convective Mach number, the theoretical explanation proposed by Pantano & Sarkar [174] was examined for DGA, attributing the reduction in momentum thickness growth rate to a decrease in normalized pressure fluctuations. The inquiry extends to determine if this reduction in normalized pressure fluctuations is also evident for DGB, DGC, and DGD. Illustrated in Figure 6.19, the normalized growth rate is depicted as a function of normalized pressure fluctuations computed at the center of the mixing layer. Notably, for perfect gas (PG) flow, a substantial reduction is observed, with both growth rate and normalized pressure fluctuations halved between $M_c = 1.1$ and $M_c = 2.2$. Similarly, for dense gas (DG), the decline in normalized growth rate correlates with a reduction in pressure fluctuations. However, among the cases at $M_c = 2.2$, establishing a ranking solely based on the level of pressure fluctuations proves somewhat unsatisfactory, potentially due to standard deviations resulting from variations in the plateaus of integrated turbulent production. Additionally, other effects specific to dense gases must be considered.

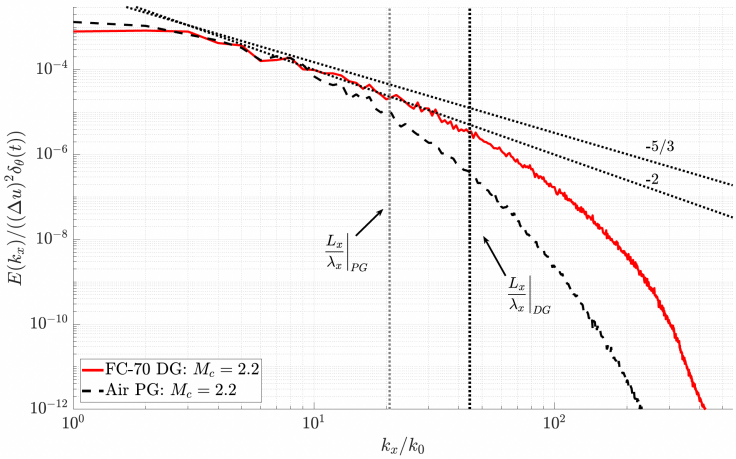


Figure 6.17: Streamwise specific TKE spectra computed at the centerline. (from [19])

#### 6.4.2.3 Analysis of discrepancies between DG and PG flows

Dense gas exhibits a notable impact on the well-documented reduction in momentum thickness growth rate associated with compressibility effects. Beyond a convective Mach number of $M_c = 1.1$, dense gas effects alter this reduction. Notably, between $M_c = 1.1$ and $M_c = 2.2$, there is minimal variation in the growth rate slope for dense gas. Several contributing factors can be identified to elucidate the observed disparities between dense gas (DG) and perfect gas (PG) mixing layers. The primary distinction lies in the ratio between enthalpy and kinetic energy, linked to the Eckert number, defined for the mixing layer as:

$$Ec = \frac{(\Delta u)^2}{c_{p_0} T_0} \tag{6.15}$$

The initial Eckert numbers, computed for each DNS, are compiled in Table 6.3, where $c_{p_0}$ represents the initial specific heat capacity at constant pressure and $T_0$ denotes the initial temperature. For dense gas (DG) flows, these values are approximately two orders of magnitude lower than those for perfect gas (PG) flows. Two characteristics of DG mixing layers contribute significantly to these distinctions: the high heat capacity of FC-70 and the minimal differential speed $\Delta u$. The differential speed is defined to maintain the same initial convective Mach number between DG and PG mixing layers. Due to the considerably lower sound speed in dense gases, achieving a comparable convective Mach number necessitates a much lower differential speed, consequently reducing the Eckert number mechanically. With diminished Eckert numbers, kinetic energy becomes negligible compared to enthalpy or internal energy. This holds true for all DG flows examined in this study, despite their relatively high convective Mach numbers. As evidenced by the findings, kinetic energy disengages from thermodynamic compressibility effects, enabling the momentum thickness growth rate to reach higher values. The close correspondence between the momentum thickness growth rates of DGA/DGC and DGB/DGD, as well as their respective initial Eckert numbers, underscores this relationship. Lower Eckert numbers for DGA/DGC correspond to higher growth rates for these shear layer configurations, stemming from a more pronounced decoupling between internal and kinetic energy compared to DGB/DGD. However, the Eckert number alone cannot fully account for the dense gas effect on the growth rate, as observed in the slightly lower growth rate of DGC compared to DGA, despite having a slightly lower initial Eckert number.

In dense gas (DG) flows, there is a substantial disparity between the amounts of internal

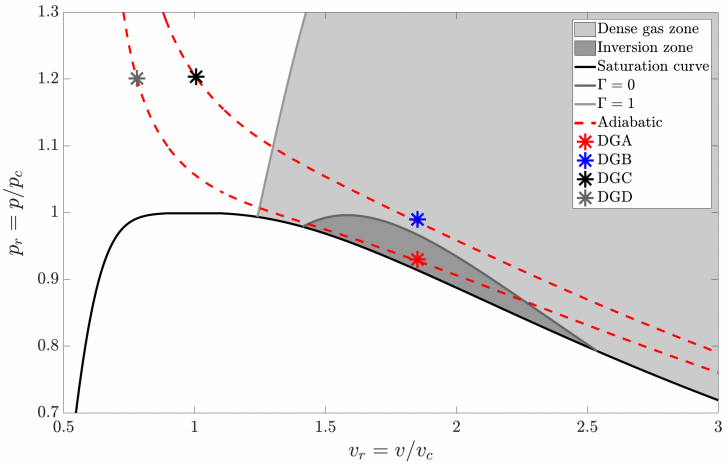


Figure 6.18: Four different initial thermodynamic states used to perform additional DNS are represented in the non-dimensional $p-v$ diagram for BZT dense gas FC-70 at $M_c = 2.2$. The dense gas zone ($\Gamma < 1$) and the inversion zone ($\Gamma < 0$) are plotted for the Martin-Hou equation of state. $p_c$ and $v_c$ are respectively the critical pressure and the critical specific volume. (from [19])

| | $M_c$ | $Ec$ | $\dot{\delta}_\theta/\dot{\delta}_{\theta,inc}$ |
|---|---|---|---|
| DG | 1.1 | 0.0040 | 0.484 |
| DGA | 2.2 | 0.0162 | 0.395 |
| DGB | 2.2 | 0.0226 | 0.352 |
| DGC | 2.2 | 0.0147 | 0.389 |
| DGD | 2.2 | 0.0203 | 0.342 |
| PG | 1.1 | 1.94 | 0.450 |
| PG | 2.2 | 7.74 | 0.188 |

Table 6.3: Eckert numbers and normalized momentum thickness growth rates are given for each simulation.

energy and kinetic energy, resulting in their decoupling. This decoupling leads to neglecting all terms in the energy conservation equation except for the temporal and convective internal energy terms. As previously demonstrated by Gloerfelt et al. [183], the Eckert number, which quantifies frictional heating, is notably diminished in DG flows. Temperature fluctuations are nearly eradicated in DG, as confirmed by Sciacovelli et al. [184] in supersonic turbulent channel flows, indicating that dense gas flows experience fewer frictional losses associated with Mach number effects. In the mixing layer, beyond $M_c = 1.1$, compressibility effects linked to the escalating convective Mach number have a diminished impact on DG flows, partly due to the reduction of frictional heating.
The evolution of the average density corroborates this reduction. In perfect gas (PG) flows, the air density undergoes a 40% reduction at the center between $M_c = 1.1$ and $M_c = 2.2$. Frictional heating in PG leads to a rise in temperature, resulting in decreased density. This mechanism is considerably mitigated in dense gas flows, where temperature remains relatively constant, and the average density displays minimal variations. At $M_c = 2.2$, the reduction in average density at the mixing layer center represents approximately 8% of the initial density for DG, compared to 45% for air. This phenomenon significantly influences the growth rate of the mixing layer, which is density-dependent. As the mixing layer develops in PG, intense friction occurs at the center, leading to density reduction and consequently a substantial decrease in the momentum thickness growth rate compared to DG.

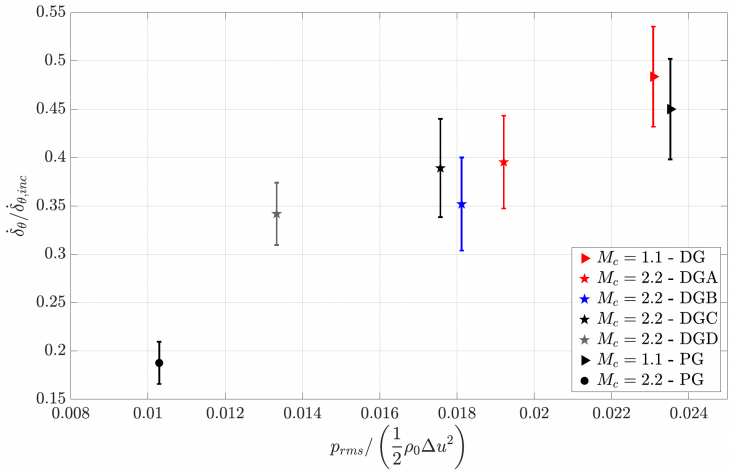


Figure 6.19: Evolution of the non-dimensional mixing layer growth rate over the center root-mean squared value of pressure normalized by $\frac{1}{2}\rho_0(\Delta u)^2$. Results are given for DG and PG at $M_c = 1.1$ and $M_c = 2.2$. (from [19])

The amplitudes of the density fluctuation distributions differ notably between DG and PG flows. In DG flows, the maximum root mean square value of density fluctuations increases by a factor of three from $M_c = 1.1$ to $M_c = 2.2$, while in PG flows, it increases by about two-fold. Compressible flows experience higher root mean square density fluctuations, which escalate with increasing Mach numbers. This phenomenon can be attributed to the large isentropic compressibility coefficient characteristic of DG flows.

$$\chi_s = \frac{1}{\rho}\frac{\partial \rho}{\partial p}\bigg|_s \tag{6.16}$$

For flows with large values of $\chi_s$, small variations of pressure lead to large variations of density. The sound speed is directly linked to the isothermal compressibility since:

$$c = \frac{1}{\sqrt{\rho \chi_s}} \tag{6.17}$$

In DG flows, the substantial isentropic compressibility factor significantly reduces the speed of sound. Consequently, the initial sound velocity in the simulated DG flows is approximately six times lower than that in the PG shear layers. Figure 6.20 illustrates the normalized momentum growth rate at $M_c = 2.2$ plotted against the normalized sound velocity. A noticeable correlation emerges between the growth rate of momentum thickness and the initial sound speed: as the sound speed increases, the growth rate decreases.
These observations lead to the primary conclusion that the lower Eckert number in DG flows results in a decoupling between internal and kinetic energy, leading to reduced friction heating. Both phenomena affect the average and fluctuating thermal properties, thereby mitigating the compressibility-induced reduction in the growth rate of momentum thickness.

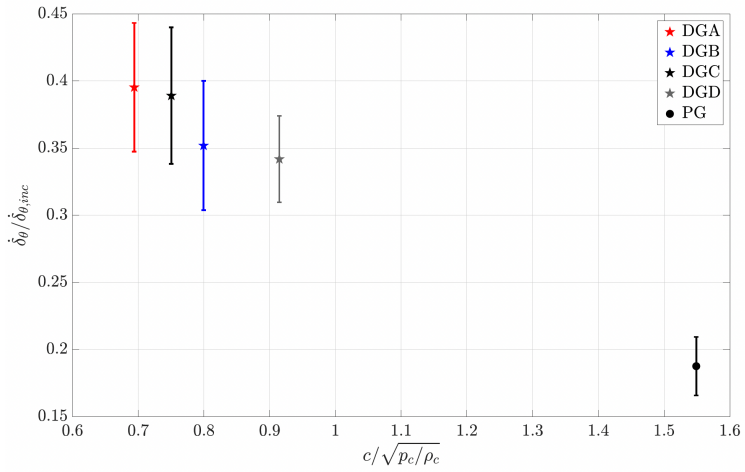


Figure 6.20: Evolution of the non-dimensional mixing layer growth rate as a function of the sound speed normalized with $\sqrt{p_c/\rho_c}$. Results are given for DG and PG at $M_c = 2.2$. (from [19])

## 6.5 Analysis of subgrid scale dynamics – *Assessment of existing sgs models*

At this step two main questions emerge:

- Is there a difference between the subgrid-scale terms in perfect gas and in dense gases?
- How do the models that are readily available and have been developed for perfect gases perform when used in dense gas flow simulations?

This last question can be split in two sub-topics because one can first evaluate a-priori the capabilities of a significant number of models by filtering the database obtained using DNS. Of course it is then important to also evaluate a-posteriori the models in the context of a LES of a real gas (of High Molecular Complexity) flow and compare with experimental measurements.

### 6.5.1 Quick overview of the Full DNS database

#### 6.5.1.1 Homogeneous Isotropic Turbulence

DNS of a compressible HIT (Illustrated in figure 6.21) with initial turbulent Mach number $M_t = 0.8$ and Taylor Reynolds number $Re_{\lambda_T} = 100$ is performed for a real gas, perfluorotripentylamine (FC-70, $C_{15}F_{33}N$)). The physical parameters defining the thermodynamic description of FC-70 are taken from Cramer et al. [26] and given in Table 6.4.
The initial thermodynamic state is defined by the reduced pressure $p_r^{init} = p^{init}/p_c = 0.9866$ and the reduced specific volume $v_r^{init} = v^{init}/v_c = 1.5733$. This initial state is selected inside the transcritical region of FC-70.
The main non-dimensional characteristic numbers of the compressible HIT are the Taylor Reynolds number $Re_{\lambda_T}$ based on the Taylor scale $\lambda_T$:

$$Re_{\lambda_T} = \frac{\lambda_T \sqrt{<u_i' u_i'/3>}}{<\nu>} \quad \text{with} \quad \lambda_T = \sqrt{2\frac{<u_i' u_i'/3>}{<\left(\frac{\partial u_1'}{\partial x_1}\right)^2>}}, \tag{6.18}$$

Table 6.4: Physical parameters of FC-70 [26]. The critical pressure $p_c$, the critical temperature $T_c$, the boiling temperature $T_b$ and the compressibility factor $Z_c = p_c v_c/(RT_c)$ are the input data for the Martin-Hou Equation of State (EoS)[27, 28]. The critical specific volume $v_c$ is deduced from the aforementioned parameters. The exponent $n$ and the $c_v(T_c)/R$ ratio are used to compute the heat capacity $c_v(T)$ (with $R = \mathcal{R}/M$, the specific gas constant computed from the universal gas constant $\mathcal{R}$ and the molar mass $M$).

| | $M$(kg/mol) | $T_c$(K) | $p_c$(atm) | $Z_c$ | $T_b$(K) | $m = c_v(T_c)/R$ | $n$ |
|---|---|---|---|---|---|---|---|
| FC-70 | 0.821 | 608.2 | 10.2 | 0.270 | 488.2 | 118.7 | 0.493 |

and the turbulent Mach number:

$$M_t = \frac{\sqrt{< u_i' u_i' >}}{< c >}, \tag{6.19}$$

where Einstein implicit summation is used. Operator $< \cdot >$ represents the space averaging operator, $u_i'$ denotes the fluctuating velocity in direction $x_i$, $\nu$ is the kinematic viscosity and $c$ the speed of sound.
The flow domain is a cube with edge length $L$. Periodic boundary conditions are applied in the three space directions. Given the low speed of sound obtained using the Martin & Hou (MH) EoS [27] for the chosen initial thermodynamic point, a 20 m/s turbulent velocity translates into a turbulent Mach number equal to 0.8. The computational setup is summarized in Table 6.5. The $675^3$ resolution corresponds to a discretization of the Kolmogorov length scale with 2.5 points. The detailed analysis of the turbulence statistical properties for this case and the comparison with the perfect gas flow case is found in a previous publication of the authors [18].

Table 6.5: Key features of the HIT test case.

| EoS | Turbulent velocity (m/s) | Viscosity and Conductivity | Domain size L (m) | Kolmogorov length (m) |
|---|---|---|---|---|
| MH | 20 | Chung et al.[30] | 4.58727e-06 | 1.72e-8 |

#### 6.5.1.2 Compressible Mixing layer

DNS of temporal compressible mixing layers are performed at three convective Mach number $M_c = 0.1 - 1.1 - 2.2$ for FC-70 described using the Martin & Hou EoS[27, 28]. Results are extracted from Vadrot *et al.*[181, 19]. The configuration consists in two streams flowing in opposite direction as sketched in figure 6.22. The main non-dimensional characteristics of the compressible mixing layer are the convective Mach number (equation (6.20)) and the Reynolds number based on the initial momentum thickness $\delta_{\theta,0}$ (equation (6.21)).

$$M_c = (U_1 - U_2)/(c_1 + c_2) = \Delta u/(c_1 + c_2), \tag{6.20}$$

where $u_i$ and $c_i$ denote respectively the flow speed and the sound speed of stream $i$ (upper or lower) of the mixing layer. $\Delta u$ denotes the differential speed between streams 1 and 2.

$$Re_{\delta_{\theta,0}} = \Delta u \delta_{\theta,0}/\nu. \tag{6.21}$$

The momentum thickness at time $t$ is defined as:

$$\delta_\theta(t) = \frac{1}{\rho_0(\Delta u)^2} \int_{-\infty}^{+\infty} \overline{\rho} \left( \frac{(\Delta u)^2}{4} - \widetilde{u}_x^2 \right) dy, \tag{6.22}$$

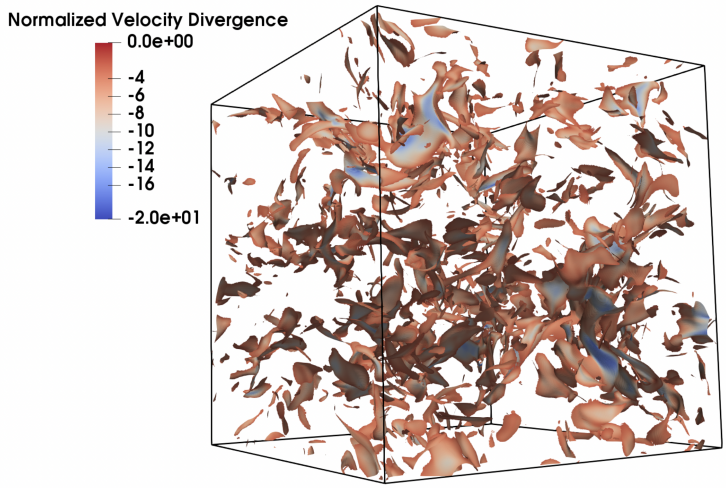


Figure 6.21: Configuration of the Homogenous Isotropic Turbulence (HIT). Compression shocklets colored by the normalized velocity divergence. (from [21])

with $\rho_0 = (\rho_1 + \rho_2)/2$ the averaged density.
The Reynolds number based on the initial momentum thickness is set equal to 160 following the reference work of Pantano & Sarkar [174]. Table 6.6 reports the simulation parameters (domain size, grid resolution, differential speed and initial momentum thickness).

Table 6.6: Simulation parameters. $L_x$, $L_y$ and $L_z$ denote computational domain lengths measured in terms of initial momentum thickness. $N_x$, $N_y$ and $N_z$ denote the number of grid points. All grids are uniform.

| | $M_c$ | $L_x \times L_y \times L_z$ | $N_x \times N_y \times N_z$ | $\Delta u$ $(m.s^{-1})$ | $\delta_{\theta,0}$ $(nm)$ |
|---|---|---|---|---|---|
| FC-70 | 0.1 | $344 \times 344 \times 86$ | $1024 \times 1024 \times 256$ | 5.67 | 2070 |
| FC-70 | 1.1 | $344 \times 172 \times 86$ | $1024 \times 512 \times 256$ | 62.32 | 188.2 |
| FC-70 | 2.2 | $688 \times 344 \times 172$ | $1024 \times 512 \times 256$ | 125.1 | 93.8 |

The initialization of the mixing layer requires to set the initial thermodynamic operating point in the $p-v$ diagram. The initial state is chosen within the transcritical zone of FC-70. The reduced pressure and specific volume are respectively set to $p_r^{init} = p^{init}/p_c = 0.926$ and $v_r^{init} = v^{init}/v_c = 1.851$.
The temporal mixing layer requires periodic boundary conditions in $x$ and $z$ directions. A non-reflective boundary condition is imposed in the $y$ direction to prevent the reflection of acoustic waves inside the computational domain. The NSCBC model proposed by Poinsot & Lele [77] is used. The mean streamwise velocity is initialized with a hyperbolic tangent profile:

$$\overline{u}_x(y) = \frac{\Delta u}{2} \tanh\left(-\frac{y}{2\delta_{\theta,0}}\right). \tag{6.23}$$

The complete streamwise velocity field is obtained by adding a fluctuating component to the mean component. For the $y-$ and $z-$ components of the velocity, the mean part is set equal to zero. A Passot-Pouquet spectrum is used for the initial velocity fluctuation. The velocity field is then filtered to initialize turbulence only inside the initial momentum thickness. The detailed analysis of this case and the comparison with the perfect gas flow

case are found in previous works of the authors[181, 19].

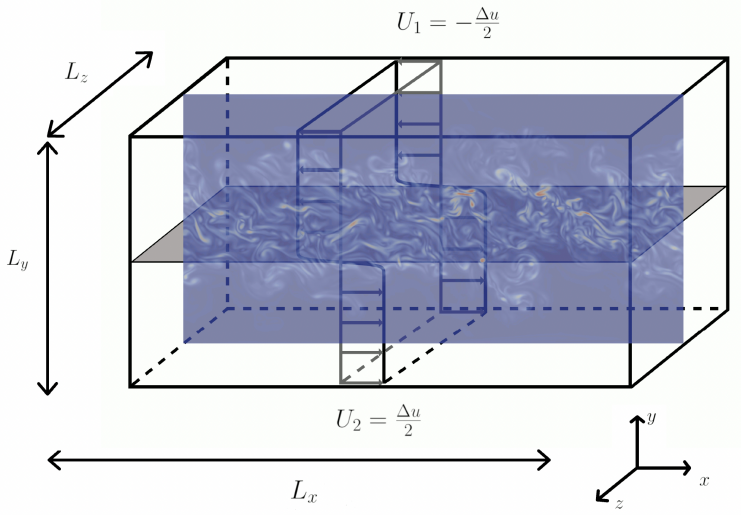


Figure 6.22: Configuration of the temporal mixing layer. The vorticity magnitude is plotted at $M_c = 2.2$ and $\tau = t\Delta u/\delta_{\theta,0} = 4000$. (from [21])

#### 6.5.1.3 Supersonic channel flow

DNS of a supersonic channel flow is performed for Perfluorophenanthrene ($C_{14}F_{24}$), also commercially known as PP11. This real gas is thermodynamically described via the Martin & Hou EoS[27, 28], using the parameters given in Guardone et al. [185] and summarized in Table 6.7. The computational domain consists of a rectangular parallelepiped ($L_x = 8\pi h$, $L_y = 2h, L_z = 2\pi h, h = 6 \cdot 10^{-6}[m]$) in which two opposite flat faces, perpendicular to the $y-$ direction, represent solid isothermal boundary walls, while periodicity is imposed on the four remaining ones. The domain is discretized using hexahedral mesh elements ($N_x = 3668, N_y = 294, N_z = 930$). Figure 6.23 shows the domain with Q-criterion iso-surfaces. The fluid flows in the $x-$ streamwise direction. Temperature is fixed at walls, at a reduced value of $T_r = T/T_c = 1.001$, in order to control the thermodynamic working point, which is inside the transcritical zone for PP11. In addition, since the speed of sound $c$ and dynamic viscosity $\mu$ are function of temperature, imposing the wall temperature allows to assess the bulk Reynolds and Mach number ($Re_B$ and $M_B$) defined as follows:

$$Re_B = \frac{\rho_B \overline{u}_B h}{\overline{\mu}_w}, \qquad M_B = \frac{\overline{u}_B}{\overline{c}_w}. \tag{6.24}$$

Subscripts $(\cdot)_B$ and $(\cdot)_w$ stand respectively for bulk and wall quantities, while $\overline{(\cdot)}$ refers to Reynolds averaged quantities. The fluid is forced to flow inside the channel at $M_B = 3$ and $Re_B = 6500$. A source term in the momentum conservation equation balances the wall friction to maintain flow conditions. The DNS calculation is initialized starting from an LES solution where the flow has been fully transitioned to turbulence. The main statistics are collected once the steady state is reached and verified through comparison with results in Sciacovelli *et al.*[35].

Table 6.7: PP11 physical parameters used by the Martin-Hou equation of State.

| | $M$(kg/mol) | $T_c$(K) | $p_c$(atm) | $Z_c$ | $T_b$(K) | $m = c_v(T_c)/R$ | $n$ |
|---|---|---|---|---|---|---|---|
| PP11 | 0.624 | 650.2 | 14.41 | 0.2688 | 488.15 | 97.3 | 0.5776 |

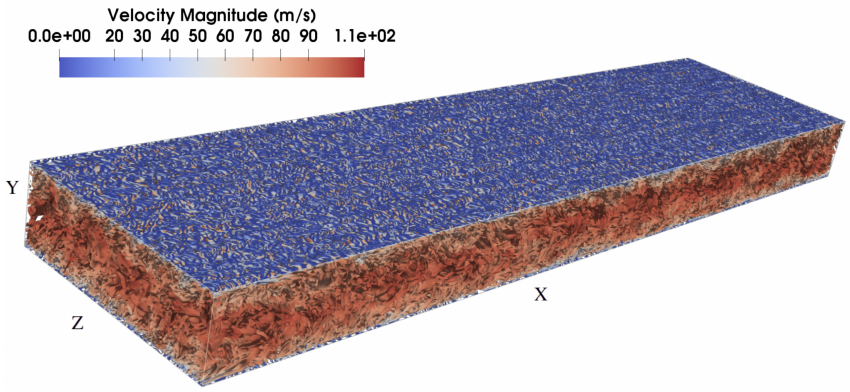


Figure 6.23: Visualization of flow structures inside the supersonic channel flow: Q-Criterion iso-surfaces colored by velocity magnitude (from [21])

### 6.5.2 A-priori analysis of SGS terms - focus on the momentum equation

The comparative analysis of the SGS terms appearing in the filtered momentum equations is performed for the three real gas configurations under study (HIT, Mixing layer and Channel flow). Six terms appear for each direction in the filtered momentum equations (equation 3.12): the resolved and SGS pressure, viscous and turbulent stress terms. Let us recall that SGS turbulent stress term is the main focus of modeling effort in the LES community, as other SGS terms do not even appear in the incompressible equations. However, even for compressible LES, SGS terms other than the SGS turbulent stress are generally not taken into account in the modeling process. The following analysis aims therefore at providing a well-grounded assessment of the SGS terms relative importance in the real gas context, which will guide further modeling effort.

Figure 6.24 shows the RMS amplitude of resolved and SGS quantities in the HIT configuration over the whole range of filtering sizes. One can first observe that all three vector components $x$, $y$, $z$ of the momentum equation contributions are almost superimposed thereby confirming the isotropic nature of the HIT flow. Note that all these terms are averaged during steady turbulence for which averaged enstrophy and turbulent kinetic energy are almost constant [18].

As expected, the resolved turbulent stress and pressure terms are the most important quantities over the whole wavenumber range and these terms increase when the filtering size tends to the DNS resolution on the right part of the plot. However, the SGS turbulent stress terms, which are generally the only ones modeled, are clearly not the only important terms: the three components of the SGS pressure are of the same order of magnitude. The previous analysis provided in Giauque *et al.*[18] indicates that the inertial zone for the HIT is located in $k/k_{min} \in [4; 20]$. At these scales, turbulent stress and pressure SGS terms are larger than the resolved viscous terms: both pressure and turbulent stress SGS quantities should thus be modeled. This is a major difference with the perfect gas EoS. Note that the SGS viscous terms remain negligible in this real gas analysis (as is also the case for the perfect gas analysis in Vreman *et al.*[186]).

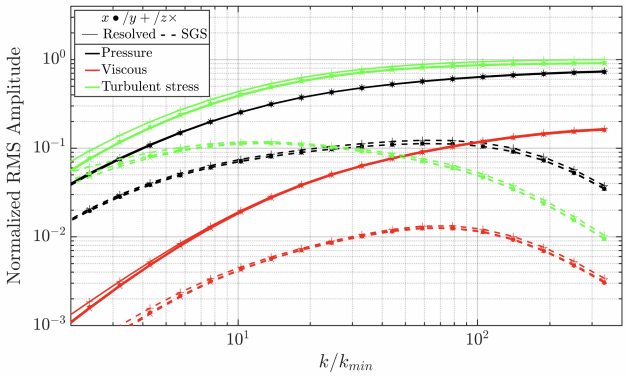


Figure 6.24: RMS amplitude of resolved and SGS terms in equation (3.12) for the real gas HIT case. (from [21])

Figure 6.25 shows the same plot for the mixing layer at convective Mach number 2.2 ($M_c = 2.2$). Consistently with the HIT configuration, the resolved turbulent stress and pressure terms are the most important whereas the SGS viscous terms remain negligible. Since the mixing layer is not isotropic, the three vector components are different at the largest scales but they tend to superimpose as the filter size diminishes leading to isotropic small scales dynamics. Results are averaged over each self-similar period and steadiness is well achieved.

Erlebacher et al. [187] suggest that SGS pressure terms, which are related in that case to the trace of the SGS turbulent stress tensor, can be neglected for a turbulent Mach number satisfying $M_t < 0.6$. Our real gas results show the importance of SGS pressure terms even at $M_t \approx 0.4$ (corresponding to $M_c = 1.1$) where their amplitudes are similar to resolved viscous terms at the end of the inertial zone around $k/k_{min} \approx 20$ (See Vadrot et al. [181]). At $M_c = 2.2$, the turbulent Mach number becomes larger ($M_t \approx 0.67$) and the normalized amplitude of SGS pressure terms increases, reaching the same order as SGS turbulent stress terms. The amplitude is also closer to the one of the HIT configuration where the turbulent Mach number is equal to $M_t = 0.8$.

In order to show the importance of the SGS pressure in the mixing layer at convective

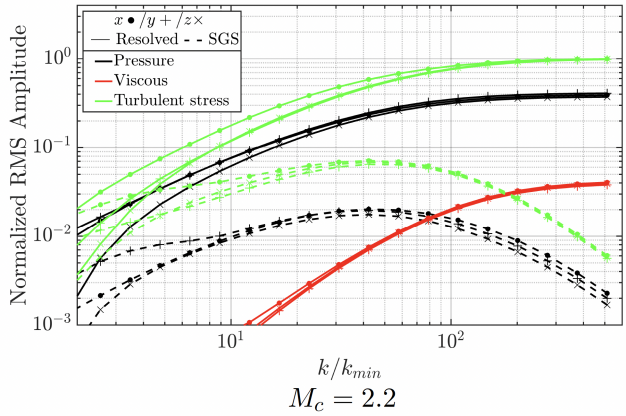


Figure 6.25: RMS amplitude of terms in equation (3.12) for the real gas mixing layer at $M_c = 2.2$. Results are averaged over the domain and over the self-similar period growth phase of the mixing layer. The turbulent Mach number (equation 6.19) averaged over the centerplane is equal to 0.67. The SGS viscous terms is very small and does not appear on the plot. (from [21])

Mach number 2.2, Figure 6.26 displays the z-centerplane contours colored by both fluxes of SGS pressure (on the left) and SGS turbulent stress tensor (on the right) for the mixing layer at Mc = 2.2, $\bar{\Delta}/\Delta_{DNS} = 8$ and $\tau = 6000$ (which corresponds to the end of the DNS self-similar period): similar orders of magnitude are observed.

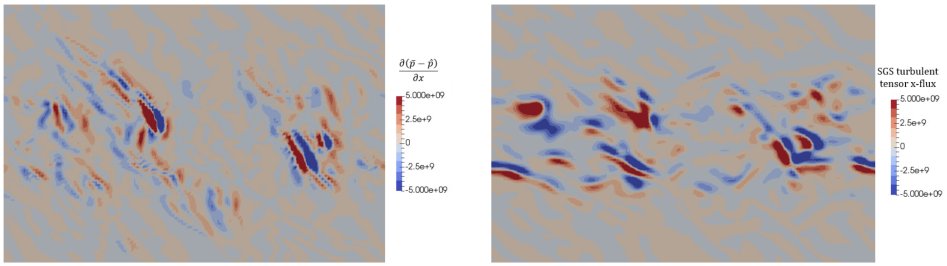


Figure 6.26: z-centerplane contours colored by (left) SGS pressure and SGS turbulent stress tensor fluxes for the mixing layer at Mc = 2.2 and $\bar{\Delta}/\Delta_{DNS} = 8$ in the x-direction. Results are plotted at $\tau = 6000$. (from [22])

To further illustrate the influence of the EoS on the amplitude of SGS terms, the FC-70 HIT is also computed (in a purely numerical experiment) using the perfect gas EoS. The results, reported in Giauque et al. [18], are used to compare the physical properties of turbulence in real and perfect gas flows. DNS results are explicitly filtered and analyzed. Resolved and SGS terms are then averaged during steady turbulence for which averaged enstrophy and turbulent kinetic energy are almost constant.
Figure 6.27 show the RMS amplitudes of resolved and SGS terms in equations 3.12 . For the momentum equation, only the SGS turbulent stress term is significant when compared to resolved terms. It should be noted that even if in this case the SGS pressure is negligible, this result should not be generalized too rapidly. Indeed, it can be shown that in the perfect gas case, the SGS pressure term is proportional to the trace of the SGS turbulent stress tensor ($\bar{p} - \hat{p} = -\frac{\gamma-1}{2} t_{ii}$). Even though the trace of the SGS turbulent stress tensor has been found negligible by previous authors [187], largely compressible flows may contradict this statement. Yet in our case, $\gamma = 1.008$ is very close to unity leading to a very small SGS pressure term regardless of the amplitude of the trace of the SGS turbulent stress tensor.

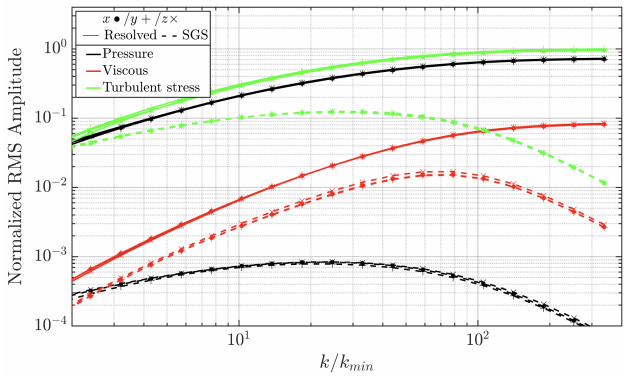


Figure 6.27: RMS amplitude of resolved and SGS terms in equation (3.12) for the perfect gas HIT case. (from [21])

### 6.5.3 A-priori analysis of existing SGS models - focus on eddy viscosity based models

The models studied here are gathered in Table 6.28. The theoretical context of static and dynamic SGS models in LES is recalled in section 3.4. The reader should refer to the original publications for further details.

| Model type | Name | Model for $t_{ij}$ | Model constant | |
|---|---|---|---|---|
| | | | PG | RG |
| Eddy-viscosity | Smagorinsky | $-2(C_s\Delta)^2\overline{\rho}F_s(\widetilde{\boldsymbol{u}})\widetilde{S}_{ij}$ | $C_s = 0.165$ | $C_s = 0.165$ |
| | D-Smagorinsky | $-2(C_s\Delta)^2\overline{\rho}F_s(\widetilde{\boldsymbol{u}})\widetilde{S}_{ij}$. | $C_{ds} = 0.324$ | $C_{ds} = 0.302$ |
| | Vreman | $-2(C_v\Delta)^2\overline{\rho}F_v(\widetilde{\boldsymbol{u}})\widetilde{S}_{ij}$ | $C_v = 0.26$ | $C_v = 0.26$ |
| | D-Vreman | $-2(C_{dv}\Delta)^2\overline{\rho}F_v(\widetilde{\boldsymbol{u}})\widetilde{S}_{ij}$ | $C_{dv} = 0.256$ | $C_{dv} = 0.279$ |
| | WALE | $-2(C_w\Delta)^2\overline{\rho}F_w(\widetilde{\boldsymbol{u}})\widetilde{S}_{ij}$ | $C_w = 0.5$ | $C_w = 0.5$ |
| | D-WALE | $-2(C_{dw}\Delta)^2\overline{\rho}F_w(\widetilde{\boldsymbol{u}})\widetilde{S}_{ij}$ | $C_{dw} = 0.4$ | $C_{dw} = 0.372$ |
| Gradient | Gradient | $\overline{\rho}\mathcal{G}_{ij} - 2(C_g\Delta)^2\overline{\rho}F_s(\widetilde{\boldsymbol{u}})\widetilde{S}_{ij}$ | $C_g = 1.0$ | $C_g = 1.0$ |
| | D-Gradient | $\overline{\rho}\mathcal{G}_{ij} - 2(C_{dg}\Delta)^2\overline{\rho}F_s(\widetilde{\boldsymbol{u}})\widetilde{S}_{ij}$ | $C_{dg} = 0.096$ | $C_{dg} = 0.112$ |
| | Liu Gradient | $c\overline{\rho}\mathcal{G}_{ij}$ | NA | NA |
| | Mod. Gradient | $2(C_{mg}\Delta)^2\overline{\rho}k_{SGS}(\widetilde{\boldsymbol{g}})(\frac{\widetilde{\mathcal{G}}_{ij}}{\widetilde{\mathcal{G}}_{kk}})$ | $C_{mg} = 1.0$ | $C_{mg} = 1.0$ |
| | D-Mod. Gradient | $2(C_{dmg}\Delta)^2\overline{\rho}k_{SGS}(\widetilde{\boldsymbol{g}})(\frac{\widetilde{\mathcal{G}}_{ij}}{\widetilde{\mathcal{G}}_{kk}})$ | $C_{dmg} = 0.543$ | $C_{dmg} = 0.608$ |

Figure 6.28: List of the models used in this study (from [23])

A selective tool to evaluate the prediction of a model is the $R^2-$score between the model and the DNS. It represents the proportion of variance of a variable $Y$ that is explained by the variable $f$ predicted by the model. It is defined as:

$$R^2 = 1 - \frac{\sum(y_i - f_i)^2}{\sum(y_i - \mu_Y)^2}, \tag{6.25}$$

If $R^2 = 1$, the prediction is exact. It is worth noting that a model that predicts a constant value equal to the mean value of $Y$ ($\mu_Y$) will have a $R^2-$score of zero. The coefficient of determination is here computed using the DNS as the exact data set and the modeled component $t_{xy}$ as the predictions. Since the configuration under study is isotropic with a mean flow equal to zero, the average of $t_{xy}$ is almost zero. As a result, a model that predicts a constant null SGS turbulent stress tensor (no-model case) will have a $R^2-$score of zero. Coefficients of determination are displayed in Figure 6.29. All $R^2-$scores are negative showing that the models make strong errors in the local determination of the SGS Reynolds turbulent stress tensor. Very large negative values of the $R^2-$score especially go with a strong error in the computation of the variance of the term to be modeled. Only the Smagorinsky, Vreman, D-Vreman and WALE models have coefficient of determination that are above -2. Those four models even achieve $R^2-$scores above -1 but in the PG case only. It is worth noting that Perfect gas (PG) coefficients are always superior to Real Gas (RG) ones. The results in this section show that Gradient models which have significant correlation levels also have very poor coefficient of determination which implies that if the trend of the SGS Reynolds turbulent stress tensor is correctly recovered, its amplitude (i.e. the variance of the term) is not correctly captured.

As detailed previously, the eddy-viscosity models are best fitted to predict the functional character of the turbulence than its structural properties. A less structure-oriented way to evaluate the models' predictions is to compute the space probability density function (PDF) for the tensor component $t_{xy}$ at hand.

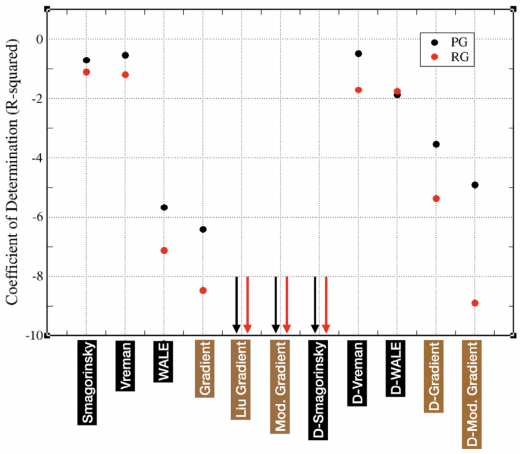


Figure 6.29: Coefficient of determination ($R^2-$score) for Perfect Gas (PG) and Real Gas (RG) cases as a function of the model used for predicting the SGS Reynolds turbulent stress tensor component $t_{xy}$. Arrows correspond to determination coefficients lower than -10. (from [23])

Figure 6.30 examines the PDF of $t_{xy}$ for the different eddy-viscosity based models as well as for the DNS solution. The $x-$axis is normalized with the RMS value of $t_{xy}$ taken from the respective PG and RG DNS. The first observation from Figure 6.30 is the differences between the PDF of $t_{xy}$ in the DNS that arise from the change in the EoS. Indeed, in the RG flow, the PDF almost follows a Laplace distribution for terms smaller than the variance. This shows that the amplitude distribution could be predicted by a model following a Laplace motion description. This is quite different in the PG case in which the distribution much more closely follows the Gaussian distribution.
As far as the models are concerned, for terms smaller than the DNS variance, one should distinguish between the PG and RG cases. For the PG case, all eddy-viscosity based models (except the D-Smagorinsky model) perform fairly well and manage to reproduce quite accurately the space distribution of $t_{xy}$. Better than all others the D-WALE model matches the PDF in the DNS within a few percents. For large values of $t_{xy}$ (beyond the DNS variance), a clearer ordering of the models appear with Vreman and Smagorinsky models outperforming WALE, D-WALE and D-Smagorinsky models.
For the RG case, given the different shape of the PDF, no model accurately captures the shape and levels of the distribution. For moderate terms, smaller than the variance in the DNS, only the D-WALE model manages to recover the probability of occurrence of very small terms. All other models tend to underestimate this probability and over-estimate that of large terms. For terms larger than the DNS variance, this trend is confirmed. All models tend to overestimate by an order of magnitude the probability of occurrence of $t_{xy}$ having an amplitude equal to five times the DNS variance.

To better compare PDFs, Figure 6.31 presents the normalized L2 errors (computed using Eq 6.26 for $n = 1$) with respect to the DNS for the different models and EoS. As $n$ increases, the normalized L2 error focuses more on the capability of the model to accurately predict the probability of occurrence of large $t_{xy}$ terms.

$$L2_{err}(n\sigma) = \frac{\int_{-10\sigma}^{-n\sigma}[\mathrm{PDF}_{\mathrm{DNS}}(x) - \mathrm{PDF}_{\mathrm{model}}(x)]^2 dx + \int_{n\sigma}^{10\sigma}[\mathrm{PDF}_{\mathrm{DNS}}(x) - \mathrm{PDF}_{\mathrm{model}}(x)]^2 dx}{\int_{-10\sigma}^{-n\sigma}\mathrm{PDF}_{\mathrm{DNS}}(x)^2 dx + \int_{n\sigma}^{10\sigma}\mathrm{PDF}_{\mathrm{DNS}}(x)^2 dx} \tag{6.26}$$

Figure 6.32 for the RG EoS, displays $t_{xy}$ for the models providing the predictions closest

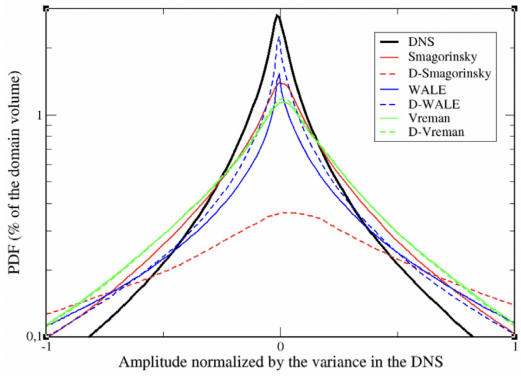


(a)

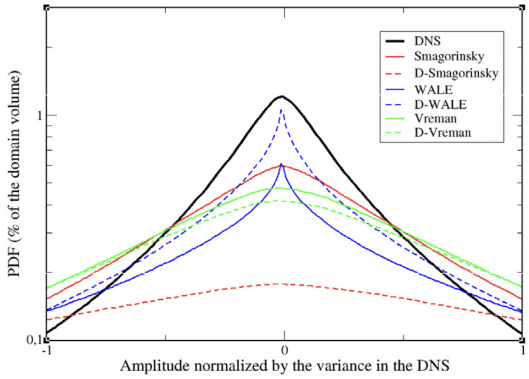


(b)

Figure 6.30: Eddy viscosity models : Comparison of $t_{xy}$ PDF between models and DNS. (a) Perfect Gas, (b) Real Gas. (from [23])

to the DNS. A lack of correlation between the models and the DNS can be observed in Figure 6.32. For example, a strong positive region at the left-bottom corner ($x \approx 0.25$, $y \approx 0.2$) is missed by all models. Yet, in that case, extra filaments of positive $t_{xy}$ are present in the modeled fields only. This is one of the possible reasons for the general overestimation of the spectrum of $t_{xy}$ in the RG case.

To summarize the results and rank all studied models, Figure 6.33 is proposed which depicts the following picture. As one could imagine, regardless of the EoS, only gradient-based models significantly correlate with the SGS Reynolds turbulent stress tensor extracted from the DNS with correlation level reaching 0.9. Yet, even for those models the dynamic of the SGS term is not well captured locally and coefficients of determination remain negative. This conclusion also applies indiscriminately of the EoS.
Regarding the capability of models to recover the PDF of the modeled term, differences between the PG and RG cases appear. The general picture is that of a worsening of the results in the RG case. Only the Smagorinsky and D-WALE models achieve fair to good results in that case. For the D-WALE model, this mostly comes from its capability to accurately predict the probability of small values of $t_{xy}$ in the 3D field. For Smagorinsky, it comes from its better prediction of the probability of occurrence of large values of $t_{xy}$.
Finally, the prediction of 2D-spectrum of $t_{xy}$ is also worsened in the EoS change. All Eddy-viscosity based models (except the D-Smagorinsky model) achieve comparable results for the RG case and all tend to overestimate the energy of large scale structures of $t_{xy}$.

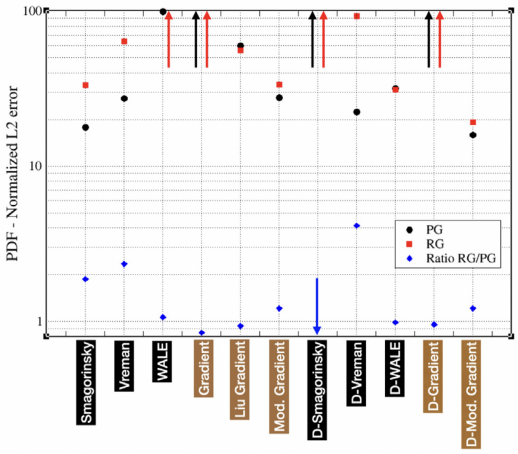


Figure 6.31: PDF - Normalized L2 error (in %) and Ratio of L2 errors as a function of the EoS for an integration limit equal to $\sigma$ (see Equation 6.26). Red and black arrows respectively correspond to errors larger than 100% for the RG and PG EoS cases. Blue arrow corresponds to a ratio of the error RG over PG smaller than 0.8. (from [23])

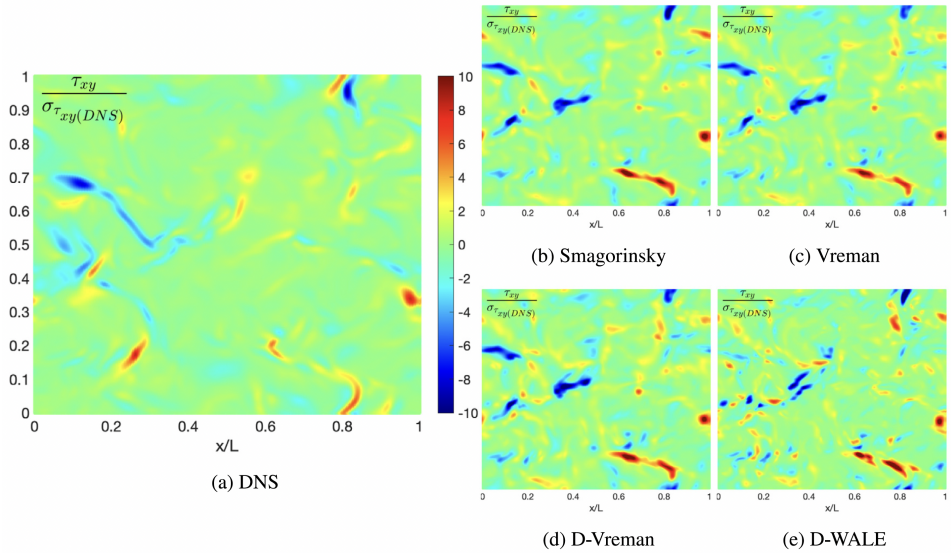


Figure 6.32: $t_{xy}$ in the $(x, y)$ plane. RG case. Turbulent SGS viscosity models providing spectrum closest to the DNS. (from [23])

Correlation criteria : - if ($P < 0.3$); o if ($0.3 < P < 0.8$); + if ($0.8 < P$).
R-Squared criteria : - - if ($R_2 < -2$); - if ($-2 < R_2 < 0$).
3D-PDF criteria : – if ($L_2 > 100\%$); - if ($50\% < L_2 < 100\%$); o if ($30\% < L_2 < 50\%$); + if ($10\% < L_2 < 30\%$); ++ if ($L_2 < 10\%$).
2D-spectrum criteria : + if both spectrum collapse ; o if the error is less than an order of magnitude; - or - - if the error is larger than an order of magnitude.

| Model type | Model | Correlation | | R-Squared | | 3D-PDF | | 3D-PDF large values | | 2D-spectrum | |
|---|---|---|---|---|---|---|---|---|---|---|---|
| | | PG | RG | PG | RG | PG | RG | PG | RG | PG | RG |
| Eddy-viscosity | Smagorinsky | - | - | - | - | + | + | + | o | o | o |
| | D-Smagorinsky | - | - | - - | - - | - | - | - - | - - | - - | - - |
| | Vreman | - | - | - | - | + | + | + | - | + | o |
| | D-Vreman | - | - | - | - | + | + | + | - | + | o |
| | WALE | - | - | - - | - - | + | + | - | - - | - | - |
| | D-WALE | - | - | - | - | ++ | ++ | o | o | - | o |
| Gradient | Gradient | + | + | - - | - - | o | o | - - | - - | - | - |
| | D-Gradient | + | + | - - | - - | + | o | - - | - - | - | - |
| | Liu Gradient | + | + | - - | - - | - - | - - | - | - | - - | - - |
| | Mod. Gradient | o | o | - - | - - | - - | - - | + | o | - - | - - |
| | D-Mod. Gradient | o | o | - - | - - | - - | - - | + | + | - - | - - |

Figure 6.33: Summary of the performance associated to the models used in this study. (from [23])

### 6.5.4 A-posteriori evaluation of existing SGS models against Cambridge measurements

The configuration under study is an annular cascade tested at Cambridge University by Baumgärtner, Otter and Wheeler [188]. This cascade is composed of eight stator blades. As shown in Figure 6.34, the numerical configuration comprises a single sector of angle 45°.
The radius of the hub is 15mm and the radius of the casing is 20mm which leads to a blade

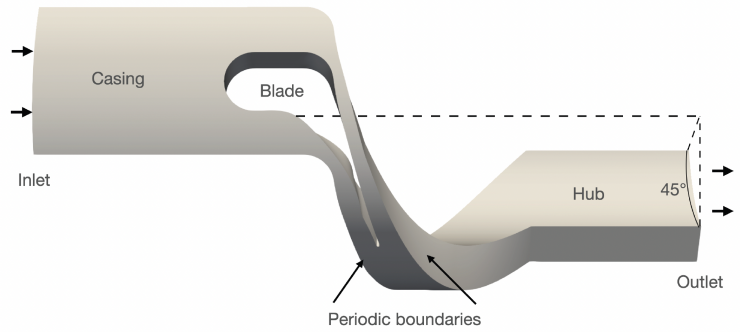


Figure 6.34: Annular cascade configuration (from [24])

span of 5mm. In the simulation, the inlet is set at approximately one chord upstream of the leading edge and the outlet is set at approximately two chords downstream of the trailing edge in the axial direction. Non reflecting boundary conditions are used at the inlet and outlet [77]. Without knowledge regarding the inlet turbulence levels (not measured in the experiment), it has been decided to run the LES without turbulence injection and to assess the impact of this inlet condition in the RANS simulations. The fluid is R134a, a real gas commonly used in industrial systems as a working fluid.
Computations are distributed with Message Passing Interface (MPI) on 15360 cores using the IRENE High Performance Computing (HPC) facilities at Commissariat à l'Energie Atomique - Très Grand Centre de Calcul (CEA-TGCC). Figure 6.35 shows an isosurface of the instantaneous Q-criterion [189] colored by the Mach number. The development of the turbulent boundary layer on the suction side of the blade is identified, along with its strong interaction with the shock wave that form close to the trailing edge.

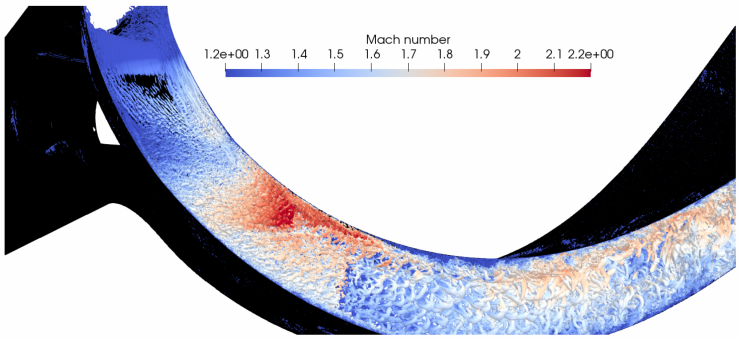


Figure 6.35: **LES** – Suction side of the stator: Isosurface of the instantaneous Q-criterion ($Q * \Delta_x^2 = 250$) colored by the Mach number (from [24])

To validate the numerical approach followed by the authors to study the real gas flow in the complex geometry of the Cambridge University annular turbine cascade, RANS and LES results are compared to experimental measurements obtained at the casing and in the

wake of the blade at mid-span [188]. Figure 6.36 illustrates and localizes on an arbitrary axial cut in the domain the available measurements to which the numerical results are compared. The azimuthal pitch later used to display the comparisons and taking into account the periodicity of the domain is also defined.
In the following, $\sigma$ represents the experimental uncertainty applied to the different measured quantities. To mimic this uncertainty and have a sense of the dynamics around the converged mean quantities obtained in the LES, the RMS is also displayed for each quantity at each location.

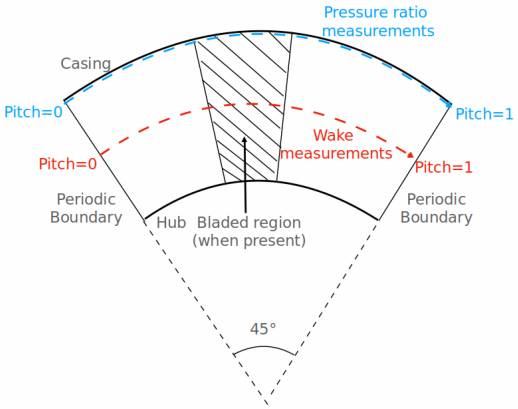


Figure 6.36: Sketch of an arbitrary axial cut in the domain featuring the boundary conditions, the location of the available measurements and the pitch definition. (from [24])

#### 6.5.4.1 Comparison with casing measurements

Figures 6.37 and 6.38 compare the evolution of the static pressure at the casing as a function of the pitch in the experiment to the data obtained by RANS and LES. Overall, the pressure ratio is expected to decrease as one moves to larger z values following the expansion of the flow along the stator blade. This expansion is also linked to the evolution of the local velocity so that it does not occur evenly as a function of the pitch. The flow accelerates more quickly on the suction side (on the left of the bladed regions) so that the pressure is expected to decrease more sharply on that side of the blade. From Figure 6.37, it can be seen that upstream of the trailing edge (located at $z \approx 9$mm), a very good agreement is reached between experimental measurements and numerical results. As one gets closer to the transition region of the suction side boundary layer ($z = 7.2mm$ : bottom right figure), RANS results obtained with inlet turbulence injection start to diverge from those obtained without. RANS results obtained without turbulence injection are closer to the experimental measurements and LES results.
This phenomenon is further amplified downstream as clearly shown by Figure 6.38. Overall, numerical profiles are slightly above experimental ones. Yet results obtained without inlet turbulence injection are slightly closer to the experiment. More specifically, at $z = 8.1mm$ pressure at the suction side (left side of the curve) does not drop in the simulations as much as it does in the experiment. It suggests that the mean tangential velocity in this region is underestimated in the numerics hinting to some degree of error in the prediction of the turbulent boundary layer profiles. Yet LES and RANS results remain very close from each other at this location. Away from the blade (beyond a pitch of 0.5), LES and RANS obtained without inlet turbulence injection (ITI) are closer to the experimental measurements. At $z = 9mm$, one sits at the trailing edge. At this location the sharp decrease of the static pressure in the wake is missed by the experiment. Again, RANS and LES obtained without

ITI perform better and agree very well with each other. The same comments can be given downstream of the blade at $z = 9.5mm$ and $z = 10.9mm$. RANS and LES results without ITI only depart from each other in the free stream for pitch values comprised between 0.8 and 1. In this region the scattering of the experimental results is large making it difficult to determine whether LES or RANS without ITI performs better.

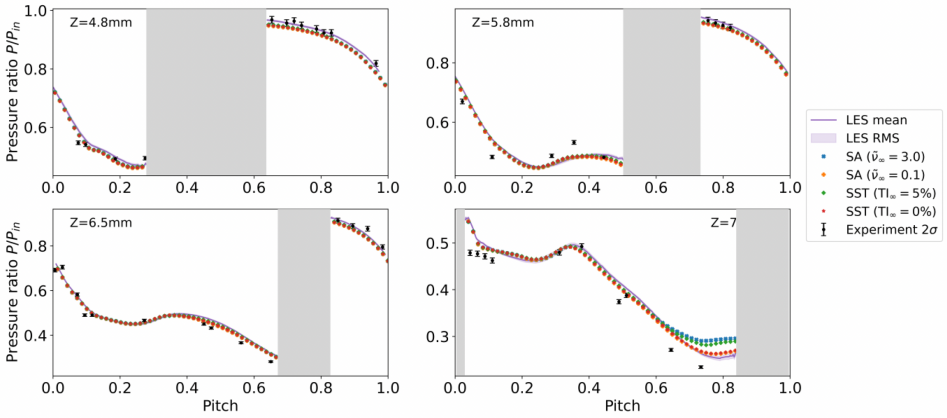


Figure 6.37: Experimental measurements of static pressure ratio at the casing (R=20mm), upstream of the trailing edge compared to RANS and LES results. Grayed areas correspond to the bladed regions. (from [24])

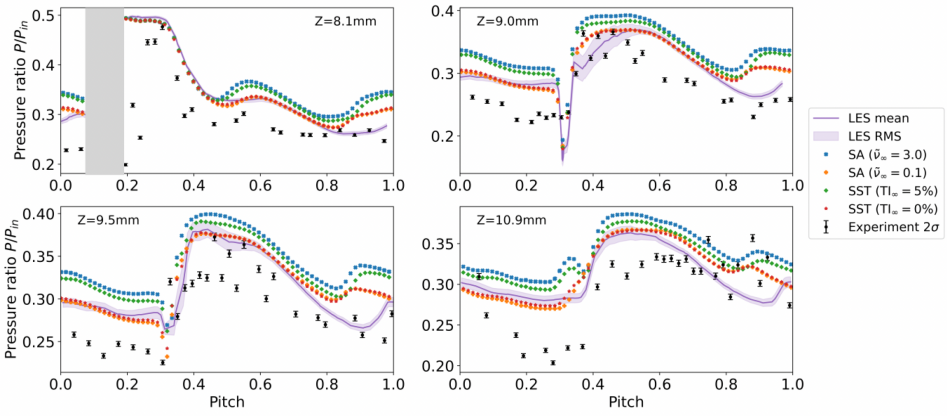


Figure 6.38: Experimental measurements of static pressure ratio at the casing (R=20mm), at the trailing edge and downstream compared to RANS and LES results. Grayed areas correspond to the bladed regions (from [24])

#### 6.5.4.2 Comparison with wake measurements

In the wake of the blade, probes measuring the stagnation pressure induce a bow shock [190], which has to be corrected for in the post-processing of the simulation results by computing the shock corrected total pressure:

$$p_{t,\text{shock}} = p_t \frac{(\gamma+1)Ma^2}{(\gamma-1)Ma^2+2}^{\frac{1}{\gamma-1}} \frac{(\gamma+1)}{2\gamma Ma^2-(\gamma-1)}^{\frac{1}{\gamma-1}}. \tag{6.27}$$

where a constant value for $\gamma = 1.07$ is chosen to match the treatment done in the experiment. Note that he assumption of a normal bow shock is only valid when the probes are aligned with the flow direction. Figure 6.39 shows that all simulations without turbulence injection were able to predict the azimuthal location and total pressure ratio of the blade wake within the experimental uncertainty. However, there is a slight displacement between numerics and experiment in the position of the shock at pitch$\approx$ 0.25 as well as a discrepancy on the total pressure level in the freestream region of the flow. This might be due to either or both of the following explanation arguments: (i) the inability of the numerical models to accurately describe the interaction of the oblique shock with the boundary layer which leads to a slight misprediction in the trailing edge shock angle or (ii) a slight misalignment of the probes in the experimental measurements.
In summary, probes measuring stagnation pressure in the wake of the blade induce a bow shock, which, when corrected in post-processing using a shock corrected total pressure formula, is found to match fairly well with numerical simulations. Slight discrepancies in shock position and total pressure levels may be attributed to challenges in modeling oblique shock / boundary layer interactions or a slight misalignment of experimental probes.

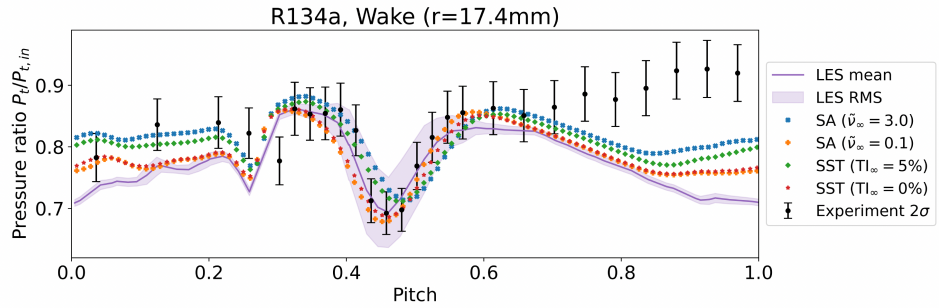


Figure 6.39: Experimental measurements of shock corrected total pressure ratio in the wake region compared to RANS and LES results (from [24])

Overall, RANS and LES results obtained without ITI agree fairly well with the experimental measurements especially before the boundary layers transition, in the wake and even more specifically on the pressure side of the wake where velocities are slightly lower leading to a smaller drop of the static pressure when compared to the suction side.

#### 6.5.4.3 Presence of a corner separation

Figures 6.40 (a) and (b) focus on the suction side and trailing edge regions. In these figures, the flow comes from the right and goes toward the top-left of the image. Streamlines originating from the two visible white lines along the hub and suction side of the blade are also displayed and colored by the magnitude of the velocity. In Figure 6.40 (a), it can be seen that in the RANS results, streamlines originating from the suction side quickly join those from the hub leading to a single well defined stream-tube. Streamlines then tend to rotate along the longitudinal axis without much dispersion. These observations are consistent with the presence of a vortical structure originating at the corner between the hub and suction side of the blade. In the LES results ( Figure 6.40 (b) ), streamlines originating from the suction side quickly move away from the wall and display large velocity values. In parallel those originating from the hub also move away from the wall. Both streamline systems keep significantly different velocities but intertwine with each other above the blade-hub corner in the region characterized by the boundary layer - shock wave interaction. Once the trailing edge is passed, they progressively tend to form a single structure that can be evidenced by the computation of the Q-criterion in the flow. Since at the time of the writing it cannot be validated by experimental measurements, the presence of this corner separation still has to

be confirmed by future studies.

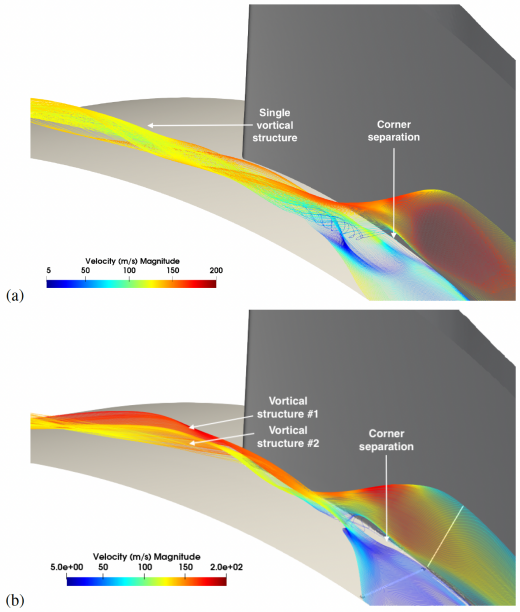


Figure 6.40: Visualization of the corner separation at the hub: Streamlines colored by the velocity magnitude in (a) RANS without inlet turbulence injection and (b) LES. The bulk flow goes from right to left. (from [24])

#### 6.5.4.4 Analysis of the losses

To more precisely quantify the amount of losses due to the boundary layers, the wake and the vortical structures related to the corner separation, the following loss coefficient is introduced:

$$\zeta_{\text{loss}}(x) = \left\langle \frac{H - H_s}{H_0 - H_s} \right\rangle_x ,$$

where $H$ is the specific enthalpy, $H_0$ is the specific total enthalpy, $H_s$ is the specific isentropic enthalpy and $< . >_x$ stands for the averaging operator at section $x$. Since $(H - H_s)(x) = \int_{ref}^{x} (Tds)$ where $s$ is the entropy, this ratio compares the share of enthalpy related to entropy to the sum of itself with the available kinetic energy. In regions where the cross section does not change, it can only grow and accounts both for the entropy generation at the hub and casing walls and in the wake.
Table 6.8 presents the values obtained by RANS and LES for $\zeta_{loss}$ at some sections of interest. To determine the influence of the corner separation, $\zeta_{\text{loss}}(x)$ is both averaged over the full section or at the mid-span radius only. Regardless of the extraction location, levels

Table 6.8: Comparison of the loss coefficient $\zeta_{loss}$ at the trailing edge and at the outlet obtained by RANS and LES.

| Numerical method (extraction location) | $\zeta_{loss}$ at trailing edge | $\zeta_{loss}$ at outlet | % of $\zeta_{loss}$ after blade |
|---|---|---|---|
| RANS (whole span) | 0.2831 | 0.3815 | 34.75 |
| LES (whole span) | 0.2574 | 0.3446 | 33.88 |
| RANS (midspan) | 0.2546 | 0.3153 | 23.84 |
| LES (midspan) | 0.2269 | 0.2905 | 28.03 |

gathered at mid-span are systematically 15% lower as they ignore losses at the hub and casing. RANS tends to predict loss levels 10% larger than LES. Yet when the whole span is considered, both methods agree on the share, equal to roughly 33%, associated to the unbladed region of the flow after the trailing edge. This agreement may be incidental given the large difference in the turbulence modeling used in both methods and RANS does not fully agree with LES on the share associated with the wake but places it around 25%. Even though the computation method for $\zeta_{loss}$ is slightly different, it is interesting to note however that these results confirm and extend the original findings of Baumgartner *et al.* [190].

## 6.6 Modelling turbulence in real/dense gas flows using Machine learning

### 6.6.1 Artificial Neural Networks (ANNs)

Artificial neural networks (ANNs) are inspired by biological neural networks, comprising basic units known as artificial neurons. These neurons are arranged in layers and interconnected, with transfer functions governing the inputs and outputs of neurons described by simple mathematical functions. ANNs consist of two main components: parameters and hyperparameters. Parameters are adjusted during the supervised training phase of the ANN using an error back-propagation mechanism, which involves computing the disparity between predicted and actual output values. On the other hand, hyperparameters are predetermined and significantly influence the network's performance. The parameters of the network consist of weights (w), which modulate the strength of connections between neurons, and biases (b), which are added to the computed activation as follows:

$$Y = \phi(wX + b)$$

The activation function, denoted as $\phi$, varies between layers in an artificial neural network (ANN), except for the output layer, which typically employs a linear function for regression tasks. This activation function, alongside other hyperparameters, defines the characteristics of the ANN. Key hyperparameters include the number of layers, the varying number of neurons per layer, the activation function itself (e.g., Sigmoid, Tanh, ReLU), the method of data normalization (e.g., minimum/maximum or average/standard deviation), and the initialization technique for biases and weights (e.g., Xavier, He). Additionally, the optimizer (e.g., Adam, AdaGrad) plays a crucial role in error correction by adjusting biases and weights during backpropagation. The learning rate schedule, if not automatically determined by the optimizer, and the choice of loss function (e.g., mean square error) are also significant hyperparameters. Batch size, regularization techniques (e.g., L1, L2), and other related hyperparameters further influence the ANN's performance. The selection of optimal hyperparameters is essential for achieving the desired performance, and various methods, including empirical rules and database-specific considerations, are employed for their determination.

### 6.6.2 Modeling the SGS pressure in LES using ANN

The objective of this study is to develop a model for the Sub-Grid-Scale (SGS) pressure term, a crucial component in dense gas Large-Eddy Simulation (LES). Given the intricacy of this term, Artificial Neural Networks (ANN) are employed to uncover the relationships between the SGS term and the filtered or computable variables. ANN training utilizes a dataset comprising filtered DNS results from forced Homogeneous Isotropic Turbulence (HIT) and mixing layers at Mach numbers of 1.1 and 2.2. Specifically for the mixing layers, only self-similar temporal solutions are included in the dataset. To maintain Galilean invariance of the Navier-Stokes equations (as proposed by Speziale [191]) and enhance ANN prediction

accuracy, the filtered conservative variables are transformed into a new set of variables that satisfy Galilean invariance. This requirement imposes a mild constraint on the ANN to uphold Galilean invariance. Further elucidation on these constraints is provided in the subsequent section.
Once the filtered conservative variables undergo transformation, they serve as inputs to the ANN, which then predicts the SGS pressure term. Throughout the training phase, data extracted from filtered DNS are fed into the ANN. Subsequently, the error between predicted and actual values is computed and utilized to adjust the weights and biases of the ANN through backpropagation.

#### 6.6.2.1 Design of the input data

The inputs of the model are chosen among available variables, taking into account the nature of the SGS pressure term to assess their relevance in a preliminary screening process. The equation below shows the link of the SGS pressure term with thermodynamic quantities

$$\begin{aligned}\overline{p}-\widehat{p}=&\overline{\left(\frac{r\overline{\rho}\widetilde{T}}{1-b\rho}\right)}-\frac{r\overline{\rho}\widehat{T}}{1-b\overline{\rho}}+\overline{\left(\frac{r(\rho'\overline{T}+\overline{\rho}T')}{1-b\rho}\right)}\\&+\sum_{i=2}^{5}\left[\overline{\left(\frac{A_i\overline{\rho^i}+B_i\overline{\rho^iT}+C_i\overline{\rho^ie^{-\frac{kT}{T_c}}}}{(1-b\rho)^i}\right)}\right.\\&\qquad+\overline{\left(\frac{\overline{\rho^i}Q_i'(T)+\rho^{i'}\overline{Q_i(T)}}{(1-b\rho)^i}\right)}\\&\qquad\left.-\frac{A_i\overline{\rho}^i+B_i\overline{\rho}^i\widehat{T}+C_i\overline{\rho}^ie^{-\frac{k\widehat{T}}{T_c}}}{(1-b\overline{\rho})^i}\right]\end{aligned}$$

(the computable temperature $\hat{T}$ and the computable density $\hat{\rho}$). Moreover, this equation depends on the filtered temperature $\bar{T}$ which is itself computed by reversing the caloric EoS which introduces a kinetic energy dependence. The set of inputs should thus contain thermodynamic and kinetic energy information. The design of the models must also respect the physical constraints of the problem. The most simple way to weakly impose physical constraints to ANN models is to apply the constraints over the inputs. For SGS models, Speziale [191] demonstrates the necessity to respect Galilean invariance comprising spatial rotations (which implies isotropy) and translations in space and time. To this aim, the invariants of the velocity gradient are chosen to provide the necessary kinetic energy source of information [192].
The following set of data is therefore chosen as input to the ANN:

$$\left[\bar{\rho};\hat{T};\hat{p};\bar{\rho}\tilde{E};||\nabla(\bar{\rho})||;||\nabla\left(\hat{T}\right)||;||\nabla(\hat{p})||;||\nabla\left(\bar{\rho}\tilde{E}\right)||;\Delta(\bar{\rho});\Delta\left(\hat{T}\right);\Delta(\hat{p});\Delta\left(\bar{\rho}\tilde{E}\right);I_1;I_2;I_3\right]$$

where

$$I_1=tr\left(\nabla(\vec{u})\right),$$

$$I_2=\frac{1}{2}\left[tr\left(\nabla(\vec{u})\right)^2-tr\left(\nabla(\vec{u})\nabla(\vec{u})^T\right)\right]\text{ and}$$

$$I_3=det\left(\nabla(\vec{u})\right).$$

Note that in this set, inputs which depend on differentiation (gradients, Laplacians and invariants) are normalized with the a priori filter size $\bar{\Delta}$ in order to not depend on the difference of resolution and filtering of each configuration (HIT and mixing layers). This set of 15 inputs satisfies the constraints of the physical problem and contains diverse variables

correlated to the SGS pressure. The highest rate of correlations are obtained for the norm of the thermodynamic variables gradients for the mixing layers and for the thermodynamic variables themselves and their Laplacians in the forced HIT flow. The fundamental difference between the mixing layer and the forced HIT is the presence of a mean flow. This mean flow modifies the dynamics of the SGS.

#### 6.6.2.2 Design of the ANN

The ANN is designed using the Scikit-Learn library [193]. Since the database contains a large amount of data (roughly 500 Million samples), a parallel computing method is employed to train the ANN. An optimization of the ANN hyperparameters is then performed, especially using grid search methods. The parallelization of the ANN answers two main issues: large size networks (in deep learning) and large databases. In the present work, since the training of the ANN on several configurations using all the available data raises memory issues, a process using data parallelism is implemented. To enable the loading of a large amount of data, the Dask library [194] is used in complement to the Scikit-Learn library. Sklearn and Dask are both open-source Python libraries. The first one provides machine learning tools (ANN, random forest, classification, regression and clustering algorithms, ...) and the second one enables to manage large database by distributing the data over several processors. It is compatible with NumPy, Pandas and Sklearn.

The parallelism of the ANN's training is described in Figure 6.41. The database comprising the three filtered DNS is first read with the Dask library. Dask creates a Python object named a dataframe which is divided into partitions. The three dataframes are then gathered into a single one. Data are scaled using the most popular average / standard deviation normalization computed over the entire database and randomly mixed to prevent any bias in the ANN learning. The transformed database is divided in two: the training part, which contains 80% of the database, and the testing part, which contains 20% of the database. The testing part is used to evaluate the ANN performance over elements which were not included in the training set. At the first epoch, an identical ANN is replicated over each processor. Each partition is distributed over one processor and is passed into each ANN. Once all ANN have finished the first epoch, weights and bias are aggregated. The averaged ANN is replicated over each processor. The process continues until the end of the training phase. This method is simple and enables a rapid convergence to the optimal ANN when dealing with large databases.

**HSIC analysis: principles**

The objective of the so-called Hilbert-Schmidt Independence Criterion (HSIC) analysis is to fully exploit grid search results by computing HSIC coefficients which measure the independence between two probability distributions. The present work is based on Novello et al. [195]. The authors first evaluate the probability distribution of hyperparameters among arms randomly selected by the hyperparameters search method (denoted P (hyperparameter)) and then compute the probability distribution for an ANN of being among the best decile networks (the 10% of the best ANN). This last probability is denoted P (hyperparameter|Z), where Z is a random variable which is equal to one if the ANN is among the best decile. By measuring the dependency between the two probability distributions, HSIC coefficients provide a classification of the importance of hyperparameters. They also can be used to measure the independence of joint probability distributions. That way, one can emphasize interactions between hyperparameters.

The computation of the HSIC coefficients is done in the post-processing step using the hyperband search results. However, the three aforementioned algorithms introduce a bias in

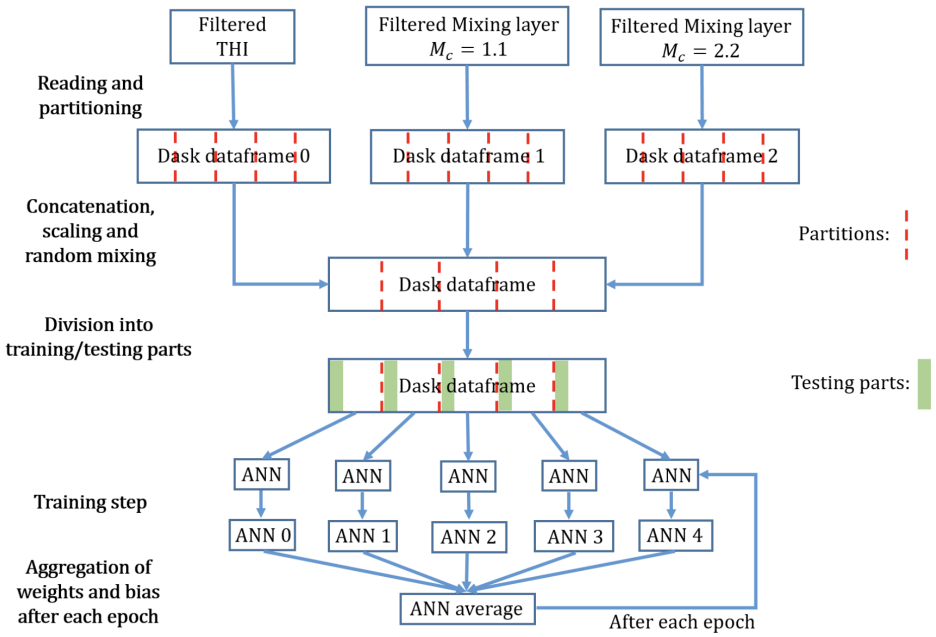


Figure 6.41: Multi-processors training strategy for the ANN (from [22])

the results because ANN are not equally trained. The best ANN are indeed trained longer and their scores tend therefore to be much improved with respect to the first eliminated ANN. To avoid this issue, classic grid searches are performed: all ANN are equally trained and HSIC coefficients are not influenced by the elimination process. The method is applied to the grid searches relevant for the design of the SGS pressure model. All ANN are trained during 10 epochs which enables to reach a good compromise between the convergence and the computational time. This number of epochs can be seen as a low limit to reach convergence but this value has to be analyzed in lights of the size of data. Knowing that the grid search database (smaller than the entire database) contains 4 million elements, this choice of 10 epochs corresponds to 40 million ANN predictions.

**HSIC analysis: results**

Three different grid searches are performed. The first two ones are only performed over the mixing layer at Mc = 2.2. It has been indeed observed that this case is the most demanding one among the three configurations for the ANN to achieve good performance. The first grid search is performed over a small hyperparameters space which enables us to test all the possible combinations. The second grid search browses a large hyperparameters space. Only 750 randomly selected arms are tested over the 128 000 possibilities. The third grid search evaluates the same hyperparameters space using this time the three cases: both mixing layers and the forced HIT. The first grid search evaluates ANN comprising two hidden layers with a number of neurons varying from 25 to 100 with a step of 25. The other hyperparameters are the activation function and the optimizer yielding a small total number of explored ANN, equal to 96, which allows the computation of every single ANN.

Figure 6.42 displays the HSIC coefficients computed for simple PDF. Results show the greater importance of the number of neurons in the first two layers but also hints at the importance of the regularization coefficient $\alpha$. Once known the importance of each hyperparameter, it is also important to get an indication about the best range for each hyperparameter. The HSIC analysis also allows to produce Figure 6.43, which displays two PDF for each hyperparameter. The first one (P (hyperparameter)) corresponds to the initial

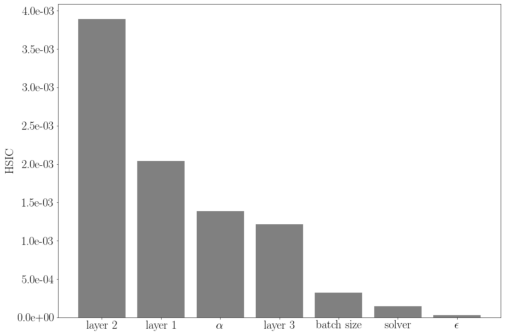


Figure 6.42: Classification of HSIC for Grid Search (from [22])

probability in the hyperparameters space and is therefore uniform. The second one (P (hyperparameter|Z)) is the probability conditioned to the best decile. For instance, it is clear choosing a value for $\alpha$ close to $5 \times 10^{-4}$ improves the quality of the ANN. Performing the same analysis for the other hyperparameters, it is advised to increase the number of neurons in both layers, to choose the Adam solver and the leaky ReLU activation function. It can be useful to cross-check these information with Figure 6.42 in order to take into account the relative importance of each hyperparameter: in the present case, for a given computational cost of the ANN, it is recommended to add more neurons in the first layer than in the second one.

All the choices made for the selected hyperparameters are gathered in Figure 6.44. They

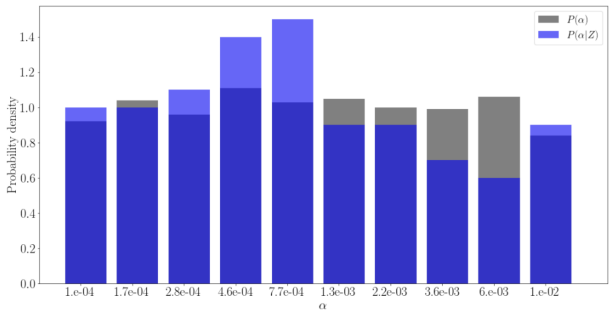


Figure 6.43: Probability density functions among hyperparameters choices for the $\alpha$ parameter used for L2 regression. (from [22])

include both the choices justified by the previous HSIC analysis and the other choices based on recommendations taken from reference textbooks [196] and options available in Sklearn. Note that the number of layers and the number of neurons per layer are not provided in this table. Since all grid searches results show that the ANN performance increases with the number of neurons in the tested range ($[25 : 100]$), the structure of the ANN is determined thanks to an analysis of the maximum realistic extra cost induced by the ANN model when performing an LES using the AVBP code.

#### 6.6.2.3 Training of the ANN

In addition to the issue of managing a very large amount of data, the ANN training using a database which combines several configurations causes learning disparities, which have been carefully investigated for a two hidden layers network, with 55 neurons in each hidden

| | |
|---|---|
| | **Results of the HSIC study** |
| Activation function | Leaky ReLU |
| Regularization | L2 with $\alpha = 0.0005$ |
| Optimizer | Adam |
| $\epsilon$ (Adam parameter) | $10^{-11}$ |
| Batch size | 800 |
| | **Other hyperparameters choices** |
| Initialization | Glorot (Glorot & Bengio, 2010) (The He initialization is not available in Sklearn) |
| Loss function | Mean Square Error (MSE) |
| Data Normalization | Avg-std |
| Test ratio | 0.2 |
| ($\beta_1$,$\beta_2$) (Adam parameter) | (0.9,0.999) |

Figure 6.44: Appropriate hyperparameters for the present work (from [22])

layer, yielding a total of 4016 degrees of freedom (weights and bias). Let us remind the reader that the ANN is trained using a training database (or sub-database or partition) corresponding to 80% of the full database which combines the three flow configurations: HIT, mixing layer at Mc = 1.1 and Mc = 2.2. The remaining 20% define the testing database (or sub-database or partition) on which the ANN designed in the training stage can be assessed using information not included in the training partition.

Figure 6.45 displays the learning curves (r2-score and mean square error (MSE)) for the (15; 55; 55; 1) network (with hyperparameters defined in Figure 6.44). Note these accuracy indicators are computed after each epoch by applying the current ANN (with its weights and bias computed from the optimization step) to the testing database only. The "Full database" plots correspond to r2-score and MSE computed for the totality of the testing database or partition (which includes 20% of the three flow configurations data). The "HIT" (respectively "Mc = 1.1", "Mc = 2.2") plots correspond to r2-score and MSE computed only for the subset of the testing database corresponding to the HIT flow configuration (respectively the mixing layer at Mc = 1.1 and Mc = 2.2). Consequently, Figure 6.45 reports the training behavior of a single ANN but with an enriched information on the predictive efficiency on the network since given not only for the whole testing partition but also for the subsets associated with each flow configuration. The network accuracy indicators converge very quickly, in approximately 10 epochs, to their asymptotic value. This is due to the very large amount of data: after each epoch, about 575 million elements have passed through the network. Although the overall performance of the network is about 0.97 at the end of the learning step, it is much smaller when computed for both mixing layers only: 0.92 at Mc = 1.1 and 0.88 at Mc = 2.2. Its performance when computed for the forced HIT only remains however satisfactory with a r2-score of 0.97.

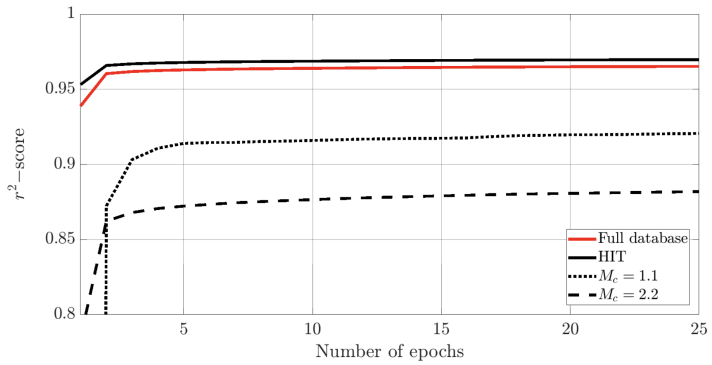


Figure 6.45: Evolution of the r2-score as a function of the number of epochs. r2-scores are evaluated on the testing partition (full partition or subset corresponding to a given flow configuration). The (15;55;55;1) ANN contains 4016 degrees of freedom and the training is performed using the Laplacians inputs as indicated by the 15 input data. (from [22])

#### 6.6.2.4 A-priori validation of the ANN

Figure 6.46 compares predicted versus true (or observed) output values plotted for the three configurations and for the overall database. Let us emphasize again the predicted values are those given by the unique ANN defined at the end of the training stage depicted in Figure 6.45. The various plots of Figure 6.46 actually detail the final values of the global accuracy indicators (r2-score and MSE) by successively providing an overview of "ANN predictions vs observations" for the subsets of the testing partition (plots (a) to (c)) and the full testing partition (plot (d)). These plots confirm the comments made on the curves of Figure 6.45. The magnitude of the predicted and true values is significantly larger for the forced HIT. When the r2-score is evaluated over the entire testing partition, residuals for both mixing layers are flattened by the forced HIT. When evaluated separately for each flow configuration, the ANN prediction shows much larger discrepancies. As a result, no visible difference can be detected between the forced HIT (Figure 6.46(c)) and the overall (testing) database (Figure 6.46(d)). Finally, although the performance is inhomogeneous over the different configurations, when looking at the correlation coefficients, the trained ANN remains very effective in comparison to the literature [197, 198, 199]. Note that very few authors use the r2-score [200] whereas this measure is a much more discriminant metric when compared to the correlation coefficient. An ANN with an acceptable (generally a value over 0.7) correlation coefficient between predicted and true values would not necessarily lead to a good r2-score.

Figure 6.47 displays SGS pressure contours for true (left) and ANN-predicted (right) values respectively for the temporal testing solution with a large time separation with respect to the training solutions. It can be clearly observed on these plots that the contours of SGS pressure are very well predicted by the ANN both in the positive and negative regions.

#### 6.6.2.5 A-posteriori validation of the ANN

At that step, we were quite convinced that we were able to accurately (see Figure 6.47) model an important (see Figure 6.26) new term only present in LES of dense gas flows. The next logical step in the validation process consists in testing the ability of the LES using the SGS pressure model to reproduce the temporal evolution of the momentum thickness (integrated over the whole domain).

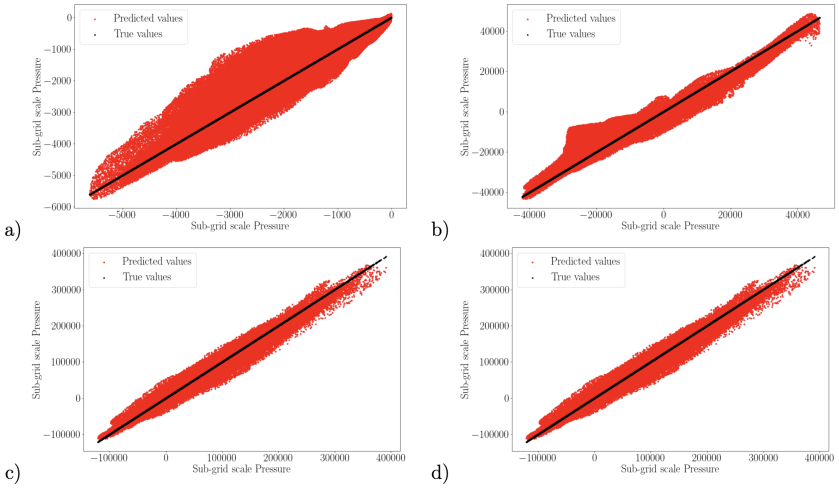


Figure 6.46: In red, representation of the values predicted by a (15;55;55;1) ANN model (4016 degrees of freedom) versus the true values and in black, representation of true values versus true values. Flow configuration(s) (a) mixing layer only at Mc = 1.1, (b) mixing layer only at Mc = 2.2, (c) forced HIT only, (d) full testing partition. (from [22])

Figure 6.48 displays this temporal evolution at Mc = 2.2 for two types of LES: one with the SGS pressure model and one without. This comparison is available for each tested filtering size (from $\bar{\Delta}/\Delta_{DNS} = 32$ to $\bar{\Delta}/\Delta_{DNS} = 4$). The DNS result is also provided for reference. The effect of the SGS pressure model on the prediction of the momentum thickness time evolution is not visible since curves overlap for LES with and without the model. The SGS pressure seems actually to have no effect on the mixing layer growth.
With and without the SGS pressure model, the evolution is well captured by the LES at $\bar{\Delta}/\Delta_{DNS} = 4$ for Mc = 2.2 mixing layers. As the filter size increases, results depart from the DNS reference. At $\bar{\Delta}/\Delta_{DNS} = 8$, the value is about 10% larger when compared to the DNS evolution, but the growth rate slope tends to stabilize and becomes close to the DNS slope as the non-dimensional time increases. At $\bar{\Delta}/\Delta_{DNS} = 16$, the growth is successively under-predicted and over-predicted by SGS models for both convective Mach numbers. At $\bar{\Delta}/\Delta_{DNS} = 32$, the momentum thickness is significantly under-predicted with a growth rate decrease of about 50% for both convective Mach numbers when compared to DNS. SGS models fail to reproduce the overall behavior of DG compressible mixing layers at medium to large filtering sizes. The well-known compressibility-related decrease of the momentum thickness growth rate (related to the increase of the Mach number) is thus not reproduced by LES using the aforementioned SGS models in DG flows. Unfortunately, accounting for the SGS pressure does not allow to capture this effect either.

This results (or rather absence of result) might be the strongest lesson I received in the last ten years. Indeed, it turns out a quite simple explanation can be found for the fact that no effect of the SGS pressure is observed when analyzing the temporal evolution of the momentum thickness. It might just be that the SGS pressure force does not significantly induce or damp turbulence roll-up which is the mechanism at the heart of the mixing layer growth. To substantiate this assumption, the vorticity equation (Bailly & Comte-Bellot, 2003) can be used which shows that the SGS pressure term contribution depends on the

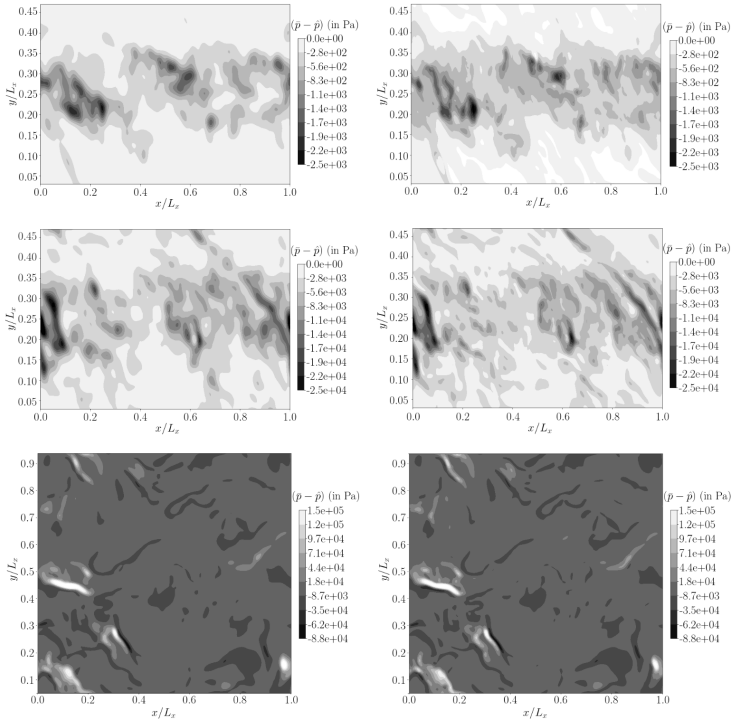

Figure 6.47: z-centerplane contours colored by sgs pressure for true (left) and ANN predicted (right) values. Results are plotted for the second stored temporal solution (see Table 6.1) for each configuration: (top) the mixing layer at Mc = 1.1 ($\tau = 1750$), (middle) the mixing layer at Mc = 2.2 ($\tau = 4050$) and (bottom) the forced HIT (Solution 2). The (11;55;55;1) ANN model comprises 3796 degrees of freedom and is trained without Laplacian inputs. None of the flow solutions have been included into the ANN training. (from [22])

alignment of its gradient vector with that of the filtered density (See Equation 6.28).

$$\begin{aligned}\frac{\partial\hat{\boldsymbol{\omega}}}{\partial t}+\nabla\times(\hat{\boldsymbol{\omega}}\times\bar{\mathbf{u}}) \quad = \quad & \frac{1}{\bar{\rho}^2}\nabla\bar{\rho}\times\nabla\hat{p}+\hat{\nu}\nabla\times\left(\nabla^2\bar{\mathbf{u}}\right)\\ & -\left[\frac{1}{\bar{\rho}^2}\nabla\bar{\rho}\times\nabla(\hat{p}-\bar{p})\right]-\left[\frac{1}{\bar{\rho}^2}\nabla\bar{\rho}\times\nabla\bar{p}-\overline{\left(\frac{\nabla\rho\times\nabla p}{\rho^2}\right)}\right]\\ & -\left[\hat{\nu}\nabla\times\left(\nabla^2\bar{\mathbf{u}}\right)-\overline{\nu\nabla\times\left(\nabla^2\mathbf{u}\right)}\right]+\left[\nabla\times(\hat{\boldsymbol{\omega}}\times\bar{\mathbf{u}})-\nabla\times\overline{(\boldsymbol{\omega}\times\mathbf{u})}\right]\end{aligned} \tag{6.28}$$

where $\hat{\boldsymbol{\omega}}=\nabla\times\bar{\mathbf{u}}$

Figure 6.49 compares the contours of both terms in the x-direction. These contours are found to be very close between the two quantities. This observation shows therefore that it is indeed possible to have a significant SGS pressure term, of amplitude comparable to that of the SGS turbulent stress tensor, but which has no effect on the mixing layer growth. An attempt could be made at explaining the observed alignment between the gradient of the SGS pressure term and the gradient of the filtered density. It is known that, for dense gases, the large heat capacity leads to almost isothermal flows regardless of the Mach number. In that context, it is expected that pressure and density fluctuations are strongly related. However, it remains to explain how quantities at different scales (resolved density on one hand and SGS pressure on the other hand) can display such a similar behavior.

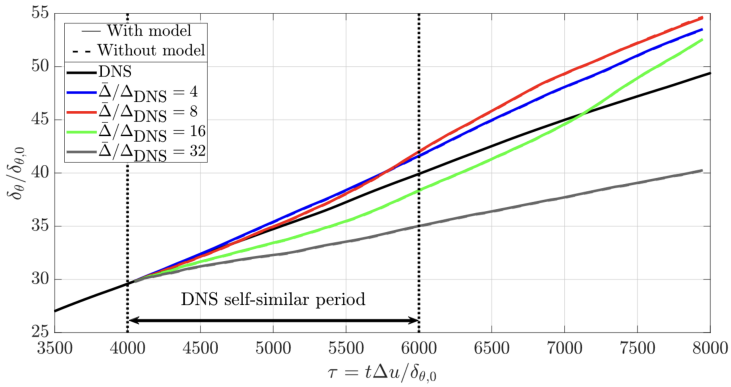


Figure 6.48: Temporal evolution of the momentum thickness. Comparison is made between DNS and a posteriori LES at four filtering sizes ( $\bar{\Delta}/\Delta_{DNS}$= [4, 8, 16, 32]) with and without the SGS pressure model. No difference is visible since curves overlap. (from [22])

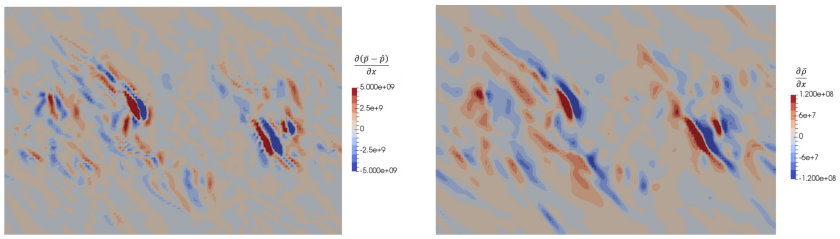

Figure 6.49: z-centerplane contours colored by (left) the SGS pressure gradients and (right) the density gradients for the mixing layer at Mc = 2.2 and $\bar{\Delta}/\Delta_{DNS} = 8$ in the x-direction. Results are plotted at $\tau = 6000$. (from [22])

At this step we thought it was important to evaluate the effect of the dynamic Smagorinsky model on the momentum thickness growth and thereby make sure the model for the SGS Turbulent Reynolds Tensor indeed had an influence on the momentum thickness growth. Figure 6.50 displays LES at Mc = 1.1 and Mc = 2.2 performed with and without the dynamic Smagorinsky model. The removal of the model for the SGS turbulent stress tensor consistently leads to a larger growth rate of the mixing layer with respect to the case where the model is active. This could be expected since the model dissipates part of the TKE energy at the filter scale, which damps the growth of the mixing layer. This effect of the SGS turbulent stress tensor removal leads therefore to an over-prediction of the growth rate when the LES using the SGS model yields an already acceptable prediction, which is the case for $\bar{\Delta}/\Delta_{DNS} = 16$. For other filtering sizes, removing the dynamic model tends actually to improve the prediction because of the under-prediction trend of the LES with the SGS turbulent stress model.

### 6.6.3 Modeling the SGS Turbulent Reynolds Tensor

Using the same process described earlier and recalled in Figure 6.51 we now turn our attention to the SGS Turbulent Reynolds Tensor. The training process uses the complete training database, combining HIT, channel and mixing layer data with preprocessing to enforce Galilean invariance, over several epochs to optimize the weights and biases of the ANN until the optimization process converges and the accuracy of the model reaches an asymptotic value. One observes that for the testing database, values of the $r^2$-score larger than 0.9 are reached after 20 to 30 epochs. To illustrate this level of correlation between

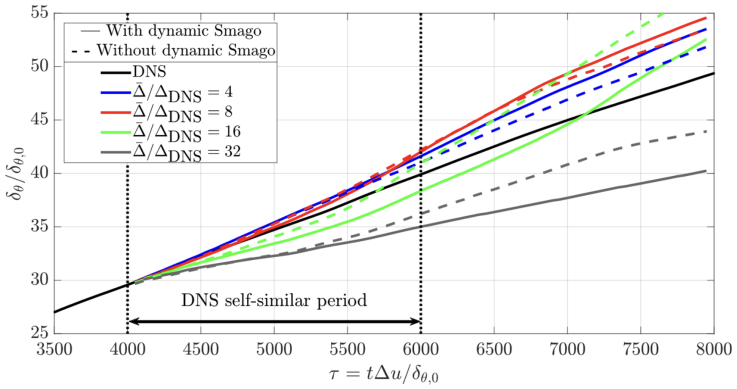


Figure 6.50: Temporal evolution of the momentum thickness for the mixing layers at (top) Mc = 1.1 and (bottom) Mc = 2.2. Comparison is made between DNS and a posteriori LES at four filtering sizes ( $\bar{\Delta}/\Delta_{DNS}$= [4, 8, 16, 32]) with and without the dynamic Smagorinsky model. (from [22])

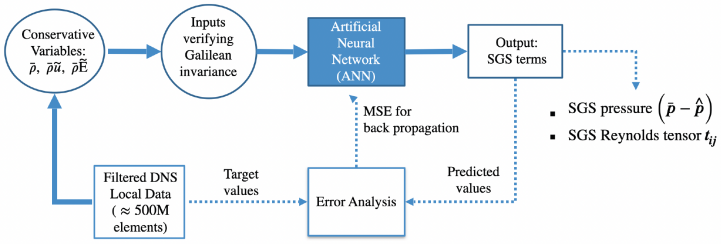


Figure 6.51: Schematic representation of the ANN training process (from [25])

the filtered DNS data and the ANN model, Figure 6.52 shows a side-by-side comparison of $t_{xy}$ for the mixing layer at $M_c = 2.2$ from the filtered DNS (Figure 6.52 a)) and the ANN prediction (Figure 6.52 b)). $M_c = \frac{\Delta u}{c_1 + c_2}$ is the convective Mach number ($\Delta u$ is the differential speed between upper and lower parts of domain and $c_1$ and $c_2$ are the corresponding sound speeds). Note that the prediction is computed for a temporal solution which was not included in the training database. It can be observed in Figure 6.52 that the local nature of the ANN model does not preclude the accurate reproduction, both in size and amplitude, of the $t_{xy}$ peak regions.

The tuned ANN model is implemented in the LES solver AVBP developed at CERFACS, as an alternative to state-of-the-art SGS models available in this solver. The mixing layer case at $M_c = 2.2$ is considered as a first validation test-case. Four different meshes are designed to assess the accuracy of the ANN-based model as a function of the grid resolution. For this numerical experiment, the following spatial resolutions are considered : $\Delta/\Delta_{DNS}$ =4, 8, 16 and 32. The first two resolutions are too close to the DNS to be reachable by practical LES. The two coarsest are representative of LES designed to have the turbulent kinetic energy spectrum cut in the inertial regime for large enough Reynolds numbers. Figure 6.53 compares the reference DNS temporal evolution of the mixing layer thickness with the LES simulations using the grid $\Delta/\Delta_{DNS} = 32$ and (i) the ANN model, (ii) the Sigma model and (iii) implicit LES. Because of the coarse grid resolution, the initial solution starts for all LES with a mixing layer thickness larger than in the DNS. The evolution of the mixing layer thickness is initially very similar between implicit LES and the ANN model but both strategies start to depart from each other after a non-dimensional time $\tau$

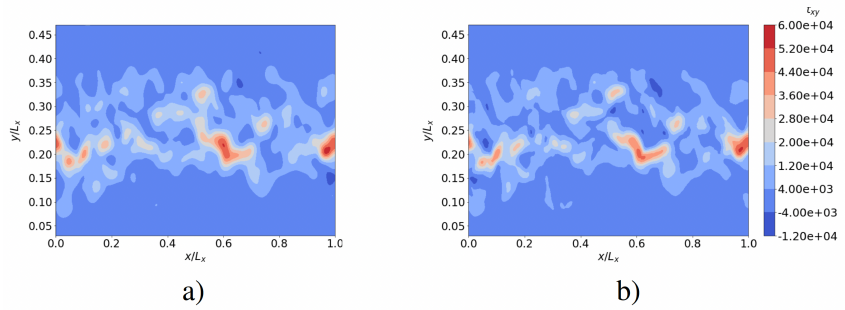


Figure 6.52: Comparison of $t_{xy}$ between the (a) true values and (b) the predicted ones. (from [25])

larger than 4000 and eventually the ANN model better recovers the growth rate of the DNS. The Sigma model at first predicts a larger mixing layer but quickly saturates and strongly under-predicts the growth rate later in time. Note that the comparison of the growth rates is meaningful when each computation reaches a linear regime, that is for $\tau \in [6000, 7000]$.

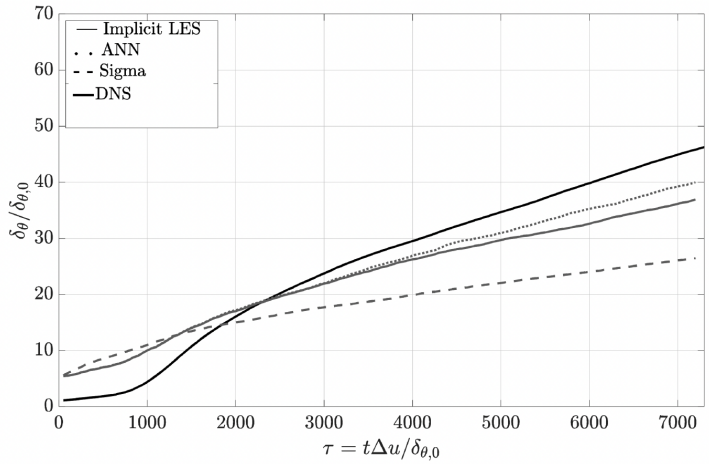


Figure 6.53: Temporal evolution of the momentum thickness for a mixing layer at $M_c = 2.2$. Comparison is made between DNS and three LES at $\Delta/\Delta_{DNS} = 32$. (from [25])

Figure 6.54 directly compares the mixing layer growth rates reached in the self-similar regime by each model as a function of the space resolution. It can be seen that for this $M_c = 2.2$ dense gas mixing layer the ANN model consistently better predicts the mixing layer thickness for all four spatial resolutions considered, with an error of 10% maximum with respect to the DNS.

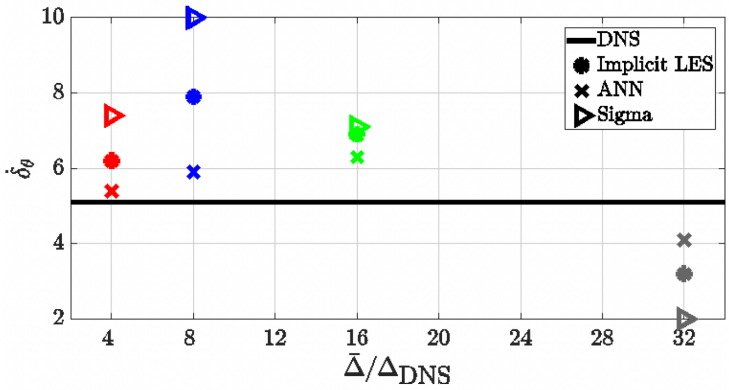


Figure 6.54: Comparison of growth rates for DNS and three LES as a function of the resolution ($\Delta/\Delta_{DNS}$) (from [25])

## 6.7 Conclusion and future Directions

### 6.7.1 Conclusion

Since 2015, the complex behavior of turbulence in dense gas flows has been studied using DNS and this research has lead to numerous significant results. It is clearly shown that in the case of Homogeneous Isotropic Turbulence mostly small scales are influenced by the thermodynamic complexity of the fluid. In particular, a strong activity of the vortical structures at or near the Taylor micro-scale is evidenced. Also, expansion shocklets are found in the flow and their statistical characteristics analyzed. The relation between the density and entropy jumps is shown to be quite different from what is observed for compression shocklets in perfect gas flows.
In the mixing layer, it has been shown during the PhD of Aurelien Vadrot that the macroscopic behavior (namely the growth rate) of the mixing layer remains very close between the perfect and the dense gas flows up to a convective Mach number of 1.1. Yet very interestingly, it is also found that if the growth rates continues to decrease for the perfect gas, it remains almost unchanged between $M_c = 1.1$ and $M_c = 2.2$ in the dense gas. Although numerous additional analysis are achieved to better understand this phenomenon, no clear explanation emerges. We however show that this phenomenon is strongly related to the decoupling between the internal and kinetic energy in the dense gas, evidenced by the small Eckert number in these flows. It should also be noted that the phenomenon still has to be reproduced by other researchers.

Using the very large database coming from the DNS of dense gas flows we first analyze the accuracy of existing subgrid scale models for the Reynolds turbulent stress tensor. We find that existing functional models relying on the turbulent Boussinesq assumption perform somewhat better that structural models. Unfortunately, these models predictions worsen when used in the context of dense gas flows as the statistical distribution of the SGS term is modified by the nature of the flow. This analysis further shows the need for specific SGS models to be devoted to dense gas flow LES.

To focus on the most important aspects of the LES closure in dense gas flows, we then analyze the behavior of subgrid scale (SGS) terms in an a-priori study. It is shown that contrary to the perfect gas, additional terms to the usual Reynolds turbulent stress tensor arise. We find that the SGS pressure has a much more important amplitude in the dense gas flow. For this reason and because this term is completely negligible in the per-

fect gas, we first concentrated on this term for the modeling of dense gas effects in LES. To model the SGS pressure, Artificial Neural Networks (ANN) are used. At this step numerous aspects have to be taken into account such as the statistical characteristics of the inputs for the network, the identification of the most significant hyperparameters and their optimization,...Maybe one of the most overlooked aspect is the verification of the Galilean invariance of the network predictions. To ensure this invariance behavior, we enforced it on the input data through the random dynamic rotation of the data. A-priori predictions of the developed model are satisfactory but not those obtained a-posteriori. It is shown that this discrepancy comes from the fact that although of a significant amplitude in the filtered DNS and LES, the SGS pressure does not influence the growth rate of the mixing layer.

We then decided to turn our attention to the modeling of the Reynolds turbulent stress tensor with success. We showed that the model was indeed able to improve the prediction capabilities of the LES in the case of the dense gas mixing layer. However, it still shows some robustness defaults that prevents it from been as versatile as usual models. Current developments are described hereafter in the section devoted to future directions.

### 6.7.2 Future directions

My current research project leads me to further try to develop innovative turbulence closure models for Large Eddy Simulation (LES) and Reynolds-Averaged Navier-Stokes (RANS) equations, specifically tailored for dense gas flows in industrial geometries like ORC turbines. Given the intricacies of dense gas thermodynamics, machine learning techniques will be employed to derive pertinent models. Part of this work is done in collaboration with Emilie Sauret at QuT with whom we co-supervize the PhD of Isa Helal. The developed models will be rigorously evaluated across various configurations, including those relevant to ENOGIA, a French ORC turbine manufacturer and project partner. During this thesis, the objective is to address the two main avenues of Machine Learning modeling.

- **Supervised machine learning techniques**
  This approach is the one we already used to model the SGS terms in dense gas flow during the PhD of Aurelien Vadrot and the postdoc of Dominik Schuster. Yet we will now focus on the modeling of turbulence in RANS with one additional ingredient. The Artificial Neural Networks will be modified to incorporate more physics in their training mechanism. The Physics Informed strategy will be followed by modifying the loss pattern. This work has already begun with a database arising from the numerous high fidelity simulations undertaken during the last five years.
- **Unsupervised machine learning techniques**
  This approach is somewhat more innovative and is newer to the team. In this case, no database is used. Rather, the turbulent model is represented as an agent that acts in the CFD solver to ensure the right behavior of the macroscopic quantities of interest. We will use recent developments to incorporate an actor-critic model into the solver SU2 for that purpose. A parametric analysis of the reward definitions, essential to this approach, will be done that should lead to a deeper understanding of the behavior of turbulence in dense gas flows.

In the near future, my intention is also to explore the influence of supercritical thermodynamic effects for $CO_2$. In the last years, we have shown that some of the thermodynamics effects on turbulence are damped in the dense gas flows we considered due to their very large heat capacity that prevents almost any coupling between the internal and kinetic energy. This picture has been shown by many authors to be drastically different in $CO_2$ which makes it an interesting candidate for further research in thermodynamically influenced turbulence modeling. On top of this research interest, $CO_2$ applications will further grow as industrial partners turn always more their attention to renewable applications in the energy domain.

## 6.8 Summary of contributions and collaborations

We conclude this chapter by summarizing the key communications regarding Turbulence Modeling in Dense Gas Flows and the collaborations at their origins.

| Topic | articles | people | status | place |
|---|---|---|---|---|
| Turbulence modeling | [17, 201, 202] | Matteo Menghetti | PhD student | LMFA |
| | [18, 181, 203] | Aurelien Vadrot | PhD student | LMFA |
| in dense gas flows using DNS, | [19, 21, 25] | Isa Helal | PhD Student | LMFA |
| | [204, 24, 23] | Corentin Giguet | M1 Student | LMFA |
| LES and Machine learning | | Paolo Errante | PostDoc | LMFA |
| | | Dominik Schuster | PostDoc | LMFA |
| | | Christophe Corre | Collaborator | LMFA |
| | | Emilie Sauret | Collaborator | QUT (Australia) |

Table 6.9: key research elements and their context

# Chapter 7

# Conclusion and future directions

Contents

## 7.1 Conclusion

My contributions to the field of combustion noise can be categorized into three main themes. Firstly, I pioneered the development of a novel and efficient method for computing the Flame Transfer Function (FTF) from unsteady Large Eddy Simulations (LES) of flames, employing the Wiener-Hopf signal processing technique. Secondly, I formulated a new framework for quantifying disturbances energy in reactive flows, a crucial parameter linked to the challenge of thermo-acoustic instabilities frequently encountered by engine designers. The effectiveness of this newly derived disturbance energy measure was successfully validated within the context of more intricate flame scenarios. Lastly, I devised a novel semi-analytical 1D tool designed to predict indirect combustion noise in nozzles. Utilizing this tool facilitated the resolution of shape optimization problems devoted to the experimental study of indirect combustion noise. This method, which relies solely on knowledge of geometry and initial amplitude of temperature fluctuations, was subsequently expanded to turbine flows, introducing innovative approaches for predicting indirect combustion noise in gas turbines.

My studies focusing on noise in a Fan/OGV stage underscore the impact of separation bubbles on pressure fluctuations in turbomachinery, revealing their role in generating high-frequency peaks (HFPs) attributed to spanwise vortical structures. This insight holds promise for modeling acoustic sources, particularly at low mass flow rates. Additionally, the complexity of flow in the tip region of the ECL5 rotor is highlighted, with various vortical structures influencing Wall Pressure Spectra (WPS) at different frequencies. The blade and tip-gap region are identified as primary noise sources, with the latter dominating at higher frequencies. Direct propagation of sound waves in Large Eddy Simulations (LES) offers a comprehensive understanding of acoustic emissions, showcasing good agreement with experimental data. Notably, LES accurately reproduces flow characteristics and acoustic modal decomposition. These LES reveal significant vortical structures and acoustic waves, contributing to an enhanced understanding of acoustic propagation in turbomachinery systems. These findings lay the groundwork for further comparisons and advance our knowledge of acoustic emissions in complex turbomachinery configurations, with potential implications for noise mitigation strategies.

The complex behavior of turbulence in dense gas flows has been studied using DNS and Machine Learning techniques. This research has lead to numerous significant results.
In Homogeneous Isotropic Turbulence, vortical structures near the Taylor micro-scale are highly active, with shocklets exhibiting unique statistical characteristics in dense gas flows. Contrary to perfect gas flows, dense gas flows exhibit intriguing behavior in mixing layers, with growth rates remaining nearly constant at high convective Mach numbers, possibly due to decoupling between internal and kinetic energy. Existing subgrid scale (SGS) models for Reynolds turbulent stress tensor perform less accurately in dense gas flows, highlighting the need for specific models tailored to such conditions. A-priori analysis of SGS terms reveals significant differences from perfect gas flows, leading to the development of Artificial Neural Networks (ANN) for modeling SGS pressure in LES. Challenges such as ensuring Galilean invariance and optimizing hyperparameters are addressed. While the developed model shows satisfactory a-priori predictions, discrepancies arise in a-posteriori predictions, attributed to the negligible influence of SGS pressure on mixing layer growth rates. Attention is then shifted to modeling the Reynolds turbulent stress tensor, which improves LES prediction capabilities in dense gas mixing layers, albeit with some robustness limitations. Future directions include addressing these limitations and further refining SGS modeling for dense gas flows.

Research in fluid dynamics is a never ending process and one of the purpose of researchers is to carry on the flame of curiosity towards a better understanding of the complex intrica-

cies of fluctuations in flows, let it be of an entropic, acoustic or turbulent nature.
During the last twenty years I hope I managed to participate to the wider spreading of high fidelity simulation as a powerful tool for that purpose. In the course of this research endeavor truly unresolved results were found. I can for example mention the peculiar behavior of indirect combustion noise in the Bake experiment which still comes to my mind after all those years. Also, one can think of the ground reasons for the drop of the mixing layer growth rate which is not observed in the dense gas beyond a turbulent Mach number of 2.2. More recently, a low frequency fluctuation (way below the Blade Passing Frequency) has been found in the ECL5 fan configuration at nominal speed that is also seen in the experiments but remains to be explained.

So much still has to be done and high fidelity simulations will remain as a tool of choice. Machine learning techniques will help further improve its modeling capabilities if we manage to increase the explainability of its models and the robustness of its predictions. As our computational capabilities further grow, it will certainly help design (at some point in real time) the engineering systems that we need in so many fields to tackle the technological cliff that lies in front of us because of climate change.

## 7.2 Future directions

My research now concentrates mostly on the topics presented in the last two chapters of this manuscript.

**Broadband noise in turbomachinery**
Regarding the analysis of broadband noise in turbomachinery, it is now understood that the LES analysis methodology is mature enough to address in detail complex flows involving broadband acoustic sources. The next steps involve applying this research methodology to:

- **Understand the physical mechanisms behind broadband acoustic sources when the fan operates at its nominal speed:**
  In this case, the relative flow at the leading edge becomes supersonic, leading to the formation of a supersonic pocket at the blade's leading edge. The associated shock prevents acoustic waves from freely propagating upstream. As illustrated in Figure 7.1, the directivity and local intensity of the broadband noise resulting from the rotor-stator interaction are significantly altered. This preliminary result, obtained from a calculation on a single radial slice of the complete stage, seems to indicate the potential value of a specific case study. This research is currently being conducted by Allan Beurville as part of his thesis, which began in November 2022.

- **Understand the physical mechanisms behind broadband acoustic sources in the case of unducted fans:**
  To achieve a significant increase in dilution rates, manufacturers, particularly SAFRAN, are leaning toward unducted propulsion architectures. An example is the RISE configuration currently under study at SAFRAN [139]. This research has just begun at LMFA (in December 2023) as part of Pierre-Louis Pape's doctoral thesis, supervised by Marc Jacob (LMFA), which is part of the European project PANDORA aimed at improving the design and modeling of unducted fan architectures.

- **Develop new low-order models for the broadband noise** emitted by (i) the recirculating bubble that forms at partial load, (ii) the tip-gap complex vortical structures, (iii) the shock wave that develops at nominal speed above the suction side of the rotor blade. This work will be part of both Allan Beurville and Pierre-Louis Pape

PhD thesis.
This research which will be pursued in collaboration with the acoustic group will lead to the development of a tool capable of describing noise emissions from fans (including BBN) with very small turnover times. This brick is essential for the optimization of fan/OGV stage architectures in future engine configurations.

- **Assess new noise mitigation techniques** such as the one described in a patent application recently filed by the author.

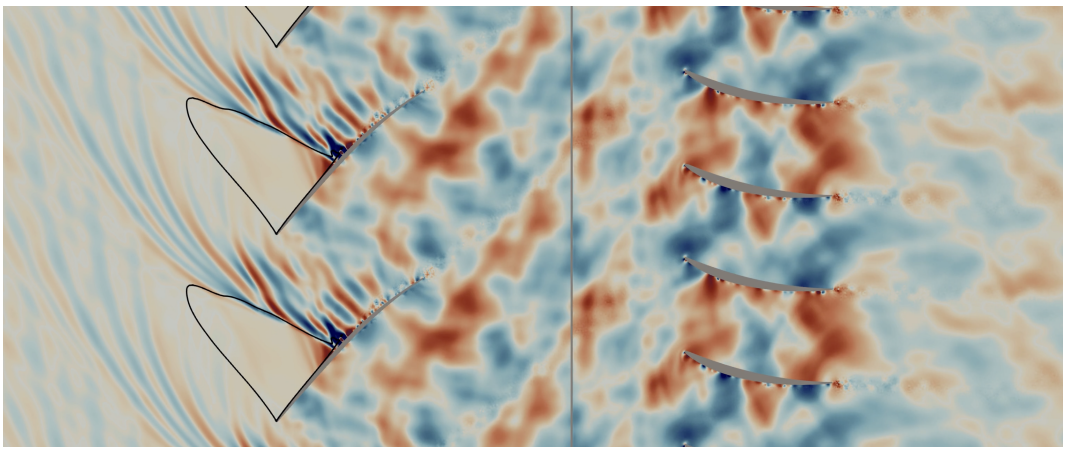

Figure 7.1: Blade-to-blade view of the pressure fluctuation. Black lines mark the locations of $M_r = 1$ (Source: Allan Beurville [15])

**Turbulence in dense gas flows**
Regarding the modeling of turbulence in dense gas flows, my current research project leads me to further try to develop innovative turbulence closure models for Large Eddy Simulation (LES) and Reynolds-Averaged Navier-Stokes (RANS) equations, specifically tailored for dense gas flows in industrial geometries like ORC turbines. Given the intricacies of dense gas thermodynamics, machine learning techniques will be employed to derive pertinent models. Part of this work is done in collaboration with Emilie Sauret at QuT with whom we co-supervize the PhD of Isa Helal. The developed models will be rigorously evaluated across various configurations, including those relevant to ENOGIA, a French ORC turbine manufacturer and project partner. During this thesis, the objective is to address the two main avenues of Machine Learning modeling.

- **Supervised machine learning techniques**
  This approach is the one we already used to model the SGS terms in dense gas flow during the PhD of Aurelien Vadrot and the postdoc of Dominik Schuster. Yet we will now focus on the modeling of turbulence in RANS with one additional ingredient. The Artificial Neural Networks will be modified to incorporate more physics in their training mechanism. The Physics Informed strategy will be followed by modifying the loss pattern. This work has already begun with a database arising from the numerous high fidelity simulations undertaken during the last five years.

- **Unsupervised machine learning techniques**
  This approach is somewhat more innovative and is newer to the team. In this case, no database is used. Rather, the turbulent model is represented as an agent that acts in the CFD solver to ensure the right behavior of the macroscopic quantities of interest. We will use recent developments to incorporate an actor-critic model into the solver SU2 for that purpose. A parametric analysis of the reward definitions, essential to this

approach, will be done that should lead to a deeper understanding of the behavior of turbulence in dense gas flows.

In the near future, my intention is also to explore the influence of supercritical thermodynamic effects for $CO_2$. In the last years, we have shown that some of the thermodynamics effects on turbulence are damped in the dense gas flows we considered due to their very large heat capacity that prevents almost any coupling between the internal and kinetic energy. This picture has been shown by many authors to be drastically different in $CO_2$ which makes it an interesting candidate for further research in thermodynamically influenced turbulence modeling. On top of this research interest, $CO_2$ applications will further grow as industrial partners turn always more their attention to renewable applications in the energy domain.

# Bibliography


[1] Nicolas Lamarque. Schémas numériques et conditions limites pour la simulation aux grandes échelles de la combustion diphasique dans les foyers d'hélicoptère. PhD thesis, Institut National Polytechnique de Toulouse-INPT, 2007. vii, 16

[2] Gaofeng Wang, Florent Duchaine, Dimitrios Papadogiannis, Ignacio Duran, Stéphane Moreau, and Laurent YM Gicquel. An overset grid method for large eddy simulation of turbomachinery stages. Journal of Computational Physics, 274:333–355, 2014. vii, 25, 57

[3] Alexis Giauque, T Poinsot, and F Nicoud. Validation of a flame transfer function reconstruction method for complex turbulent configurations. In 14th AIAA/CEAS Aeroacoustics Conference, Vancouver, Canada, pages 1–22, 2008. vii, 31, 32, 48

[4] Alexis Giauque, Maxime Huet, and Franck Clero. Analytical Analysis of Indirect Combustion Noise in Subcritical Nozzles. Journal of Engineering for Gas Turbines and Power, 134(11):111202, nov 2012. vii, 34, 38, 48

[5] Alexis Giauque, Maxime Huet, Franck Clero, F Richecoeur, and S. Ducruix. Thermoacoustic shape optimization of a subsonic nozzle. In Journal of Engineering for Gas Turbines and Power, pages 1–15, San Antonio, TX, USA, 2013. vii, 36, 37, 48

[6] A. Emmanuelli, J. Zheng, M. Huet, A. Giauque, T. Le Garrec, and S. Ducruix. Description and application of a 2D-axisymmetric model for entropy noise in nozzle flows. Journal of Sound and Vibration, 472, 2020. vii, 38, 39, 40, 48

[7] Alexis Giauque. FONCTIONS DE TRANSFERT DE FLAMME ET ENERGIES DES PERTURBATIONS DANS LES ECOULEMENTS REACTIFS. PhD thesis, INP Toulouse, 2007. vii, 43, 44, 48

[8] Michael J. Brear, Franck Nicoud, Mohsen Talei, Alexis Giauque, and Evatt R. Hawkes. Disturbance energy transport and sound production in gaseous combustion. Journal of Fluid Mechanics, 2012. vii, viii, 46, 47, 48

[9] Stéphane Moreau. Turbomachinery noise predictions: present and future. Acoustics, 1(1):92–116, 2019. viii, 51, 52

[10] Christoph Brandstetter, Valdo Pages, Pierre Duquesne, Benoit Paoletti, Stéphane Aubert, and Xavier Ottavy. Project phare-2a high-speed uhbr fan test facility for a new open-test case. Journal of Turbomachinery, 141(10):101004, 2019. viii, 54, 55, 56

[11] Jean Al-Am, Vincent Clair, Alexis Giauque, Jérôme Boudet, and Fernando Gea-Aguilera. Direct noise predictions of an uhbr turbofan stage: periodic sector vs full annulus large-eddy simulations. AIAA Journal, 2024. viii, ix, 57, 73, 74, 75, 76, 77, 78, 81

[12] Jean Al Am, Vincent Clair, Alexis Giauque, Jérôme Boudet, and Fernando Gea-Aguilera. On the effects of a separation bubble on fan noise. Journal of Sound and Vibration, 537, 2022. viii, 59, 60, 61, 62, 63, 64, 81

[13] Jean Al-Am, Vincent Clair, Alexis Giauque, Jérôme Boudet, and Fernando Gea-Aguilera. Aeroacoustic analysis of the tip-leakage flow of an ultrahigh bypass ratio fan stage. Physics of Fluids, 35(4), 2023. viii, ix, 66, 67, 68, 69, 70, 71, 72, 81

[14] JE Ffowcs Williams and David L Hawkings. Sound generation by turbulence and surfaces in arbitrary motion. Philosophical Transactions for the Royal Society of London. Series A, Mathematical and Physical Sciences, pages 321–342, 1969. ix, 72

[15] Allan Beurville, Jérôme Boudet, Vincent Clair, and Alexis Giauque. Large eddy simulation and direct noise prediction of a fan stage in transonic regime. In Direct and Large Eddy Simulation (DLES) , April 10-12, Erlangen, 2024. ix, xiii, 81, 142

[16] Tosto F. Modeling and characterization of nonideal compressible flows in unconventional turbines. PhD thesis, Delft Univ. Technol., Delft, Neth., 2023. x, 88

[17] Alexis Giauque, C Corre, and Matteo Menghetti. Direct numerical simulations of homogeneous isotropic turbulence in a dense gas. In Journal of Physics: Conference Series, volume 821 (1), page 012017. IOP Publishing, 2017. x, 89, 90, 91, 138

[18] Alexis Giauque, Christophe Corre, and Aurélien Vadrot. Direct numerical simulations of forced homogeneous isotropic turbulence in a dense gas. Journal of Turbulence, 2020. x, 94, 95, 96, 97, 98, 99, 100, 108, 111, 113, 138

[19] Aurélien Vadrot, Alexis Giauque, and Christophe Corre. Direct numerical simulations of temporal compressible mixing layers in a bethe–zel'dovich–thompson dense gas: influence of the convective mach number. Journal of Fluid Mechanics, 922:A5, 2021. x, xi, 101, 102, 103, 104, 105, 106, 107, 108, 110, 138

[20] Tobias Rossmann, M Godfrey Mungal, and Ronald K Hanson. Evolution and growth of large scale structures in high compressibility mixing layers. In TSFP Digital Library Online. Begel House Inc., 2001. x, 101, 102

[21] Alexis Giauque, Aurélien Vadrot, Paolo Errante, and Christophe Corre. A priori analysis of subgrid-scale terms in compressible transcritical real gas flows. Physics of Fluids, 33(8), 2021. xi, 109, 110, 111, 112, 113, 138

[22] Aurélien Vadrot. Numerical simulation and modeling of compressible turbulence in dense gas flows. PhD thesis, Ecole Centrale de Lyon, ED MEGA, 2021. xi, xii, 113, 127, 128, 129, 130, 131, 132, 133, 134

[23] Alexis Giauque, Corentin Giguet, Aurélien Vadrot, and Christophe Corre. A priori test of large-eddy simulation models for the sub-grid scale turbulent stress tensor in perfect and transcritical compressible real gas homogeneous isotropic turbulence. Computers & Fluids, 268:106091, 2024. xi, 114, 115, 116, 117, 118, 138

[24] Alexis Giauque, Dominik Schuster, and Christophe Corre. High-fidelity numerical investigation of a real gas annular cascade with experimental validation. Physics of Fluids, 35(12), 2023. xi, xii, 119, 120, 121, 122, 123, 138

[25] Alexis Giauque, Aurélien Vadrot, and Christophe Corre. Development, validation and application of an ann-based large eddy simulation subgrid-scale turbulence model for dense gas flows. In Proceedings of the 4th International Seminar on Non-Ideal Compressible Fluid Dynamics for Propulsion and Power. NICFD 2022. ERCOFTAC Series, volume 29, pages 43–52. Springer Nature Switzerland, 2023. xii, 134, 135, 136, 138

[26] M. S. Cramer. Negative nonlinearity in selected fluorocarbons. Physics of Fluids A: Fluid Dynamics, 1(11):1894–1897, November 1989. 1, 91, 92, 107, 108

[27] Joseph J. Martin and Yu-Chun Hou. Development of an equation of state for gases. AIChE Journal, 1(2):142–151, June 1955. 1, 15, 18, 20, 21, 92, 108, 110

[28] Joseph J. Martin, Rajendra M. Kapoor, and Noel De Nevers. An improved equation of state for gases. AIChE Journal, 5(2):159–160, June 1959. 1, 18, 108, 110

[29] Thilo Schonfeld and Michael Rudgyard. Steady and unsteady flow simulations using the hybrid flow solver avbp. AIAA journal, 37(11):1378–1385, 1999. 16, 56, 57

[30] Ting Horng Chung, Mohammad Ajlan, Lloyd L. Lee, and Kenneth E. Starling. Generalized multiparameter correlation for nonpolar and polar fluid transport properties. Industrial & Engineering Chemistry Research, 27(4):671–679, April 1988. 15, 17, 20, 108

[31] William Sutherland. LII. the viscosity of gases and molecular force. The London, Edinburgh, and Dublin Philosophical Magazine and Journal of Science, 36(223):507–531, December 1893. 17

[32] E. Garnier, N. Adams, and P. Sagaut. Large Eddy Simulation for Compressible Flows. Springer Netherlands, 2009. 18

[33] Laurent C Selle, Nora A Okong'o, Josette Bellan, and Kenneth G Harstad. Modelling of subgrid-scale phenomena in supercritical transitional mixing layers: an a priori study. Journal of Fluid Mechanics, 593:57–91, 2007. 19

[34] Bert Vreman, Bernard Geurts, and Hans Kuerten. A priori tests of large eddy simulation of the compressible plane mixing layer. Journal of engineering mathematics, 29(4):299–327, 1995. 19

[35] Luca Sciacovelli, Paola Cinnella, and Xavier Gloerfelt. Direct numerical simulations of supersonic turbulent channel flows of dense gases. Journal of Fluid Mechanics, 821:153–199, 2017. 19, 89, 110

[36] Rene Pecnik and Ashish Patel. Scaling and modelling of turbulence in variable property channel flows. Journal of Fluid Mechanics, 823:R1, 2017. 19

[37] Andrew W. Cook and William H. Cabot. A high-wavenumber viscosity for high-resolution numerical methods. Journal of Computational Physics, 195(2):594–601, apr 2004. 20

[38] Joseph Boussinesq. Essai sur la théorie des eaux courantes, volume XXIII. Imprimerie nationale, Paris, 1877. Mémoires présentés par divers savants à l'Académie des sciences de l'Institut de France. 21

[39] Joseph Smagorinsky. General circulation experiments with the primitive equations: I. the basic experiment. Monthly weather review, 91(3):99–164, 1963. 22

[40] James W Deardorff et al. A numerical study of three-dimensional turbulent channel flow at large reynolds numbers. J. Fluid Mech, 41(2):453–480, 1970. 22

[41] F. Nicoud and F. Ducros. Subgrid-scale stress modelling based on the square of the velocity gradient tensor. Flow, Turbulence and Combustion, 62:183–200, 1999. 22

[42] M. Germano, U. Piomelli, P. Moin, and W.H. Cabot. A dynamic subgrid-scale eddy viscosity model. Physics of Fluids A, 3:1760–1765, 1991. 22

[43] M. Germano. A proposal for a redefinition of the turbulent stresses in the filtered navier–stokes equations. Physics of Fluids, 29(7):2323, 1986. 23

[44] Charles G. Speziale. Galilean invariance of subgrid-scale stress models in the large-eddy simulation of turbulence. Journal of Fluid Mechanics, 156(-1):55, July 1985. 23

[45] D.K. Lilly. A proposed modification of the germano subgrid-scale closure method. Physics of Fluids A, 4:633–635, 1992. 24

[46] A Refloch, B Courbet, A Murrone, P Villedieu, C Laurent, P Gilbank, J Troyes, L Tessé, G Chaineray, JB Dargaud, et al. Cfd platforms and coupling. Aerospace Lab, 2011. 24

[47] John William Strutt. The theory of sound, volume 9781108032. Dover Publications, New York, 2011. 28, 41

[48] Simon R. Stow and Ann P. Dowling. Thermoacoustic oscillations in an annular combustor. Proceedings of the ASME Turbo Expo, 2, 2001. 29

[49] Charles Etienne Martin. Etude énergétique des instabilités thermo-acoustiques et optimisation génétique des cinétiques réduites. PhD thesis, INP Toulouse, 2005. 29

[50] F. Nicoud, L. Benoit, C. Sensiau, and T. Poinsot. Acoustic modes in combustors with complex impedances and multidimensional active flames. AIAA Journal, 45(2):426–441, 2007. 29, 30

[51] Peter Bergmann, G. The Wave Equation in a Medium with a Variable Index of Refraction. The Journal of the Acoustical Society of America, 17(4), 1946. 29

[52] F. C.E. Culick. Combustion instabilities in liquid- fuelled propulsion systems. In AGARD Conference Proceedings, number 450 in 1, 1988. 30

[53] L. CROCCO. Aspects of Combustion Stability in Liquid Propellant Rocket Motors Part I: Fundamentals. Low Frequency Instability With Monopropellants. Journal of the American Rocket Society, 21(6):163–178, 1951. 30

[54] L. CROCCO. Aspects of Combustion Stability in Liquid Propellant Rocket Motors Part II: Low Frequency Instability with Bipropellants. High Frequency Instability. Journal of the American Rocket Society, 22(1):7–16, 1952. 30

[55] Bruno B.H. Schuermans, Wolfgang Polifke, and Christian Oliver Paschereit. Modeling transfer matrices of premixed flames and comparison with experimental results. Proceedings of the ASME Turbo Expo, 2, 1999. 30

[56] H. S. Tsien. The Transfer Functions of Rocket Nozzles. Collected Works of H. S. Tsien (1938-1956), pages 650–660, 2012. 33

[57] LUIGI CROCCO and SIN-I CHENG. High-Frequency Combustion Instability in Rocket Motor with Concentrated Combustion. Journal of the American Rocket Society, 23(5):301–313, 1953. 33

[58] F. E. Marble. Acoustic disturbance from gas non-uniformities convected through a nozzle. In Interagency Symposium on University Research in Transportation Noise, 1973. 33

[59] NA Cumpsty and F.E. Marble. THE GENERATION OF NOISE BY THE FLUCTUATIONS IN GAS TEMPERATURE INTO A TURBINE. Technical report, Caltech, 1974. 33

[60] J. E. Ffowcs Williams and M. S. Howe. The generation of sound by density inhomogeneities in low Mach number nozzle flows. Journal of Fluid Mechanics, 70(03):605, mar 1975. 33

[61] E. E. Zukoski. Experiments Concerning the Response of Supersonic Nozzles To Fluctuating Inlet Conditions. American Society of Mechanical Engineers (Paper), GT-40:60–64, 1975. 33

[62] M. S. Bohn. Response of a subsonic nozzle to acoustic and entropy disturbances. Journal of Sound and Vibration, 52(2):283–297, 1977. 33

[63] Friedrich Bake, Christoph Richter, Bernd Mühlbauer, Nancy Kings, Ingo Röhle, Frank Thiele, and Berthold Noll. The Entropy Wave Generator (EWG): A reference case on entropy noise. Journal of Sound and Vibration, 326(3-5):574–598, oct 2009. 33

[64] B. Mühlbauer, B. Noll, and M. Aigner. Numerical investigation of the fundamental mechanism for entropy noise generation in aero-engines. Acta Acustica united with Acustica, 95(3):470–478, 2009. 33

[65] M. Leyko, F. Nicoud, and T. Poinsot. Comparison of direct and indirect combustion noise mechanisms in a model combustor. AIAA Journal, 47(11):2709–2716, 2009. 33

[66] FE Marble and S. Candel. ACOUSTIC DISTURBANCE CONVECTED FROM GAS NON-UNIFORMITIES THROUGH A NOZZLE. Journal of Sound and Vibration, 55(2):225–243, 1977. 33

[67] M Huet, F Vuillot, N Bertier, M Mazur, N Kings, W Tao, P Scouflaire, F Richecoeur, S Ducruix, C Lapeyre, and T Poinsot. Recent Improvements in Combustion Noise Investigation Challenges in Combustion for Aerospace Propulsion Recent Improvements in Combustion Noise Investigation: from the Combustion Chamber to Nozzle Flow. Journal AerospaceLab, pages 1–17, 2016. 35

[68] A. W. Bloy. The pressure waves produced by the convection of temperature disturbances in high subsonic nozzle flows. Journal of Fluid Mechanics, 94(3):465–475, 1979. 35

[69] J Zheng. Étude analytique et numérique du bruit de combustion indirect généré par l'injection d'ondes entropiques dans une tuyère. PhD thesis, Université Paris Saclay, 2016. 38, 48

[70] A Emmanuelli. Numerical simulation and modelling of entropy noise in nozzle and turbine stator flows. PhD thesis, Université Paris Saclay, 2019. 38, 48

[71] Ignacio Duran and Stephane Moreau. Solution of the quasi-one-dimensional linearized Euler equations using flow invariants and the Magnus expansion. Journal of Fluid Mechanics, 723:190–231, 2013. 38

[72] C. L. Morfey. Sound radiation due to unsteady dissipation in turbulent flows. Journal of Sound and Vibration, 48(1):95–111, 1976. 41

[73] M. K. Myers. Transport of energy by disturbances in arbitrary steady flows. Journal of Fluid Mechanics, 226:383–400, 1991. 41, 42, 46

[74] F. Nicoud and T. Poinsot. Thermoacoustic instabilities: Should the Rayleigh criterion be extended to include entropy changes? Combustion and Flame, 142(1-2):153–159, 2005. 41, 42

[75] G. J. Bloxsidge, P. J. Langhorne, and A. P. Dowling. Reheat buzz: An acoustically coupled combustion instability. Part 2. Theory. Journal of Fluid Mechanics, 193:445–473, 1988. 41

[76] P Le Helley. Etude théorique et expérimentale des instabilités de combustion et de leur contrôle dans un brûleur laminaire prémélangé. PhD thesis, Université Paris Saclay, 1994. 42

[77] TJ Poinsot and SK Lele. Boundary conditions for direct simulations of compressible viscous flows. Journal of computational physics, 101:104–129, 1992. 42, 109, 119

[78] Boa Teh Chu. On the energy transfer to small disturbances in fluid flow (Part I). Acta Mechanica, 1(3):215–234, 1965. 45

[79] P. E. Doak. Momentum potential theory of energy flux carried by momentum fluctuations. Journal of Sound and Vibration, 131(1):67–90, 1989. 46

[80] Alexis Giauque, L. Selle, L. Gicquel, T. Poinsot, H. Buechner, P. Kaufmann, and W. Krebs. System identification of a large-scale swirled partially premixed combustor using LES and measurements. Journal of Turbulence, 6(21):N21, jan 2005. 48

[81] Maxime Huet and Alexis Giauque. A nonlinear model for indirect combustion noise through a compact nozzle. Journal of Fluid Mechanics, 733:268–301, sep 2013. 48

[82] J. Zheng, M. Huet, F. Cléro, A. Giauque, and S. Ducruix. A 2D-axisymmetric analytical model for the estimation of indirect combustion noise in nozzle flows. In 21st AIAA/CEAS Aeroacoustics Conference, 2015. 48

[83] Alexis Giauque, Franck Nicoud, and Michael Brear. Numerical Assessment of Stability Criteria from Disturbance Energies in Gaseous Combustion. 13th AIAA/CEAS Aeroacoustics Conference (28th AIAA Aeroacoustics Conference), 2007. 48

[84] M. Talei, M. Brear, F. Nicoud, D. Bodony, and Alexis Giauque. Transport of disturbance energy in hot and cold turbulent jets. In 13th AIAA/CEAS Aeroacoustics Conference, 2007. 48

[85] Thomas Planès, Scott Delbecq, and Antoine Salgas. Aeromaps: a framework for performing multidisciplinary assessment of prospective scenarios for air transport. Submitted to Journal of Open Aviation Science, 2023. 50

[86] Carlyle Reid. Overview of flight testing of ge aircraft engines' udf engine. In 24th Joint Propulsion Conference, page 3082, 1988. 50

[87] S. Goldstein and Aeronautical Research Council (Great Britain). Modern Developments in Fluid Dynamics: An Account of Theory and Experiment Relating to Boundary Layers, Turbulent Motion and Wakes. Number v. 2 in Modern Developments in Fluid Dynamics: An Account of Theory and Experiment Relating to Boundary Layers, Turbulent Motion and Wakes. Clarendon Press, 1950. 50

[88] Michael James Lighthill. On sound generated aerodynamically i. general theory. Proceedings of the Royal Society of London. Series A. Mathematical and Physical Sciences, 211(1107):564–587, 1952. 50

[89] Alan Powell. The reduction of choked jet noise. Proceedings of the Physical Society. Section B, 67(4):313, 1954. 50

[90] Alan Powell. On the aerodynamic noise of a rigid flat plate moving at zero incidence. The Journal of the Acoustical Society of America, 31(12):1649–1653, 1959. 50

[91] T Fukano, Y Takamatsu, and Y Kodama. The effects of tip clearance on the noise of low pressure axial and mixed flow fans. Journal of sound and vibration, 105(2):291–308, 1986. 50, 52

[92] K. Imaichi, M. Yama Oto, and M. Ichikawa. Experimental investigation into an axial fan noise. In Proceedings of the 4th Technical Application Conference, 790-8, pages 29–32, 1979. 50

[93] Thomas Rötger, Chris Eyers, and Roberta Fusaro. A review of the current regulatory framework for supersonic civil aircraft: Noise and emissions regulations. Aerospace, 11(1):19, 2023. 50

[94] Valdo Pagès, Pierre Duquesne, Stephane Aubert, Laurent Blanc, Pascal Ferrand, Xavier Ottavy, and Christoph Brandstetter. Uhbr open-test-case fan ecl5/catana. International Journal of Turbomachinery, Propulsion and Power, 7(2):17, 2022. 51, 56

[95] SAL Glegg, SM Baxter, and AG Glendinning. The prediction of broadband noise from wind turbines. Journal of sound and vibration, 118(2):217–239, 1987. 51

[96] Edmane Envia. Contra-rotating open rotor tone noise prediction. In 20th AIAA/CEAS Aeroacoustics Conference, page 2606, 2014. 51, 52, 53

[97] Richard Woodward, Christopher Hughes, Robert Jeracki, and Christopher Miller. Fan noise source diagnostic test–far-field acoustic results. In 8th AIAA/CEAS Aeroacoustics Conference & Exhibit, page 2427, 2002. 51

[98] Harold D Meyer and Edmane Envia. Aeroacoustic analysis of turbofan noise generation. Technical report, NASA, 1996. 52

[99] Thomas F Brooks and TH Hodgson. Trailing edge noise prediction from measured surface pressures. Journal of sound and vibration, 78(1):69–117, 1981. 52

[100] A McAlpine and MCM Wright. Acoustic scattering by a spliced turbofan inlet duct liner at supersonic fan speeds. Journal of Sound and Vibration, 292(3-5):911–934, 2006. 52, 53

[101] John M Tyler and Thomas G Sofrin. Axial flow compressor noise studies. Technical report, SAE Technical Paper, 1962. 53, 73

[102] Arthur Finez, Marc Jacob, Emmanuel Jondeau, and Michel Roger. Broadband noise reduction with trailing edge brushes. In 16th AIAA/CEAS aeroacoustics conference, page 3980, 2010. 53

[103] P Chaitanya, Phillip Joseph, Subramanyam Narayanan, Christina Vanderwel, Jacob Turner, Jae-Wook Kim, and Bharathram Ganapathisubramani. Performance and mechanism of sinusoidal leading edge serrations for the reduction of turbulence–aerofoil interaction noise. Journal of Fluid Mechanics, 818:435–464, 2017. 53

[104] Björn Greschner, Julien Grilliat, Marc C Jacob, and Frank Thiele. Measurements and wall modeled les simulation of trailing edge noise caused by a turbulent boundary layer. International Journal of Aeroacoustics, 9(3):329–355, 2010. 53

[105] Edmane Envia, Alexander G Wilson, and Dennis L Huff. Fan noise: a challenge to caa. International Journal of Computational Fluid Dynamics, 18(6):471–480, 2004. 53

[106] Andreas Herrig, Werner Würz, Thorsten Lutz, and Ewald Krämer. Trailing-edge noise measurements using a hot-wire based coherent particle velocity method. In 24th AIAA Applied Aerodynamics Conference, page 3876, 2006. 53

[107] Adil Cader, Cyril Polacsek, Thomas Le Garrec, Raphaël Barrier, François Benjamin, and Marc C Jacob. Numerical prediction of rotor-stator interaction noise using 3d caa with synthetic turbulence injection. In 2018 AIAA/CEAS Aeroacoustics Conference, page 4190, 2018. 53

[108] Vincent Jurdic, Antoine Moreau, Philip Joseph, Lars Enghardt, and John Coupland. A comparison between measured and predicted fan broadband noise due to rotor-stator interaction. In 13th AIAA/CEAS Aeroacoustics Conference (28th AIAA Aeroacoustics Conference), page 3692, 2007. 53, 54

[109] CH Sieverding, T Arts, R Dénos, and J-F Brouckaert. Measurement techniques for unsteady flows in turbomachines. Experiments in fluids, 28:285–321, 2000. 53, 54

[110] Maxime Fiore and Romain Biolchini. Numerical simulation of a counter-rotative open rotor using phase-lagged conditions: Initial validation on a single rotor case. Journal of Turbomachinery, 142(12):121002, 2020. 54

[111] Christoph Brandstetter, Valdo Pagès, Pierre Duquesne, Xavier Ottavy, Pascal Ferrand, Stéphane Aubert, and Laurent Blanc. Uhbr open-test-case fan ecl5/catana part 1: geometry and aerodynamic performance. In 14th European Conference on Turbomachinery Fluid dynamics & Thermodynamics, 2021. 56

[112] Valdo Pagès, Pierre Duquesne, Xavier Ottavy, Pascal Ferrand, Stephane Aubert, Laurent Blanc, and Christoph Brandstetter. Uhbr open-test-case fan ecl5/catana, part 2: Mechanical and aeroelastic stability analysis. In 14 th European Conference on Turbomachinery Fluid dynamics & Thermodynamics, 2021. 56

[113] Anne-Lise Fiquet, Xavier Ottavy, and Christoph Brandstetter. Uhbr open-test case fan ecl5/catana: non-linear analysis of non-synchronous blade vibration at part-speed conditions. In ISUAAAT-16, Toledo, Spain. September 19-23, 2022. 56

[114] Anne-Lise Fiquet, Alexandra P Schneider, Benoît Paoletti, Xavier Ottavy, and Christoph Brandstetter. Experiments on tuned uhbr open-test case fan ecl5/catana: stability limit. In ASME Turbo Expo, Boston, MA, USA. June 26 - 30, 2023. 56

[115] Man Mohan Rai and Nateri K Madavan. Multi-airfoil navier–stokes simulations of turbine rotor–stator interaction. Journal of Turbomachinery, 112(3), 1990. 56

[116] Olivier Colin and Michael Rudgyard. Development of high-order taylor–galerkin schemes for les. Journal of computational physics, 162(2):338–371, 2000. 57

[117] F. Nicoud, H. B. Toda, O. Cabrit, S. Bose, and J. Lee. Using singular values to build a subgrid-scale model for large eddy simulations. Physics of fluids, 23(8), 2011. 57

[118] T J&amp Poinsot and SK Lelef. Boundary conditions for direct simulations of compressible viscous flows. Journal of computational physics, 101(1):104–129, 1992. 57, 100

[119] Patrick Schmitt, Thierry Poinsot, Bruno Schuermans, and Klaus-Peter Geigle. Large-eddy simulation and experimental study of heat transfer, nitric oxide emissions and combustion instability in a swirled turbulent high-pressure burner. Journal of Fluid Mechanics, 570:17–46, 2007. 57

[120] Sheng-xian Shi, Ying-zheng Liu, and Jian-min Chen. An experimental study of flow around a bio-inspired airfoil at reynolds number 2.0× 103. Journal of Hydrodynamics, 24(3):410–419, 2012. 59

[121] Hui Hu and Zifeng Yang. An experimental study of the laminar flow separation on a low-reynolds-number airfoil. Journal of Fluids Engineering, 130(5), 2008. 59

[122] Theodoros Michelis, Serhiy Yarusevych, and Marios Kotsonis. On the origin of spanwise vortex deformations in laminar separation bubbles. Journal of Fluid Mechanics, 841:81–108, 2018. 59

[123] John William Kurelek, Marios Kotsonis, and Serhiy Yarusevych. Transition in a separation bubble under tonal and broadband acoustic excitation. Journal of Fluid Mechanics, 853:1–36, 2018. 59

[124] Richard D Sandberg and Neil D Sandham. Direct numerical simulation of turbulent flow past a trailing edge and the associated noise generation. Journal of Fluid Mechanics, 596:353–385, 2008. 59

[125] RD Sandberg, LE Jones, ND Sandham, and PF Joseph. Direct numerical simulations of tonal noise generated by laminar flow past airfoils. Journal of Sound and Vibration, 320(4-5):838–858, 2009. 59

[126] Lloyd E Jones, Neil D Sandham, and Richard D Sandberg. Acoustic source identification for transitional airfoil flows using cross correlations. AIAA journal, 48(10):2299–2312, 2010. 59

[127] Hao Wu, Marlene Sanjose, Stephane Moreau, and Richard D Sandberg. Direct numerical simulation of the self-noise radiated by the installed controlled-diffusion airfoil at transitional reynolds number. In 2018 AIAA/CEAS Aeroacoustics Conference, page 3797, 2018. 59

[128] Mathieu Deuse and Richard D Sandberg. Different noise generation mechanisms of a controlled diffusion aerofoil and their dependence on mach number. Journal of Sound and Vibration, 476:115317, 2020. 59

[129] Shubham Shubham, Richard D Sandberg, Stephane Moreau, and Hao Wu. Surface pressure spectrum variation with mach number on a cd airfoil. Journal of Sound and Vibration, 526:116762, 2022. 59

[130] Matthieu Queguineur, LYM Gicquel, F Dupuy, A Misdariis, and G Staffelbach. Dynamic mode tracking and control with a relaxation method. Physics of Fluids, 31(3), 2019. 61, 75

[131] Julien Grilliat, Marc Jacob, Roberto Camussi, and Giovanni Caputi-Gennaro. Tip leakage experiment-part one: Aerodynamic and acoustic measurements. In 13th AIAA/CEAS Aeroacoustics Conference (28th AIAA Aeroacoustics Conference), page 3684, 2007. 65

[132] Marc C Jacob, Emmanuel Jondeau, and Bo Li. Time-resolved piv measurements of a tip leakage flow. International Journal of Aeroacoustics, 15(6-7):662–685, 2016. 65

[133] Jérôme Boudet, Joëlle Caro, Bo Li, Emmanuel Jondeau, and Marc C Jacob. Zonal large-eddy simulation of a tip leakage flow. International Journal of Aeroacoustics, 15(6-7):646–661, 2016. 65

[134] Tao Zhu, Dominic Lallier-Daniels, Marlène Sanjosé, Stéphane Moreau, and Thomas Carolus. Rotating coherent flow structures as a source for narrowband tip clearance noise from axial fans. Journal of Sound and Vibration, 417:198–215, 2018. 65

[135] David Lamidel, Guillaume Daviller, Michel Roger, and Hélène Posson. Numerical prediction of the aerodynamics and acoustics of a tip leakage flow using large-eddy simulation. International Journal of Turbomachinery, Propulsion and Power, 6(3):27, 2021. 65

[136] Régis Koch, Marlène Sanjosé, and Stéphane Moreau. Large-eddy simulation of a single airfoil tip-leakage flow. AIAA Journal, 59(7):2546–2557, 2021. 65

[137] S Kang and C Hirsch. Tip leakage flow in linear compressor cascade. In Turbo Expo: Power for Land, Sea, and Air, volume 78910, page V03BT16A059. American Society of Mechanical Engineers, 1993. 65

[138] Donghyun You, Meng Wang, Parviz Moin, and Rajat Mittal. Large-eddy simulation analysis of mechanisms for viscous losses in a turbomachinery tip-clearance flow. Journal of Fluid Mechanics, 586:177–204, 2007. 65

[139] Mathilde Barrée and Ghislain Guerrero. Flight test: A key milestone for climate-neutral aircraft concepts validation and certification. International Foundation for Telemetering, 2021. 80, 141

[140] Jean Al-Am, Vincent Clair, Alexis Giauque, Jérôme Boudet, and Fernando Gea-Aguilera. A parametric study on the les numerical setup to investigate fan/ogv broadband noise. International Journal of Turbomachinery, Propulsion and Power, 6(2):12, 2021. 81

[141] Jean Al-Am, Vincent Clair, Alexis Giauque, Jérôme Boudet, and Fernando Gea-Aguilera. Effet du débit sur le bruit propre d'un étage soufflante/redresseur en régime d'approche. In Congrès des Jeunes Chercheurs en Mécanique-Méca-J, 2021. 81

[142] Jean Al Am, Vincent Clair, Alexis Giauque, Jérôme Boudet, and Fernando Gea-Aguilera. Direct noise predictions of fan broadband noise using les and analytical models. In 28th AIAA/CEAS Aeroacoustics 2022 Conference, page 2882, 2022. 81

[143] Jean Al-Am, Vincent Clair, Alexis Giauque, Jérôme Boudet, and Fernando Gea-Aguilera. Fan/ogv broadband noise predictions using les. In EuroHPC Summit Week 2022, 2022. 81

[144] Jean Al Am, Vincent Clair, Alexis Giauque, Jérôme Boudet, and Fernando Gea-Aguilera. Effet du débit sur le bruit propre dun étage soufflante/redresseur en présence dune bulle de recirculation. In 16ème Congrès Français d'Acoustique, CFA2022, 2022. 81

[145] Jean Al Am, Vincent Clair, Alexis Giauque, Jérôme Boudet, and Fernando Gea-Aguilera. Direct noise predictions of a 360 full fan stage using les. In AIAA AVIATION 2023 Forum, page 4295, 2023. 81

[146] Colin N Waters, Jan Zalasiewicz, Colin Summerhayes, Anthony D Barnosky, Clément Poirier, Agnieszka Gałuszka, Alejandro Cearreta, Matt Edgeworth, Erle C Ellis, Michael Ellis, et al. The anthropocene is functionally and stratigraphically distinct from the holocene. Science, 351(6269):aad2622, 2016. 85

[147] Alberto Guardone, Piero Colonna, Matteo Pini, and Andrea Spinelli. Nonideal compressible fluid dynamics of dense vapors and supercritical fluids. Annual Review of Fluid Mechanics, 56:241–269, 2024. 86, 87

[148] Philip A Thompson. A fundamental derivative in gasdynamics. The Physics of Fluids, 14(9):1843–1849, 1971. 86

[149] W. D. Hayes. The basic theory of gasdynamic discontinuities, fundamentals of gas dynamics (ed. HW Emmons), High Speed Aerodynamics and Jet Propulsion 3, 416-481, 1958. 86

[150] M. S. Cramer. Nonclassical dynamics of classical gases. In Nonlinear waves in real fluids, pages 91–145. Springer, 1991. 86

[151] H. A. Bethe. On the Theory of Shock Waves for an Arbitrary Equation of State, pages 421–495. Springer New York, New York, NY, 1998. 86

[152] Ya B ZelDovich. On the possibility of rarefaction shock waves. Zh. Eksp. Teor. Fiz, 4(16):337–363, 1946. 86

[153] Francisco J. Durá Galiana, Andrew P.S. Wheeler, Jonathan Ong, and CA de M Ventura. The effect of dense gas dynamics on loss in ORC transonic turbines. In Journal of Physics: Conference Series, volume 821:1. IOP Publishing, 2017. 86

[154] L Iapichino, W Schmidt, JC Niemeyer, and J Merklein. Turbulence production and turbulent pressure support in the intergalactic medium. Monthly Notices of the Royal Astronomical Society, 414(3):2297–2308, 2011. 87

[155] Akira Yoshizawa. Statistical theory for compressible turbulent shear flows, with the application to subgrid modeling. The Physics of fluids, 29(7):2152–2164, 1986. 87

[156] Parviz Moin, Kyle Squires, W Cabot, and Sangsan Lee. A dynamic subgrid-scale model for compressible turbulence and scalar transport. Physics of Fluids A: Fluid Dynamics, 3(11):2746–2757, 1991. 87

[157] Shigeo Kida and Steven A Orszag. Energy and spectral dynamics in decaying compressible turbulence. Journal of Scientific Computing, 7:1–34, 1992. 87, 90

[158] Kyle Squires and Otto Zeman. On the subgrid-scale modeling of compressible turbulence. Studying Turbulence Using Numerical Simulation Databases. 3: Proceedings of the 1990 Summer Program, 1990. 87

[159] P Colonna and ALBERTO Guardone. Molecular interpretation of nonclassical gas dynamics of dense vapors under the van der waals model. Physics of Fluids, 18(5), 2006. 88

[160] P. Bradshaw. Compressible turbulent shear layers. Annual Review of Fluid Mechanics, 9(1):33–52, 1977. 88

[161] Lishu Duan, Qinmin Zheng, Zhou Jiang, and Jianchun Wang. Dense gas effect on small-scale structures of compressible isotropic turbulence. Physics of Fluids, 33(11):115113, 2021. 89

[162] S.H. Fergason, T.L. Ho, B M Argrow, and G Emanuel. Theory for producing a single-phase rarefaction shock wave in a shock tube. Journal of Fluid Mechanics, 445:37–54, 2001. 91

[163] M. G. Costello, R. M. Flynn, and J. G. Owens. Fluoroethers and fluoroamines. Kirk-Othmer Encyclopedia of Chemical Technology, 2000. 91

[164] P. Colonna and A. Guardone. Molecular interpretation of nonclassical gas dynamics of dense vapors under the van der Waals model. Physics of Fluids, 18(5), 2006. 91

[165] T. S. Lundgren. Linearly forced isotropic turbulence. Annual Research Briefs, (2):461–473, 2003. 93

[166] Carlos Rosales and Charles Meneveau. Linear forcing in numerical simulations of isotropic turbulence: Physical space Implementations and convergence properties. Physics of Fluids, 17(9):1–8, 2005. 93

[167] Mark R. Petersen and Daniel Livescu. Forcing for statistically stationary compressible isotropic turbulence. Physics of Fluids, 22(11), 2010. 93

[168] Alexei G Kritsuk, Michael L Norman, Paolo Padoan, and Rick Wagner. The statistics of supersonic isothermal turbulence. The Astrophysical Journal, 665(1):416, 2007. 93

[169] Ravi Samtaney, D. I. Pullin, Branko Kosović, Branko Kosovic, and I Introduction. Direct numerical simulation of decaying compressible turbulence and shocklet statistics. Physics of Fluids, 13(5):1415–1430, 2001. 95

[170] A Giauque, C Corre, and M Menghetti. Direct numerical simulations of homogeneous isotropic turbulence in a dense gas. Journal of Physics: Conference Series, 821(1):1–10, mar 2017. 95

[171] Hussein Aluie. Scale locality and the inertial range in compressible turbulence. Bulletin of the American Physical Society, 57, 2012. 97

[172] Hussein Aluie, Shengtai Li, and Hui Li. The conservative cascade of kinetic energy in compressible turbulence. The Astrophysical Journal Letters, 751(2), 2012. 97, 99

[173] Hussein Aluie, Shengtai Li, and Hui Li. Scale decomposition in compressible turbulence. Physica D: Nonlinear Phenomena, 247(1):54–65, 2013. 97

[174] C. Pantano and S. Sarkar. A study of compressibility effects in the high-speed turbulent shear layer using direct simulation. Journal of Fluid Mechanics, 451:329–371, 2002. 101, 103, 109

[175] J. B. Freund, S. K. Lele, and P. Moin. Compressibility effects in a turbulent annular mixing layer. Part 1. Turbulence and growth rate. Journal of Fluid Mechanics, 421:229–267, 2000. 101

[176] Azeddine Kourta and R Sauvage. Computation of supersonic mixing layers. Physics of Fluids, 14(11):3790–3797, 2002. 101

[177] S. Fu and Q Li. Numerical simulation of compressible mixing layers. International journal of heat and fluid flow, 27(5):895–901, 2006. 101

[178] Q. Zhou, F. He, and M. Y. Shen. Direct numerical simulation of a spatially developing compressible plane mixing layer: flow structures and mean flow properties. Journal of Fluid Mechanics, 711:1–32, 2012. 101

[179] P. J. Martínez Ferrer, G. Lehnasch, and A. Mura. Compressibility and heat release effects in high-speed reactive mixing layers I.: Growth rates and turbulence characteristics. Combustion and Flame, 180(M):284–303, 2017. 101

[180] Kristen Matsuno and Sanjiva K Lele. Compressibility effects in high speed turbulent shear layers–revisited. In AIAA Scitech 2020 Forum, page 0573, 2020. 101

[181] Aurélien Vadrot, Alexis Giauque, and Christophe Corre. Analysis of turbulence characteristics in a temporal dense gas compressible mixing layer using direct numerical simulation. Journal of Fluid Mechanics, 893(A10), 2020. 102, 108, 110, 112, 138

[182] S. Pirozzoli, M. Bernardini, S. Marié, and F. Grasso. Early evolution of the compressible mixing layer issued from two turbulent streams. Journal of Fluid Mechanics, 777:196–218, 2015. 102

[183] Xavier Gloerfelt, Jean Christophe Robinet, Luca Sciacovelli, Paola Cinnella, and Francesco Grasso. Dense-gas effects on compressible boundary-layer stability. Journal of Fluid Mechanics, 893, 2020. 105

[184] L. Sciacovelli, P. Cinnella, and X. Gloerfelt. Direct numerical simulations of supersonic turbulent channel flows of dense gases. Journal of Fluid Mechanics, 821:153–199, 2017. 105

[185] Alberto Guardone and B M Argrow. Nonclassical gasdynamic region of selected fluorocarbons. Physics of Fluids, 17(11):1–17, 2005. 110

[186] Bert Vreman, Bernard Geurts, and Hans Kuerten. A priori tests of large eddy simulation of the compressible plane mixing layer. Journal of engineering mathematics, 29(4):299–327, 1995. 111

[187] G. Erlebacher, M. Y. Hussaini, C. G. Speziale, and T. A. Zang. Toward the large-eddy simulation of compressible turbulent flows. Journal of Fluid Mechanics, 238:155–185, May 1992. 112, 113

[188] David Baumgärtner, John J Otter, and Andrew PS Wheeler. The effect of compressibility factor on turbine performance. In Turbo Expo: Power for Land, Sea, and Air, volume 84966, page V004T06A020. American Society of Mechanical Engineers, 2021. 119, 120

[189] Jinhee Jeong and Fazle Hussain. On the identification of a vortex. Journal of Fluid Mechanics, 285:69–94, 1995. 119

[190] David Baumgärtner, John J. Otter, and Andrew P. S. Wheeler. The Effect of Isentropic Exponent on Transonic Turbine Performance. Journal of Turbomachinery, 142(8):081007, 2020. 121, 124

[191] Charles G Speziale. Galilean invariance of subgrid-scale stress models in the large-eddy simulation of turbulence. Journal of fluid mechanics, 156:55–62, 1985. 124, 125

[192] Antoine Vollant, Guillaume Balarac, and C Corre. Subgrid-scale scalar flux modelling based on optimal estimation theory and machine-learning procedures. Journal of Turbulence, 18(9):854–878, 2017. 125

[193] Fabian Pedregosa, Gaël Varoquaux, Alexandre Gramfort, Vincent Michel, Bertrand Thirion, Olivier Grisel, Mathieu Blondel, Peter Prettenhofer, Ron Weiss, Vincent Dubourg, et al. Scikit-learn: Machine learning in python. the Journal of machine Learning research, 12:2825–2830, 2011. 126

[194] Dask Development Team. Dask: Library for dynamic task scheduling, 2016. 126

[195] Paul Novello, Gaël Poëtte, David Lugato, and Pietro M Congedo. Explainable hyperparameters optimization using hilbert-schmidt independence criterion. 2021. 126

[196] Aurélien Géron. Hands-on machine learning with scikit-learn and tensorflow: concepts, tools. In And Techniques to Build Intelligent Systems. Nd. 2017. 128

[197] Masataka Gamahara and Yuji Hattori. Searching for turbulence models by artificial neural network. Physical Review Fluids, 2(5):054604, 2017. 130

[198] Zhuo Wang, Kun Luo, Dong Li, Junhua Tan, and Jianren Fan. Investigations of data-driven closure for subgrid-scale stress in large-eddy simulation. Physics of Fluids, 30(12), 2018. 130

[199] Alvaro Prat, Theophile Sautory, and S Navarro-Martinez. A priori sub-grid modelling using artificial neural networks. International Journal of Computational Fluid Dynamics, 34(6):397–417, 2020. 130

[200] Suraj Pawar, Omer San, Adil Rasheed, and Prakash Vedula. A priori analysis on deep learning of subgrid-scale parameterizations for kraichnan turbulence. Theoretical and Computational Fluid Dynamics, 34(4):429–455, 2020. 130

[201] Alexis Giauque, Christophe Corre, and Aurélien Vadrot. Direct numerical simulation of turbulent dense gas flows. In International Seminar on Non-Ideal Compressible-Fluid Dynamics for Propulsion & Power, pages 76–87. Springer International Publishing Cham, 2018. 138

[202] A Vadrot, A Giauque, and C Corre. Investigation of turbulent dense gas flows with direct numerical simulation. Congrès français de mécanique. AFM, 2019. 138

[203] Alexis Giauque, Aurélien Vadrot, Paolo Errante, and Christophe Corre. Towards subgrid-scale turbulence modeling in dense gas flows. In Proceedings of the 3rd International Seminar on Non-Ideal Compressible Fluid Dynamics for Propulsion and Power: NICFD 2020, pages 71–77. Springer International Publishing, 2021. 138

[204] D Schuster, Y Ince, Alexis Giauque, and Christophe Corre. Assessment of density and compressibility corrections for rans simulations of real gas flows using su2. In Proceedings of the 4th International Seminar on Non-Ideal Compressible Fluid Dynamics for Propulsion and Power. NICFD 2022., volume 29, pages 82–90. Springer Nature Switzerland, 2023. 138